

PHD THESIS

co-tutored by

UNIVERSITÉ DE RENNES 1

Institut d'Electronique et de Télécommunications de Rennes
Ecole doctorale MATISSE, Groupe Image et Télédétection

and

UNIVERSITÀ DEGLI STUDI DI ROMA TOR VERGATA

Dipartimento di Informatica, Sistemi e Produzione
Scuola di dottorato in GEOINFORMAZIONE

prepared by

Marco Lavalle

Full and Compact Polarimetric Radar Interferometry for Vegetation Remote Sensing

Presented to the jury composed by

15 December 2009, Rome

Riccardo LANARI

CNR-IREA, Napoli, Italy

Fabrizio LOMBARDINI

Università di Pisa, Pisa, Italy

Laurent FERRO-FAMIL

Université de Rennes 1, France

Domenico SOLIMINI

co-tutor of thesis

Università Tor Vergata, Rome, Italy

18 December 2009, Rennes

Alberto MOREIRA

DLR, Oberpfaffenhofen, Germany

Fabio ROCCA

Politecnico di Milano, Italy

Juan M. LOPEZ-SANCHEZ

Universidad de Alicante, Spain

Shane CLOUDE

University of York, United Kingdom

Yves-Louis DESNOS

European Space Agency, ESRIN, Frascati, Italy

Laurent FERRO-FAMIL

Université de Rennes 1, France

Eric POTTIER

co-tutor of thesis

Université de Rennes 1, France

Domenico SOLIMINI

co-tutor of thesis

Università Tor Vergata, Rome, Italy

December 2009

*In basic research,
intellectual rigor and sentimental freedom necessarily alternate.*

Victor Vasarely (1906-1997)

*To my parents,
who always let me follow my own route.*

Abstract

This dissertation addresses primarily the role that polarimetric and interferometric radars play in geosciences applications, with particular focus on forest remote sensing. It is shown that current simplified models of spatial correlation of natural media are able to retrieve robustly the forest height and the biomass when the topography is predominantly flat or its effects are properly compensated. Temporal correlation is addressed more accurately by defining a height-dependent temporal correlation function in the vegetation canopy. The effects of this improvement on the forward and inverse modeling are discussed. At lower frequencies, a simplified relationship of these models is proposed and validated. We use both polarimetric space-borne data and scattering numerical simulations to illustrate the results. For compact polarimetric radars, the pseudo-reconstruction is generalized to the interferometric scenario and it is demonstrated to be effective only for certain combinations of volume and ground surface components. Finally, the aspect of data quality is considered, proving that Faraday rotation can be estimated and corrected from unfocussed radar echoes and that gridded corner reflectors may serve as radiometric calibrators of dual polarimetric data.

Contents

Symbols and acronyms	xii
Preface	xvii
1 Introduction	1
1.1 Background and motivation	1
1.2 SAR remote sensing	2
1.2.1 SAR polarimetry	4
1.2.2 SAR interferometry	5
1.2.3 SAR tomography	6
1.3 Scope, objectives and novelties of the thesis	7
1.4 Thesis outline	9
2 Microwave scattering and system modeling	11
2.1 Microwave scattering	11
2.1.1 General problem formulation	12
2.1.2 Review of scattering vegetation models	14
2.2 Synthetic aperture radar imaging model	16
2.3 Scattering and SAR image numerical simulator PPSIM	19
2.3.1 Ground surface	20
2.3.2 Trees and short vegetation	20
2.3.3 Coherent image formation	21
3 Full Polarimetric SAR Interferometry	25
3.1 Forward models of interferometric coherence	25
3.1.1 Basics of polarimetric SAR interferometry	26
3.1.2 Spatial correlation model	29
3.1.3 Temporal correlation model	37
3.2 Methods for coherence parameter estimation	43
3.2.1 Estimation of the temporal correlation function	45
3.2.2 Best polarization selection	47
3.2.3 Estimation of ground phase topography	53
3.2.4 Estimation of vegetation height	55

CONTENTS

3.3	Parametric analysis using PSPSIM	60
3.3.1	Validity range of RVOG model	60
3.3.2	POLINSAR descriptor extraction and sensitivity	76
3.4	ALOS/PALSAR observations	77
3.4.1	Description of the dataset	78
3.4.2	Results of the POLINSAR processing	81
3.5	P-band modeling	85
3.5.1	Introduction	86
3.5.2	P-band dual-polarimetric interferometric model	87
3.6	Conclusions	93
4	Compact Polarimetric SAR Interferometry	95
4.1	Compact polarimetry	95
4.1.1	Theoretical formulation	98
4.1.2	Pseudo-reconstruction of the coherency matrix	100
4.2	Compact polarimetric SAR interferometry	105
4.2.1	Theoretical formulation	107
4.2.2	Experimental results	112
4.2.3	Simplified model analysis	117
4.3	Effects of the SAR processor and receiver	122
4.4	Conclusions	127
5	Polarimetric calibration and Faraday rotation estimation	129
5.1	Background	129
5.1.1	Polarimetric data calibration	130
5.1.2	Faraday rotation correction	132
5.2	Faraday rotation from unfocussed SAR data	133
5.2.1	Unfocussed Faraday rotation model	134
5.2.2	PALSAR data observations	137
5.3	Dual Polarimetric calibration model	142
5.3.1	Calibration distortion model	142
5.3.2	Targets	143
5.3.3	Calibration Procedure	147
5.3.4	Sentinel-1 performance analysis	149
5.4	Conclusions	152
	Conclusions and future perspectives	154
	Bibliography	163

List of Figures

2.1	Scattering problem scenario and coordinate system.	12
2.2	Representation of the SAR imaging system model of equations (2.7), (2.8) and (2.9). The x - and h -axes are rotated by 90 deg with respect to the coordinate system of Fig. 2.1.	17
2.3	Example of PPSIM simulation at L-band of Scots pines 24 m tall, acquired with 45 deg angle of incidence. The total backscatter images, the direct-volume $\sigma^{(dv)}$, the direct-ground $\sigma^{(dg)}$ and the ground-volume $\sigma^{(gv)}$ at HH, HV and VV polarization are shown.	23
3.1	Geometrical scenario of a SAR interferometer.	27
3.2	Schematic representation of coherence models for a random distribution of scatterers. Input parameters to the models are highlighted in red color.	31
3.3	Interferometric coherence of a layer of randomly oriented scatterers corresponding to equation (3.14).	33
3.4	Coherence magnitude and phase of a random volume layer of scatterers over a ground surface.	35
3.5	Line models in the complex plane of the spatial correlation of RVoG (a) and of the temporal decorrelated RVoG using the temporal correlation function (b).	36
3.6	Temporal correlation function versus canopy vertical dimension and time.	39
3.7	Schematic representation of temporal decorrelated RVoG model. Red parameters characterize the spatial (volume) correlation; blue parameters account for the characterization of temporal decorrelation effects.	40
3.8	Coherence magnitude and phase of a temporal decorrelated random volume layer of particles over a ground surface. Only the temporal decorrelation factor is plotted.	44
3.9	Example of coherence region and approximate polygons in the complex plane for $N = 6$ (a). The Magnitude Difference algorithm gives potentially higher coherence amplitude than the Phase Diversity optimization (b).	50
3.10	Methods for estimating line model parameters discussed in Sec. 3.2.3.	53
3.11	Geometrical interpretation of the inversion strategies adopted for the canopy height estimation.	56

LIST OF FIGURES

3.12 Logical steps for the assessment of the RVoG model using PSPSIM assuming different forest height and terrain slope. 61

3.13 Total and selective backscatter of a Pine forest obtained through numerical simulations using PSPSIM. The near-range is the bottom of the images. . . . 70

3.14 Ground-to-volume ratio of a Pine forest versus forest height obtained through numerical backscatter simulation (a). Performance of RVoG model inversion (b). The grey intensity in vertical bars is proportional to RMS error. . . . 70

3.15 Coherence of a Pine forest obtained through POLINSAR processing of backscattering numerical simulations. 71

3.16 Coherence of a Pine forest obtained through POLINSAR processing of numerical simulations of complex backscatter (PSPSIM). 71

3.17 Total and selective backscatter of a Pine forest obtained through numerical simulations using PSPSIM. The near-range is the bottom of the images. . . . 72

3.18 Ground-to-volume ratio of a Pine forest versus azimuth terrain slope obtained through numerical simulation (a). Performance of RVoG model inversion (b). The grey intensity in vertical bars is proportional to RMS error. 72

3.19 Total coherence of a Pine forest obtained through POLINSAR processing of backscattering numerical simulations. The near-range is the bottom of the images. 73

3.20 Residual coherence of a Pine forest obtained through POLINSAR processing of numerical simulations of complex backscatter (PSPSIM). 73

3.21 Total and selective backscatter of a Pine forest obtained through numerical simulations using PSPSIM. The near-range is the bottom of the images. . . . 74

3.22 Ground-to-volume ratio of a Pine forest versus azimuth terrain slope obtained through numerical simulation (a). Performance of RVoG model inversion (b). The grey intensity in vertical bars is proportional to RMS error. 74

3.23 Total coherence of a Pine forest obtained through POLINSAR processing of backscattering numerical simulations. The near-range is the bottom of the images. 75

3.24 Residual coherence of a Pine forest obtained with POLINSAR processing of numerical simulations of complex backscatter (PSPSIM). 75

3.25 Example of parametric analysis using PPSIM simulation to assess the impact of the look angle on the POLINSAR observable and ground-to-volume ratio. . . 76

3.26 POLINSAR ALOS/PALSAR acquisitions over Amazon forest (Brazil). 79

3.27 Polarimetric ALOS/PALSAR acquisition over Amazon forest (Brazil). 80

3.28 Polarimetric ALOS/PALSAR acquisitions over Amazon forest (Brazil). 82

3.29 Histograms of the optimized coherence shown in Fig. 3.28c and of the uncompensated forest height shown in Fig. 3.28d 83

3.30	Examples of X- and P-band GEOSAR acquisitions of an area containing tropical forest and cultivation. Color scales differ between bands.	86
3.31	Scenario of the P-band scattering model.	87
3.32	Coherence magnitude and phase of the two models (3.77). Model 1 is the uniform profile, Model 2 is the exponential profile.	88
3.33	Examples of PSPSIM outputs at P-band. Vegetation height is 20 m.	90
3.34	Test of the approximations using PSPSIM simulations.	91
3.35	Test of the inversion procedure using PSPSIM simulations. Model 1 is the uniform profile, Model 2 is the exponential profile.	92
4.1	Classification of emerging compact SAR modes in contrast with the classical SAR modes.	96
4.2	Diagram of the relationships among the elements of the covariance matrix under different symmetry assumptions.	102
4.3	Original full polarimetric Pauli decomposition (a) over Flevoland (The Netherlands) and associated pseudo-reconstruction from compact polarimetry using the $\pi/4$ mode (b) and the $\pi/2$ mode (c). Note the presence of all color components in the reconstructed images. The matching between full-pol and compact-pol, however, depends on the symmetry assumptions.	106
4.4	Logical steps for the assessment of the performances of compact POLINSAR.	113
4.5	Full polarimetric image of the Traunstein forest acquired by the DLR E-SAR sensor (a) and reconstructed polarimetric image from a compact polarimetric dataset (b)-(c). Color coding: red ($ VV $), blue ($ HH $), green ($ HV $). Notice the presence of all color components in the reconstructed images.	114
4.6	Coherence maps (top) and interferograms (bottom) of the HH polarization in the three considered architectures: full polarimetry, compact polarimetry with linear transmission and compact polarimetry with circular transmission. Color coding: black ($ \gamma = 0$), white ($ \gamma = 1$), red ($\angle\gamma = -\pi$), blue ($\angle\gamma = \pi$).	115
4.7	Row profiles of the magnitude (left plots) and phase (right plots) of the interferometric coherence for the polarizations HH (top), HV (middle), VV (bottom). The transect is across the vegetated area of Fig. 4.5.	116
4.8	Row profiles of the indicators of reflection symmetry and rotation invariance of cross-polarization terms. The transect is across the vegetated area of Fig. 4.5.	117
4.9	Comparison between left (F_1) and right (F_2) hands of equations (4.37) and (4.39), indicated respectively by F_i^{xrot} and F_i^{az} , $i = 1, 2$	121
4.10	Comparison of the four Stokes parameters in the synthesis of the $\pi/4$ mode before and after the SAR focusing.	123
4.11	Simplified architecture of a SAR receiver chain similar to that of ALOS/PALSAR (courtesy of Dr. M. Shimada).	124

LIST OF FIGURES

4.12 Simulation of compact polarimetric data with synthesis after coherent reception. 125

4.13 Simulation of compact polarimetric data with synthesis before coherent reception. 126

5.1 Logical scheme of the SAR acquisition process showing the sources of polarimetric distortions (system transmission/reception and ionosphere) and the associated matrices (**T**, **R** and **F**). 131

5.2 Synthetic aperture and ionospheric effect. In the case of ALOS/PALSAR $D_{iono} = 27$ km, $d_g = 16$ km and $\Delta d_g = 1.8$ m. 133

5.3 Full polarimetric image acquired by ALOS/PALSAR over South Italy. Note the features in the Faraday rotation angle estimated from SLC data. 138

5.4 Comparison of Faraday rotation angle estimated from SLC data and raw data using the PALSAR product of Fig. 5.3. Histograms and profiles averaged along range and azimuth directions are shown. 139

5.5 Extensive analysis over several PALSAR products for the assessment of the effects of the SAR processor (a) and the effects of the polarimetric calibration matrices (b). 140

5.6 Targets proposed for the polarimetric calibration of a dual-pol SAR data. The gridded trihedral is depicted with the modification proposed by Ainsworth (2008). 144

5.7 Basic steps for the polarimetric calibration of dual-pol SAR data. 149

5.8 Plots of targets beamwidth and polarimetric noise for the gridded trihedral and dihedral using the system parameters of the future ESA mission SENTINEL-1. 150

Symbols and acronyms

Throughout this thesis dissertation, simple physical variables are usually indicated by lower case letters, taken from the Greek or Latin alphabet. Matrices are indicated by capital letters. For vectors and matrices the boldface version of the letter is used. The dependence of the variable on the polarization state or interferometric pass is indicated by a lower script notation. As an example, σ_{hh_1} is the total HH backscatter of the first interferometric measurement. When the pass is not specified (e.g. σ_{hh}) we indicate a generic acquisition; when the polarization is not specified (e.g. σ_1) we refer to any generic polarization state. If necessary, direct-volume (dv), direct-ground (dg) and ground-volume (gv) components are indicated with an upper script notation, e.g. $\sigma_{hh}^{(dv)}$. Radar images are showed along with two axes indicating the increasing direction of range and azimuth coordinates. The following list contains the symbols and the acronyms adopted along with the associated meaning.

z	Vertical dimension of the imaged medium
$\sigma_s(z)$	Mean radar cross section (backscattering) of a single scatterer
$n(z)$	Density of scatterers per unit length
ς	Mean radar cross section per unit length
μ	Ground-to-volume scattering ratio
σ	Total radar cross section of the medium
$L(z)$	Total extinction through the medium
κ_e	Extinction coefficient
$\tau(z)$	Time constant of the temporal correlation function $\xi(z, t)$
τ_g	Time constant of the ground surface
τ_v	Time constant of the canopy at reference height h_r .
t	Time
σ_B	Standard deviation of the Brownian motion of the scatterers
λ	Radar wavelength
γ	Complex (degree of) coherence of two radar measurements
γ_s	Spatial correlation (coherence)
γ_t	Temporal correlation (coherence)

SYMBOLS AND ACRONYMS

γ_{snr}	SNR correlation (coherence)
$\gamma^{(td)}$	Complex coherence of temporal decorrelated radar measurements
γ_v	Complex coherence of RV model
$\gamma_{g,v}$	Complex coherence of RVOG model
$\xi(z, t)$	Temporal correlation function
$\mathbf{\Pi}$	Whitened cross-coherency POLINSAR matrix
\mathbf{E}^i	Incident electric field
E_h^i	Incident electric field amplitude (horizontal component)
E_v^i	Incident electric field amplitude (vertical component)
\mathbf{E}^s	Scattered electric field
E_h^s	Scattered electric field amplitude (horizontal component)
E_v^s	Scattered electric field amplitude (vertical component)
$\hat{\mathbf{h}}$	Unit vector of horizontal polarization
$\hat{\mathbf{v}}$	Unit vector of vertical polarization
\mathbf{S}	Complex scattering (or Sinclair) matrix
s_{pq}	Complex Scattering amplitude, $p, q = h, v$
f_{pq}	Forward model function, $p, q = h, v$
r	Distance between radar and target
θ	Angle of incidence on the zero-Doppler plane (range)
$\Delta\theta$	Interferometric angle of incidence difference
ϕ	Angle of squint incidence (azimuth)
k_0	Wavenumber (spatial frequency)
k_z	Vertical wavenumber
ϵ_g	Complex permittivity of soil
ϵ_v	Complex permittivity of vegetation
Q_{pq}	System point spread function, $p, q = h, v$
\mathbf{s}	Spatial location of the effective scattering center
B_s	Spatial interferometric baseline
B_{\perp}	Spatial interferometric normal baseline
T	Temporal baseline
\mathbf{k}_P	Pauli polarimetric target vector
\mathbf{k}_L	Lexicographic polarimetric target vector
\mathbf{w}	Scattering mechanism vector
φ	Interferometric phase (coherence phase)
χ	Optimized interferometric phase difference

φ_g	Interferometric ground phase
$\varphi_{h/2}$	Interferometric half-canopy phase
$\varrho(z)$	Vertical complex reflectivity per unit length
$\rho(z)$	Vertical structure function
z_g	Ground reference height
z_v	Top-canopy reference height
h_v	Vegetation height
h_b	Vegetation height bias
h_r	Vegetation reference height for temporal decorrelation
H	Normalized interferometric phase height
H_s	Satellite altitude
m	Polarization-dependent factor, $m = \mu/(\mu + 1)$
$\delta(z)$	Dirac's delta
\mathbf{T}	Coherency matrix
\mathbf{C}	Covariance matrix
$\mathbf{\Omega}_{12}$	Cross-covariance matrix
\mathbf{T}_6	POLINSAR coherency matrix
$\tilde{\mathbf{T}}_6$	Whitened POLINSAR coherency matrix
\mathbf{C}_6	POLINSAR covariance matrix
N	Number of samples for computing the coherence region
a	Slope of the coherence line model
b	Intercept of the coherence line model
ν	Calibration parameter for coherence inversion
N_f	Number of carrier frequencies operated by the radar
N_b	Number of interferometric baselines
α_c	Calibration parameter for the estimation of μ
F_{pq}	General forward model function, $p, q = h, v$
r	Slant-range distance
\mathcal{F}	Fourier operator
\mathcal{N}	Gaussian probability density function
α_{ref}	Estimator of reflection symmetry
α_{xrot}	Estimator of cross-rotation symmetry

SYMBOLS AND ACRONYMS

CODE	Center for Orbit Determination in Europe
CP	Compact Polarimetry
C-POLINSAR	Compact Polarimetric SAR Interferometry
DEM	Digital Elevation Model
DLR	German Space Agency
DSM	Digital Surface Model
ESA	European Space Agency
FR	Faraday Rotation
F-POLINSAR	Full Polarimetric SAR Interferometry
GT	Gridded Trihedral
INSAR	Interferometric SAR
IPCC	Intergovernmental Panel on Climate Change
JAXA	Japan Aerospace Exploration Agency
JPL	Jet Propulsion Laboratory
LAI	Leaf Area Index
MD	Magnitude Difference
PALSAR	Phased Array type L-band Synthetic Aperture Radar
PCT	Polarization Coherence Tomography
PD	Phase Diversity
POLINSAR	Polarimetric SAR Interferometry
POLSAR	Polarimetric SAR
POLSARPRO	Polarimetric SAR Data Processing and Educational Tool
PRF	Pulse Repetition Frequency
PSPSIM	PolSARPro Simulator
RV	Random Volume
RVoG	Random Volume Over Ground
SAR	Synthetic Aperture Radar
SNR	Signal Noise Ratio
SPM	Small Perturbation Model
SQNR	Signal Quantization Noise Ratio
SRTM	Shuttle Radar Topography Mission
TD	Temporal Decorrelation
TD-RV	Temporal Decorrelated Random Volume
TD-RVoG	Temporal Decorrelated Random Volume Over Ground
TEC	Total Electron Content

Preface

This PhD dissertation collects the progress and the results obtained from September 2006 through December 2009 while I was enrolled in the PhD program at University of Rennes 1, Rennes, France, and University of Rome Tor Vergata, Rome, Italy.

The thesis work was carried out in the frame of two co-tutorship programs signed between University of Rome Tor Vergata and University of Rennes 1, and between University of Rome Tor Vergata and the European Space Research Institute (ESRIN) of the European Space Agency (ESA). Most of the time during the three-year PhD program was spent at ESA/ESRIN in Frascati, Italy, with regular visits to the laboratory of GeoInformation and Applied Electromagnetics at Tor Vergata University and to the laboratory of Radar Signal Processing at University of Rennes. Therefore, this thesis is the result of the stimulus and interactions that I have collected during my stay at ESRIN, in Rome and in Rennes. The material presented here is the product of extremely various discussions with people that I had the opportunity to meet.

Looking back into the past three years, I would like to thank Prof. Domenico Solimini who first introduced myself in the field of radar remote sensing, followed actively every single advance of my research and left me with the freedom necessary to develop my own ideas. I would like to express also my sincere gratitude to Prof. Eric Pottier who let me join his team and was always available for discussions and explanations. Many thanks also to the members of the PhD committee listed on the cover of this dissertation who reviewed the dissertation and provided valuable feedback to improve the work.

My gratitude goes to all people from the European Space Agency in Frascati, Rome, who made possible the collaboration with the University of Rennes and University Tor Vergata in Rome. Among those, Francesco Sarti, Henri Laur and Yves-Louis Desnos deserve special thanks as they were the main promoters of the collaboration and were always ready to offer their support. I would like also to thank Betlem Rosich, Maurizio Fea, Luigi Fusco, Nuno Miranda, Olivier Colin, Roberto Cossu and Fabio Martinelli who played important roles for achieving the results presented in this dissertation.

During international conferences I had the opportunity to talk with many people from the scientific community. They really provided me with material, help and suggestions to recover from mistakes and to advance in this thesis. I would like to thank M.L. Williams, M. Shimada, D. Small, K.P. Papathanassiou, S.R. Cloude, T. Ainswoth, P. Pasquali, D. D'Aria, P. Dubois and W.M. Boerner.

PREFACE

Thanks to the members of the GeoInformation laboratory in Rome, with whom I had the privilege to share in a friendly atmosphere and most of my PhD experience. I would like to thank for this Chiara S., Andrea M., Andrea D., Riccardo D., Cosimo P., Alessandro B., Antonio B., Federico D., Emanuele L., Lino S., Emanuele A., Giorgio L. and Fabio P., Jolanda P., Nicole D. and Manuel B.

During my stay at the University of Rennes 1, I found as well an exceptional atmosphere with Joëlle D., Yue H., Sophie A., Sandrine D., Cécile L., Laurent F., Stéphane M., Shaharyar A.K., Stéphane M., Nicolas L., Cédric L., Frank F., Thomas R., Mauro E. and Cao F.

I hope the dissertation will be helpful to students and scientists who conduct their research on radar remote sensing and are inspired by Richard Feynman's quote reported in Chapter 1: "The worthwhile problems are the ones you can really solve or help solve, the ones you can really contribute something to. No problem is too small or too trivial if we can really do something about it."

Marco Lavalle, December 2009

Chapter 1

Introduction

The worthwhile problems are the ones you can really solve or help solve, the ones you can really contribute something to. No problem is too small or too trivial if we can really do something about it.

Richard Feynman (1918-1988)

This chapter introduces the role of synthetic aperture radars (SAR) for monitoring the terrestrial environment. Emphasis is given to the problem of biomass estimation, which in turn motivates this PhD work. Its importance for Earth's ecosystem is briefly discussed in Sec. 1.1. The general aspects of the radar remote sensing are provided in Sec. 1.2, along with an overview of three major techniques: polarimetry, interferometry and tomography. It is not intended to give an exhaustive presentation of these arguments, but rather to provide the reader with the boundaries of the topics treated in the dissertation. Sec. 1.3 summarizes the scope, the objectives and our novel ideas introduced in the field of SAR vegetation remote sensing. Finally, Sec. 1.4 concludes the chapter with an outline of this dissertation.

1.1 Background and motivation

Earth observation from space has been recognized as an invaluable tool for monitoring the terrestrial environment. The need to obtain timely and accurate measurements of Earth's ecosystem is driven by scientific and pragmatic reasons. The former aims at gaining a deeper understanding of the complex processes ongoing on the Earth; the latter is related with the applications and in particular with the correct management of natural resources and planning of human activities. Indeed, nowadays there are evidences that climate and climate changes on the Earth have anthropogenic influences, especially on the release of carbon dioxide (CO₂) into the atmosphere (IPCC, 2007). The present PhD work is motivated by the actual lack of complete understanding of the *carbon cycle*, i.e. the ensemble of processes by which carbon is exchanged between the atmosphere, land and oceans. It is known that *forest biomass*, i.e. the amount of living organic matter in a given forested area, represents an important sink of carbon in

the *carbon budget*. However, there are still large uncertainties in quantifying its spatial distribution and variation over the time (Davidson, 2008).

Microwave remote sensing of vegetation offers two separate methods to estimate forest biomass. The first method relies on the relationship between the electromagnetic energy backscattered by plants and trees and their carbon content (Le Toan et al., 1992; Beaudoin et al., 1994)

$$\text{radar backscatter} = f(\text{biomass}) \quad (1.1)$$

where $f(\cdot)$ is found by regression of the radar intensity at single or multiple channels. While this approach is general and provides a simple inverse problem, it gives unacceptable uncertainty in the estimation of large biomass stocks (Imhoff, 1995). For this reason, a second complementary method based on the theoretical relationship between biomass and vegetation height (Enquist et al., 1998) was developed

$$\text{biomass} \propto (\text{forest height})^\alpha \quad (1.2)$$

wherein α is a model parameter. This approach is based on the estimation of forest height by means of *polarimetric and interferometric SAR* (POLINSAR), hence requires a greater system complexity but ensures the retrieval of the biomass on a wider range of values (Treuhaft and Siqueira, 2000; Cloude and Papathanassiou, 1998).

Due to the major system complexity of polarimetric radars with respect to single-channel radars, very recently there have been emerging simplified polarimetric SAR architectures, named *compact polarimetric SAR* (Souyris et al., 2005; Raney, 2007). A compact polarimetric SAR is essentially a dual polarimetric SAR wherein the transmission is a linear combination of horizontal and vertical polarizations. While this architecture relaxes the system constraints in terms of coverage and downloading rate, its effectiveness for geosciences applications needs still to be addressed. The next sections give more details on the technical aspects of the SAR remote sensing and its related multi-channel extensions.

1.2 SAR remote sensing

According to a general definition, *synthetic aperture radar* is a microwave imaging method used to map the scattering properties of the Earth's surface. The main difference with conventional *real aperture radar* is its higher resolution, achieved by exploiting the Doppler shifts of the received electromagnetic echoes, as discovered by Wiley in 1951. SAR technology is based on the active illumination of portions of the Earth and on the coherent recording of the scattered field. In the science of remote sensing, and particularly in geosciences, SAR has the advantage to operate almost in-

dependently of the natural illumination (as an active sensor) and weather conditions (as a microwave sensor). Moreover, its inherent imaging characteristic makes SAR measurements sensitive to dielectric and morphological properties of natural media, and consequently complementary to optic observations. For these reasons, SAR technology has found in the last four decades several applications in many fields such as geology, hydrology, agriculture, forestry, oceanography, snow and ice, land cover and height mapping, urban planning, volcanology, disaster and emergency prediction and management (Henderson and Lewis, 1998). Besides these advantages, raw SAR acquisitions are far to be conventional images; they rather resemble holograms wherein the useful information is hidden. In order to form the image, a considerable amount of signal processing needs to be done (Cumming and Wong, 2005). With the advent of DSP techniques and powerful computational resources, however, this is not anymore a limiting factor for the development of SAR applications.

Since the launch of the first spaceborne SAR (SEASAT, L-band) by the Jet Propulsion Laboratory, several SAR missions have been operating and many are planned in the next future. Among those, notables are the SIR-C, the NASA SAR system on-board the Space Shuttle in 1994 with multi-polarization and multi-frequency capabilities (cf. Sec. 1.2.2); ERS-1/2, the C-band twin European Remote Sensing satellites launched by ESA in 1991 and 1995 respectively, that allowed the demonstration of repeat-pass interferometry (cf. Sec. 1.2.2); J-ERS, the L-band Japanese Earth Remote Sensing Satellite launched in 1992; RADARSAT-1/2, the C-band satellites launched by the Canadian Space Agency in 1995 and 2007 respectively, now with full-polarimetric capabilities; SRTM, the Shuttle Radar Topography Mission in 2000 that delivered the first almost complete topographic height map of the Earth's surface; ENVISAT/ASAR, the European Environment Satellite with its C-band Advanced SAR launched in 2002; ALOS/PALSAR, the Japanese Phased Array L-band SAR operating since the beginning of 2006; the X-band SAR TERRASAR-X launched in 2009 by the German Aerospace Center (DLR); COSMO-SKYMED, the recent Italian Constellation of Small Satellites for Mediterranean basin Observation that comprises four X-band SARs, three of them already in orbit. New SAR missions are planned in the future, such as SENTINEL-1, ALOS-2, DESDYNI, TANDEM-X, TERRASAR-L/TANDEM-L and SAOCOM.

A peculiarity of the SAR imaging process is the mapping of semi-transparent and volumetric media from a 3-dimensional space to a 2-dimensional space. Inevitably, a dimension about the structure of the medium is lost. In the last 2 decades, it has been recognized that the extension of SAR data to multi-polarization, multi-frequency, multi-pass and multi-angle observations has the potential to discern the structural properties of natural media. Two of these extensions are already implemented in operative scenarios, namely SAR polarimetry (Sec. 1.2.1) and SAR interferometry (Sec. 1.2.2). Finally, the most complete technique for retrieving the 3-dimensional structure of the

imaged medium is named SAR tomography and is discussed in Sec. 1.2.3.

1.2.1 SAR polarimetry

Electromagnetic waves have an intrinsic vector nature, and the complete description of propagation and scattering phenomena requires the introduction of the wave polarization concept. *SAR polarimetry* (POLSAR) is the technique that is concerned with the acquisition, processing and analysis of polarization states or radar images. This yields a matrix formulation in place of a scalar formulation typical of the single channel SAR. Indeed, studies on radar polarimetry began with the scattering matrix introduced by Sinclair (1950) and later formalized by several pioneers, notably Ken- nough (1951) and Huynen (1970). Their work was promoted by Boerner et al. (1981) and found application with the availability of first polarimetric data acquired by the NASA/JPL AIRSAR system (Zebker and van Zyl, 1991). Since then, other polarimet- ric SAR missions followed, such as those mentioned previously. For the purpose of our work, a crucial event was the launch of ALOS/PALSAR in 2006, when this PhD work started. PALSAR was the first spaceborne polarimetric L-band SAR and made possible the on-orbit demonstration of polarimetric techniques, especially related to vegetation. The power of polarimetry lies in the ability to classify the scattering mechanisms and hence to decompose complex scattering from natural media into elementary scatter- ing processes. This turns useful for detection, segmentation, classification and inverse problems in geosciences (Cloude and Pottier, 1996, 1997; Lee et al., 1999; Rignot and Chellappa, 1992; van Zyl, 1989).

From an architectural point of view, a polarimetric SAR system is more complex than a single-polarization system concerning both the transmitter and the receiver side. It transmits microwave energy interleaved at horizontal and vertical polariza- tions, and must record coherently all four combinations of polarization states. The former characteristic reduces the swath width compared to a single-channel transmitter with same characteristics; the latter yields a larger amount of data to be stored and downloaded. For these reasons, an operational polarimetric SAR has also single- and dual-polarimetric capabilities, meaning the possibility to transmit only one polarization state and to receive simultaneously two orthogonal polarizations.

Very recently, a hybrid approach between full and dual polarimetry has become pop- ular in SAR remote sensing. The approach is concerned with the transmission of a generic polarized wave (neither vertical nor horizontal) and the reception of vertical and horizontal wave components (Raney, 2007; Souyris et al., 2005). In this configura- tion the system complexity is reduced, the interleaved transmission is avoided and the amount of data is halved as in the dual-polarimetric mode. Moreover, a hybrid SAR has the potential to carry more information about the scattering mechanisms observed

by a dual polarimetric mode. Whether this information is sufficient for SAR remote sensing applications and can replace the full polarimetric SAR is currently matter of debates. Further details on compact polarimetry and its state of the art are provided in Chapter 4.

1.2.2 SAR interferometry

When two or more coherent SAR images of the same scene are formed from (slightly) different look directions, the complex correlation between pairs of images can be evaluated and the system is said to operate as a *SAR interferometer* (INSAR). The basic principles of SAR interferometry were first introduced by Graham (1974) and the first attempt of single-pass interferometry was conducted by Zebker and Goldstein (1986) using the AIRSAR system. Later, Gabriel and Goldstein (1988) demonstrated the repeat-pass interferometry on SEASAT data and new results followed (Prati et al., 1989). With the launch of ERS-1 and ERS-2 satellites by ESA, a large amount of data was available for the purpose of this technique and SAR interferometry was used as a potential tool to map the topography worldwide. The most effective mission operating SAR interferometry was the SRTM mission mentioned above, that provided for the first time an almost complete topography map of the Earth's surface.

Today it is generally accepted that SAR interferometry is an extremely powerful and invaluable technique, which brings benefits to a large number of applications. It can be used mainly in three different ways. First, the phase difference between the SAR images contains information about the topographic height and hence SAR interferometry can be used to map the elevation of the Earth's surface. Secondly, using at least two image pairs, the *differential* interferometry allows mapping geodynamic phenomena with high accuracy of the order of fractions of the wavelength. This method has been successfully applied to measure seismic displacements (Massonnet et al., 1993; Zebker et al., 1994), volcanic events (Massonnet et al., 1995; Lanari et al., 1998), subsidence (Lanari et al., 2004), ice and glaciers dynamics (Kwok and Fahnestock, 1996; Joughin et al., 1998). The third method consists in using coherence maps and phase information for the quantitative retrieval of biophysical parameters. This method has found applications especially in vegetation remote sensing, because SAR interferometry is able to provide information along the vertical structure of semi-transparent random media (Rodriguez and Martin, 1992; Treuhaft and Siqueira, 2000). However, the complexity of the scattering process forced the design of models with more input parameters than those estimable by single-channel interferometry.

The need to increase the observation space of the image medium accelerated the development of extensions of SAR interferometry towards multi-dimensional SAR data. Among these extensions, the technique named *polarimetric SAR interferometry* is a

well accredited technique to retrieve structural parameters of vegetation. The basic idea relies on the potential of SAR polarimetry to discriminate among scattering mechanisms inside the radar resolution cell and of SAR interferometry to associate to them a phase center height. The reference model that combines these two aspects is the *random volume over ground* (RVOG) model (Cloude and Papathanassiou, 1998, 2003). Part of this thesis aims at gaining some insights of polarimetric SAR interferometry for forest remote sensing, and at proposing improvements to the RVOG model. Chapter 3 is entirely dedicated to POLINSAR technique.

1.2.3 SAR tomography

The term *tomography* in the context of SAR remote sensing denotes those methods capable of reconstructing the 3-dimensional inner structure of distributed semi-transparent media. In this sense, tomography is the technique that recovers the missing dimension when 3-dimensional media are mapped onto the 2-dimensional SAR image plane. Often, SAR tomography is concerned with the exploitation of several observations of the same target performed by different look directions. In contrast with SAR interferometry, the classical tomographic approach resolve the height ambiguity inherent to the SAR imaging process using a processing similar to the SAR image formation, hence by focusing the set of observations along the vertical dimension of the medium (Reigber and Moreira, 2000; Fornaro et al., 2003; Lombardini and Pardini, 2008). Since a large number of repeated observations is required to obtain high vertical resolution, this approach is most suitable using airborne SAR and results rather difficult to implement with spaceborne data.

As discussed previously, however, the synergy of polarimetric and interferometric techniques makes it possible to retrieve information about the vertical structure of the vegetation and, in this sense, it can be considered as an attempt of tomographic reconstruction. This method is usually based on constructing scattering models that are sufficiently simple to be inverted and equally well accurate to preserve the vertical structure. The RVOG model that we have mentioned partially constrains the shape of the vertical structure to retrieve more accurately the ground topography and the canopy height.

Recently, a novel approach to vegetation tomography has been proposed by Cloude (2006) and is named *polarization coherence tomography* (PCT). PCT reconstructs a generic vertical profile of a random medium at an arbitrary selected polarization (as the classical tomographic technique) but using a minimum of two observations (as the POLINSAR technique). In this sense, PCT can be considered a sort of hybrid approach to tomography. The employed model is essentially a series expansion of the unknown vertical profile, whose coefficients can be estimated by interferometric coherence ob-

servations. The method requires the knowledge of the vegetation height (that may be calculated inverting the RVOG model) and seems today a good compromise to retrieve more accurately the structural parameters of forests.

Although this thesis is not focused on PCT, some considerations discussed in Chapter 3 and Chapter 4 about the RVOG model may be readily extended to PCT, as both PCT and RVOG originate from a common root formulation.

1.3 Scope, objectives and novelties of the thesis

In previous sections we have outlined the motivations and the general context of our studies. Four elements can be identified and thought as sides of a quadrilateral that circumscribes this PhD work. First, the *application*: here we focus on the estimation of biophysical parameters of forests, in particular tree height that represents an input for assessing the worldwide biomass. Second, the *technique*: we work with the combination of polarimetry and interferometry, and consider the most recent compact POLINSAR technique. Third the *model*: the starting point of our investigations is the formulation at the base of the RVOG model. Fourth, the *data*: ALOS/PALSAR satellite acquisitions and numerical scattering simulations (cf. Chapter 2) are used to illustrate the results.

Beside the definition of the scope, these elements and their chronological evolution are fundamental to understand the objectives and the development of this thesis. In late 2006, when this PhD work started, ALOS/PALSAR had just been launched and for the first time L-band space-borne polarimetric data became available. Before testing polarimetric and POLINSAR algorithms, an assessment of the data quality in terms of ionospheric effects and system-induced distortions was necessary. At that time, the RVOG inversion was tested only over airborne data acquired by DLR and there was a need to improve both the forward and the inverse models, especially about the effect of temporal artifacts. In parallel, compact polarimetry was emerging as an alternative to full polarimetry and the investigation of compact POLINSAR was not yet conducted. Finally, in January 2007, the ESA Toolbox POLSARPRO (Pottier et al., 2009) was issued with a new coherent and POLINSAR scattering simulator (PSPSIM) that represented a novelty in the SAR community of forest remote sensing.

Some of the gaps and open issues investigated at the beginning of the thesis are now solved or well accepted. In Chapter 6 a list of these issues is provided. Here, we focus more on our original contribution during these three years. This PhD thesis collects different ideas for full and compact polarimetric and interferometric SAR modeling and processing. With reference to the scenario illustrated above, the work has been carried out looking at three main objectives listed hereafter.

1. To gain some insights in the polarimetric and interferometric modeling at L- and

P-band. In particular, the objective is to investigate the robustness of the RVOG model and its inversion procedure when the scene characteristics deviate from the underlying hypothesis, and to define a better model of temporal decorrelation to cope with repeat-pass interferometers, such as ALOS/PALSAR.

2. To investigate the potential of the compact polarimetric and interferometric SAR for estimating forest height. Since no spaceborne or airborne mission is operating with compact polarimetric modes, the objective is to provide a general framework for the comparison between compact and full POLINSAR data over forested areas using current full polarimetric data.
3. To explore alternative approaches for polarimetric data calibration. In particular, the objective is to improve the estimation and the correction of Faraday rotation in spaceborne acquisitions, such as those of ALOS/PALSAR, and to design a specific procedure for calibrating dual-polarimetric data using passive reflectors.

The effort made to accomplish the three objectives above has led to a certain number of innovations and novelties that characterize this PhD dissertation. Some of them address the forward modeling of the POLINSAR technique, others cope with processing and algorithmic aspects, some others are related to systems and devices. A complete list follows hereafter.

1. The POLINSAR capabilities of ALOS/PALSAR have been exploited, with attention to every single step of the POLINSAR processing. Although the large temporal baseline limits the use of the interferometric coherence over volumetric media for model-based inversion, we provide evidence that polarimetry does play a role in spaceborne SAR interferometry.
2. The range of validity of the current POLINSAR models has been assessed both in terms of forward modeling and inversion procedure using coherent numerical simulations. We have found that range-sloped terrain may be a limitation for the retrieval of forest height and vertical structure if not properly accounted in the modeling.
3. Temporal decorrelation has been included in the coherence modelisation as a function depending on the vertical profile, affecting more the top of the canopy than the ground. Because of this improvement, we show that the line model shrinks, and the top-phase scattering center lowers while the temporal baseline increases.
4. The scattering and SAR image simulator PPSIM distributed within POLSARPRO is demonstrated to be a valuable tool not only for algorithm testing, but also for parametric and sensitivity analysis. As an example, we show how the polarimetric and interferometric properties of trees change according to the SAR look angle.

5. At P-band, we have found a relationship linking two polarization channels independently of the forest height. This yields a simplified expression of the RVOG model and the possibility to evaluate directly from the data one model parameter for a more robust inversion procedure.
6. The role of polarimetry in SAR interferometry is enhanced with an improved coherence optimization algorithm that aims at maximizing the phase separation while keeping the coherence magnitude relatively high. Better performance is observed for large ambiguity height and moderate speckle filtering.
7. The theoretical formulation of the compact POLINSAR is developed and an algorithm to compare full and compact POLINSAR is proposed based on the symmetry properties of natural media. We show that the performance of compact polarimetry on height retrieval worsens when symmetries are not satisfied and non-detectable scattering mechanisms are present in the scene.
8. The impact of the SAR processor and SAR receiver has been investigated in the synthesis of compact polarimetric data from full polarimetric data. While the SAR processor that we tested does not present particular non-linearities that affect the synthesis, we point out that the SAR receiver might increase the relative noise between polarimetric channels.
9. The estimation and correction of Faraday rotation have been proposed on unfocused data rather than focused data. The main advantages in using this approach are the possibility to detect rapid spatial variations of ionospheric anomalies and compensate for them before the image formation.
10. The radiometric calibration of dual polarimetric data has been addressed using a variant of the corner reflector, named gridded corner reflector. We developed the data calibration approach for SENTINEL-1 and assessed the performance through electromagnetic scattering simulations.

Each topic above is presented with a theoretical formulation and, where possible, with results on simulated or real data. Due to the nature of some arguments that address extremely new topics, the demonstration and the full implementation of the algorithms cannot be accomplished yet. However, most of the recent and future SAR missions, such as the airborne BIOSAR-2 and the spaceborne mission TERRASAR-L or DESDYNI, will enable the complete demonstration of the algorithms presented in this dissertation.

1.4 Thesis outline

The arguments are classified into three main topics: full polarimetric SAR interferometry, compact polarimetric SAR interferometry and data quality issues. They are

associated with as many chapters that comprise the novelties 1–10 listed above. As consequence of the variety of the arguments, the state of art and a brief bibliographic review are provided at beginning of each chapter. In conclusion, the present dissertation is organized as follows.

Chapter 2 describes the principal characteristics of the scattering and SAR image numerical simulator PSPSIM. The basics of the scattering formulation and SAR image formation are also provided.

Chapter 3 deals with the full polarimetric SAR interferometry and presents the spatial and temporal decorrelation models. ALOS/PALSAR observations and the parametric analysis using PSPSIM at L- and P-band are illustrated. This chapter includes the novelties 1-6 listed in the previous section.

Chapter 4 treats the compact polarimetric architecture and the associated interferometric formulation. We summarize the limitations and advantages of compact polarimetry with respect to full polarimetry. This chapter includes the novelties 7-8 described in the previous section.

Chapter 5 addresses the procedure to ensure high data quality, in terms of Faraday rotation and dual-polarimetric calibration. This chapter includes the novelties 9-10 described in the previous section.

Chapter 6 is the conclusive chapter in which we draw the conclusions and look at future perspectives.

Chapters 3, 4 and 5 contain material published, submitted or to be submitted to peer-reviewed journals and international conferences. We invite the reader to check the latest published papers for an accurate and updated description of the arguments treated in this dissertation.

Chapter 2

Microwave scattering and system modeling

Truth is much too complicated to allow anything but approximations.

John von Neumann (1903-1957)

The objective of this chapter is to provide the reader with a basic knowledge of PSPSIM, the tool adopted in our studies for numerical scattering simulations. PSPSIM is a detailed scattering and radar image calculator distributed recently within the ESA Polarimetric SAR Data Processing and Educational Toolbox (POLSARPRO) (Pottier et al., 2009). It combines two fundamental aspects of SAR data modeling, namely the electromagnetic scattering from natural media and the imaging process by the radar sensor. Therefore, the chapter naturally divides into three sections. The first one introduces the scattering problem with an electromagnetic approach and gives an overview of the models of vegetation scattering used in literature. The second section treats the end-to-end radar imaging model with a signal processing approach. Finally, the last section describes in detail the characteristics of PSPSIM and discusses the theoretical models implemented for the numerical simulation.

2.1 Microwave scattering

Electromagnetic microwave scattering is an active discipline in many scientific fields and has found a wide range of applications (Tsang et al., 2000). In terrestrial remote sensing, microwave scattering presents great theoretical challenges due to the complexity of interactions between waves and random media (Ishimaru, 1978; Fung, 1994). This aspect, combined with the benefits brought by remote sensing applications discussed in Chapter 1, stimulated the development of simplified models of random media, and in particular vegetation and rough surfaces. Progresses have been done for both simplified

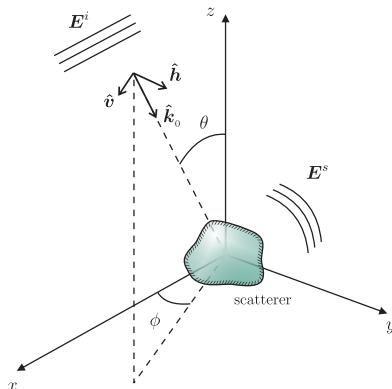


Figure 2.1: Scattering problem scenario and coordinate system.

theories and numerical approaches. The following sections introduce the basic definitions used throughout the dissertation and present a brief review of current approaches in modeling microwave scattering from vegetation and soil.

2.1.1 General problem formulation

The problem of scattering of an electromagnetic wave impinging upon a generic target can be formulated as follows (Tsang et al., 2000; Ulaby and Elachi, 1990). Let us consider a scatterer illuminated by a plane electromagnetic wave with incident electric field \mathbf{E}^i

$$\mathbf{E}^i = E_h^i \hat{\mathbf{h}} + E_v^i \hat{\mathbf{v}} \quad (2.1)$$

wherein $\hat{\mathbf{h}}$ and $\hat{\mathbf{v}}$ are the unitary vectors associated with the horizontal and vertical polarizations, respectively. In the following, we assume the BSA standard convention (IEEE, 1983) and a Cartesian coordinate system as depicted in Fig. 2.1. The interaction of the wave with the scatterer induces currents which reradiate energy in the form of *scattered* wave. In the *far-field approximation*, a plane wave can be assumed for the scattered electric field \mathbf{E}^s

$$\mathbf{E}^s = E_h^s \hat{\mathbf{h}} + E_v^s \hat{\mathbf{v}}. \quad (2.2)$$

The components of the fields \mathbf{E}^i and \mathbf{E}^s are related by the complex 2×2 *scattering matrix* or *Sinclair matrix* \mathbf{S} characteristic of the scatterer (Sinclair, 1950; Kennaugh,

1951)

$$\begin{pmatrix} E_h^s \\ E_v^s \end{pmatrix} = \frac{e^{jk_0 r_0}}{r_0} \begin{pmatrix} s_{hh} & s_{hv} \\ s_{vh} & s_{vv} \end{pmatrix} \begin{pmatrix} E_h^i \\ E_v^i \end{pmatrix} = \frac{e^{jk_0 r_0}}{r_0} \mathbf{S} \mathbf{E}^i \quad (2.3)$$

wherein s_{pq} , $p, q = h, v$ are the complex scattering amplitudes, k_0 is the wavenumber of the impinging wave and r_0 the distance between the scatterer and a receiving antenna that detects and measures the scattered field. As discussed in Chapter 1, a monostatic and coherent polarimetric radar measures the complex scattering amplitudes and associates a scattering matrix to each image sample. Scattering amplitudes are, in general, functions of the radar characteristics, the illumination geometry and the target properties.

A *forward model* may be defined as a relationship F_{pq} , $p, q = h, v$, linking the radar output to the observation parameters and to n variables $a_{t_1}, a_{t_2}, \dots, a_{t_n}$ that characterize the scatterer

$$s_{pq} = F_{pq}(k_0, \theta, \phi, a_{t_1}, a_{t_2}, \dots, a_{t_n}), \quad p, q = h, v \quad (2.4)$$

where θ and ϕ are observation angles of the radar as shown in Fig. 2.1. The form of F_{pq} has been defined in several textbooks (Tsang et al., 2000; Ulaby and Elachi, 1990; Ulaby et al., 1986a) for a large variety of scatterers, both point targets and distributed media. In remote sensing applications of vegetation, the variables $a_{t_1}, a_{t_2}, \dots, a_{t_n}$ represent soil and vegetation properties. The most significant properties are classified hereafter. Most of them are currently used as inputs for microwave forward models.

- Dielectric properties of the ground, expressed by the soil permittivity $\epsilon_g = \epsilon'_g + j\epsilon''_g$, depending on soil moisture content (SMC), texture, bulk density, temperature and salinity.
- Geometric properties of the ground surface, in particular surface roughness, expressed by its autocorrelation function and, in a single-scale description by two variables, namely height standard deviation and correlation length.
- Properties related to the amount of vegetation matter per unit area such as fresh biomass, plant water content (PWC), plant density and leaf area index (LAI).
- Dielectric properties of the vegetation elements, expressed by the permittivity $\epsilon_v = \epsilon'_v + j\epsilon''_v$, related to the gravimetric moisture, dry matter density, temperature and salinity.
- Geometric and structural properties of vegetation such as height and diameter of stems and trunks, length, width and thickness of leaves, and the associated distributions of element orientation.

Estimating some of these properties from radar measurements is the objective of the *inverse modeling*. In the classical approach, the *measured* radar observable is compared with the *predicted* observable in order to minimize the uncertainty in the retrieval process. Note that (2.4) represents only the predicted radar scattering amplitude.

Other observables can be defined when several measurements over the same target are available, yielding more complex modeling and consequently more powerful inversion strategies. This is the case of more advanced radar techniques such as polarimetry and interferometry. As an example, the natural interferometric observable is the complex correlation coefficient, i.e. the *degree of coherence*, between two complex amplitudes. Hence, (2.4) may be extended to model descriptors more advanced than the backscatter.

2.1.2 Review of scattering vegetation models

Several theoretical models of scattering from natural media have been developed in the last four decades. Due to the complexity of the interactions between wave and distributed targets, a certain number of assumptions and approximations is necessary. Exact solutions of scattering problems have been achieved only in the last years with numerical simulations. We report hereafter a brief review of the scattering models along with their main characteristics (Ulaby et al., 1986b; Fung, 1994; Della Vecchia, 2006).

Semi-empirical models. These models aim at describing the vegetation scattering by means of a parametric function based on simplified scattering scenarios. The coefficients of the function may be assessed by fitting collected measured data. The *water cloud* model proposed by Attema and Ulaby (1978) belongs to this family of models. The four coefficients were initially fitted over multi-frequency, multi-angle and multi-polarization radar data in order to increase the robustness of the fitting. Variables of the model are typically PWC, LAI and SMC introduced by Prevot et al. (1993). Further improvements have been made to the water cloud model, notably the introduction of the cross-polarized backscattering coefficient by de Roo et al. (2001). The advantage of using semi-empirical models is their simplicity, which in turn provides easy implementation and high computational efficiency. Since the input parameters are few, however, the general validity of the model is limited.

Continuous layer models. Models belonging to this family are characterized by a layered scenario of the natural medium. In particular, both vegetation and soil are represented as dielectric slabs. While the permittivity of the soil is often considered as an average constant complex value, the permittivity of the vegetated layer is obtained by superimposing an average component with a fluctuating component. This latter component depends upon the dielectric inhomogeneity, typically due to leaves. A theoretical approach for these models was proposed by Fung and Ulaby (1978); Fung (1979); Tsang and Kong (1981), based on the random media theory proposed by Tatarskii (1964). Layered models are still simple, allowing a better representation of the natural media with respect to the water cloud model.

However, the difficulties in relating the permittivity fluctuations with the dielectric properties and the poor realistic flat interface between the layers represent the main limitations of this approach.

Discrete models. This third family of models is characterized by quasi-realistic realization of the natural medium. Vegetation and soil are modeled with simplified bodies and the electromagnetic characterization of each scatterer is conducted with high fidelity. Soil is assumed as a half space with a rough interface. Its permittivity is usually computed using the semi-empirical formula of Dobson et al. (1985), later refined by Ulaby et al. (1986a), or the empirical formulation derived by Hallikainen et al. (1985). Vegetation is divided in elementary components with simple geometry such as cylinders, discs or elliptical sheets. In order to compute the vegetation permittivity, empirical approaches were followed by Ulaby and El-Rayes (1987); Matzler (1994). The scattering of the soil and of each single element of the vegetation must be estimated. Soil backscatter is computed with two asymptotic approximations, namely *small perturbation model* (SPM) and *geometrical optics* (GO) (Ulaby et al., 1986b), or the more advanced *integral equation model* (Fung, 1994). Other approximations are used for computing the scattered field by vegetation elements, based on permittivity, shape and ratio between wavelength and geometrical dimensions (Karam et al., 1988; Stiles and Sarabandi, 2000; Eom and Fung, 1984; Della Vecchia et al., 2004). The overall backscattering is finally computed taking into account the interactions among the vegetation elements and soil. Discrete models may be classified into incoherent, partially coherent or full-wave. The order of the scattering interaction further differentiates the models. An incoherent discrete model is MIMICS, based on the first order solution of the *radiative transfer theory* (RTT) (Ulaby et al., 1990). To overcome the underestimation of the cross- and co-polarized backscatter given by the first order solution, a second order solution of the RTT equations was proposed by Karam et al. (1992). Multiple scattering of all orders were initially developed by Eom and Fung (1984), based on the matrix doubling algorithm (Twomey et al., 1966), and further exploited by Ferrazzoli and Guerriero (1995). In the partially coherent and full-wave approaches, the information about the phase is retained and considered in the computation of the total field. In partially coherent models (Stiles and Sarabandi, 2000), however, the attenuation is computed using the incoherent Foldy's theory (Tsang et al., 1985). Fully coherent approximations developed by Tsang et al. (1995); Oh et al. (2002), on the contrary, consider the scattering in terms of electromagnetic wave propagation.

In our studies, we adopt a partially coherent discrete model, implemented in the numerical simulator PSPSIM distributed by ESA within POLSARPRO (Pottier et al., 2009). PSPSIM provides also SAR imaging capabilities which are discussed in the next section

from a general point of view.

2.2 Synthetic aperture radar imaging model

Synthetic aperture radar is a coherent active microwave imaging method. In remote sensing applications, a SAR system represents a convenient way to map the scattering properties of the Earth's surface. It is essentially a record system that associates the scattered electromagnetic field with a gray value of image pixel. In order to exploit SAR data for geosciences applications, knowledge of the SAR imaging process is required. In this section, we review the basic end-to-end SAR system model from a signal processing point of view. This model is the basis for the forward SAR simulation adopted in this thesis to study the POLINSAR properties of forests. It is presented for a single-channel SAR but can be readily extended to the multi-channel case.

A SAR illuminates the Earth's surface in a side-looking fashion. While the sensor is moving along its trajectory, it transmits microwave pulses with a *pulse repetition frequency* (PRF) and receives the echo of each pulse scattered from the illuminated portion of the Earth. The illuminated area is determined by the antenna footprint and can be several kilometers in both *along-* and *across-track* directions. The system records and samples the stream of echoes for each transmitted pulse and arranges the samples side-by-side, yielding a 2-dimensional representation called *raw data*. Raw data are the results of two different scanning methods. The first comes from the transmitted pulses that sweep the Earth's surface across-track and the second is the consequence of the platform motion along-track. There is a rich selection of publications and excellent textbooks on the theoretic aspects of the acquisition and image formation process (Curlander and McDonough, 1991; Elachi, 1988; Cumming and Wong, 2005; Bamler, 1992; Davidson, 1997; Raney et al., 1994). For our purpose, we review the expression of the *impulse response function* that models the SAR as an all-pass (phase only) filter operation (Bamler and Hartl, 1998; Cumming and Wong, 2005).

The model idealizes the acquisition process, assuming straight platform trajectory, undisturbed wave propagation, noise free reception and look direction perpendicular to the flight path. The considered scenario comprises an ideal point scatterer located at (x_0, y_0, z_0) , i.e. $\delta(x - x_0, y - y_0, z - z_0)$. The response of the point scatterer in the final image will be centered at its *zero-Doppler* coordinates

$$u_\delta(x, r) = Q(x - x_0, r - r_0) e^{-j2k_0 r_0} = \text{Sinc}(W_x x) \text{Sinc}(W_r r) e^{-j2k_0 r_0} \quad (2.5)$$

where $Q(x, r)$ is the 2-dimensional impulse response function, assuming rectangular filters with bandwidth W_x and W_r in azimuth and range respectively, and $\text{Sinc}(\cdot)$ the cardinal sine function. The filter bandwidths are related to the imaging resolution

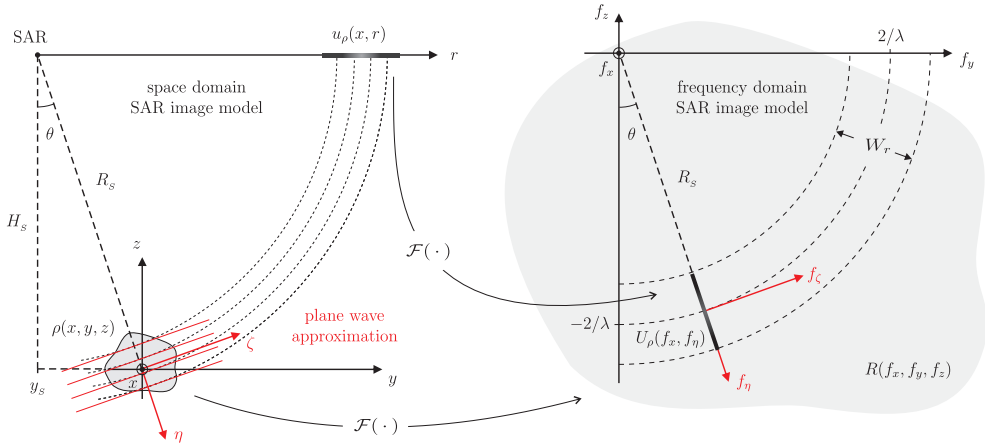


Figure 2.2: Representation of the SAR imaging system model of equations (2.7), (2.8) and (2.9). The x - and h -axes are rotated by 90 deg with respect to the coordinate system of Fig. 2.1.

and system characteristics, $W_x \simeq 2/L_a$ and $W_R = 2W_p$, where L_a is the real antenna length and W_p the bandwidth of the transmitted pulse. The geometrical coordinates in (2.5) are cylindrical with axes on the flight trajectory and radial distance equal to the slant-range distance

$$r = \sqrt{r_0 + (x - x_0)^2}, \quad r_0 = \sqrt{(y_0 - y_s)^2 + (H_s - z_0)^2} \quad (2.6)$$

where H_s is the platform altitude and y_s is illustrated in Fig. 2.2. A generic random medium can be modeled as the ensemble of individual point scatterers (as the one considered above) characterized by only their density or, more in general, by a *structure function* $\rho(x, y, z)$ accounting for the backscatter per unit volume. The first Born approximation (Ishimaru, 1978) states that the total scattered field is the linear superposition of the backscatter from individual points. Under this approximation, the linear SAR imaging operator (2.5) is equivalent to the projection of $\rho(x, y, z)$ onto the 2-dimensional cylindrical coordinates centered on the zero-Doppler reference, followed by the 2-dimensional convolution with the impulse response function

$$\begin{aligned} u_\rho(x, r) &= \iiint \rho(x_0, y_0, z_0) e^{-j2k_0 r_0} Q(x - x_0, r - r_0) dx_0 dy_0 dz_0 \\ &= \left(e^{-j2k_0 r} \int \rho(x_0, y_0, z_0) r d\theta \right) ** Q(x, r) \end{aligned} \quad (2.7)$$

where $u_\rho(x, r)$ denotes the complex SAR image and $**$ stands for the 2-dimensional convolution. Eq. (2.7) represents the general SAR focused image model under the assumptions mentioned above. The projection of the imaged medium from a 3-dimensional space to a 2-dimensional space causes the loss of information about the full structure of the medium. In particular, all scatterers on the zero-Doppler plane with same distance from the sensor are mapped in a single point on the image. As anticipated in Chapter 1, interferometric and tomographic techniques offer a way to recover somehow the lost dimension. Starting from (2.7), the *plane wave approximation* gives another expression of the image model by substituting the cylindrical impinging wave with a plane wave in a small portion of the medium. Fig. 2.2 depicts the plane wave and the new convenient coordinates ζ and η respectively parallel and perpendicular to the wavefront. The SAR image model under the plane wave approximation and introducing the new range coordinate η becomes

$$\begin{aligned} u_\rho(x, \eta) &\simeq e^{-j2k_0 r_s} \left(e^{-j2k_0 \eta} \int \rho(x, y z) d\zeta \right) ** Q(x, \eta) \\ &= e^{-j2k_0 (R_s + \eta)} \int \rho(x, y z) d\zeta ** Q(x, \eta) e^{-j2k_0 \eta} \end{aligned} \quad (2.8)$$

wherein it appears how the SAR imaging process provides the 2-dimensional projection along ζ onto the η -axis of the 3-dimensional medium structure. Equivalently, it is said that the SAR image provides a *single tomographic projection* of the scattered medium, filtered by the frequency-shifted point response function.

The intrinsic tomographic projection of the backscatter properties pose the question of how much information about the observed medium is transferred into the SAR image and what are the optimal sensor parameters (e.g. angle of incidence, frequency, etc.) for the maximization of such information. A useful way to look into this aspect is the frequency domain SAR model (Cafforio et al., 1991; Gatelli et al., 1994) which corresponds straightforward to the Fourier transform of (2.8)

$$U_\rho(f_x, f_\eta) = \mathcal{F} [u_\rho(x, \eta)] \simeq e^{-j2k_0 R_s} R(f_x, f_y, f_z) H(f_x, f_\eta) \quad (2.9)$$

where $\mathcal{F}(\cdot)$ is the 2-dimensional Fourier operator, and $R(f_x, f_y, f_z)$, $H(f_x, f_\eta)$ indicate the Fourier transform of $\rho(x, y, z)$ and $Q(x, \eta)$ respectively. Fig. 2.2 illustrates also the SAR model in the frequency domain. The portion of the whole medium spectrum that the SAR observes depends on the wavelength λ , on the range bandwidth W_r and on the angle of incidence θ . This portion is selected by the SAR transfer function $H(f_x, f_\eta)$ which lies on the plane given by

$$f_y = \left(f_\eta + \frac{2}{\lambda} \right) \sin \theta, \quad f_z = - \left(f_\eta + \frac{2}{\lambda} \right) \cos \theta. \quad (2.10)$$

Fig. 2.2 gives some elements to understand how SAR interferometry and (conventional) SAR tomography work. These two techniques acquire information about the medium from different look angles, hence exploit different slices of its spectrum to recover the dimension lost by the projection onto the SAR image plane.

The end-to-end SAR system model allows having a straightforward representation of the SAR image given the backscattering properties of the target. Indeed, combining theoretical backscatter models and image model allows simulating SAR images as it is discussed in the next section.

2.3 Scattering and SAR image numerical simulator PPSIM

PPSIM is a Maxwell equation-based wave propagation and scattering model used to predict the polarimetric radar response of forests and soils (Williams, 2006a,b; Williams et al., 2007; Lucas et al., 2006). The model simulates the complex scattering matrix associated with airborne and space-borne SAR acquisition, assuming an ideal platform motion with straight and uniform trajectory. Moreover, by changing the observation geometry, the model is able to generate pairs of idealized polarimetric SAR images without co-registration errors, or problems associated with temporal and SNR decorrelation. Due to the imaging and coherent nature, PPSIM is suitable for the prediction of the *interferometric degree of coherence* between two radar images as it will be discussed in Chapter 3.

Following scene generation, the forward SAR simulation divides naturally into a number of stages. The scene is divided into a large number of elements, each much smaller in dimension than the SAR resolution. For each scene element, the 3-dimensional realization of the element is used, along with the SAR parameters and appropriate scattering models, to determine its in-situ scattering amplitude. The spatial location of the scene element, and the SAR imaging geometry, are used to determine the phase centers both of the direct (first-order) backscatter, and of the indirect (second-order) ground-element backscatter. Account is taken of attenuation by tree-foliage and understorey vegetation in the calculations. The complex scattering amplitude is used to weight the focused contribution of the element to the SAR image, and the phase centre is used to determine the location of the contribution in the image. Polarimetric scattering contributions from all elements are summed coherently in the simulated SAR imagery, thus preserving the polarimetric and interferometric properties of the modeled acquisition. The following is a brief description of some of the more pertinent aspects of the SAR simulation.

2.3.1 Ground surface

The ground is described by a set of geometrical and biophysical parameters including surface roughness, correlation length, azimuth/range tilt of the mean terrain, moisture content and soil type (Dobson et al., 1985). The ground surface scattering calculation employs a two-scale model that superposes a small-scale local roughness on a large-scale undulation. The large-scale surface is modeled as a truncated Fourier series (Tsang et al., 1985), with coefficients chosen to model a Gaussian surface. The small-scale surface roughness is also modeled as Gaussian, with parameters chosen such that SPM is valid locally (Ogilvy, 1991). The total roughness contributes to the scaling of the Fresnel reflection coefficients according to the Rayleigh roughness parameter (Ogilvy, 1991). In order to calculate the direct-ground backscattering coefficients, a hybrid deterministic/stochastic approach is used. The large-scale surface is divided into small, triangular, flat (on the scale of the resolution and wavelength) and rough facets and each facet backscattering response is computed according to facet orientation, area and small-scale roughness coupled in the SPM approximation. In general, each facet has a unique realization of surface roughness, leading to a speckle distribution over the ground surface, and this is accommodated in the simulation using Monte-Carlo realization of speckle phase and amplitude at the facet level, which is preserved between the ends of the interferometric baseline. Soil moisture is used to calculate the soil permittivity that is incorporated into the backscattering coefficient calculation (Dobson et al., 1985). The facet centre position is used in conjunction with the SAR imaging geometry to determine the point of focus of the facet contribution to the SAR image, and, automatically, its contribution to the interferometric phase.

2.3.2 Trees and short vegetation

Trees and underlying short vegetation constitute the forest environment in the modeled scene. The main parameters that describe the forest are the mean tree height and the tree species, the area of the forest stand, the forest stand density in stems/ha and the height, density and composition of the short vegetation layer. Trees are located initially on a regular grid, and then their positions are shuffled, in a neighbor-avoiding fashion, in order to recover a realistic spatial stem distribution. Each tree in the forest stand is realized in detail in order to preserve interferometric phase, and each tree realization is unique; described by allometric equation parameters drawn from statistical distributions. Terms for large scatterers, i.e. stems, primary and secondary branches are calculated using a deterministic approach. Branches are divided into short segments, and in-situ scattering is modeled using an approximate form for the truncated infinite cylinder approximation (Karam et al., 1988). The illuminating field is taken to be the mean field, calculated within the tree crown, in the forest stand. Tree crowns are taken

to display mean azimuthal symmetry, and assigned anisotropic permittivity tensors calculated in the appropriate low-frequency Foldy's approximation (Tsang et al., 1985), based on mean tree crown constitution. Attenuation factors are calculated according to ray path traversal through both crowns and the short vegetation layer. The tree architectures have biophysical properties that correspond closely to those reported in the literature (Tsang et al., 1985). The branching structure is calculated to second order and includes stems, primary branches originating in stems, and secondary branches originating in primary branches. The branching algorithm generates curved branches terminating on crown volume surfaces. Tertiary level elements such as twigs, leaves and needles, are simulated as a homogeneous cloud constrained within the tree crown. Both tree architecture and randomly generated tertiary element positions are preserved across the interferometric baseline to ensure proper coherence between imagery. Short vegetation on the ground is modeled as a homogeneous cloud of twigs and leaves, confined to a layer above the ground surface. The approaches employed to calculate both the short vegetation and forest tertiary element scattering contributions are similar. The numerous small plant elements in each crown, and in the short vegetation layer, are treated using a hybrid stochastic/deterministic approach chosen to ensure computational efficiency. Rather than simulate all such elements, a fraction of the total number are realized in a random fashion that ensures both uniform orientational distribution, and spatial distribution throughout the tree crowns and understorey layer. Calculated scattering amplitudes are scaled to preserve the full backscatter contribution, keeping a high number of simulated elements in order to ensure fully-developed speckle where appropriate. Scattering by small elements is calculated using the Rayleigh-Gans approach (Shiffer and Thielheim, 1979), whilst vegetation permittivities are calculated following El-Rayes and Ulaby (1987), using predetermined plant element water contents. For contributions to backscattering from the interaction of surface and vegetation elements, the reflection polarimetry is determined using the mean terrain surface orientation and scattering element properties, and reflection magnitudes are modulated by surface roughness.

2.3.3 Coherent image formation

The SAR image is treated as the coherent superposition of focused scattering events with scattering amplitudes calculated in the manner previously described. The coherent calculation proceeds according to scattering mechanism: direct-ground, direct-volume and ground-volume. Ground-volume-ground interactions (and other high-order scattering events) are generally not significant and have been omitted in the SAR imaging process. The scattering amplitudes for each discrete scene element have associated effective scattering centers. Together with the SAR imaging geometry, these effective

scattering centers determine the point of focus of backscatter in the two-dimensional SAR image plane. The simulated SAR images may be expressed succinctly using this discrete approximation

$$s_{pq}(x_0, r_0) = \sum_j F_{pqj} Q_{pq}(x_0, r_0, \mathbf{r}_j), \quad p, q = h, v \quad (2.11)$$

where $s_{pq}(x_0, r_0)$ is the resultant, complex pixel of the SAR image for receiving polarization p and transmitting polarization q , at azimuth platform position x_0 and ground-range distance r_0 . The scattering amplitudes F_{pqj} result modulated by the complex system point-spread-function Q_{pq} , which depends upon azimuth and range, and the location of the effective scattering center \mathbf{r}_j . The function Q_{pq} is calculated from the SAR viewing geometry, bandwidth and processing options. It appears clear how (2.11) merges in a single expression the general forward model (2.4) and the imaging model (2.8), discussed in Sec. 2.1 and Sec. 2.2 respectively. In the practical implementation, image calculation proceeds by accumulating focused returns in the image until all discrete scene elements have been processed. The process is performed once for the first or master track at one end of the interferometric baseline, and then repeated for the second, or slave track, to form an interferometric pair of polarimetric images. One of the unique features of this approach is the possibility to separate the scattering mechanisms in the simulation and to process the total backscatter, the direct-volume, the direct-ground and the ground-volume images. Fig. 2.3 shows an example of such images for a forest of Scots pines. In the figure, the detailed realization of two pines is shown along with their individual interactions $\sigma^{(dv)}$ (direct-volume), $\sigma^{(dg)}$ (direct-ground) and $\sigma^{(gv)}$ (ground-volume). The backscatter (intensity) images are generated by simulating several hectares of such pines with 24 m as average height and using the acquisition geometry of the DLR E-SAR airborne SAR. Note the diversity of features among polarizations and scattering mechanisms. Simulations like the ones in Fig. 2.3 will be used in next chapters for investigating the properties of the POLINSAR coherence.

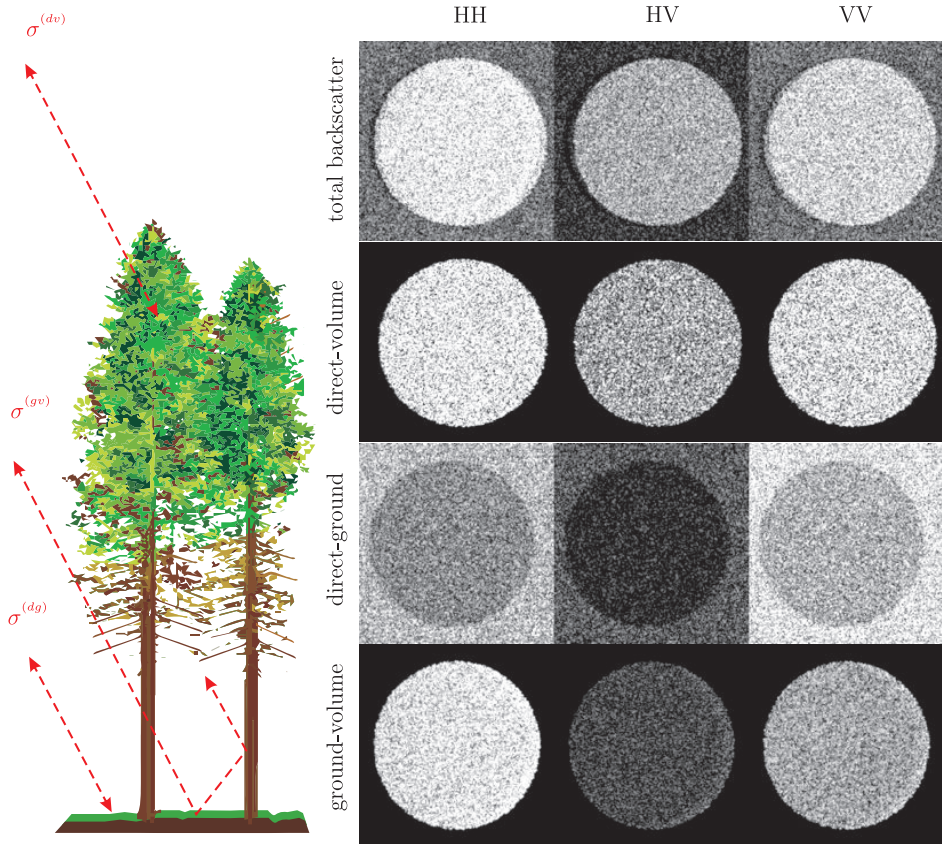


Figure 2.3: Example of PSPSIM simulation at L-band of Scots pines 24 m tall, acquired with 45 deg angle of incidence. The total backscatter images, the direct-volume $\sigma^{(dv)}$, the direct-ground $\sigma^{(dg)}$ and the ground-volume $\sigma^{(gv)}$ at HH, HV and VV polarization are shown.

Chapter 3

Full Polarimetric SAR Interferometry

In every branch of knowledge the progress is proportional to the amount of facts on which to build, and therefore to the facility of obtaining data.

James Clerk Maxwell (1831-1879)

This chapter aims at presenting our progress related to *polarimetric SAR interferometry* introduced in Chapter 1. Several demonstrations of this technique have been published through recent years, ranging from higher to lower frequency systems. Almost all of them were based on airborne SAR data and on the simplified POLINSAR model developed by Cloude and Papathanassiou (1998). In the following, we first review the form of such model with the inclusion of our temporal decorrelation model (Sec. 3.1); then, we discuss the implications of our improvement on the inversion strategies for model parameter estimation (Sec.3.2). In Sec. 3.3, we assess the range of validity of the model by contrasting RVOG model predictions with numerical SAR simulations. Sec. 3.4 shows some POLINSAR observations from ALOS/PALSAR and discusses the difficulties to invert the model due to temporal artifacts. Finally, in Sec. 3.5 we present a variant of the RVOG model, suitable for P-band measurements, which improves the estimation of ground topography.

3.1 Forward models of interferometric coherence

One of the most effective approaches for the quantitative estimation of physical quantities is the model-based inversion. In this approach, a simplified model of the physical phenomenon is constructed using few model parameters in order to make predictions of the physical observable. The model parameters can be estimated by minimizing the error between real measurements and model predictions, usually in a

least-square sense. In our context, the physical observable is the interferometric coherence at different polarizations and the model is the *random volume over ground* (RVOG) model.

Polarimetric SAR interferometry was first introduced by Cloude and Papathanassiou (1997), and developed some years later with the RVOG model (Treuhft and Siqueira, 2000; Cloude and Papathanassiou, 1998; Papathanassiou and Cloude, 2001) and its inversion procedure (Cloude and Papathanassiou, 2003). Nowadays, POLINSAR is recognized as a powerful technique to retrieve structural information in many fields, such as forestry (Papathanassiou et al., 2005; Mette et al., 2004), agriculture (Sagues et al., 2000; Ballester-Berman et al., 2005), urban (Schneider et al., 2005; Garestier et al., 2006) and snow/ice (Papathanassiou et al., 2005). A rich selection of papers were also published about the statistic characterization of the POLINSAR coherence and its optimization (Ferro-Famil and Neumann, 2008; Ferro-Famil et al., 2009; Papathanassiou and Cloude, 2001; Neumann et al., 2008; Lavallo et al., 2007; Flynn et al., 2002; Colin et al., 2006). For the purpose of forest biomass retrieval, significant works have been carried out by DLR using airborne campaigns. As a main outcome, POLINSAR inversions have been successfully applied and validated over different types of forests such as boreal and tropical forests (Mette et al., 2004; Hajnsek et al., 2009), and at different frequencies, ranging from X- to P-band (Garestier et al., 2008; Kugler et al., 2006). Despite the good results obtained so far, some aspects of the forward and inverse modeling still need to be addressed, namely the polarization-dependence of the temporal decorrelation and the effects of the terrain slope. Before dealing with these two arguments, the basics of SAR interferometry and of coherence modeling are discussed.

3.1.1 Basics of polarimetric SAR interferometry

Let us consider a monostatic, fully polarimetric coherent radar system that observes a natural medium from two slightly different look angles, respectively θ and $\theta + \Delta\theta$. The considered scenario is depicted in Fig. 3.1, wherein the distance between the position of the radars, i.e. the *spatial baseline*, is indicated by B_s and its projection to the slant range by B_\perp . The observations may be simultaneous (single-pass interferometer) or separated by a time interval named *temporal baseline* T (repeat-pass interferometer). Such a system yields two complex scattering matrices, \mathbf{S}_1 and \mathbf{S}_2 , associated with the backscattered energy from the imaged scene. The only constraint that exists among the elements of the scattering matrices is reciprocity, which constrains the scattering matrix to be complex symmetric, i.e. $s_{vh_i} = s_{hv_i}^*$, $i = 1, 2$. The exploitation of polarimetric radar measurements often starts from the vectorization of the scattering matrices onto a matrix basis. Depending on the basis, a different representation of the scattering or *target* vector is obtained. In this section, we adopt the 3-dimensional Pauli vector \mathbf{k}_{P_i} ,

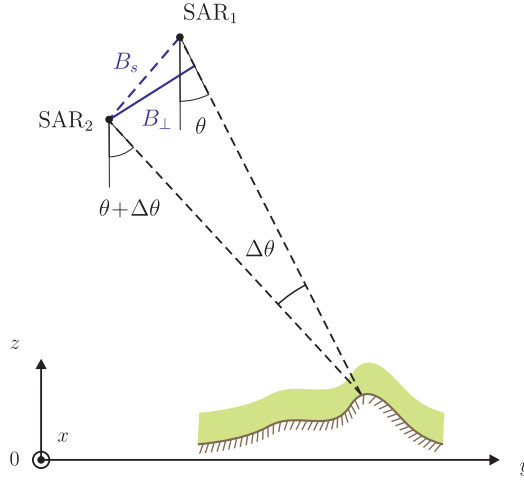


Figure 3.1: Geometrical scenario of a SAR interferometer.

$i = 1, 2$

$$\mathbf{k}_{P_i} = \frac{1}{\sqrt{2}} (s_{hh_i} + s_{vv_i} \quad s_{hh_i} - s_{vv_i} \quad 2s_{hv_i})^T, \quad i = 1, 2 \quad (3.1)$$

whose elements are closely related to the *canonical scattering mechanisms* (Cloude and Pottier, 1996). Different polarimetric combinations than those in (3.1) select different scattering mechanisms. In the most general case, this selection can be formally done by introducing a 3-element complex (projection) vector \mathbf{w}_i , $i = 1, 2$ that indeed represents the scattering mechanism selected by the polarimetric interferometer

$$s_1 = \mathbf{w}_1^\dagger \mathbf{k}_{P_1}, \quad s_2 = \mathbf{w}_2^\dagger \mathbf{k}_{P_2} \quad (3.2)$$

wherein the superscript \dagger stands for transpose conjugate. Scattering amplitudes s_1 and s_2 in (3.2) represent the constitutive elements of POLINSAR technique: the *polarimetric* essence is embedded in the physical scattering mechanisms \mathbf{w}_i and the *interferometric* essence follows from the two repeated observations. From a statistical point of view, s_1 and s_2 are stochastic processes assumed to be jointly circular Gaussian. The synergy of polarimetry and interferometry is conveniently described by the degree of coherence between the two radar images. The degree of coherence γ is the complex correlation

coefficient of two radar images. A (biased) estimator for such descriptor is

$$\gamma = |\gamma|e^{j\varphi} = \frac{\langle s_1 s_2^* \rangle}{\sqrt{\langle s_1 s_1^* \rangle \langle s_2 s_2^* \rangle}} \quad (3.3)$$

with $0 \leq |\gamma| \leq 1$, $-\pi \leq \varphi \leq \pi$ and angular brackets standing for spatial averaging over several samples (Novak and Burl, 1990). Spatial averaging aims at reducing the speckle noise (Goodman, 1976), hence at providing a more reliable estimate of the correlation degree (Lee et al., 2003). Several methods exist for speckle filtering and a list of them can be found in Lee and Pottier (2009). In the case of forest remote sensing, the mean of the samples within an average window (boxcar filtering) is often sufficient. Although the dependence on the scattering mechanism is omitted in (3.3), the coherence magnitude and phase change according to the selected scattering mechanism. This fact represents the fundamental concept of a polarimetric interferometer. From a statistical point of view, the joint probability density function of the magnitude and phase of an interferogram sample has been derived by Lee et al. (1994) and it is known in closed form.

For the purpose of quantitative remote sensing, the objective is to model the dependence of γ upon the characteristics of the imaged medium and of the observation system. The complex value of the coherence between two radar measurements depends on many factors, namely *correlation sources*¹ (Zebker and Villasenor, 1992a). Correlation sources are modeled as multiplicative quantities responsible for varying both the mean (real-valued correlation) and the variance of the coherence (complex-valued correlation). In general, they affect the magnitude and the phase of the interferometric coherence. Depending on their origin, the contributions can be classified into three classes:

1. decorrelations due to the scatterer, mainly its structure and temporal stability, as consequence of the different observation directions and of the repeated acquisition in time;
2. decorrelations due to propagations and atmospheric artifacts, which are most significant at lower frequencies (typically L- or P-band);
3. decorrelations originated by the system and the processing, including the additive and quantization noise, focusing ambiguities, calibration, co-registration and interpolation errors and estimation bias due to the limited number of samples (Lee et al., 1994).

Among these contributions, we focus on three main decorrelation sources that are significant for forestry applications. They are the spatial correlation γ_s , the temporal

1. The term correlation and decorrelation are often used indifferently in literature. We indicate γ as the correlation and $1 - \gamma$ the corresponding decorrelation.

correlation γ_t and system noise correlation γ_{snr} . The spatial and temporal correlations belong to the first class mentioned above, whereas the SNR correlation is a system correlation. If these three sources of decorrelation are known at different polarizations, the total degree of coherence γ may be predicted by

$$\gamma = \gamma_s \gamma_t \gamma_{snr}. \quad (3.4)$$

Separating the correlation sources from the estimated coherence γ is the first objective of the vegetation remote sensing by means of POLINSAR technique. Given the signal-to-noise ratio SNR of the radar system, the SNR decorrelation is given by (Just and Bamler, 1994; Zebker and Villasenor, 1992b)

$$\gamma_{snr} = \frac{1}{1 + SNR^{-1}} \quad (3.5)$$

which is a real-valued correlation affecting only the coherence magnitude. Typical values of SNR are around -30 dB, which leads to a small SNR decorrelation compared to the other two terms. In general, spatial and temporal decorrelations carry information about the structure of the imaged medium. It is furthermore reasonable to assume that they do depend upon the selected scattering mechanisms. Spatial correlation is less than one in magnitude because the target is seen under different look angles and different slices of its spectrum are transferred into the SAR image. Semi-transparent media are more affected by this decorrelation due to the combined effects of the wave penetration and SAR interferometric acquisition. Temporal decorrelation arises from the natural dynamic changes of the target mainly due to weather conditions and biological evolution². Addressing the expressions of spatial and temporal correlations is the objective of the following two sections. In the context of this study, the imaged media are forests, hence we will present coherence models of vertical distribution of scatterers.

3.1.2 Spatial correlation model

Let the observed medium be modeled as a vertical distribution of scatterers. In order to derive an expression of the spatial correlation, the interferometric coherence (3.3) must be adapted for such target (Rodriguez and Martin, 1992; Treuhaft and Siqueira, 2000). In our particular case, the total correlation between radar returns can be expressed as the coherent sum of the correlation among pairs of infinitesimal slabs

2. Spatial decorrelation means that the coherence is sensitive on the structural parameters of the medium, hence it is a desiderate effect. Temporal decorrelation, on the contrary, depends (also) on external and unpredictable phenomena and it is considered, at least up to now, as a disturbing effect.

dz along the vertical dimension (cf. Fig. 3.2), resulting in the following integrals

$$\gamma_s = \frac{\langle s_1 s_2^* \rangle}{\sqrt{\langle s_1 s_1^* \rangle \langle s_2 s_2^* \rangle}} = \frac{\int \langle \varrho_1(z) \varrho_2^*(z) \rangle dz}{\sqrt{\int \langle \varrho_1(z) \varrho_1^*(z) \rangle dz \int \langle \varrho_2(z) \varrho_2^*(z) \rangle dz}} \quad (3.6)$$

where $\varrho_i(z)$, $i = 1, 2$, represents the complex reflectivity per unit length³. If the radar system observes the medium from two slightly different look angles, θ and $\theta + \Delta\theta$ as in Fig. 3.1, the two measures of reflectivity differ by only a phase term

$$\varrho_2(z) = \varrho_1(z) e^{-jk_z z}, \quad k_z = \frac{4\pi\Delta\theta}{\lambda \sin \theta} \quad (3.7)$$

where k_z is the *vertical wavenumber* which depends on the observation directions and system wavelength. With the assumption (3.7), the spatial correlation of a vertical extent of particles is given by (Treuhaft and Siqueira, 2000)

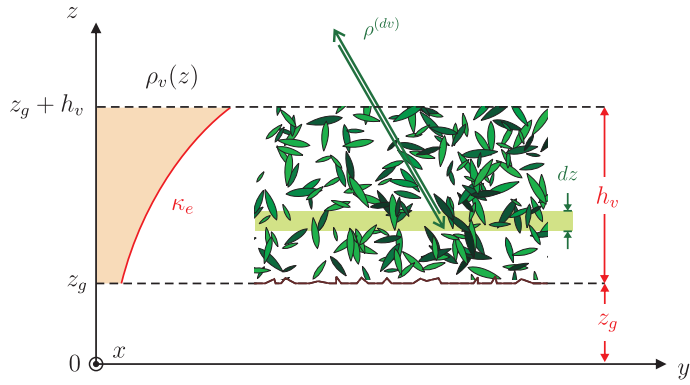
$$\gamma_s = \frac{\int \langle \varrho_1(z) \varrho_1^*(z) \rangle e^{jk_z z} dz}{\int \langle \varrho_1(z) \varrho_1^*(z) \rangle dz} = \frac{\int \rho(z) e^{jk_z z} dz}{\int \rho(z) dz} \quad (3.8)$$

wherein $\rho(z) = \langle |\varrho_1(z)|^2 \rangle$ is often called *structure function* and physically represents the average *attenuated* backscatter per vertical unit length of the medium. In the structure function, the information of the position and geometry of particles and their backscattering properties are all mixed. Estimating the shape of this function is the objective of tomographic techniques (Reigber and Moreira, 2000; Cloude, 2006).

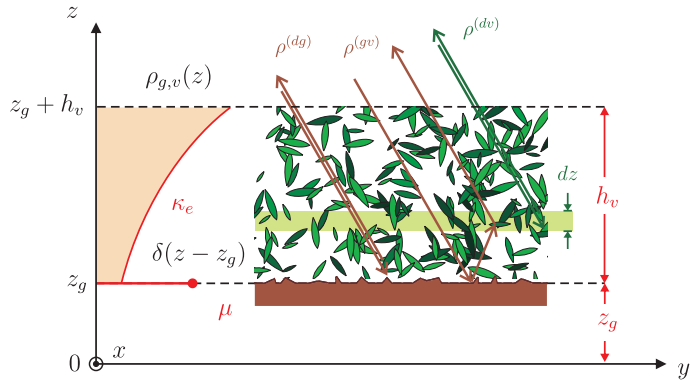
In order to evaluate the coherence (3.8) in closed form, we expand the reflectivity function by modeling forests as a layer of randomly oriented scatterers⁴ with an underlying rough surface, as depicted in Fig. (3.7). For simplicity, we start from the case of Fig. (3.2a) in absence of ground contribution. This *random volume* (RV) model is characterized by the thickness of the canopy layer h_v , the density of the particles per unit length $n(z)$, and the mean direct-volume radar cross section $\sigma_s^{(dv)}(z)$ of the single scatterer. Note that both the density and the scatterer cross section vary, in general, with depth and that in the RV model the nature of backscattering is direct-volume only.

3. Formally the dimensions of $\varrho(z)$ are $\text{dB m}^{-\frac{1}{2}}$

4. Random orientation means that the probability of a scatterer's being oriented in a particular direction is equal to that of its being oriented in any other.



(a) RV model scenario



(b) RVoG model scenario

Figure 3.2: Schematic representation of coherence models for a random distribution of scatterers. Input parameters to the models are highlighted in red color.

In this general case, the structure function can be expressed as

$$\rho(z) = n(z) \sigma_s^{(dv)}(z) L(z) \quad (3.9)$$

wherein $L(z)$ accounts for the power loss due to the travel path of the wave through the volume and depends on the thickness h_v , the incident angle θ and the mean extinction coefficient κ_e . If we assume homogeneity of the particles, i.e. $\sigma_s(z) = \text{const}$ within $z_g < z \leq z_g + h_v$, and uniformity of the layer, i.e. $n(z) = \text{const}$ within $z_g < z \leq z_g + h_v$, then the product of the two terms in (3.9) is constant⁵ and the attenuation is expressed by an exponential decay with power extinction coefficient per unit length κ_e

$$n(z) \sigma_s^{(dv)}(z) = \rho^{(dv)} \text{rect}\left(\frac{z - z_g - h_v/2}{h_v}\right), \quad L(z) = e^{\frac{2\kappa_e}{\cos\theta}(z - z_g - h_v)} \quad (3.10)$$

where $\rho^{(dv)}$ is the total backscatter per unit length of the volume layer and the $\text{rect}(\cdot)$ function ensures that above and below the layer the backscatter is zero. The total attenuation includes also the angle θ of incident wave and its double travel in the medium. Inserting (3.10) into (3.9), the structure function of the RV model becomes

$$\rho_v(z) = \rho^{(dv)} e^{\frac{2\kappa_e}{\cos\theta}(z - z_g - h_v)}, \quad z_g < z \leq z_g + h_v. \quad (3.11)$$

The numerator in (3.8), i.e. the complex correlation between the radar signals, can be expressed in closed form as

$$\int_{z_g}^{z_g + h_v} \rho^{(dv)} e^{\frac{2\kappa_e}{\cos\theta}(z - z_g - h_v)} e^{jk_z z} dz = \rho^{(dv)} e^{jk_z z_g} e^{-\frac{2\kappa_e}{\cos\theta} h_v} \frac{e^{\left(\frac{2\kappa_e}{\cos\theta} + jk_z\right) h_v} - 1}{\frac{2\kappa_e}{\cos\theta} + jk_z}, \quad (3.12)$$

as well as the denominator, which represents the total backscattered power from the canopy layer

$$\sigma^{(dv)} = \int_{z_g}^{z_g + h_v} \rho^{(dv)} e^{\frac{2\kappa_e}{\cos\theta}(z - z_g - h_v)} dz = \rho^{(dv)} \frac{\cos\theta}{2\kappa_e} \left(1 - e^{-\frac{2\kappa_e}{\cos\theta} h_v}\right). \quad (3.13)$$

Therefore, the spatial degree of coherence γ_v of a layer of scatterers identified by the structure function $\rho_v(z)$ reduces to the following expression, function of the thickness

5. The product of all three terms in (3.9) may be also considered constant without any assumptions on the single terms. In this case a variant of the model presented in this section is obtained. This model leads to a $\text{Sinc}(\cdot)$ expression for the coherence and is useful for the estimation of model parameters discussed in Sec. 3.2

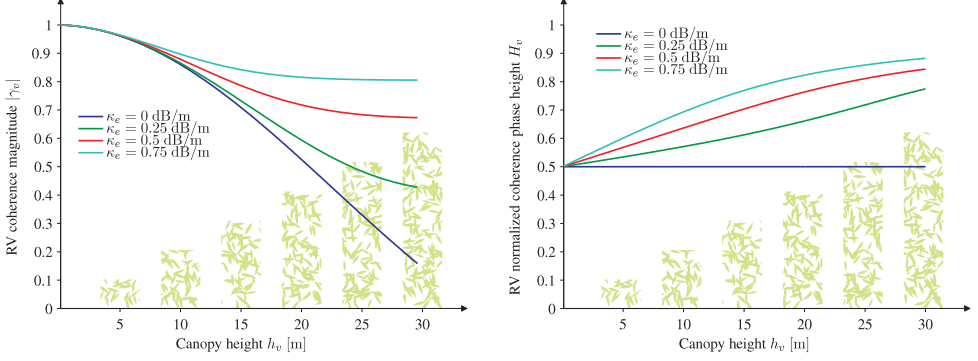


Figure 3.3: Interferometric coherence of a layer of randomly oriented scatterers corresponding to equation (3.14).

of the layer h_v , the mean canopy extinction κ_e and the bottom reference z_g

$$\gamma_v = \frac{\int \rho_v(z) e^{jk_z z} dz}{\int \rho_v(z) dz} = e^{jk_z z_g} \frac{\frac{2\kappa_e}{\cos \theta}}{\frac{2\kappa_e}{\cos \theta} + jk_z} \frac{e^{\left(\frac{2\kappa_e}{\cos \theta} + jk_z\right) h_v} - 1}{e^{\frac{2\kappa_e}{\cos \theta} h_v} - 1}. \quad (3.14)$$

In this model, the coherence has no dependence on the polarization, hence the POLINSAR technique reduces to the single-channel radar interferometry. A more compact form of (3.14) is obtained by collecting similar terms and defining the ground phase $\varphi_g = k_z z_g$

$$\gamma_v = e^{j\varphi_g} \frac{p_1 (e^{p_2 h_v} - 1)}{p_2 (e^{p_1 h_v} - 1)}, \quad \text{with} \quad p_1 = \frac{2\kappa_e}{\cos \theta}, \quad p_2 = \frac{2\kappa_e}{\cos \theta} + jk_z. \quad (3.15)$$

Fig. (3.3) shows the magnitude and the normalized phase height $H_v = \arg(\gamma_v)/(k_z h_v)$ of the RV coherence (3.14) for an L-band system with vertical wavenumber $k_z \simeq 0.2 \text{ m}^{-1}$. The maximum sensitivity of the coherence magnitude versus canopy height is obtained in the zero-extinction case. This case shows also that the minimum phase center height associated with the RV model is located at half canopy height, i.e. $H_v = 0.5$. It is also interesting to note that, if the canopy extinction augments, the wave penetrates less the canopy and consequently the volume correlation is higher (i.e. the decorrelation is lower) and the scattering phase center lifts.

Let us consider now a more complex scenario that includes a rough surface beneath the volume layer at $z = z_g$ as in Fig. (3.2b). This random volume over ground model has the same hypothesis as the RV case, i.e. homogeneity and uniformity of the canopy, and does not require additional assumptions on the ground surface. Following a similar development as before, the resulting structure function of the RVOG model includes now two additional contributions, the direct-ground and the ground-volume returns, with $z_g < z \leq z_g + h_v$

$$\rho_{g,v}(z) = \left(\rho^{(dg)} + \rho^{(gv)} \right) e^{-\frac{2\kappa_e}{\cos\theta} h_v} \delta(z - z_g) + \rho^{(dv)} e^{\frac{2\kappa_e}{\cos\theta} (z - z_g - h_v)} \quad (3.16)$$

where $\delta(z - z_g)$ is the Dirac's delta located at $z = z_g$ and $\rho^{(dg)}$, $\rho^{(gv)}$ are the *effective*⁶ attenuated scattering per unit length of the direct-ground and ground-volume components. Although from (3.16) the two ground factors look similar, their nature is very different. As depicted in Fig. (3.2b), the direct-ground component depends exclusively on the ground characteristics, whilst the ground-volume component depends on both the ground and canopy characteristics. Therefore, the latter is formally derived using equations similar to (3.9) and (3.10) used for the direct-volume component. Substituting (3.16) into (3.8) and evaluating the integrals, the complex coherence $\gamma_{g,v}$ of the RVOG model is

$$\gamma_{g,v} = e^{jk_z z_g} \frac{\sigma^{(dg)} + \sigma^{(gv)} + \rho^{(dv)} e^{-p_1 h_v} (e^{p_2 h_v} - 1)/p_2}{\sigma^{(dg)} + \sigma^{(gv)} + \rho^{(dv)} (1 - e^{-p_1 h_v})/p_1} = e^{jk_z z_g} \frac{\mu + \gamma_v e^{-jk_z z_g}}{\mu + 1} \quad (3.17)$$

where γ_v , p_1 and p_2 are defined in (3.15) and $\gamma_v e^{-jk_z z_g}$ indicates the volume-only coherence with zero ground reference and hence depending only on h_v and κ_e . The new real parameter μ is the *ground-to-volume attenuated scattering ratio* defined as

$$\mu = \frac{\sigma^{(dg)} + \sigma^{(gv)}}{\sigma^{(dv)}} = \frac{\sigma^{(dg)} + \sigma^{(gv)}}{\rho^{(dv)} \frac{\cos\theta}{2\kappa_e} \left(1 - e^{-\frac{2\kappa_e}{\cos\theta} h_v} \right)}. \quad (3.18)$$

The numerator in (3.18) is the total attenuated backscatter for direct-ground and ground-volume components. The denominator is the total attenuated backscatter of the volume layer only⁷. Eq. (3.17) addresses the RVOG coherence model in terms of four real parameters: the ground reference z_g , the canopy height h_v , the mean extinc-

6. Effective means that the scattering phase center has been located on the ground, although the ground-volume interaction occurs at different heights.

7. Note that in (3.18) the factor $e^{-\frac{2\kappa_e}{\cos\theta} h_v}$ multiplies both the numerator and the denominator. Sometimes in literature this factor is omitted. While this appears mathematically licit, the physical meaning of the terms results changed.

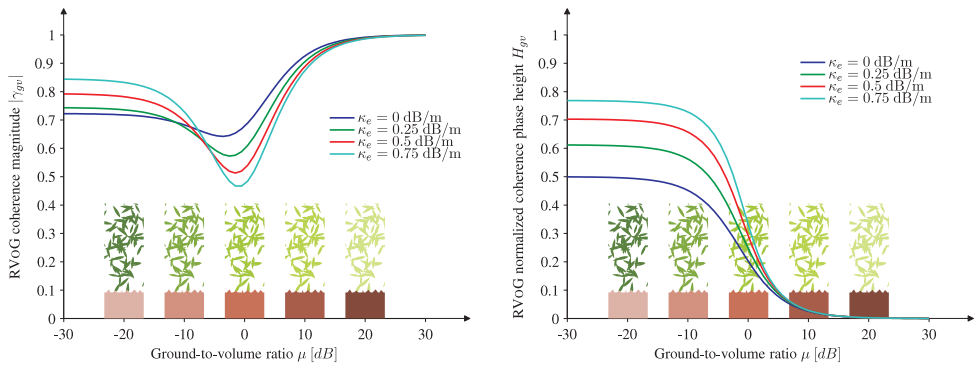


Figure 3.4: Coherence magnitude and phase of a random volume layer of scatterers over a ground surface.

tion κ_e and the ground-to-volume ratio μ . The canopy height and the ground reference are physical characteristics of the medium, really representing the forest height and the ground topography. The extinction and the ground-to-volume ratio are rather secondary parameters, which globally depend on geometric and dielectric characteristics of the medium. In particular, the extinction of a randomly oriented cloud of scatterers does not depend on the polarization of the impinging wave; on the contrary, the ground-to-volume ratio does depend on the polarization state. Hence, the dependence of the coherence on the polarization lies exclusively on the relative scattering interaction between canopy and soil.

In Fig. 3.4 the RVoG coherence is plotted versus the ground-to-volume ratio. The coherence phase position decrease monotonically as the ground backscatter becomes stronger with respect to the canopy backscatter. In the limit of $\mu \gg 1$ (i.e. dominant ground component), the canopy extinction becomes meaningless and all curves tend to the ground reference. Interesting is the case of the coherence magnitude. Adding more ground contribution does not necessarily increases the coherence. In particular, the coherence starts for small μ at some value depending on the volume scattering contribution γ_v . With increasing surface contribution it initially decreases, until reaching a point of absolute minimum which depends on the mean extinction. After that, it increases with μ and approaches asymptotically to one for any values of κ_e . This leads to the important conclusion that there is no direct relationship between the maximization/minimization of the coherence and the maximization/minimization of μ . This fact has some implications especially in the context of best polarization selection as discussed in Sec. 3.2.2.

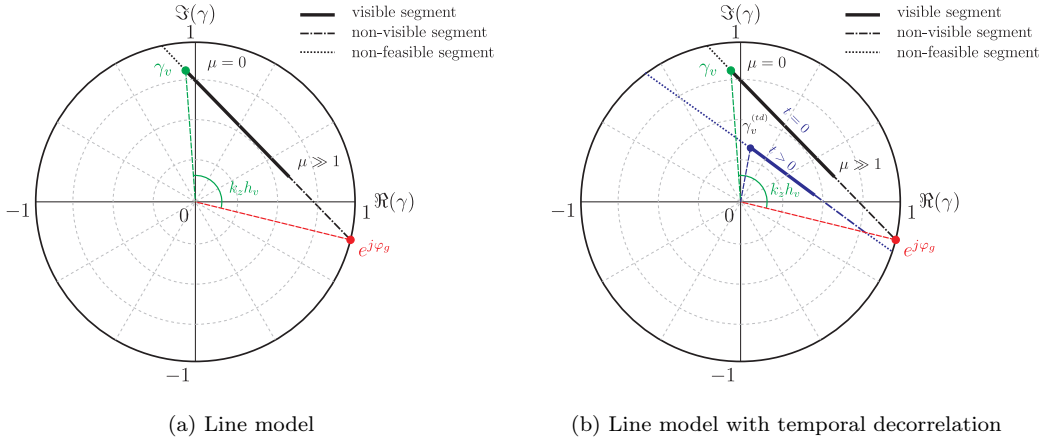


Figure 3.5: Line models in the complex plane of the spatial correlation of RVoG (a) and of the temporally decorrelated RVoG using the temporal correlation function (b).

The RVoG model offers an interesting geometrical interpretation. Let us consider again (3.17) and collect the polarization-dependent terms in a single factor $m = \mu/(\mu + 1)$, with $0 \leq m < 1$. The resulting expression is

$$\begin{aligned} \gamma_{g,v} &= e^{jk_z z_g} \frac{\mu + \gamma_v e^{-jk_z z_g}}{\mu + 1} = e^{j\varphi_g} \left[\gamma_v e^{-j\varphi_g} + \frac{\mu}{\mu + 1} (1 - \gamma_v e^{-j\varphi_g}) \right] \\ &= e^{j\varphi_g} [\gamma_v e^{-j\varphi_g} + m (1 - \gamma_v e^{-j\varphi_g})] \end{aligned} \quad (3.19)$$

which can be interpreted as a parameterization through m of a segment in the complex plane with x - and y -axis being the real and imaginary part of $\gamma_{g,v}$, respectively. The segment lies on the straight line passing through the volume-only coherence γ_v and ground-only coherence $e^{j\varphi_g}$. For this geometrical aspect, the RVoG model is often called the *line model*, which has been validated and used in several tests over forests at L- and P-band (Isola and Cloude, 2001; Papathanassiou et al., 2005). However, due to the violation of underlying assumptions of the random volume formulation, plotting the interferometric observations at different polarizations generates rather an ellipse or, in general, a 2-dimensional region, called *coherence region*. This aspect is closely related to the coherence optimization and to the best polarization selection treated in Sec. 3.2.2.

3.1.3 Temporal correlation model

In this section we review the expression of the RVOG coherence to include the effects of temporal decorrelation in a more accurate way than those proposed in literature. In previous works, the temporal decorrelation from a vertical distribution of scatterers has been accounted for by a constant term multiplying the volume correlation. A more advanced approach has been proposed by Papathanassiou and Cloude (2003) by splitting the effects of temporal decorrelation into ground decorrelation and canopy decorrelation. Since the ground is expected to be more stable than canopy against temporal artifacts, the RVOG has been modified to include two *real* temporal correlation factors, γ_{t_g} and γ_{t_v} for soil and vegetation respectively,

$$\gamma_{gv}^{(td)} = e^{j\varphi_g} \frac{\gamma_{t_g} \mu + \gamma_{t_v} \gamma_v e^{-j\varphi_g}}{\mu + 1}. \quad (3.20)$$

Both temporal correlation factors in (3.20) have been assumed real-valued and usually the ground decorrelation has been omitted, i.e. $\gamma_{t_g} \simeq 1$ (Papathanassiou and Cloude, 2003). The value of γ_{t_v} , on the contrary, has been estimated by several repeat-pass interferometric acquisitions at different temporal baselines (Lee et al., 2009).

A theoretical expression of γ_t in (3.4) may be derived considering that the decorrelation is primarily due to the motion of the scatterers between consecutive acquisitions. With this assumption, Zebker and Villasenor (1992a), and more recently Rocca (2007), have modeled the particles motion as a *Brownian motion*, i.e. the sum of many successive independent and equally distributed movements so that the Gaussian approximation holds. The resulting expression of the temporal correlation is

$$\gamma_t = e^{-\frac{t}{\tau}}, \quad \tau = \frac{2}{\sigma_B^2} \left(\frac{\lambda}{4\pi} \right)^2 \quad (3.21)$$

where τ is a time constant of the temporal decay of the coherence and σ_B the standard deviation per time-unit of the Brownian motion along the line-of-sight. Usually the time is expressed in day, and the motion standard deviation results expressed in $\text{m}/\sqrt{\text{day}}$. Eq. (3.21) states that the magnitude of the coherence decreases exponentially with the time, and with larger rate if the scatterers move and the system frequency is high.

Inspired by (3.20)-(3.21), we define a more accurate inclusion of temporal decorrelation effects in the coherence model. The key idea is to add a *temporal correlation function* which shapes the structure function of the canopy layer, so that the ground and the canopy particles experienced a different temporal decorrelation varying with the depth. Though this was known in the community as a possible improvement (Hagberg et al., 1995; Askne et al., 1997), in our knowledge nobody went deeper to define the

expression of the temporal decorrelation and hence it is worth considering this aspect more in detail. In the following, we discuss the form of such a function and present our development and implications of the temporal decorrelated RVOG model.

In order to correctly model the temporal changes along the vertical dimension, it is convenient to start from the expression of the interferometric coherence. Given the structure function $\rho(z)$ of the medium, temporal decorrelation arises from the modification of this structure function over time, resulting in a new structure function $\rho_t(z, t)$

$$\gamma^{(td)} = e^{j\varphi_g} \frac{\int_0^{h_v} \rho_t(z, t) e^{jk_z z} dz}{\int_0^{h_v} \rho(z) dz} = e^{j\varphi_g} \frac{\int_0^{h_v} \rho(z) \xi(z, t) e^{jk_z z} dz}{\int_0^{h_v} \rho(z) dz} \quad (3.22)$$

where $\xi(z, t)$ is the *temporal correlation function* which is responsible for the modification of the vertical structural profile over the time⁸. The novelty of (3.22) is in the variation of the temporal decorrelation *continuously* along the vertical dimension, and its inclusion in the integral operation. The form of $\xi(z, t)$ can be derived assuming that (3.21) holds for each infinitesimal slab dz with vertical-depending time constant $\tau(z)$

$$\xi(z, t) = e^{-\frac{t}{\tau(z)}}. \quad (3.23)$$

The form of the time constant along the vertical dimension depends upon several factors and, in general, on the vegetation species. However, it is reasonable to model the variance of the Brownian motion of the particles so that canopy slabs close to the ground are steadier than those close to the top. As canopy slabs are located higher, they experience a more severe temporal decorrelation. We hypothesize a linear trend for modeling the motion variance along the vertical dimension of the volumetric medium and, according to (3.21), the time constant function becomes

$$\frac{1}{\tau(z)} = \frac{1}{2} \left(\frac{4\pi}{\lambda} \right)^2 \left[\sigma_{Bg}^2 + \left(\sigma_{Bv}^2 - \sigma_{Bg}^2 \right) \frac{z}{h_r} \right] = \frac{1}{\tau_g} + \left(\frac{1}{\tau_v} - \frac{1}{\tau_g} \right) \frac{z}{h_{v_r}} \quad (3.24)$$

where σ_{Bg} and σ_{Bv} are the motion standard deviations per day of the ground and of the canopy at a reference height h_r respectively, and τ_g and τ_v the corresponding time constants so that $\tau_g \geq \tau_v$. The linearity assumption in (3.24) is the only condition that we impose in our temporal decorrelation modelisation and should be verified experi-

8. The introduction of $\xi(z, t)$ into the integral founds a more rigorous justification looking at equation (3.7). Indeed, we state that the reflectivity of the second acquisition differs from the first one by a phase term and a temporal correlation factor, hence (3.7) becomes $\rho_2(z, t) = \rho_1(z) \xi(z, t) e^{-jk_z z}$.

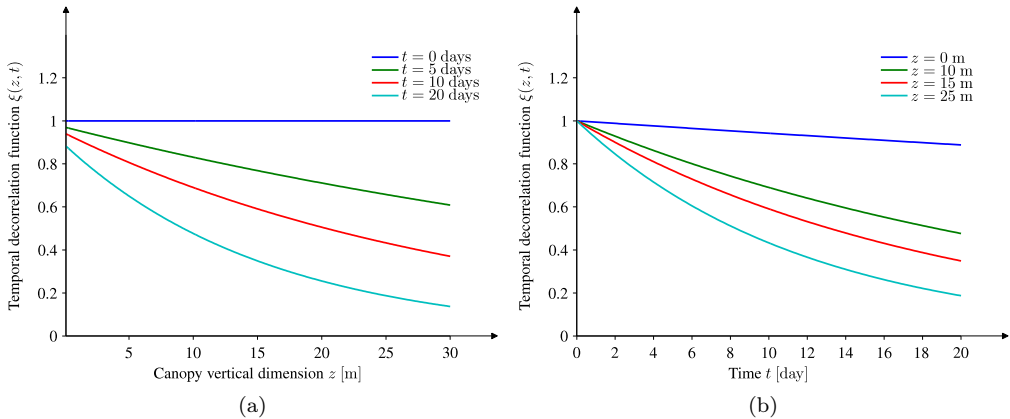


Figure 3.6: Temporal correlation function versus canopy vertical dimension and time.

mentally⁹. At the time of writing this dissertation no significant detailed study about decorrelation for different forest heights has been published. However, the experiments conducted by Zebker and Villasenor (1992a) for bare soil, lava flows or short vegetation and forests are in agreement with our assumption¹⁰. Substituting (3.24) into (3.23), the temporal correlation function becomes (cf. Fig. 3.7)

$$\xi(z, t) = e^{-\frac{t}{\tau_g} - \left(\frac{t}{\tau_v} - \frac{t}{\tau_g}\right) \frac{z}{h_r}}, \quad \tau_g \geq \tau_v. \quad (3.25)$$

Fig. 3.6 shows two plots of $\xi(z, t)$ versus the vertical dimension and the time, using $\tau_g = 2 \text{ mm}/\sqrt{\text{day}}$, $\tau_v = 5 \text{ mm}/\sqrt{\text{day}}$ and $h_r = 10 \text{ m}$. These values physically mean that the understory particles change their positions with 2 mm RMS in one day and tree particles at 10 m change their positions with 5 mm RMS in one day. As expected, both the sets of curves in Fig. 3.6a and Fig. 3.6b show a decreasing trend for taller canopy layers and longer temporal intervals. In particular, for $t = 0$, i.e. zero-temporal baseline, the ground and the canopy are perfectly correlated with themselves and $\xi(z, 0) = 1$, as confirmed by the horizontal straight line in Fig. 3.6a. As the time increases, the curve assumes lower values at $z = 0$ due to the ground decorrelation, and its shape becomes exponential, as consequence of the stronger volume decorrelation. On the other side, in Fig. 3.6b the curves origin all from the unity, decreasing exponentially

9. The temporal decorrelation model has been validated in a later publication using L-band airborne data Lavalle et al. (2012).

10. In the cited paper, plots of the coherence versus time are shown for different land covers. By comparing qualitatively those plots with the resulting decorrelation factor, we confirm that our assumptions are in agreement with results previously published.

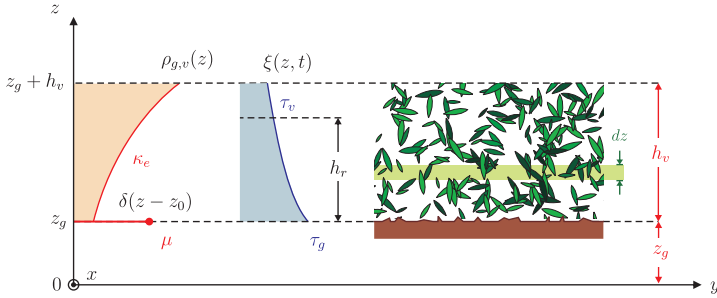


Figure 3.7: Schematic representation of temporal decorrelated RVOG model. Red parameters characterize the spatial (volume) correlation; blue parameters account for the characterization of temporal decorrelation effects.

depending on the height position into the canopy. These considerations are reasonably true for repeat-pass acquisitions over forested areas. An important peculiarity of our modelisation is that the temporal correlation function is defined with respect to the *actual height* and not to the *structure*. In other words, we believe that the temporal correlation function cannot be treated as the structure function, wherein the shape is *scaled* while increasing the tree height. Our approach, on the contrary, allows the top-canopy of trees 10 m tall to decorrelate less than the top-canopy of trees 20 m tall. The temporal correlation function (3.25) substituted into (3.22) leads to a general expression of the coherence including temporal decorrelation effects

$$\gamma_s \gamma_t = \gamma_s^{(td)} = e^{j\varphi_g} \frac{\int_0^{h_v} \rho(z) e^{-\frac{t}{\tau_g} - \left(\frac{t}{\tau_v} - \frac{t}{\tau_g}\right) \frac{z}{h_v}} e^{jk_z z} dz}{\int_0^{h_v} \rho(z) dz}, \quad \tau_g \geq \tau_v \quad (3.26)$$

wherein two additional real parameters account now for the temporal decorrelation of the target. Before dealing with the estimation of these two parameters, it is interesting to plot the predicted values of the coherence according to our model. We first cope with only the volume component, then we study the effects of the ground.

As discussed in Sec. 3.1, the structure function of a layer of uniform randomly distributed scatterers is characterized by an exponential decay. We superimpose the z -varying temporal correlation function and derive the expression of the *temporal decor-*

related RV model (TD-RV)

$$\begin{aligned}
 \gamma_v^{(td)} &= e^{j\varphi_g} \frac{2\kappa_e e^{-\frac{t}{\tau_g}}}{\cos\theta(e^{\frac{2\kappa_e h_v}{\cos\theta}} - 1)} \int_0^{h_v} e^{\frac{2\kappa_e z}{\cos\theta}} e^{-\left(\frac{t}{\tau_v} - \frac{t}{\tau_g}\right) \frac{z}{h_r}} e^{jk_z z} dz \\
 &= e^{j\varphi_g} \frac{2\kappa_e e^{-\frac{t}{\tau_g}}}{\cos\theta \left(e^{\frac{2\kappa_e h_v}{\cos\theta}} - 1 \right)} \frac{e^{\frac{2\kappa_e h_v}{\cos\theta} - \frac{h_v}{h_r} \left(\frac{t}{\tau_v} - \frac{t}{\tau_g} \right) + jk_z h_v} - 1}{\frac{2\kappa_e}{\cos\theta} - \frac{1}{h_r} \left(\frac{t}{\tau_v} - \frac{t}{\tau_g} \right) + jk_z}
 \end{aligned} \tag{3.27}$$

where $\gamma_v^{(td)}$ is analogous of γ_v calculated in (3.14) but now including temporal effects. In order to compare (3.27) with (3.14) and to highlight the peculiarities of this new expression, the coherence of temporal decorrelated RV model is written as

$$\gamma_v^{(td)} = e^{j\varphi_g} e^{-\frac{t}{\tau_g}} \frac{p_1 \left[e^{(p_2+p_3)h_v} - 1 \right]}{(p_2 + p_3) (e^{p_1 h_v} - 1)} \tag{3.28}$$

where

$$p_1 = \frac{2\kappa_e}{\cos\theta}, \quad p_2 = \frac{2\kappa_e}{\cos\theta} + jk_z, \quad p_3 = -\frac{1}{h_r} \left(\frac{t}{\tau_v} - \frac{t}{\tau_g} \right). \tag{3.29}$$

Note that (3.27) is similar to (3.15) with the exception of the term p_2 , which has become $p_2 + p_3$, and the presence of the additional multiplicative factor $e^{-\frac{t}{\tau_g}}$. The term p_3 contains information about temporal decorrelation. In the limit of $\tau_v \rightarrow \infty$ and, consequently $\tau_g \rightarrow \infty$, no temporal decorrelation occurs, hence $p_3 \rightarrow 0$ and $\gamma_v^{(td)} \rightarrow \gamma_v$. The importance of a vertical-depending motion of scatterers is outlined by the temporal correlation term only

$$\gamma_{t_v} = \frac{\gamma_v^{(td)}}{\gamma_v} = e^{-\frac{t}{\tau_g}} \frac{p_2 \left[e^{(p_2+p_3)h_v} - 1 \right]}{(p_2 + p_3) (e^{p_2 h_v} - 1)}. \tag{3.30}$$

which is complex valued since the term p_2 appears in (3.30). The peculiarity of this temporal decorrelation modelisation is the non-zero imaginary part of the temporal correlation γ_{t_v} . Eq. (3.30) clearly states that, if we assume a differential scatterer motion through the canopy depth, as reasonably happens in the reality, the coherence level decreases *and the scattering phase center shifts*. This is confirmed by Fig. 3.8a-3.8d where the magnitude $|\gamma_{t_v}|$ and the normalized phase center height $H_{t_v} = \arg(\gamma_{t_v}) / (h_v k_z)$ are plotted versus canopy height and temporal baseline. Where not specified in the plots, we have used constant values of temporal decorrelation $\sigma_{B_g} = 2 \text{ mm}/\sqrt{\text{day}}$,

$\sigma_{Bv} = 5 \text{ mm}/\sqrt{\text{day}}$, $t = 10 \text{ days}$, and $h_r = 10 \text{ m}$; constant values of the volume decorrelation are $h_v = 10 \text{ m}$, $\kappa_e = 0.2 \text{ dB/m}$ and $k_z = 0.18 \text{ m}^{-1}$. From Fig. 3.8a and 3.8b, when $\sigma_{Bv} = \sigma_{Bg} = 2 \text{ mm}/\sqrt{\text{day}}$, i.e. the soil decorrelates similarly to the canopy, we fall into the trivial case of uniform temporal decorrelation and the decorrelation function has no effects. This appears in the plots as a straight horizontal line versus the canopy height. Although not shown in the figure, if the motion of the scatterers increases (while still keeping $\sigma_{Bv} = \sigma_{Bg}$), then the line of the coherence magnitude remains straight and moves towards zero; on the contrary the normalized phase height remains unchanged at zero for different scatterer motions, as it depends on the *differential* scattering motion changing with the depth. In the case $\sigma_{Bv} > \sigma_{Bg}$, the coherence magnitude decreases with the canopy height and the time. Also, the scattering phase center moves towards the ground since the scattering interactions combine more coherently in the bottom part of the canopy layer. For instance, with a RMS canopy scatterer motion $\sigma_{Bv} = 6 \text{ mm}/\sqrt{\text{day}}$ chosen in agreement with the results published by Zebker and Villasenor (1992a), after 10 days the coherence of a 20 m canopy layer halves and the phase center moves 2 m down, only as consequence of temporal artifacts. Fig. 3.8c and 3.8d confirm these trends over time. Again, it is notable how the scattering phase center height moves towards the ground over the time, much faster when the canopy is taller.

The discussion can be extended to include the effects of the ground reflectivity. Since the decorrelation function acts in the canopy layer, no particular further modifications of the model follow with respect to the previous discussion. The vertical structure function must include now the effects of an underlying ground surface. The contribution of the ground to the reflectivity is modeled as a Dirac's delta located at $z = z_0$ weighted by the scattering amplitude of the ground σ_g . The coherence of the *temporal decorrelated random volume over ground model* (TD-RVOG) can be obtained by

$$\begin{aligned} \gamma_{g,v}^{(td)} &= e^{j\varphi_g} \frac{\int_0^{h_v} \rho_{g,v}(z) \xi(z, t) e^{jk_z z} dz}{\int_0^{h_v} \rho_{g,v}(z) dz} = e^{j\varphi_g} \frac{\mu e^{-\frac{t}{\tau_g}} + \gamma_v^{(td)} e^{-j\varphi_g}}{\mu + 1} \\ &= e^{-j\varphi_g} \left[\gamma_{tv} \gamma_v e^{-j\varphi_g} + \frac{\mu}{\mu + 1} \left(\gamma_{tg} - \gamma_{tv} \gamma_v e^{-j\varphi_g} \right) \right] \end{aligned} \quad (3.31)$$

wherein μ is the effective ground-to-volume scattering ratio, $\gamma_{tg} = e^{-\frac{t}{\tau_g}}$ is the real-valued temporal correlation of the ground surface and γ_{tv} is the complex-valued temporal correlation (3.30) of the canopy layer. Note that the ground-to-volume ratio is not affected by temporal changes, as we have assumed that temporal decorrelation is mainly

due to the motion of the particles. Fig. 3.8e and 3.8f show the temporal correlation $\gamma_{t_{g,v}}$ magnitude and its normalized phase height $H_{t_{g,v}}$, defined by

$$\gamma_{t_{g,v}} = \frac{\gamma_{g,v}^{(td)}}{\gamma_{g,v}}, \quad H_{t_{g,v}} = \frac{\arg(\gamma_{t_{g,v}})}{h_v k_z}. \quad (3.32)$$

Note that the temporal correlation factor has been defined as the ratio between the TD-RVOG model in equation (3.31) and the RVOG model in equation (3.19). This ratio contains a dependence of temporal correlation upon the ground-to-volume ratio, which is not surprising. Intuitively, if the ground surface backscatters more than the canopy, more steady scatterers contribute to the coherence and hence the temporal correlation is expected to be larger. Unfortunately, this is not true in general and more complex effects follow the interaction between ground surface and canopy particles. In particular, having more ground contribution does not necessarily increase the coherence as well as the scattering phase center as we see from the non-monotonic trend of all curves in the plots of Fig. 3.8e-3.8f. That trend is concerned with temporal decorrelation only and should be combined with Fig. 3.3 to design a parameter estimation strategy. In order to visualize the effect of the temporal decorrelation on the inversion procedures, the values of $\gamma_{g,v}^{(td)}$ is plotted in the complex plane, as shown in Fig. 3.5b. Eq. 3.31 still represents a segment while varying the values of μ and this happens for any expression of temporal decorrelation function since the line model depends on how the ground is included in the structure function. The difference with other temporal models is that the volume-only coherence point does not lie on the line between the origin and the volume-only coherence point in absence of temporal decorrelation. The main effect on the parameter estimation procedure is that the contribution to the canopy height arising from the difference between the ground phase and the volume-only coherence phase will result underestimated. This will be object of discussion in the next section.

3.2 Methods for coherence parameter estimation

An inversion procedure of the RVOG coherence has been originally formulated by Papathanassiou and Cloude (2001). It was formulated as a problem with six real variables, balancing three observed values of the complex coherence (corresponding to three different scattering mechanisms) with six model parameters, i.e. canopy height, ground topography, mean extinction and three ground-to-volume ratios. The solution of the problem was presented using a maximum likelihood estimation process, aiming at minimizing the difference between observed and predicted coherence. This process yields an estimate of all model parameters. Among those, the ground topography and the

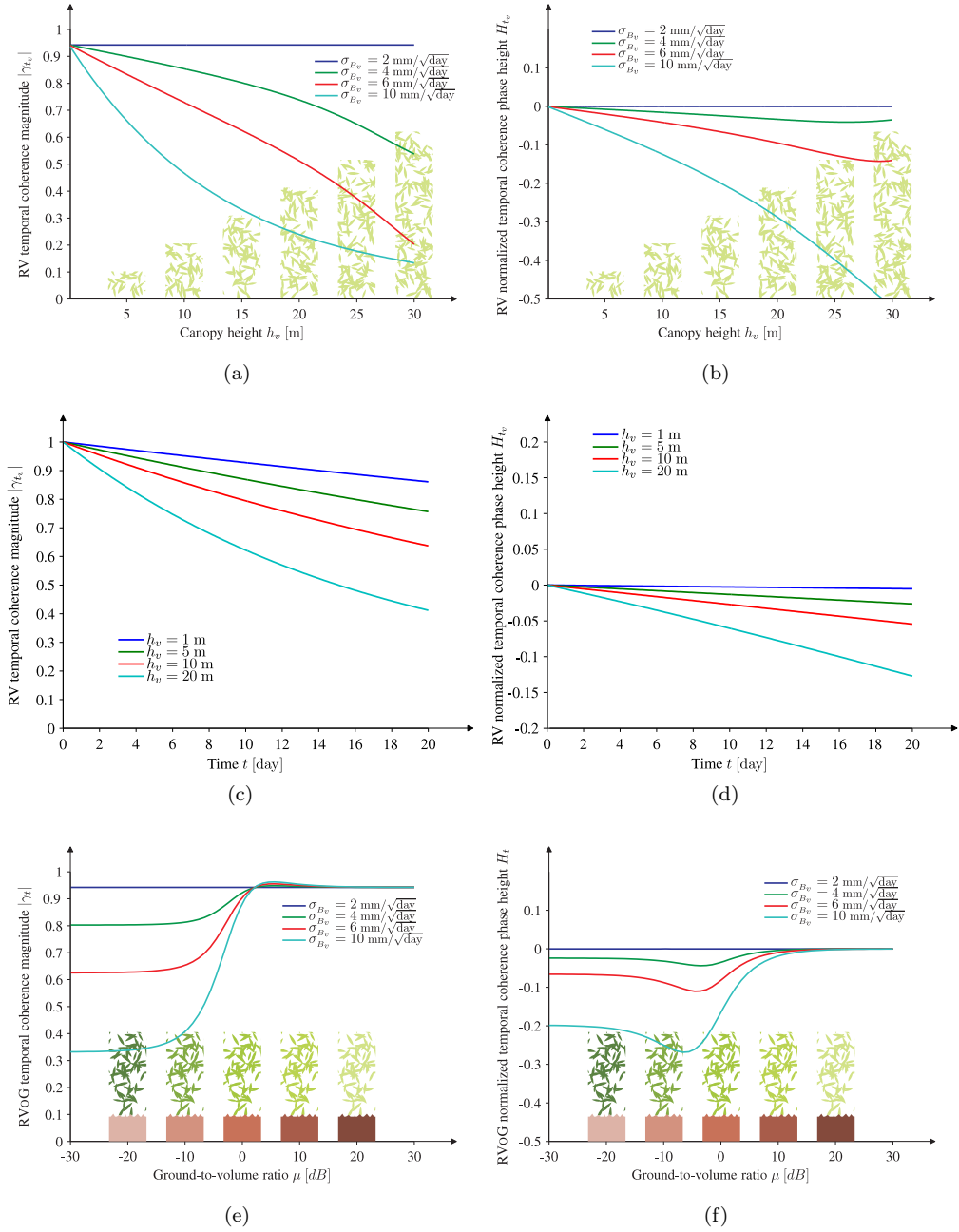


Figure 3.8: Coherence magnitude and phase of a temporal decorrelated random volume layer of particles over a ground surface. Only the temporal decorrelation factor is plotted.

vegetation height are the most significant for forestry applications. In order to provide a more robust estimation of topography and vegetation height, Cloude and Papathanassiou (2002, 2003) proposed an inversion procedure broken into three separate stages: (1) identification of the ground phase, (2) removal of the phase bias (with respect to the ground reference) from all coherence observations and (3) estimation of the canopy height. The objective of this section is to describe the main characteristics of this approach and to design a possible inversion scheme that includes the two temporal decorrelation parameters introduced in Sec. 3.1.3. The inverse problem is now based on the estimation of six real parameters from the estimated coherence at a generic polarization, i.e. the ground phase φ_g , the canopy height h_v , the ground time constant τ_g , the canopy time constant τ_v , the ground-to-volume ratio μ and the canopy mean extinction κ_e . Obviously, the inverse problem is underdetermined, since we have only 2 real observations (coherence magnitude and phase) and six real model parameters. In principle, adding more coherence observations, would increase the observation space by 2 elements (coherence magnitude and phase) and the parameter space by only one parameter (the ground-to-volume ratio which is polarization dependent). This approach is analogous to the original method mentioned above where three observations were needed (Papathanassiou and Cloude, 2001). Instead, we show in Sec. 3.2.1 that the new temporal decorrelation parameters can be estimated by making some assumptions on the vertical structure and using external estimates of ground topography and vegetation height (e.g. available from LIDAR measurements). It is assumed that temporal decorrelation parameters are assessed on selected test sites, and then used routinely in combination with coherence measurements to retrieve the unknown topography and canopy height. The retrieval process that we adopt is a minor modification of the inversion scheme presented in literature and available in the current implementation of POLSARPRO (Cloude, 2008). In the first step (Sec. 3.2.2) at least two coherence estimates must be selected at convenient polarization combinations in order to ensure a robust model parameter estimation. In the second step (Sec. 3.2.3), the ground phase is evaluated by exploiting the coherence values and the line model equation. Finally, in Sec. 3.2.4 three height inversion strategies are described, all based on simplified expressions of (3.19) and relying on the observation of a coherence with known ground-to-volume ratio, usually $\mu \simeq 0$.

3.2.1 Estimation of the temporal correlation function

The general expression of the temporal decorrelated coherence (3.28) simplifies in the case of zero-extinction ($\kappa_e \simeq 0$) and for volume-dominated coherence observations ($\mu \simeq 0$). The first assumption is a constraint on the vertical structure, stating that the vertical structure function (3.16) has a uniform profile. This is physically reasonable

since the density of the scatterers decreases with the height while the backscattered energy becomes stronger, so that their product can be assumed constant. The second assumption relies on the ability to select a polarization (or, more in general, a scattering mechanism) so that the associated ground-to-volume ratio is expected to be very low. The cross-polarized channel is sensitive to volume scattering mechanism and hence may be a good candidate for the selection. In a more general approach, all possible polarization combinations can be exploited in order to find a scattering mechanism \mathbf{w}_v corresponding to the lowest value of μ , as described in the next section. In general, the volume-dominated coherence under these assumptions can be indicated by $\gamma_{\mathbf{w}_v}$,

$$\gamma_{\mathbf{w}_v} \simeq e^{j\varphi_g} e^{-T/\tau_g} \frac{e^{(jk_z + p_3)h_v} - 1}{(jk_z + p_3)h_v} \quad (3.33)$$

where T is the temporal baseline of the interferometer and \mathbf{w}_v is a generic scattering mechanism with low ground-to-volume ratio. Although these assumptions reduce the dimensionality of the problem (from six to four variables), estimating the temporal decorrelation requires two external information. Note that this is not the consequence of the temporal correlation function; even in the case of constant temporal correlation this information is needed. They are usually available from LIDAR measurements or ground truth campaigns over selected test sites. With the a-priori knowledge of forest height h_v and topography phase φ_g over a test site, the average values of the temporal decorrelation parameters may be calculated by

$$\hat{\tau}_v, \hat{\tau}_g = \arg \min \left| \hat{\gamma}_{\mathbf{w}_v} e^{-j\varphi_g} - e^{-T/\tau_g} \frac{e^{(jk_z + p_3)h_v} - 1}{(jk_z + p_3)h_v} \right|, \quad p_3 = -\frac{1}{h_r} \left(\frac{T}{\tau_v} - \frac{T}{\tau_g} \right) \quad (3.34)$$

where T is the temporal baseline of the two observations and h_r is a reference height arbitrarily chosen (e.g. $h_r = 10$ m). Equation (3.34) states that τ_g and τ_v can be estimated by minimizing the difference between the volume-only observation $\hat{\gamma}_{\mathbf{w}_v}$ and the approximated RVOG prediction (3.33). If more repeated acquisitions at different temporal baselines are available, then the final estimate will result by averaging the estimated parameters at each baseline. In order to perform a more robust estimation, the ground temporal decorrelation may be neglected, i.e. $\tau_g \rightarrow \infty$, and consequently τ_v may be calculated by magnitude-only (or phase-only) measurements. As discussed in Sec. 3.1.3 this approach is still more general than temporal decorrelation models available in literature, as they assume a constant temporal decorrelation along the whole vertical volume layer. Obviously, this case (which is possible in principle) is not excluded in our modelisation and it is obtained by setting $\tau_g = \tau_v$.

3.2.2 Best polarization selection

A key concept in polarimetric radar interferometry is the possibility to combine polarimetric channels to select appropriate scattering mechanisms to be used for interferometric processing and inversion purposes. In earlier studies conducted by Cloude and Papathanassiou (1997) this problem has been named coherence optimization, although we adopt the general term of *best polarization selection*. In the case of forest height and topography estimation, the objective is to find two scattering mechanisms that maximize the interferometric phase separation or, in other words, correspond to the extreme values of the μ spectrum observed from the data. To this end, it is convenient to merge POLSAR and INSAR formalisms to define a 6-dimensional *interferometric scattering vector*

$$\mathbf{k}_P = (\mathbf{k}_{P_1} \ \mathbf{k}_{P_2})^T \quad (3.35)$$

that fully characterizes the POLINSAR observation. The polarimetric interferometric 6×6 *coherency matrix* contains the second-order characterization of such observation

$$\mathbf{T}_6 = \langle \mathbf{k}_P \mathbf{k}_P^\dagger \rangle = \begin{pmatrix} \mathbf{T}_{11} & \mathbf{\Omega}_{12} \\ \mathbf{\Omega}_{12}^\dagger & \mathbf{T}_{22} \end{pmatrix} \quad (3.36)$$

where superscript \dagger stands for transpose conjugate and angular brackets for spatial averaging over several samples. Matrices \mathbf{T}_{11} and \mathbf{T}_{22} are the conventional hermitian coherency matrices that describe the polarimetric properties for each image separately; $\mathbf{\Omega}_{12}$ is the 3×3 cross-coherency matrix that combines the polarimetric interferometric and orbital information. The expression of the complex coherence using (3.2), (3.3) and (3.36) becomes

$$\gamma = \frac{\langle \mathbf{w}_1^\dagger \mathbf{k}_{P_1} \mathbf{k}_{P_2}^\dagger \mathbf{w}_2 \rangle}{\sqrt{\langle \mathbf{w}_1^\dagger \mathbf{k}_{P_1} \mathbf{k}_{P_1}^\dagger \mathbf{w}_1 \rangle \langle \mathbf{w}_2^\dagger \mathbf{k}_{P_2} \mathbf{k}_{P_2}^\dagger \mathbf{w}_2 \rangle}} = \frac{\mathbf{w}_1^\dagger \mathbf{\Omega}_{12} \mathbf{w}_2}{\sqrt{(\mathbf{w}_1^\dagger \mathbf{T}_{11} \mathbf{w}_1) (\mathbf{w}_2^\dagger \mathbf{T}_{22} \mathbf{w}_2)}} \quad (3.37)$$

where vectors \mathbf{w}_1 and \mathbf{w}_2 express the selected polarization states or combination of polarization states for the two observations (cf. Sec. 3.1). A more compact definition of the POLINSAR coherence is based on the *whitened form* of the matrix \mathbf{T}_6 (Papathanassiou, 1999)

$$\tilde{\mathbf{T}}_6 = \begin{pmatrix} \mathbf{I} & \mathbf{\Pi} \\ \mathbf{\Pi}^\dagger & \mathbf{I} \end{pmatrix}, \quad \mathbf{\Pi} = \mathbf{T}_{11}^{-1/2} \mathbf{\Omega}_{12} \mathbf{T}_{22}^{-1/2} \quad (3.38)$$

where \mathbf{I} is the 3×3 identity matrix. From (3.38) the coherence and unitary projection vector expression rewrite as

$$\gamma = \mathbf{v}_1^\dagger \mathbf{\Pi} \mathbf{v}_2, \quad \mathbf{v}_i = \frac{\mathbf{T}_{ii}^{1/2} \mathbf{w}_i}{\mathbf{w}_i^\dagger \mathbf{T}_{ii}^{1/2} \mathbf{w}_i}, \quad i = 1, 2 \quad (3.39)$$

where $\mathbf{v}_1^\dagger \mathbf{v}_2 = 1$ holds. Apart from target reciprocity, no assumptions have been made on the interferometric observations. Hence, (3.37) or (3.39) are general expressions of the complex coherence when single-baseline POLINSAR acquisitions are available and can be readily extended to the case of a multi-baseline scenario. From a statistical point of view, (3.37) represents an estimator of the degree of coherence (Touzi et al., 1999), whose probability density function has been derived in closed form using the Wishart distribution for the \mathbf{T}_6 matrix (Lee et al., 1994, 1999). In practice, the need to develop algorithms and models for the coherence has led to two assumptions that simplify its expression. We limit to mention hereafter these assumptions as they are largely used. A discussion on their implications can be found in Ferro-Famil and Neumann (2008).

1. Polarimetric stationarity condition (PSC) of the target, which assumes similar coherency matrices

$$\mathbf{T}_{11} \simeq \mathbf{T}_{22}, \quad \mathbf{T} \doteq \frac{\mathbf{T}_{11} + \mathbf{T}_{22}}{2}. \quad (3.40)$$

This condition states that the target does not change its polarimetric characteristics (i.e. its polarimetric signature) between the acquisitions and it is usually satisfied for distributed targets and short temporal baselines. Statistical tests exist for assessing the validity of (3.40) and will be discussed in Chapter 4.

2. Single scattering mechanism (SSM), which assumes equal projection vectors for the two observations

$$\mathbf{w}_1 = \mathbf{w}_2 \doteq \mathbf{w}. \quad (3.41)$$

This becomes reasonable when the two acquisitions are realized in similar conditions, i.e. temporal decorrelation, atmospheric artifacts and processing or calibration distortions are negligible. It implicitly assumes the interferometric and polarimetric stationarity condition, i.e. $\mathbf{\Omega}_{12}^\dagger \mathbf{\Omega}_{12} = \mathbf{\Omega}_{12} \mathbf{\Omega}_{12}^\dagger$.

By including the previous equations (3.41) and (3.40) into (3.37), the expression of the POLINSAR coherence simplifies and becomes

$$\gamma_{SSM,PSC} = \frac{\mathbf{w}^\dagger \mathbf{\Omega}_{12} \mathbf{w}}{\mathbf{w}^\dagger \mathbf{T} \mathbf{w}} \quad (3.42)$$

with $|\gamma_{SSM,PSC}| < |\gamma|$ and $\arg(\gamma_{SSM,PSC}) = \arg(\gamma)$. Similarly, (3.39) simplifies under the two conditions of single scattering mechanisms and polarimetric stationarity yield-

ing $\mathbf{v}_1 = \mathbf{v}_2$. In the following we use the symbol γ to indicate the complex coherence under the two conditions stated above.

As mentioned in Sec. 3.1, the set of coherence values while changing the scattering mechanisms \mathbf{w} draws a 2-dimensional shape in the complex plane, the *coherence loci*, associated with each interferogram sample. An advanced and complete characterization of the shape of coherence loci under different assumptions has been conducted by Neumann (2009). In particular, it can be shown that the necessary and sufficient condition for matching the line model is that the matrix $\mathbf{\Omega}_{12}$ (or, equivalently, $\mathbf{\Pi}$) must be normal and its eigenvalues collinear. Unfortunately, it is often difficult to link the theoretical and detailed characterization of the coherence set with the physical parameters of forests. In our study, we are interested in the selection of the two most *phase-separated* coherence points: this has a simple physical reasoning because they are located respectively close to the top and to the bottom of the canopy layer.

Several approaches have been presented in literature to cope with this problem of polarization selection. The most general approach consists in a singular value decomposition (SVD) of the matrix $\mathbf{\Pi}$ (Cloude and Papathanassiou, 1997, 1998; Papathanassiou and Cloude, 2001). The advantage of this approach is that a global optimum problem is solved by selecting different scattering mechanisms and without further assumptions. However, the optimization is only on the magnitude of the coherence and the phase in this case is not necessarily optimized (Lavalle et al., 2007). Other approaches are based on the coherence region spanned by varying \mathbf{w} (Flynn et al., 2002; Tabb et al., 2002; Colin et al., 2006; Lavalle et al., 2007). It has been shown by Flynn et al. (2002) that the coherence loci is equal to the *field of values* of the matrix $\mathbf{\Pi}$. The field of values of an n -by- n complex matrix \mathbf{A} is defined as (Horn and Johnson, 1985)

$$\mathcal{V}(\mathbf{A}) = \{\mathbf{q}^\dagger \mathbf{A} \mathbf{q} : \mathbf{q} \in \mathbb{C}^3, \mathbf{q}^\dagger \mathbf{q} = 1\}, \quad (3.43)$$

and the *numerical radius* of the matrix \mathbf{A} is (Horn and Johnson, 1991)

$$r_n(\mathbf{A}) = \max \mathcal{V}(\mathbf{A}) = \max\{|\mathbf{q}^\dagger \mathbf{A} \mathbf{q}| : \mathbf{q} \in \mathbb{C}^3, \mathbf{q}^\dagger \mathbf{q} = 1\}. \quad (3.44)$$

To apply the two definitions (3.43) and (3.44) to the interferometric coherence, the problem must be constrained with the SSM and PSC conditions¹¹. There is no analytical method to find the field of values of a matrix. A numerical algorithm based on the iterative evaluation of the numerical radius can be found in Gustafson and Rao (1997). This algorithm can be used to find the best polarization combination corresponding to the maximization of the phase separation among coherence samples. A first approach

11. In Horn and Johnson (1991) the field of values is guaranteed to be a convex region in the complex plane. In the general case of (3.37) the shape of the coherence region is not guaranteed to be convex, as confirmed by real data analysis.

that copes with this problem has been presented by Tabb et al. (2002) and is named *phase diversity* (PD). We have proposed a variant of the phase diversity that improves (i.e. increases) the magnitude of the coherence while keeping the phase separation high (Lavalle et al., 2009, 2008b). Both algorithms are described hereafter.

The phase diversity algorithm is based on the maximization of the separation of the coherence phase and aims at finding the polarization vectors that maximize the cotangent of the argument of the complex coherence

$$\cot(\angle\gamma) = \frac{\operatorname{Re}\{\gamma\}}{\operatorname{Im}\{\gamma\}} = \frac{\mathbf{w}^\dagger(\boldsymbol{\Omega}_{12} + \boldsymbol{\Omega}_{12}^\dagger)\mathbf{w}}{\mathbf{w}^\dagger[-j(\boldsymbol{\Omega}_{12} - \boldsymbol{\Omega}_{12}^\dagger)]\mathbf{w}}. \quad (3.45)$$

The phase diversity algorithm works as follows.

1. Compute matrices \mathbf{T}_{11} , \mathbf{T}_{22} and $\boldsymbol{\Omega}_{12}$ using (3.1) and (3.36).
2. Compute the modified cross-coherence matrix $\widehat{\boldsymbol{\Omega}}_{12}$ obtained by a phase rotation $\varphi = \frac{\pi}{2} - \angle\operatorname{tr}(\boldsymbol{\Omega}_{12})$ of the cross-coherence matrix: $\widehat{\boldsymbol{\Omega}}_{12} = \boldsymbol{\Omega}_{12} e^{j\varphi}$.
3. Compute the two hermitian matrices $(\widehat{\boldsymbol{\Omega}}_{12} + \widehat{\boldsymbol{\Omega}}_{12}^\dagger)$ and $-j(\widehat{\boldsymbol{\Omega}}_{12} - \widehat{\boldsymbol{\Omega}}_{12}^\dagger)$.

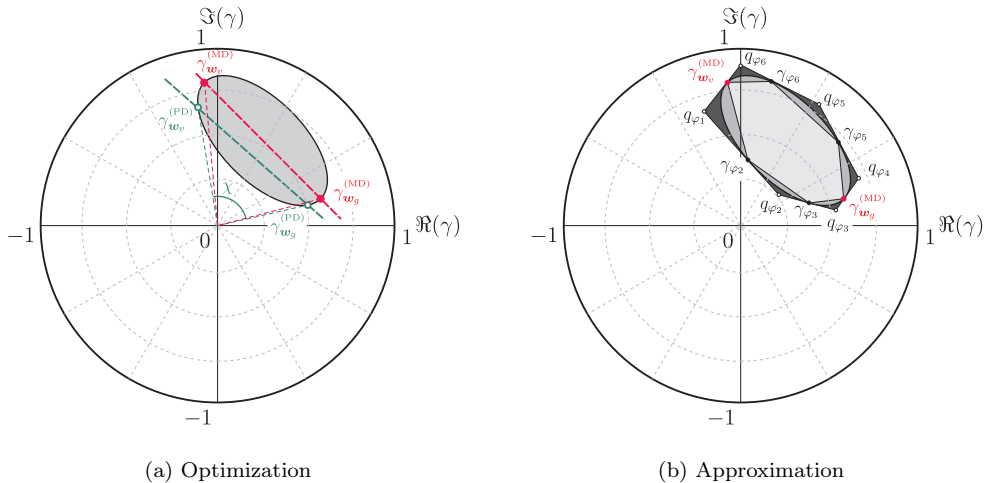


Figure 3.9: Example of coherence region and approximate polygons in the complex plane for $N = 6$ (a). The Magnitude Difference algorithm gives potentially higher coherence amplitude than the Phase Diversity optimization (b).

4. Solve the generalized eigenvalue problem

$$\left(\widehat{\mathbf{\Omega}}_{12} + \widehat{\mathbf{\Omega}}_{12}^\dagger\right) \mathbf{w} = -j\lambda \left(\widehat{\mathbf{\Omega}}_{12} - \widehat{\mathbf{\Omega}}_{12}^\dagger\right) \mathbf{w}. \quad (3.46)$$

5. Find the eigenvectors \mathbf{w}_v and \mathbf{w}_g , corresponding to the largest and smallest eigenvalue respectively of (3.46).
6. Compute the optimum coherence values $\widehat{\gamma}_{\mathbf{w}_v}^{(PD)}$ and $\widehat{\gamma}_{\mathbf{w}_g}^{(PD)}$ with highest and lowest phase center using (3.42) and the vectors \mathbf{w}_v and \mathbf{w}_g .

This approach has the main advantage of providing optimum eigenvectors that allow maximizing the phase separation among the values of coherence. However, the magnitude of coherence is not maximized, so the phase information may be not accurate (cf. Fig. 3.9b).

Since the boundary of the coherence region is approximately an ellipsis, we suggest identifying the polarization states that yield the highest *magnitude difference* (MD) between any baseline SSM coherence pair. As shown in Fig. 3.9a, this approach potentially gives a higher coherence level. The algorithm is based on the iteration used for computing the boundary of the field of values and it is detailed hereafter.

1. Compute matrices \mathbf{T}_{11} , \mathbf{T}_{22} and $\mathbf{\Omega}_{12}$.
2. Compute the matrix $\mathbf{\Pi} = \mathbf{T}_{11}^{-1/2} \mathbf{\Omega}_{12} \mathbf{T}_{22}^{-1/2}$.
3. Compute the boundary of the field of values of $\mathbf{\Pi}$ over N points by solving N eigenvalue problems (Horn and Johnson, 1991)

$$\frac{1}{2} \left(\mathbf{\Pi} e^{j\varphi_k} + \mathbf{\Pi}^\dagger e^{-j\varphi_k} \right) \mathbf{w}_{\varphi_k} = \lambda_{\varphi_k} \mathbf{w}_{\varphi_k} \quad (3.47)$$

where λ_{φ_k} is the maximum eigenvalue and, for convenience, $\varphi_k = k \frac{180}{N}$, $1 \leq k \leq N$. Let ζ be the column vector of the values of coherence for the N points. The k -th element of ζ , $1 \leq k \leq N$, has been obtained at the k -th step of the iteration by inserting \mathbf{w}_{φ_k} in (3.42).

4. Compute the $N \times N$ matrix $\Gamma = u\zeta^T - \zeta u^T$, with $u = (1 \ 1 \ \dots \ 1)^T \in \mathbb{R}^N$.
5. Find the maximum $\max\{|\gamma_{ij}| : \gamma_{ij} \in \Gamma, 1 \leq i \leq N, 1 \leq j \leq N\}$. Let i^* and j^* be the row and column, respectively, at which the maximum occurs.
6. Calculate the two values of the optimum coherence $\widehat{\gamma}_{\mathbf{w}_v}^{(MD)}$ and $\widehat{\gamma}_{\mathbf{w}_g}^{(MD)}$, i.e. $\widehat{\gamma}_{\mathbf{w}_v}^{(MD)} = \zeta_{i^*}$ and $\widehat{\gamma}_{\mathbf{w}_g}^{(MD)} = \zeta_{j^*}$ if $\arg(\zeta_{i^*} \zeta_{j^*}^\dagger) > 0$, otherwise $\widehat{\gamma}_{\mathbf{w}_v}^{(MD)} = \zeta_{j^*}$ and $\widehat{\gamma}_{\mathbf{w}_g}^{(MD)} = \zeta_{i^*}$.

The iteration gives an approximation of the boundary of the coherence region over N points. These samples are the vertices of the inner polygon with respect to coherence region (Fig. 3.9a). It is possible to choose N such that the inner polygon is arbitrarily

close to the true boundary. The robustness of the iteration above is ensured by the following observation. The boundary of the coherence region is always comprised between the inner polygon and the outer polygon with vertices (Horn and Johnson, 1991)

$$q_{\varphi_k} = e^{-j\varphi_k} \left[\lambda_{\varphi_k} + j \frac{\lambda_{\varphi_k} \cos(\varphi_{k+1} - \varphi_k) - \lambda_{\varphi_{k+1}}}{\sin(\varphi_{k+1} - \varphi_k)} \right]. \quad (3.48)$$

Thus, the difference between the areas of the two polygons can be taken as measure of the closeness of the approximation. Taking $N \geq 60$ gives in practice a close representation of the coherence region.

The MD approach considers the maximization of the magnitude difference among the coherence values on the boundary of the coherence region. The iteration increases the computational time compared to phase diversity approach, but it ensures a sub-optimum solution that is more reliable since the coherence level is higher. The two algorithms are illustrated in Fig. 3.9b. For narrow or small coherence loci they converge to the same values of the phase separation and give similar performance when the ground phase is estimated (cf. next section). This convergence is also favored by conspicuous speckle filtering, i.e. large averaging windows when the coherence is evaluated. By fixing all processing parameters, however, especially for large values of $k_z h_v$ product (e.g. $k_z h_v > 80$ deg), the performances of PD approach worsen (the ground coherence is underestimated) and the MD approach has demonstrated better results. The demonstration of this fact has been published by (Lavalle et al., 2007) and can be easily drawn from Fig. 3.9b. Rather than reporting those results, it is more useful to make a point on the coherence optimization algorithms. Coherence optimization (or best polarization selection) has been one of the first topics addressed by the POLINSAR community for its mathematical challenges and simplicity of the concept. In our experiments with POLINSAR, we have matured the idea that optimizing the coherence may be important in some cases but not always necessary (and sometimes even counter-productive). No optimization algorithm can provide a scattering center located exactly on the top or on the bottom of the canopy layer. For this reason, it is better to proceed with a specific model-based inversion as will be described in the following of this section. In this case, if the objective is to estimate the parameters of the RVOG line model, two well-separated coherence values would suffice. A model-based selection could serve this purpose: HH-VV and HV if quad-pol acquisitions are available, or HH and HV if dual-pol acquisitions are available. In presence of noise and small $k_z h_v$ values, this choice may not be appropriate and hence an optimization algorithm may be adopted. In the practical implementation, the two algorithms discussed above can be used in conjunction with a threshold on the $k_z h_v$ product. However, we must be aware that the polarization selection acts on the approximated coherence and this can lead to errors. The best approach would be to retrieve the line model directly from

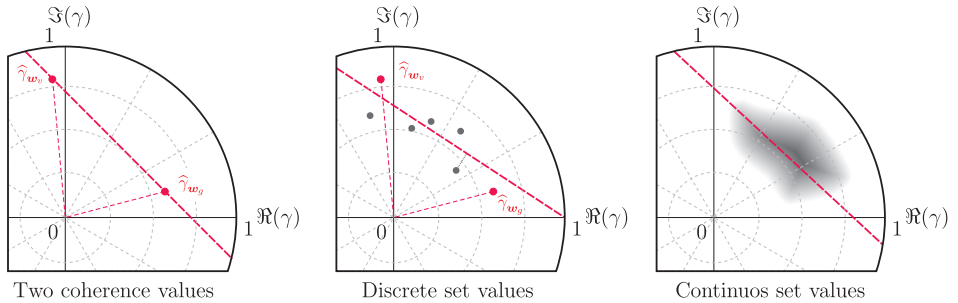


Figure 3.10: Methods for estimating line model parameters discussed in Sec. 3.2.3.

the cross-covariance matrix and to skip the discrete evaluation of the coherence. The solution to this approach has been found very recently by Ferro-Famil et al. (2009) and it is briefly mentioned in Sec. 3.2.3.

In order to illustrate the results, in this dissertation we preferred the model-based selection for PSPSIM numerical simulations (cf. Sec. 3.3), and the PD algorithm for the ALOS/PALSAR observations.

3.2.3 Estimation of ground phase topography

After the polarization selection, the next step in the height retrieval process is the estimation of the ground topography φ_g . The key idea proposed by Cloude and Papathanassiou (2003) is to calculate the equation of the RVOG line model for each POLINSAR data sample and to find the topography phase from the intersection between the line and the unit circle in the complex plane. In this process polarimetry plays a role, since two or more observations of the interferometric coherence are needed to obtain the equation of the line. In order to retrieve correctly the intersection, the temporal decorrelation contribution should be removed from the estimated coherence (cf. Fig. 3.5b). Unfortunately, the temporal contribution depends on the canopy height which is unknown at this stage of the inversion process. To overcome this limitation and to ensure a correct ground estimation, it is sufficient to assume here zero temporal decorrelation on the ground surface, i.e. $\tau_g \gg 1$. In terms of line model, this forces the intersection between the unitary circle and the line to be the true ground phase (cf. Fig. 3.5b). The line can be expressed either in its parametric form (3.19), i.e. as function of the ground-to-volume scattering ratio, or in the classical cartesian form as function of real and imaginary parts of the coherence with two real unknown parameters

a, b

$$\Im(\gamma) = a\Re(\gamma) + b. \quad (3.49)$$

There are three methods to estimate the value of the line parameters. In the first method, a and b are calculated from the equation of the line passing through the two coherence points $\hat{\gamma}_{w_g}$ and $\hat{\gamma}_{w_v}$. These coherence points can be estimated by best-polarization-selection algorithms or with a model-based approach as discussed in the previous section. For this first method, the resulting expressions can be easily obtained by

$$a = \frac{\Im(\hat{\gamma}_{w_v}) - \Im(\hat{\gamma}_{w_g})}{\Re(\hat{\gamma}_{w_v}) - \Re(\hat{\gamma}_{w_g})}, \quad b = \Im(\hat{\gamma}_{w_g}) - \Re(\hat{\gamma}_{w_g})a. \quad (3.50)$$

The second method is based on a discrete set containing more than two coherence observations. The line (3.49) can be resolved by minimizing the mean-square distance between the points and the unknown line, as shown in Fig. 3.10. The expression of the line parameters a and b will be function of the sample mean and variance of the real- and imaginary-part of the set of coherence values (Papoulis, 1991).

A more general method has been presented recently by Ferro-Famil et al. (2009). He showed that the line can be estimated in an analytical way by exploiting the whole available information contained in the matrix $\mathbf{\Pi}$. In comparison with the other two methods, this is equivalent to consider the continuous set of coherence values to fit the line (cf. Fig. 3.10). The line parameters are given by

$$a = -j \frac{\text{tr}(\mathbf{\Pi}_\Delta) \text{tr}(\mathbf{\Pi}_\Sigma) - 3\text{tr}(\mathbf{\Pi}_\Delta \mathbf{\Pi}_\Sigma^\dagger)}{\text{tr}(\mathbf{\Pi}_\Sigma) \text{tr}(\mathbf{\Pi}_\Sigma^\dagger) - 3\text{tr}(\mathbf{\Pi}_\Sigma \mathbf{\Pi}_\Sigma^\dagger)} \quad b = -\frac{a \text{tr}(\mathbf{\Pi}_\Sigma^\dagger) + j \text{tr}(\mathbf{\Pi}_\Delta)}{3} \quad (3.51)$$

wherein $\mathbf{\Pi}_\Delta$ is the *Hermitian part* of $\mathbf{\Pi}$, $\mathbf{\Pi}_\Delta = \frac{1}{2}(\mathbf{\Pi} - \mathbf{\Pi}^\dagger)$, and $\mathbf{\Pi}_\Sigma$ is the *skew-Hermitian part* of $\mathbf{\Pi}$, $\mathbf{\Pi}_\Sigma = \frac{1}{2}(\mathbf{\Pi} + \mathbf{\Pi}^\dagger)$. In order to increase the stability of this method and obtain better results, a regularization can be performed as preprocessing. The interferometric and polarimetric stationarity condition (in practice violated by the speckle) can be imposed onto $\mathbf{\Pi}$ using a matrix decomposition of $\mathbf{\Pi}$, and then the result of such a decomposition can be used in (3.51) for the parameters estimation.

Whichever method is chosen, fitting the line is highly sensitive to phase and magnitude fluctuations of the coherence, including the inherent bias of the coherence estimation and the uncompensated temporal or SNR correlation factors. The intersection between the line and the unit circle in the complex plane gives two candidate solutions for the ground phase

$$\varphi_{g1,2} = -\frac{ab \pm \sqrt{a^2 + 1 - b^2}}{a^2 + 1}. \quad (3.52)$$

The unambiguous identification of the ground phase between φ_{g_1} and φ_{g_2} is further based on two key strategies (Cloude and Papathanassiou, 2003). The first is to choose the phase point nearest (or further) from a known coherence sample which is expected to be close to (or far from) the ground. As example, the HV coherence is unlikely located closer to the ground than the HH+VV or HH-VV component. Hence, the favorite ground phase may be that one closer to the HH+VV coherence. Due to the noise, and especially in the case of small $h_v k_z$ value, this approach can lead to a wrong decision. It can be improved by adopting a sort of polarization rank for the decision and using several coherence points. A second approach consists in retrieving the canopy height for both the ground phase points, as described in the next section. The decision in this case is based on the fact that the maximum retrieved height must be lower than π/k_z , hence the ground phase yielding the minimum height is chosen. This latter approach is currently used as initialization of the PCT algorithm in POLSARPRO.

In our experiments with numerical simulations, we have tested all the combinations of the above mentioned methods. We have found that the estimation of the line parameters using two coherence observations and the polarization rank for solving the ambiguity is the best compromise between retrieval performance and computational efficiency when using numerical scattering simulations generated by PSPSIM.

3.2.4 Estimation of vegetation height

Once the ground phase $\hat{\varphi}_g$ is estimated as discussed in the previous section, the vegetation height can be retrieved using one of the four strategies described below. They are all based on the estimation of a volume-dominated coherence $\hat{\gamma}_{w_v}$, for which $\mu \simeq 0$ is assumed. The novel element here is the inclusion of the temporal correlation function affecting the inversion procedure with an iterative approach.

Complex coherence inversion. The first height retrieval approach is based on the minimization of the difference between observed and predicted coherences. This approach can be considered a particular case of the original approach mentioned at the beginning of the section. Since $\mu \simeq 0$ is assumed, the coherence predicted by the TD-RV \circ G model corresponds to the TD-RV model in equation (3.27). That expression contains five unknowns: h_v , κ_e , φ_g , τ_v and τ_g . Temporal decorrelation parameters and ground phase are estimated by the algorithms discussed in the previous sections. Hence, the height and the mean extinction rate can be retrieved by searching for optimal values that minimize the following difference (Papathanassiou et al., 2005; Mette et al., 2004; Hajnsek et al., 2009)

$$\hat{h}_v, \hat{\kappa}_e = \arg \min \left| \hat{\gamma}_{w_v} - \gamma_v^{(td)} \right| \quad (3.53)$$

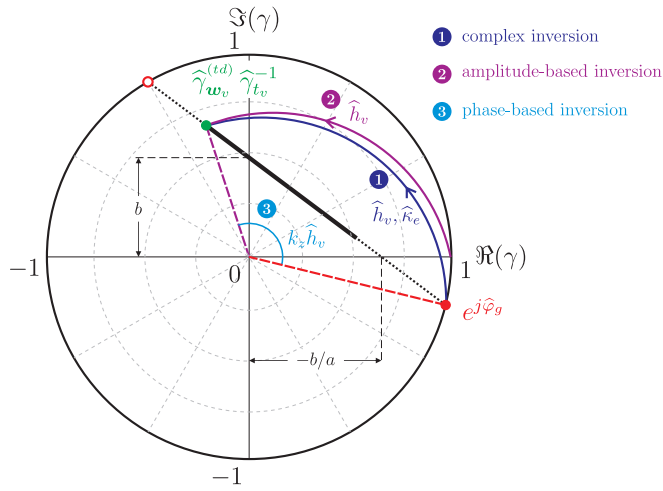


Figure 3.11: Geometrical interpretation of the inversion strategies adopted for the canopy height estimation.

where $\gamma_v^{(td)}$ is given by (3.27) and contains the estimated parameters $\hat{\varphi}_g$, $\hat{\tau}_v$ and $\hat{\tau}_g$. In this approach, both coherence phase and magnitude are employed for the inversion, hence the result is sensitive to 2-dimensional errors. In particular, the estimated extinction κ_e carries information about the *variations* of the actual structure function with respect to the exponential function imposed by the model. From the general expression (3.9), the structure function embeds both the properties of the distribution of the scatterers along the vertical dimension and their scattering/absorbing properties. It follows that $\hat{\kappa}_e$ is subject to both these sources of variation and may be noisy.

A way for improving the stability of the inversion is to constrain κ_e to include only scattering/absorbing properties; for this purpose κ_e can be set a-priori according to relationships published in literature (Cloude et al., 2001). The residual variation of the vertical structure is then accounted for by an additional parameter related to the canopy height. Finally, the solution is found by optimum search as in (3.53).

Phase-based coherence inversion. In this approach, the canopy height is estimated by assuming that there exists a scattering mechanism with phase center located close to the top of the canopy. Hence the canopy height corresponds simply to the difference between the phase of the volume-dominated coherence and the

estimated ground phase. In reality, the wave will always penetrate the canopy and the height will result underestimated: rather than the true forest height, this method provides an *uncompensated* estimate of the forest height. The amount of penetration depends on the actual structural profile of the canopy. Trees with high thin canopy will have a scattering center higher than trees with canopy extended over the full height according to the RVOG model. Nevertheless, the scattering phase center will always be located above the half true tree height¹² (cf. Fig. 3.3b). A further complication is added by the differential temporal decorrelation that we have introduced. In the modelisation exposed in Sec. 3.1.3, we have shown that the scattering phase center moves down in presence of canopy temporal decorrelation and therefore the height will be further underestimated. A way to partially correct this effect is to iterate over the estimated height and to compensate for the temporal decorrelation. The following procedure can be applied.

1. Start from a first estimate of forest height assuming constant temporal decorrelation in the canopy

$$\hat{h}_{v_0} = \frac{\arg(\hat{\gamma}_{w_v} e^{-j\hat{\varphi}_g})}{k_z} \quad (3.54)$$

2. Estimate the complex temporal decorrelation in the canopy using the height estimate \hat{h}_{v_0} and the temporal decorrelation parameters $\hat{\tau}_v, \hat{\tau}_g$

$$\hat{\gamma}_{t_v} = e^{-\frac{t}{\hat{\tau}_g}} \frac{p_2 \left[e^{(p_2+p_3)\hat{h}_{v_0}} - 1 \right]}{(p_2 + p_3) \left(e^{p_2\hat{h}_{v_0}} - 1 \right)}. \quad (3.55)$$

wherein p_2 and p_3 are given in (3.29).

3. Derive a better estimate of forest height including the complex temporal decorrelation

$$\hat{h}_v = \frac{\arg(\hat{\gamma}_{w_v} \hat{\gamma}_{t_v}^* e^{-j\hat{\varphi}_g})}{k_z} \quad (3.56)$$

and iterate the procedure between step 2 and step 3 if necessary, using \hat{h}_v in place of \hat{h}_{v_0} in (3.55).

Although this approach is named phase-based, the magnitude of the coherence is still used for retrieving the ground topography. To avoid this, it is possible to substitute the complex exponential in (3.54) and (3.56) with the ground-dominated coherence $\hat{\gamma}_{w_g}$. This is particularly useful when the coherence magnitude is highly

12. This is true only if the observed coherence corresponds to a pure volume contribution, i.e. $\mu = 0$.

affected by temporal decorrelation and resolving the line results noisy. The drawback of this latter approach is that the height is further underestimated since the ground-dominated coherence phase can lie several meters above the ground. Nevertheless, this phase-based method is applied to ALOS/PALSAR data to retrieve an uncompensated estimate of the forest height (cf. Sec. 3.4). Moreover, the inherent bias of the ground phase center will be quantified and corrected for P-band acquisitions in Sec. 3.5.

Magnitude-based coherence inversion. A third strategy similar to the previous one is the magnitude-based inversion. If the mean extinction rate is fixed in (3.14), then the inversion can be based only on the amplitude ascertaining from the phase fluctuations. The case $\kappa_e \simeq 0$ has proved to be effective. In the case of differential temporal decorrelation, the following procedure can be adopted.

1. Start from a first estimate of forest height assuming constant temporal decorrelation in the canopy

$$\hat{h}_{v_0} = \frac{2\text{Sinc}^{-1}(|\hat{\gamma}_{w_v}|)}{k_z} \approx \frac{2[\pi - 2\sin^{-1}(|\hat{\gamma}_{w_v}|^{0.8})]}{k_z} \quad (3.57)$$

where the expression in the second hand has been obtained by approximation of the Sinc function (Abramowitz and Stegun, 1965; Cloude, 2008).

2. Estimate the complex temporal decorrelation in the canopy using the height estimate \hat{h}_{v_0} and the temporal decorrelation parameters $\hat{\tau}_v, \hat{\tau}_g$

$$\hat{\gamma}_{t_v} = e^{-\frac{t}{\hat{\tau}_g}} \frac{p_2 [e^{(p_2+p_3)\hat{h}_{v_0}} - 1]}{(p_2 + p_3) (e^{p_2\hat{h}_{v_0}} - 1)}. \quad (3.58)$$

wherein p_2 and p_3 are given in (3.29).

3. Derive a better estimate of forest height including the complex temporal decorrelation

$$\hat{h}_v = \frac{2\text{Sinc}^{-1}(|\hat{\gamma}_{w_v} \hat{\gamma}_{t_v}^{-1}|)}{k_z} \approx \frac{2[\pi - 2\sin^{-1}(|\hat{\gamma}_{w_v} \hat{\gamma}_{t_v}^{-1}|^{0.8})]}{k_z} \quad (3.59)$$

and iterate the procedure between step 2 and step 3 if necessary, using \hat{h}_v in place of \hat{h}_{v_0} in (3.58)

Other values of κ_e are possible based on relationships published in literature.

Hybrid magnitude/phase inversion. The limitation of the previous two methods is their sensitivity to the vertical structure of a forest. To overcome this limi-

tation, a fourth approach that combines the phase-based and magnitude-based approaches has been proposed and it is currently preferred as initialization of the PCT algorithm (Cloude, 2006). The idea of this strategy is to compensate the underestimated result inherent to the phase-based approach with a magnitude-based term that accounts for the variation of the structure. Indeed, as the phase separation between volume- and ground-dominated coherence increases so the volume decorrelation decreases. This behavior is shown in the plot of Fig. 3.3a-3.3b. This magnitude term can be derived from the zero-extinction case. A new coefficient ν weighting the term must be introduced. As done previously, the temporal decorrelation can be included in an iterative fashion.

1. Derive a first estimate of forest height assuming constant temporal decorrelation in the canopy

$$\hat{h}_{v_0} = \frac{\arg(\hat{\gamma}_{w_v} e^{-j\hat{\varphi}_g})}{k_z} + \nu \frac{2[\pi - 2\sin^{-1}(|\hat{\gamma}_{w_v}|^{0.8})]}{k_z} \quad (3.60)$$

2. Estimate the complex temporal decorrelation in the canopy using the height estimate \hat{h}_{v_0} and the temporal decorrelation parameters $\hat{\tau}_v, \hat{\tau}_g$

$$\hat{\gamma}_{t_v} = e^{-\frac{t}{\hat{\tau}_g}} \frac{p_2 [e^{(p_2+p_3)\hat{h}_{v_0}} - 1]}{(p_2 + p_3) (e^{p_2\hat{h}_{v_0}} - 1)}. \quad (3.61)$$

wherein p_2 and p_3 are given in (3.29).

3. Derive a better estimate of forest height including the complex temporal decorrelation

$$\hat{h}_v = \frac{\arg(\hat{\gamma}_{w_v} \hat{\gamma}_{t_v}^{-1} e^{-j\hat{\varphi}_g})}{k_z} + \nu \frac{2[\pi - 2\sin^{-1}(|\hat{\gamma}_{w_v} \hat{\gamma}_{t_v}^{-1}|^{0.8})]}{k_z} \quad (3.62)$$

and iterate the procedure between step 2 and step 3 if necessary, using \hat{h}_v in place of \hat{h}_{v_0} in (3.61).

Other values of κ_e are possible based on relationships published in literature.

The parameter ν accounts for the variation of the extinction and has been found experimentally at L-band $\nu \simeq 0.4$. The expression above is in accordance with the special case of uniform structure function since both terms will give half the true height (if we set $\nu \simeq 0.5$) yielding the correct h_v estimate. The other extreme case is when the structure function in the volume channel is located near the top of the layer. In this case the phase-based term will give the true height and the second term will approach zero. The utility of this method is to provide a reasonable

estimate for arbitrary structure functions between these two extreme cases.

In our experiments with POLINSAR inversions over simulated, airborne and spaceborne data, the hybrid magnitude/phase method has demonstrated the most promising results. At this point of our investigation, we believe that this approach is also the most used by other scientists to obtain good results with the RVOG inversion especially over airborne data. Indeed, excellent results are obtained when this method is applied to PSPSIM data, as it is shown in the next section. We have also tried to invert ALOS/PALSAR data, but without complete success as it will be discussed in Sec. 3.4.

3.3 Parametric analysis using PSPSIM

In this section we consider the scattering and SAR image simulator PSPSIM introduced in Chapter 2. In previous works, Cloude and Papathanassiou (2003) used PSPSIM to test the inversion procedure over a single simulated scattering image. Similarly, Ballester-Berman and Lopez-Sanchez (2009) showed results of the POLINSAR Freeman-Durden decomposition over a single PSPSIM output.

As it will be shown hereafter, we exploit PSPSIM to perform a POLINSAR *parametric analysis* of the forest environment. This approach is new in the POLINSAR community (parametric analyses have been conducted using only the RVOG model) and has a twofold objective. From one side, numerical simulations represent a unique way to assess the range of validity of simplified models, such as the RVOG model. To this end, PSPSIM generates the scattering matrices associated with two SAR acquisitions and from these the coherence at different polarizations can be estimated and compared against model predictions (cf. Sec. 3.3.1). Secondly, a parametric analysis offers the opportunity to study in detail the effect and the sensitivity of different environment variables on the POLINSAR coherence (Lavallo et al., 2009). This investigation turns particularly useful for three main reasons: a deeper scientific understanding of the scattering interactions inside volumetric media; an improvement of the parameterization of current POLINSAR models; and the design of the optimal parameters of a SAR interferometer, such as angle of incidence, baseline and frequency (cf. Sec. 3.3.2).

3.3.1 Validity range of RVOG model

As discussed in Sec. 3.1.2, the ground-to-volume scattering ratio μ absorbs certain soil and vegetation properties into a single parameter. From the point of view of inverse modeling, this gives the opportunity to invert few coherence measurements to retrieve

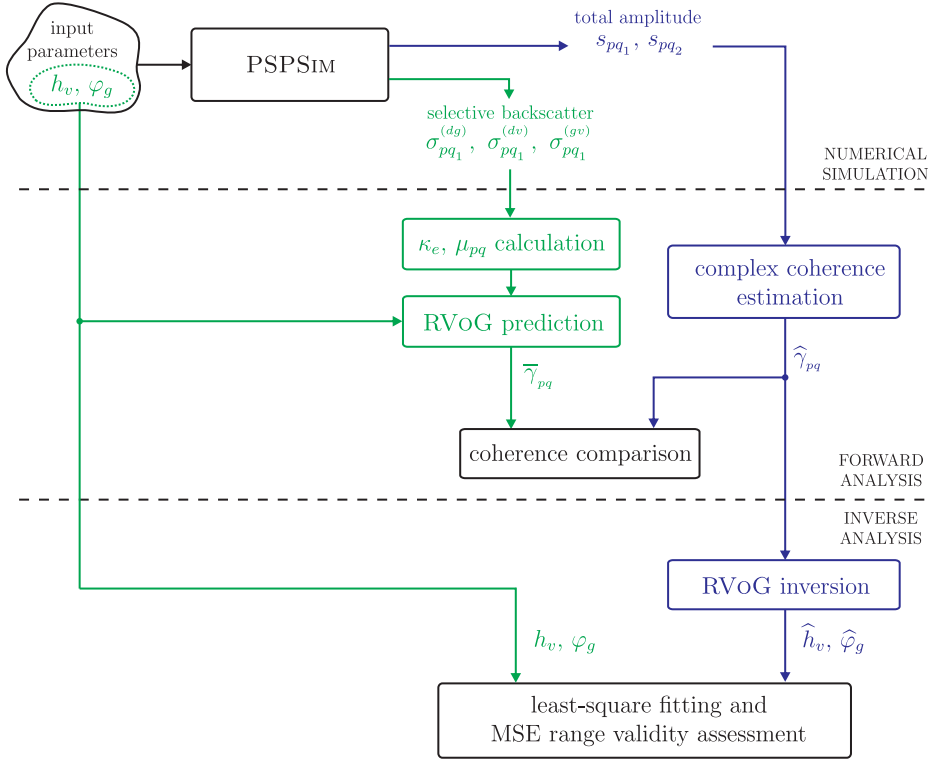


Figure 3.12: Logical steps for the assessment of the RVoG model using PPSIM assuming different forest height and terrain slope.

bio-physical parameters that are input to the model¹³, in particular forest height and ground topography. However, from the point of view of the forward modeling, a limited *parameter space*¹⁴ pose the question whether the model is able to predict reliably the coherence in different conditions. For instance, a sloped terrain induces a variation of the ground-to-volume ratio which translates into a variation of the predicted coherence (according to the RVoG model). Is this variation of model predictions in accordance with observations?

We try to answer this question for three environmental variables, i.e. the average tree

13. Obviously, the forest properties embedded into μ cannot be retrieved using the RVoG model and other approaches should be employed if we wish to retrieve them.

14. A parameter space is the manifold generated by the set of input parameters to the model (Tarantola, 2005).

height, the azimuth terrain slope and the range terrain slope. Each of these scene parameters affects the value of μ and consequently impacts on the degree of coherence. In other words, our objective here is to establish the range of validity of the RVOG model against a variation of these three parameters. To compare model predictions with observations we should be able to assess the input parameters of the model from the data. While h_v and φ_g can be available (e.g. from LIDAR measurements), estimating μ may prove to be a hard task. Indeed, if we were able to estimate μ at different polarizations with proper techniques, such as the blind separation of sources (Pham, 1996), the inversion strategies exposed in Sec. 3.2 would be much easier and accurate. Therefore in this study numerical simulations are of fundamental importance: they generate the individual scattering mechanisms (direct-ground, direct-volume, volume-ground) from which the ground-to-volume ratio can be easily determined. In the following, the general methodology is first exposed and then the analysis over the three environmental variables is presented.

The approach for the range validity assessment is based on both the forward modeling and the inverse modeling (Fig. 3.12). In the first case, we compare the coherence predicted by the RVOG model with the coherence estimated from PPSIM complex images. We indicate the former as the *predicted* coherence, and the latter as the *observed* coherence, since it requires an estimation procedure similar to real acquisitions. We do not enter into the details of the classical interferometric processing: it is known for long time (cf. Chapter 1) and several freeware and commercial packages exist for that purpose. We have implemented the interferometric processing chain for PPSIM imagery including interferogram flattening, vertical wavenumber computation, speckle filtering and complex coherence estimation (Ferretti et al., 2007).

The logical steps of our procedure are illustrated in Fig. 3.12. In that figure is shown the case of tree height, but the procedure is identical in the case of azimuth and range terrain slope. A set of simulations is generated for different forest heights h_v and fixing all other forest and acquisition parameters, including the ground topography φ_g . For each simulation, four interferometric pairs of scattering matrices are obtained: one for the total scattering return and three associated with the individual scattering returns. These three scattering matrices correspond respectively to the contribution from the trees (i.e. direct-volume, $\mathbf{S}_i^{(dv)}$), the soil beneath the canopy (direct-ground, $\mathbf{S}_i^{(dg)}$), and the soil-tree interaction (ground-volume, $\mathbf{S}_i^{(gv)}$), with $i = 1, 2$. From the total scattering matrices \mathbf{S}_i , $i = 1, 2$, the observed complex coherence $\hat{\gamma}_{pq}$, $p, q = h, v$, is estimated pixelwise using (3.3)

$$\hat{\gamma}_{pq} = \frac{\langle s_{pq_1} s_{pq_2}^* \rangle}{\sqrt{\langle s_{pq_1} s_{pq_1}^* \rangle \langle s_{pq_2} s_{pq_2}^* \rangle}}, \quad p, q = h, v. \quad (3.63)$$

Note that the coherence is evaluated here only for the three polarization states HH, HV and VV, although an optimization algorithm could be also employed. In order to calculate a predicted value of the coherence through the RVOG model, the values of the mean extinction κ_e and ground-to-volume ratio μ must be known. Given the selective backscattering matrices of the forest $\mathbf{S}_i^{(dv)}$ and of the ground interactions $\mathbf{S}_i^{(dg)}$ and $\mathbf{S}_i^{(gv)}$, the ground-to-volume ratio can be estimated at different polarizations for each acquisition

$$\widehat{\mu}_{pq_i} = \frac{\sigma_{pq_i}^{(dg)} + \sigma_{pq_i}^{(gv)}}{\sigma_{pq_i}^{(dv)}} = \frac{\langle |s_{pq_i}^{(dg)}|^2 \rangle + \langle |s_{pq_i}^{(gv)}|^2 \rangle}{\langle |s_{pq_i}^{(dv)}|^2 \rangle}, \quad p, q = h, v, \quad i = 1, 2. \quad (3.64)$$

and then averaged between the two acquisitions since the polarimetric stationarity condition holds (cf. Sec. 3.2.2)

$$\widehat{\mu}_{pq} = \frac{\widehat{\mu}_{pq_1} + \widehat{\mu}_{pq_2}}{2} \quad p, q = h, v. \quad (3.65)$$

The wave extinction in the canopy is also, in reality, polarization dependent. However, the randomly uniform nature of the volume layer in the RVOG model entails a constant extinction coefficient κ_e . Its estimated value $\widehat{\kappa}_e$ is obtained by averaging the direct and double-bounce extinctions estimated at H and V polarizations, calculated during the numerical simulation as discussed in Chapter 1. Alternatively, κ_e can be estimated from the ratio between the attenuated $s_{pq_i}^{(dg)}$ and the un-attenuated $\widetilde{s}_{pq_i}^{(dg)}$ direct-ground returns for a fixed height, e.g. $h_v = 15$ m,

$$\widehat{\kappa}_e = \frac{1}{4} \sum_{i=1,2} \sum_{p=h,v} \frac{\cos \theta}{2h_v} \ln \frac{|\widetilde{s}_{pp_i}^{(dg)}|^2}{|s_{pp_i}^{(dg)}|^2} \quad (3.66)$$

wherein the double summation means averaging among polarizations and acquisitions. Using the ground topography phase φ_g and forest height h_v outset for each simulation, and the estimated ground-to-volume ratio $\widehat{\mu}_{pq}$ and extinction $\widehat{\kappa}_e$, the predicted RVOG coherence is, for each simulation,

$$\overline{\gamma}_{pq} = \gamma_{g,v}(\varphi_g, h_v, \widehat{\mu}_{pq}, \widehat{\kappa}_e), \quad p, q = h, v \quad (3.67)$$

where $\gamma_{g,v}$ is the RVOG model function showed in (3.17). Although not shown, in (3.67) we use some system parameters of the interferometer, namely the wavelength λ , the look angle θ and the perpendicular baseline B_\perp . The temporal baseline T is meaningless here since PPSIM simulates only the spatial decorrelation. Looking at Fig. 3.12, the first qualitative assessment of the reliability of the RVOG model is the

comparison between $\widehat{\gamma}_{pq}$ and $\overline{\gamma}_{pq}$, $p, q = h, v$. Any deviation in the predicted coherence propagates through the inversion procedure and leads to errors on the height and ground topography estimates. The quantitative range of validity is established with a threshold on this error, related with the requested accuracy of the height retrieval, usually 10% of the total height (Papathanassiou et al., 2005). In order to estimate the RMS error, the observed coherence is inverted using the hybrid magnitude/phase inversion strategy outlined in Sec. 3.2.4, disregarding the temporal correlation factor. Then the estimated forest height \widehat{h}_v and topography phase $\widehat{\varphi}_g$ are compared with the respective true value given as input to the numerical simulations and the validity range is assessed. In the case of slope analysis, the procedure is the same, with the exception that h_v is fixed and $\widehat{\mu}_{pq}$ varies as consequence of the terrain tilt. The forest scenario is described hereafter along with the qualitative and quantitative results.

Varying the forest height

The imaged scenario has been described in detail in Sec. 2.3 and includes a Scots pine forest, an underlying ground surface and a layer of short vegetation above the ground. In the parametric analysis of forest height, sixteen different realizations of this scenario are generated by varying tree height from 6 m up to 25 m on a mean flat terrain. The ground surface is located at zero reference ($\varphi_g = 0$) and is characterized by a small scale roughness with 0.034 m correlation length, and a large scale roughness with 5.425 m correlation length. Dielectric value of soil is fixed at 9.717-j1.316. The short vegetation is 0.30 m tall and is a uniform random layer of stems and leaves with volume fraction 0.004 and 0.0005 respectively. The forest covers a circular area of about 31 hectares (corresponding to a radius of 240 m) and has 700 trees/Ha stem density. The mean extinction is about 0.3 dB m⁻¹. The total extent of the imaged area is approximately 500 × 500 m² and each imaged sample corresponds to an area on the ground of about 2.3 × 2.3 m². Sensor parameters are those typical of the E-SAR sensor at L-band: wavelength $\lambda = 1.27$ GHz, sensor altitude $H = 3670$ m, angle of incidence $\theta = 45$ deg and horizontal baseline $B = 20$ m. Two important derived parameters are the vertical wavenumber $k_z \simeq 0.2$ m⁻¹, which is related to the sensitivity of the interferometer, and the *critical baseline* $B_{\perp,cr} \simeq 240$ m, which is the maximum allowable perpendicular baseline before complete spatial decorrelation. Since the baseline is a degree of freedom in the design of interferometers, having a large baseline increases k_z and hence the sensitivity of the interferometer, but increases also the decorrelation as the baseline approaches the critical baseline. This aspect is well illustrated by the SAR frequency system model described in Chapter 1. The radar observes the targets from two different look angles, and two slices of the target spectrum are transferred into the images. The frequency shift of these two slices corresponds to the spatial decorrelation. A way to

reduce this effect is to apply a process named *spectral shift and filtering* (Gatelli et al., 1994) which selects the constructive common bandwidth of the two acquisitions. As a result of the spectral filtering, the correlation is unitary (for pure surface scatterers) and spatial resolution of the interferograms reduces. In our case, this process would increase the coherence of about $B_{\perp}/B_{\perp,cr} \simeq 0.05$ and hence it is disregarded.

Fig. 3.13 shows the set of backscatter outputs at different forest heights, including the total and the individual returns, i.e. direct-volume, direct-ground and ground-volume returns. For each scattering return, the backscatter in the three polarization channels HH, HV, VV is shown. As general behavior, in the total and direct-volume backscatter images the grey intensity increases as trees become taller. On the contrary, direct-ground component decreases if the forest height increases, as it is evident from the darker circular area in the image. Interesting is the case of the ground-volume mechanism. The co-polar channels HH and VV backscatter increases from 6 m to 15 m, and then decreases again above 15 m. This is due to two concurrent effects: the larger canopy depth absorbs more ground-volume co-polar power and, at the same time, increases the ground-trunk interactions (VV) and the ground-branches interactions (HH). The ground-volume cross-polar return, on the contrary, originates mainly from the interactions between ground and canopy (or curved branches), which tend to augment with the forest height. A more accurate qualitative analysis is conducted by plotting the value of μ averaged in the central vegetated area versus h_v . The plot in Fig. 3.14a shows that the ground-to-volume ratio decreases for taller trees in the co-polar channels and is almost constant in the HV channel. The value of μ in the HV channel is about 10-20 dB lower than HH and VV channels.

The interferometric coherence has been estimated over 11×11 pixels and the HH, HV, VV, HH+VV and HH-VV coherence magnitude and phase are shown in Fig. 3.15. It appears evident in all polarization channels that the scattering phase center lifts off the ground with the increment of forest height. This is in accordance with the plots of the RVOG model in Fig. 3.3b and Fig. 3.4b where the normalized phase height has a monotonic trend versus canopy height and ground-to-volume ratio¹⁵. On the contrary, it is not true in general that the coherence magnitude decreases as trees become taller. This is a peculiar aspect of volumetric media and arises from the combined contribution of ground and canopy, as confirmed by the model analysis of Fig. 3.4a. In our observations, these behaviors appear stronger in the VV channel of Fig. 3.15, wherein the coherence magnitude decreases until about 18 m and then increases again. From the polarimetric point of view, we can draw two important observations. The first is that, in general, we cannot state that certain polarimetric channels have higher coherence level than other channels. Indeed, depending on the ground-to-volume ratio, the coherence

15. Note that in the height parametric analysis the ground-to-volume ratio is expected to decrease with the forest height in all polarimetric channels.

observed in HV channel, for instance, can be higher or lower than the HH coherence, as appears for shorter trees in Fig. 3.15. Note that the coherence magnitude affects only partially the position of the POLINSAR coherence points along the line in the complex plane, since it is more the coherence phase that determines their relative position. The second observation is indeed on the coherence phase. Fig. 3.15 confirms the physical link among polarization states (or scattering mechanisms) and scattering phase center height. As an example, we notice that the HH–VV scattering phase center always lies below the HV phase center. The comparison between observed and predicted coherence is plotted in Fig. 3.16. The observed coherence is averaged in the central forested area of each simulation. Since we have used realistic values of ground-to-volume ratio combined with forest height and mean extinction, we can assess the scattering phase center location with high fidelity. For instance, in the case of forest 20 m tall with moderate density, the HH phase center is located around 5 m above the ground and the HV phase center about 5 m below the top of the canopy. The predicted coherence is also plotted with dashed lines. The main conclusion from these plots is that the RVOG model is generally very reliable for different forest heights, with some exceptions of coherence magnitude for higher canopy. However, these errors are negligible since the inversion procedure is robust enough and the forest height results retrieved with accuracy better than 10% over the range of tested forest heights (cf Fig. 3.14b). We remark that this is true for pine trees and in presence of spatial decorrelation only. In a real-like scenario, different tree species may yield different performance.

Varying the azimuth terrain slope

In the case of slope analysis, fifteen simulations are performed with ground tilt ranging from -7% to 7% , and 15 m average forest height. The remaining characteristics of the ground surface, the short vegetation layer and the forest are the same as described in the height analysis above. The backscatter and coherence output of azimuth slope parametric analysis are reported in Fig. 3.17 and Fig. 3.19 respectively. Notably, the HV ground-volume scattering return is the only channel sensitive to the azimuth terrain slope. This impacts on the ground-to-volume ratio (cf. Fig. 3.18a) which about 10 dB deviates from the zero-slope case in the HV channel, and remains almost constant in the HH and VV channels. The same trend can be observed on both the predicted coherence and the coherence estimated from PSPSIM simulations. In Fig. 3.19, the total coherence HH–VV reveals the ground tilt with a linear change of its phase. In that channel, the phase shift induced by the forest is almost negligible. In order to enhance the slope analysis and to highlight the contribution of the tilted ground, we can single out its contribution in the coherence. In other words, we can define a sort of *residual coherence factor* due to topography from the ratio between the estimated

coherence and the coherence estimated for $\alpha_a = 0$

$$\hat{\gamma}_s(\alpha_a) = \frac{\hat{\gamma}(\alpha_a)}{\hat{\gamma}(0)} \quad (3.68)$$

wherein the dependence of the polarization has been omitted. As a complex number, $\hat{\gamma}_s(\alpha_a)$ gives the variation of the magnitude and phase of the complex coherence as consequence of the tilted terrain only. Its magnitude can be greater than 1 as it is not a decorrelation source but rather a residual factor. The curves associated with $\hat{\gamma}_s(\alpha_a)$ versus the azimuth slope α_a are plotted in Fig. 3.20. Notably, the HV returns decorrelate in presence of 7% azimuth tilt of about 0.08, and their scattering phase center moves down about 2 m. Fortunately, this variation is well followed by the RVOG predictions as the dashed lines in the same plot confirm. Therefore, we conclude that predicted and observed coherences in presence of azimuth terrain slope show a very good agreement for both the magnitude and the phase. As expected, the RVOG inversion retrieves the canopy height and the underlying topography with accuracy better than 10% over the full range of tested azimuth slope (cf. Fig. 3.18b).

Varying the range terrain slope

A similar analysis has been conducted for range terrain slope, i.e. by varying the ground tilt between -7% and 7% , which corresponds to $\alpha_r \simeq \pm 7$ deg, and fixing $h_v = 15$ m. Positive values correspond to a surface facing the radar antenna. The backscatter output is illustrated in Fig. 3.21 wherein the most evident effect is the decreasing of co-polar ground-volume return in presence of sloped terrain as consequence of the deformation of the double-bounce geometry at the base of the trees. In general, the interpretation of range-sloped results is more critical due to the inherent imaging characteristics of the radar. As received samples are arranged on the basis of the range time delay, topography causes geometrical (and radiometric) distortions, usually classified as foreshortening, layover and shadowing phenomena in a single SAR image. The interferometer is also affected by the topography: as the terrain is tilted, the target is actually observed from look angles different than the nominal ones and this impacts on the spectral shift between the two received signals. Hence, to calculate the vertical wavenumber and the critical baseline $B_{\perp,cr}$, the look angle θ must be replaced by the local incidence angle $\theta - \alpha_r$, yielding (Bamler and Hartl, 1998)

$$k_z = \frac{4\pi B_{\perp}}{r_0 \lambda \sin(\theta - \alpha_r)}, \quad B_{\perp,cr} = \frac{W_r r_0 \tan(\theta - \alpha_r)}{c} \quad (3.69)$$

where W_r is the system range bandwidth (cf. Chapter 1). When α_r increases from zero, the vertical wavenumber increases and the critical baseline reduces, yielding greater

sensitivity but lower correlation; for values of α_r close to θ , i.e. in the region of *blind angles*, the sensitivity is completely loosed since the spectral shift exceeds the range bandwidth; finally, when α_r is greater than the blind angle, the radar works in the layover region. On the contrary, when α_r is negative, the sensitivity is lower and the spatial correlation is higher (the spectral shift reduces); for higher negative angle, the surface is not illuminated by the radar and the shadowing occurs. We are far away from such extreme cases in our analysis: the look angle is 45 deg and the surface slope is $\alpha_r \simeq \pm 7$ deg. The associated spatial (i.e. baseline) decorrelation in the worst case is $B_{\perp}/B_{\perp,cr} \simeq 0.07$ and hence it is still disregarded. However, there is a second point that we consider. When the coherence is evaluated, the interferometric phase is proportional to the difference between the slant-range travel paths from the antenna to the target. This difference depends on the horizontal and vertical relative target location. When the interferogram is flattened including the horizontal shift introduced by the viewing geometry, the remaining coherence phase depends only on the vertical location of the target, which is a desired effect in our context. This is clearly shown in Fig. 3.15, where flattened interferograms exhibit a variation only due to the forest layer. In the case of $\alpha \neq 0$, the relative horizontal location of the target is modified by the terrain slope, i.e. the local fringe frequency of the terrain increases or decreases with respect to the flat Earth case. It follows that the flattened interferogram, obtained removing only flat Earth fringes, still contains a residual fringe pattern induced by topography, superimposed to the fringes induced by the vertical extent of the canopy. This is shown in Fig. 3.23 where the interferograms are visibly affected by a contribution from the slope. The RVOG inversion aims at retrieving pixelwise this unknown contribution in the first stage of its process. However, if we wish to compare the averaged values of the observed and predicted coherences, this phase variation may corrupt the results. In other words, we are interested in the scattering phase location into the canopy, not in its absolute location. It follows that, for the forward analysis that compares the coherence values, the interferogram flattening is performed including the topography. After averaging those flattened interferograms in the central vegetated area, the residual magnitude and phase of the coherence

$$\hat{\gamma}_s(\alpha_r) = \frac{\hat{\gamma}(\alpha_r)}{\hat{\gamma}(0)} \quad (3.70)$$

have been plotted in Fig. 3.24. Conversely to the case of azimuth slope, μ varies only in the HH and VV channels, decreasing of about 8 dB for sloped terrain (cf. Fig. 3.22a). The cross-polar scattering ratio is almost constant, with a loss of about 1 dB in the tilted terrain case. As expected, the coherence varies mainly for the HH and VV channels: while the VV coherence level seems to benefit from the range slope, the HH coherence level exhibits slightly lower values with respect to the zero-sloped case; the

coherence phase, on the contrary, reveals that the HH and VV scattering phase centers rise further 5 m as consequence of the topography. The comparison with the RVOG predictions is generally in good agreement with the observations, though some errors can be observed in the HH coherence magnitude and phase. These errors superimpose to the ones discussed in the height analysis and lead to less accurate estimates of the ground topography and vegetation height in presence of topography. We have found, using Scots pine simulations, that a good estimation of forest height within 10% error is possible if the terrain slope is between $\pm 2\%$.

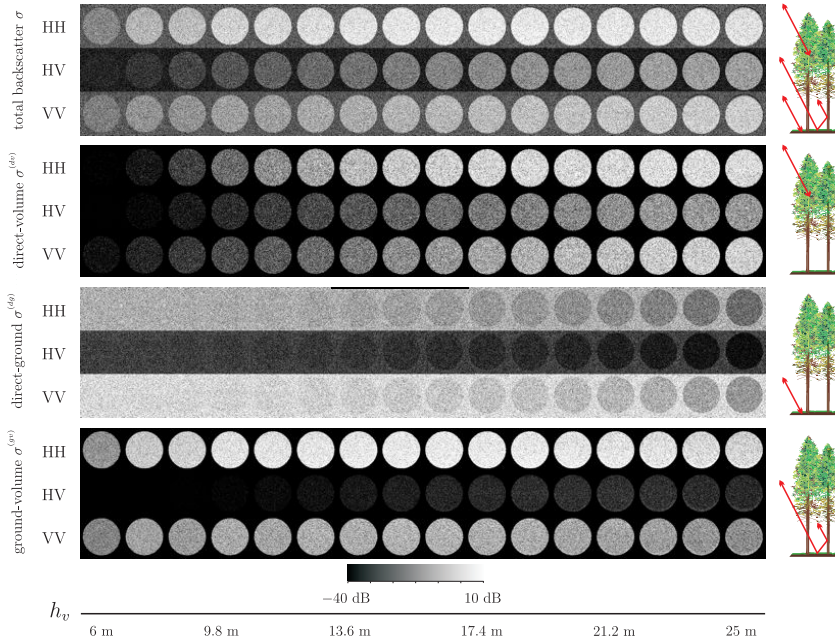


Figure 3.13: Total and selective backscatter of a Pine forest obtained through numerical simulations using PSPSIM. The near-range is the bottom of the images.

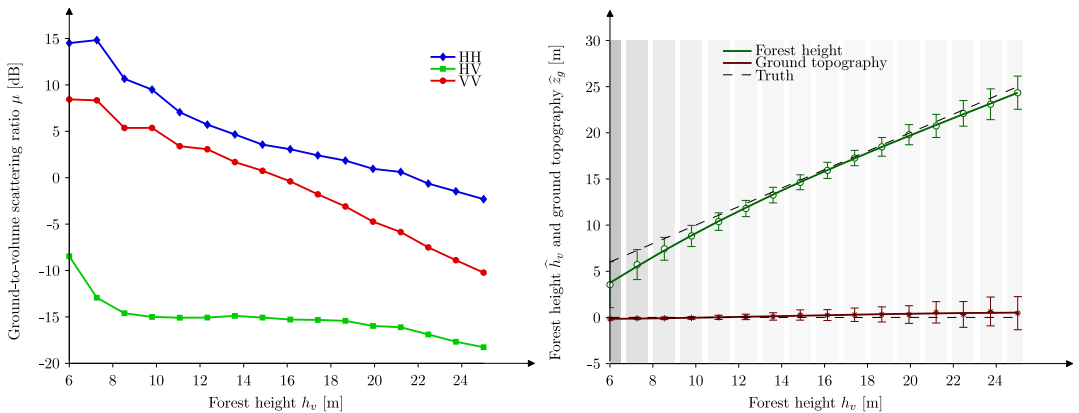


Figure 3.14: Ground-to-volume ratio of a Pine forest versus forest height obtained through numerical backscatter simulation (a). Performance of RVoG model inversion (b). The grey intensity in vertical bars is proportional to RMS error.

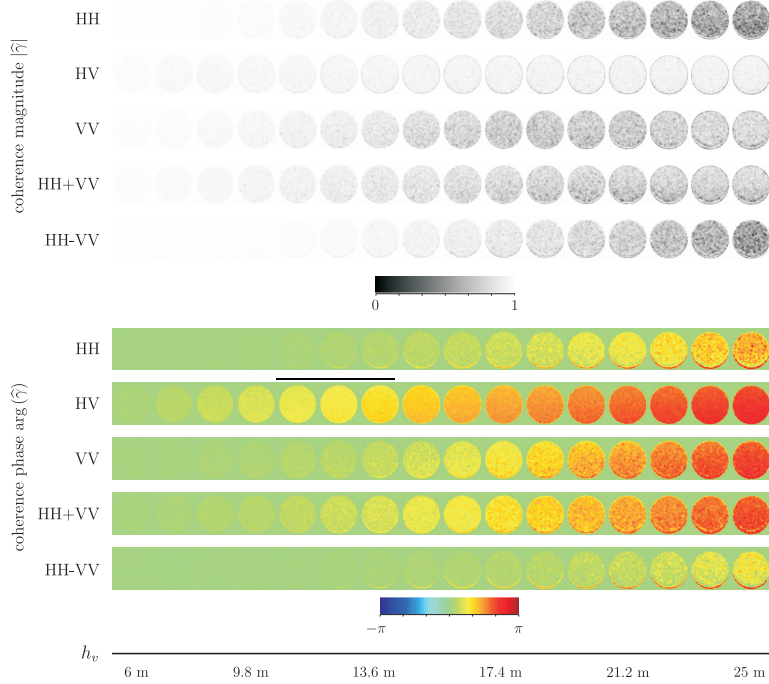


Figure 3.15: Coherence of a Pine forest obtained through POLINSAR processing of backscattering numerical simulations.

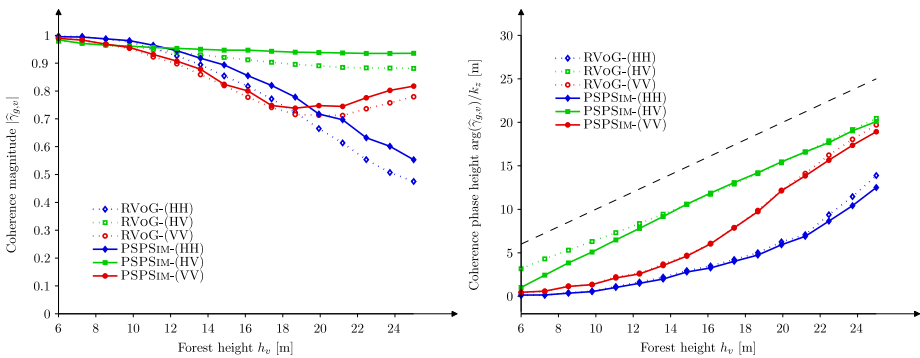


Figure 3.16: Coherence of a Pine forest obtained through POLINSAR processing of numerical simulations of complex backscatter (PSPSIM).

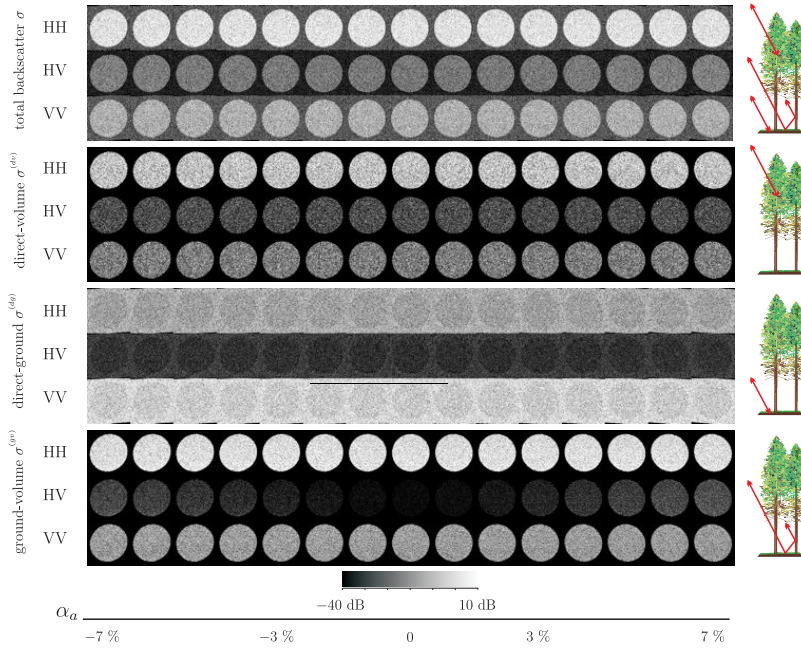


Figure 3.17: Total and selective backscatter of a Pine forest obtained through numerical simulations using PSPSIM. The near-range is the bottom of the images.

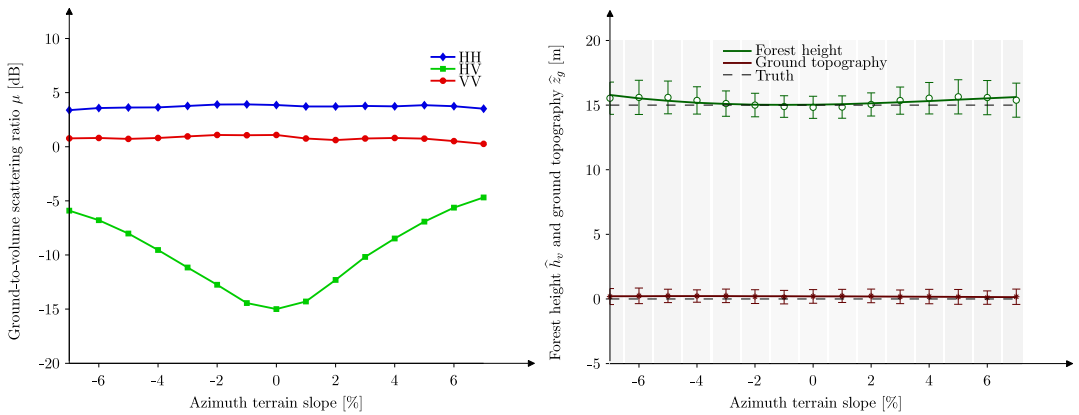


Figure 3.18: Ground-to-volume ratio of a Pine forest versus azimuth terrain slope obtained through numerical simulation (a). Performance of RVoG model inversion (b). The grey intensity in vertical bars is proportional to RMS error.

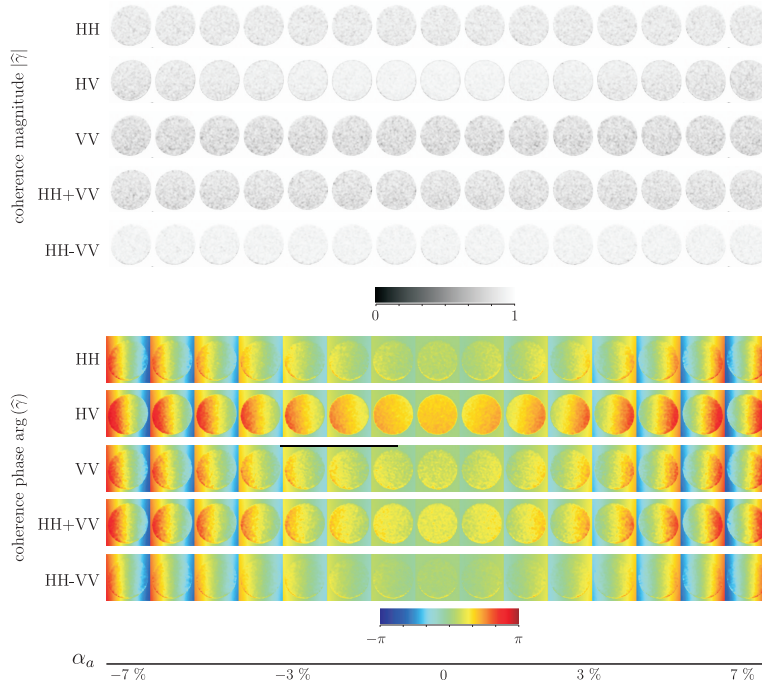


Figure 3.19: Total coherence of a Pine forest obtained through POLINSAR processing of backscattering numerical simulations. The near-range is the bottom of the images.

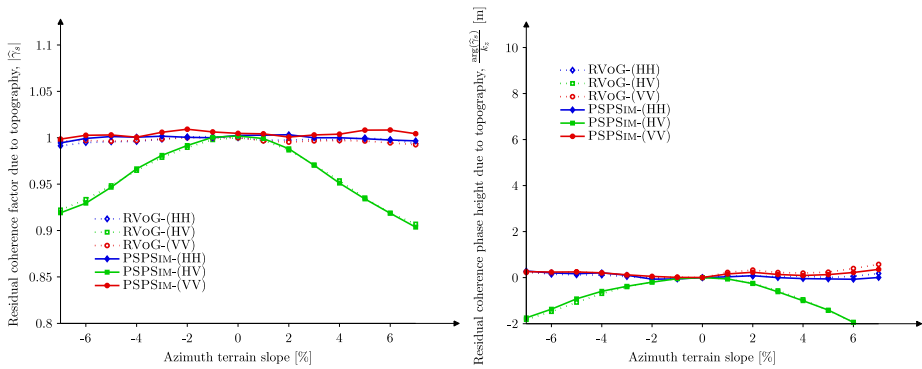


Figure 3.20: Residual coherence of a Pine forest obtained through POLINSAR processing of numerical simulations of complex backscatter (PSPSIM).

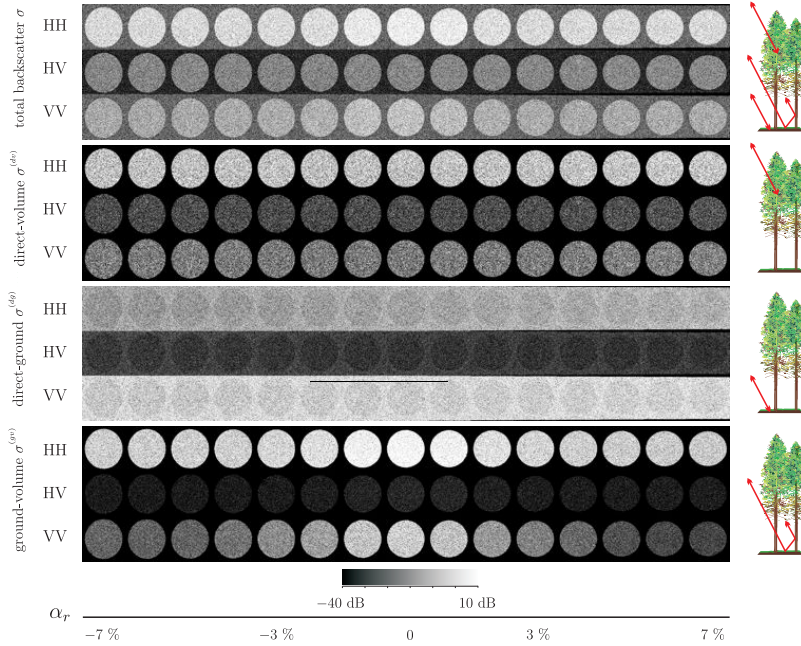


Figure 3.21: Total and selective backscatter of a Pine forest obtained through numerical simulations using PSPSIM. The near-range is the bottom of the images.

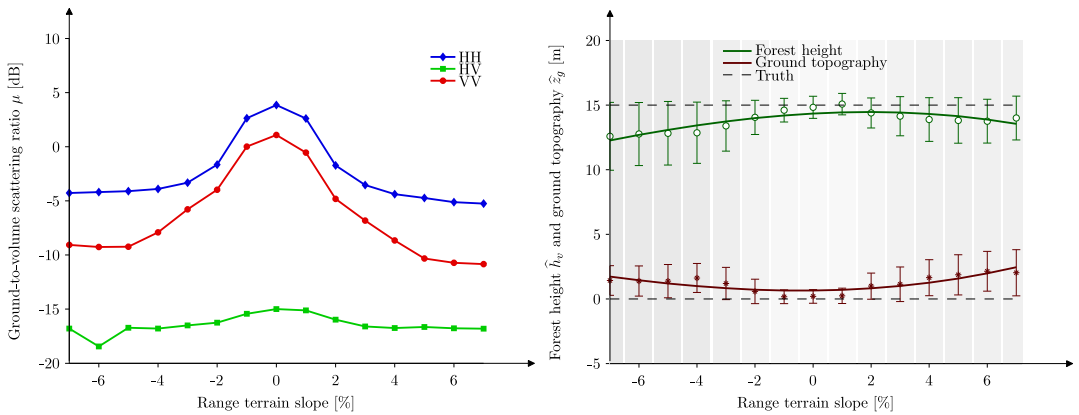


Figure 3.22: Ground-to-volume ratio of a Pine forest versus azimuth terrain slope obtained through numerical simulation (a). Performance of RVoG model inversion (b). The grey intensity in vertical bars is proportional to RMS error.

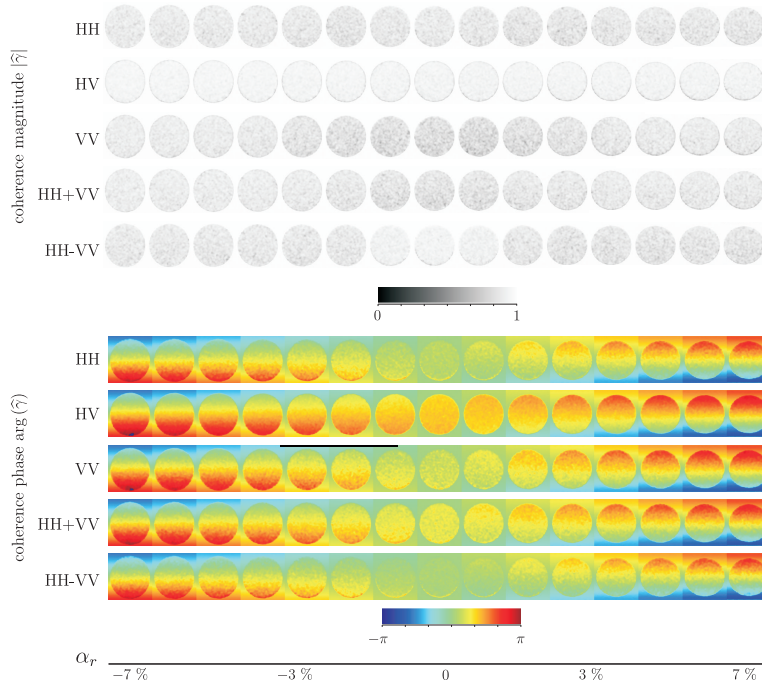


Figure 3.23: Total coherence of a Pine forest obtained through POLINSAR processing of backscattering numerical simulations. The near-range is the bottom of the images.

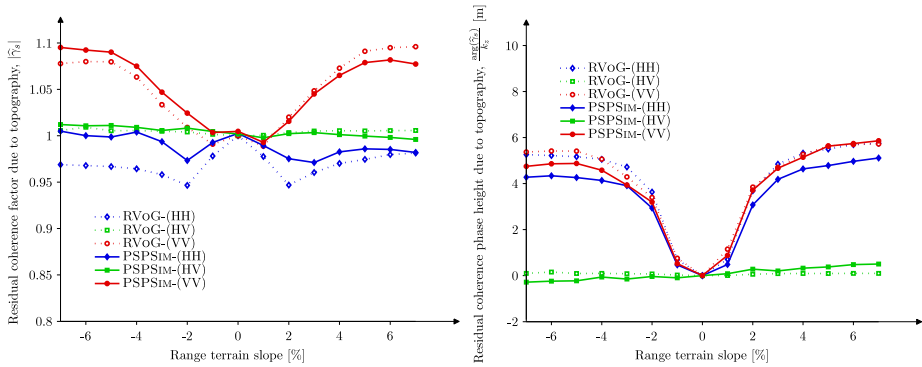


Figure 3.24: Residual coherence of a Pine forest obtained with POLINSAR processing of numerical simulations of complex backscatter (PSPSIM).

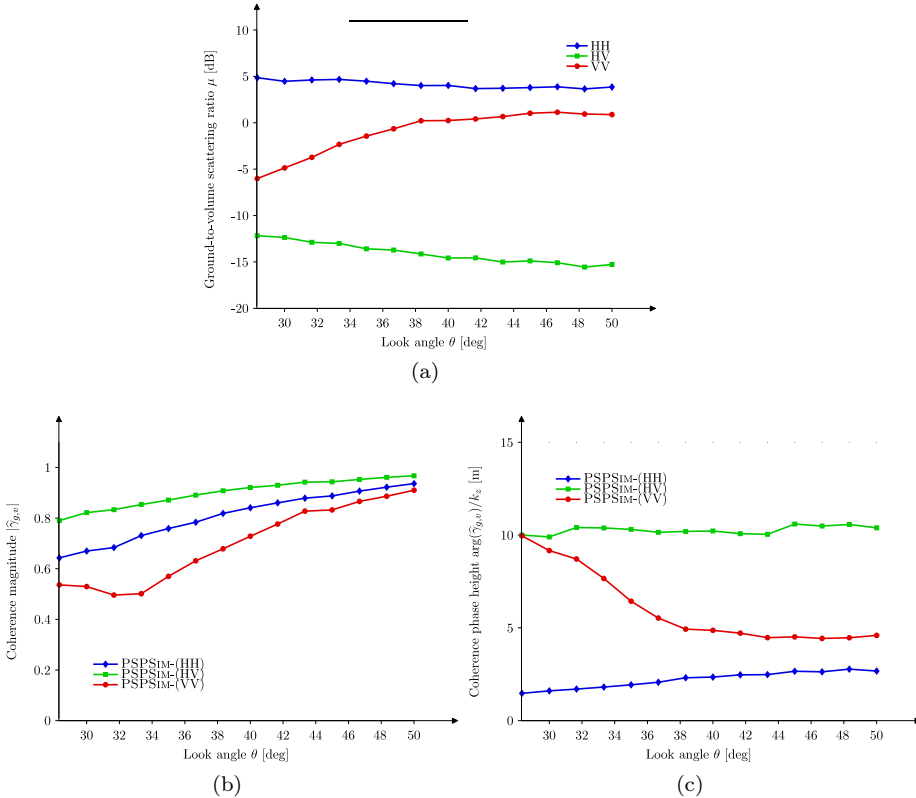


Figure 3.25: Example of parametric analysis using PSPSIM simulation to assess the impact of the look angle on the POLINSAR observable and ground-to-volume ratio.

3.3.2 POLINSAR descriptor extraction and sensitivity

In this section we cope with a complementary aspect of the numerical simulations. It is related with the extraction of the most significant POLINSAR descriptors, which has a practical utility for two reasons. From one side, identifying the descriptors that carry more information is of major importance for a correct parameterization of the model space and for designing inversion strategies. As a second outcome, studying the sensitivity of the parameters that we can control gives the possibility to optimize them for best results. An example of parametric analysis for correctly identifying the parameter space has been shown in the previous section. The slope analysis revealed that the range slope, if not properly compensated, could be a critical parameter in the inversion procedure.

Now we show an example of parametric analysis for POLINSAR system design. Among the parameters of an interferometer, the look angle is relatively easy to be set and does not depend too much on other parameters. Indeed, some SAR missions, such as RADARSAT-2 or COSMOSKY-MED, allow the users selecting the incidence angle for their acquisitions. Alternatively, space agencies fix the look angle to a proper value suitable for the applications. The polarimetric mode of ALOS-PALSAR, for instance, had initially a look angle equal to 21.5 deg and then it was changes to 23.5 deg. In any case, users or space agencies face the problem of choosing the best look angle. In the design of SAR interferometers for POLINSAR applications, a criterion may be the maximization of the μ spectrum or, in other words, the maximization of the distance between top- and bottom-phase centers. Obviously, other factors should be taken into account, such as the baseline decorrelation and the vertical resolution of the interferometer. Here, we focus on the position of the scattering phase centers into the canopy for different look angles. We have simulated the backscatter associated with the same forest as in the previous section, by setting $h_v = 15$ m and $B = 20$ m. Fifteen simulations have been generated by varying the look angle θ from about 25 deg to 50 deg. The same interferometric/polarimetric chain as before has been applied to the data: the results of the ground-to-volume ratio and complex coherence are shown in Fig. 3.25c. The main observation is that μ in the HV and HH channel does not depend much on the incident angle; the VV channel, on the contrary, increases of about 10 dB between the two extreme values. If we take the HH and HV channels as references of the ground- and volume-dominated channels respectively, we may conclude that the μ spectrum has almost no variation while the incident angle is augmented. This effect is evident in the plot of the coherence phase: for any value of the incident angle, the HV phase center remains located at 2/3 of the total height, and the HH phase center lies between 2 m and 3 m. The coherence magnitude, on the contrary, increases and approaches the unity as consequence of the lower baseline decorrelation. For the design of an interferometer, the look angle can be tuned in order to optimize the vertical resolution or the baseline decorrelation. This may be particularly useful for airborne or spaceborne future missions at L-band, such as TERRASAR-L, which aim at exploiting POLINSAR techniques over vegetation.

3.4 ALOS/PALSAR observations

The advanced land observing satellite (ALOS) launched by the Japanese Aerospace Exploration Agency (JAXA) carries a polarimetric L-band SAR (PALSAR) suitable for monitoring status and evolutions of forests (Rosenqvist et al., 2007). The mission started in January 2006, and early calibrated and validated data were available by September 2006, just at the beginning of this PhD thesis. The launch of

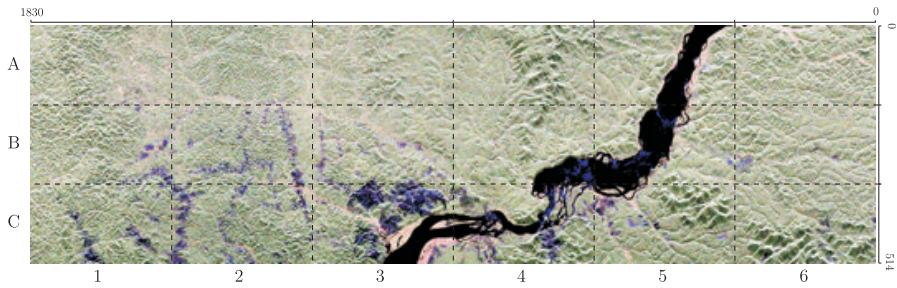
ALOS/PALSAR offered – for the first time – the opportunity to validate polarimetric SAR techniques using a space-based radar. This possibility motivated at that time the investigation on the potential of PALSAR for POLINSAR applications, although the difficulties associated with its large temporal baseline (46 days) were already anticipated.

Today, it is largely accepted that temporal decorrelation in PALSAR data is a critical factor for interferometric processing and forestry applications (Papathanassiou et al., 2008). Indeed, the major difficulty in our investigation has been to find a polarimetric and interferometric dataset acquired over a vegetated area with a relatively high interferometric coherence. In most of our experiments, we observed a mean coherence level around 0.2, which is a poor value for our purpose. Even after *magnitude* coherence optimization (SVD, cf. Sec. 3.2.2), this value did not exceed 0.3. Obtaining a spatial baseline suitable for forest height retrieval was a second constraint in the selection of POLINSAR data.

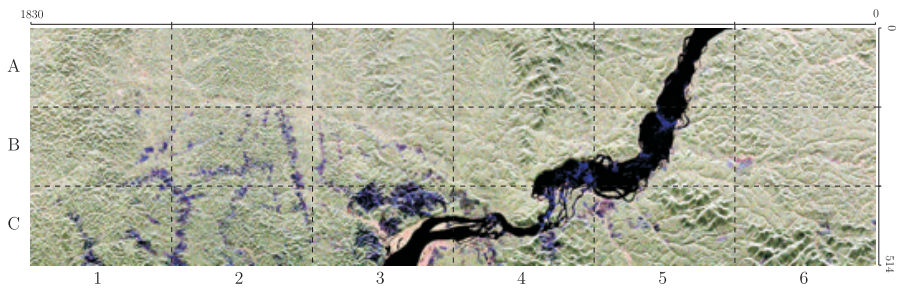
Fortunately, we have found a dataset with slightly better value of coherence and acceptable spatial baseline, as described in Sec. 3.4.1. This still does not allow demonstrating quantitatively the POLINSAR technique over ALOS/PALSAR data: even if the phase information may be considered reliable, the temporal correlation factor remains unknown. It follows that we cannot apply the inversion procedure proposed in Sec. 3.2.4 for retrieving forest height. However, we can successfully separate the ground and top-canopy phase centers, and hence derive an *uncompensated* forest height, sensitive to variations in the structure. This is sufficient for demonstrating that polarimetry does play a role in space-borne interferometric applications, as illustrated in Sec. 3.4.2.

3.4.1 Description of the dataset

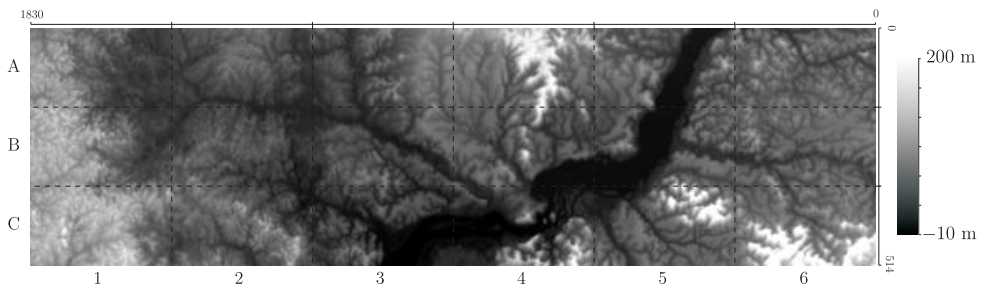
The PALSAR dataset that we found suitable for POLINSAR applications corresponds to two acquisitions over the Amazon Forest (Brazil) located at about 4.45 deg south of the equator and 56.33 deg at east of the central meridian. The data were acquired with two consecutive ascending passes on 13 March 2007 at 2:27:43 UTC and 28 April 2007 at 2:27:59 UTC respectively, with temporal baseline $T = 46$ days. As night acquisitions, a minimum of solar activity in the ionosphere is expected (Wright et al., 2003a) with benefits in terms of Faraday rotation (cf. Chapter 5). The viewing geometry corresponds to the standard polarimetric mode of ALOS/PALSAR: the nominal look angle is 21.5 deg in both acquisitions, which yields roughly 24 deg the local incident angle, the swath width (range) is about 30 km and the strip length (azimuth) is about 80 km. Fig. 3.26a and Fig. 3.26b shows the Pauli decomposition images associated with the acquisitions, obtained after a multi-look of 12 samples in azimuth and 2 samples in range. The resulting sample corresponds roughly to a square area



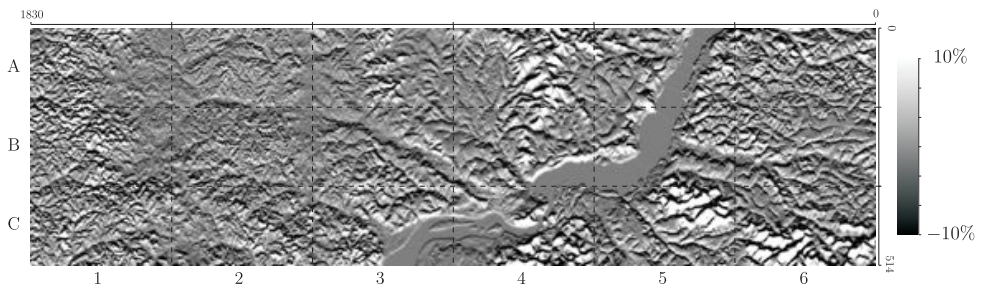
(a) Pauli decomposition of the first PALSAR acquisition



(b) Pauli decomposition of the second PALSAR acquisition



(c) SRTM digital elevation model of the area in slant range geometry



(d) Range terrain slope of the area in slant range geometry

Figure 3.26: PolINSAR ALOS/PALSAR acquisitions over Amazon forest (Brazil).

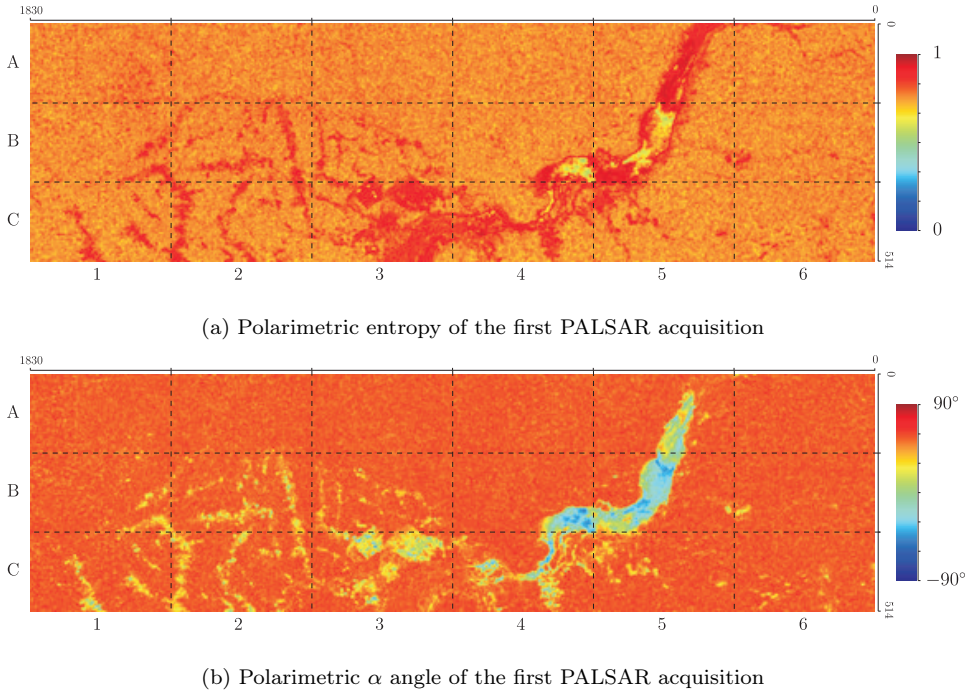


Figure 3.27: Polarimetric ALOS/PALSAR acquisition over Amazon forest (Brazil).

on the ground of $45 \times 45 \text{ m}^2$. Although there is little information available on the land cover of that area (which in turn justifies our investigation) the evidence from polarimetric qualitative analysis reveals that the scene is dominated by forests, i.e. volume-dominant scattering mechanisms. The polarimetric entropy and the alpha angle provided in Fig. 3.27 further confirm that the area is covered by vegetation.

From the interferometric point of view, the two acquisitions are separated by a normal spatial baseline $B_{\perp} = 130.2 \text{ m}$. Given the rather short baseline, the volume correlation is expected to be relatively high, at expense of the phase accuracy, which suffers from the increased ambiguity height¹⁶. The ambiguity height results about 252.5 m , which implies that, in order to observe a 20 m tall forest, the interferometric phase shift between ground and top-canopy will be about 30 deg . As an advantage, since the actual baseline is considerably smaller than the critical baseline $B_{\perp,cr} = 3300 \text{ m}$, the range spectral shift and filtering between the interferometric acquisitions can be disregarded

16. The ambiguity height is the vertical height of the target that corresponds to a complete 2π phase cycle. Conversely to the vertical wavenumber, when the ambiguity height is higher the interferometric phase wraps slower but the vertical resolution decreases.

(Gatelli et al., 1994; Hanssen, 2001). Finally, the ratio between the Doppler centroids difference (8.6 Hz) and the chirp length (1915.7 Hz) is also very small in this dataset and the azimuth spectral shift and filtering is in practice not necessary. These considerations are *also* justified by the topographic features of the area¹⁷. Fig. 3.26c shows the Shuttle Radar Topography Mission (SRTM) digital elevation model (DEM) projected on the slant range plane. To obtain that map the SRTM DEM has been resampled according to the SAR image resolution and further coded/interpolated on the natural SAR geometry (Pasquali et al., 2007). From the projected DEM, the range slope map is computed by differentiating along range and the result is shown in Fig. 3.26d. Notably, the terrain slope is relatively smooth, with variations comprised between $-10\% < \alpha_r < 10\%$. While these variations lead to some distortions in the POLINSAR coherence, the separation of the ground and top-canopy scattering centers is still possible and it is discussed in the next section.

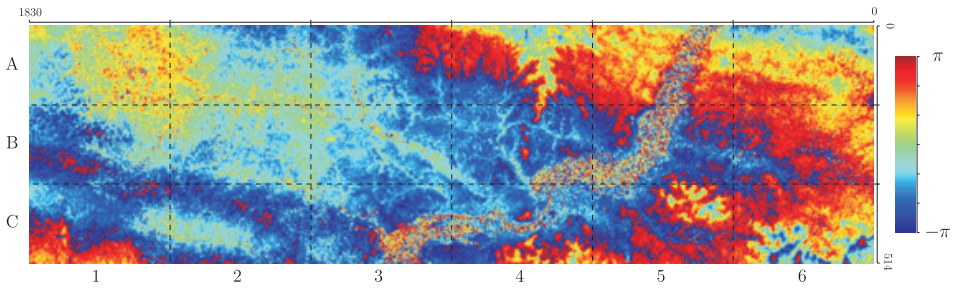
3.4.2 Results of the POLINSAR processing

The ESA verification PALSAR processor (Pasquali et al., 2007) has been used for focusing the PALSAR raw data identified by standard codes

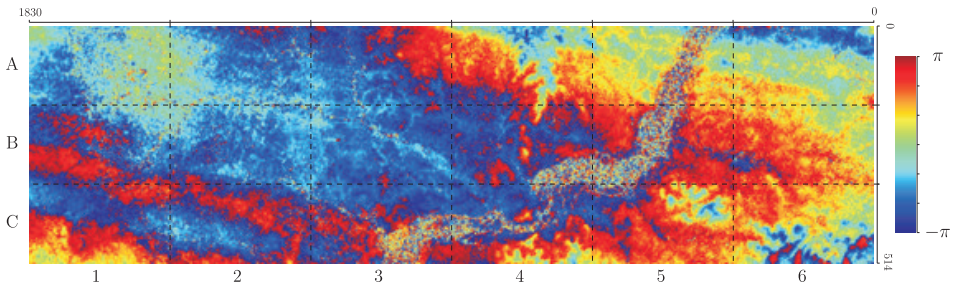
ALPSRP060247100-P1.0__A and ALPSRP066957100-P1.0__A.

The data have been radiometrically and polarimetrically calibrated according to the most recent calibration matrices provided by Shimada et al. (2007). The Faraday rotation angle estimated from the data is less than 1 deg and no Faraday rotation correction is required (cf. Chapter 5). The subsequent processing is a classical interferometric processing for each polarimetric channel separately. We follow the guidelines published by (ESA, 2007), although several freeware and commercial packages are available for this purpose. These steps are out of the scope of this thesis and will be omitted; instead, we focus on the POLINSAR exploitation of the data. After spatial co-registration and flattening of the products with the processing option discussed above, the matrix \mathbf{T}_6 is estimated through a multi-look factor 12×2 ; the complex degree of coherence is then estimated using a 5×5 boxcar filter, i.e. over about 500 independent looks, yielding 220 m the spatial resolution in the final interferogram. Some tests revealed that the coherence phase in the HV and HH-VV channels has similar phase location. This is not surprising since terrain slope and temporal decorrelation reduce the effective visible length of the model line in the complex plane (according to the RVOG model). Given the conditions of acquisition of the data, i.e. relatively small vertical wavenumber $k_z \simeq 0.025 \text{ m}^{-1}$ and large temporal baseline, we recognize the benefits of optimization algorithms for selecting the scattering mechanisms with greater phase

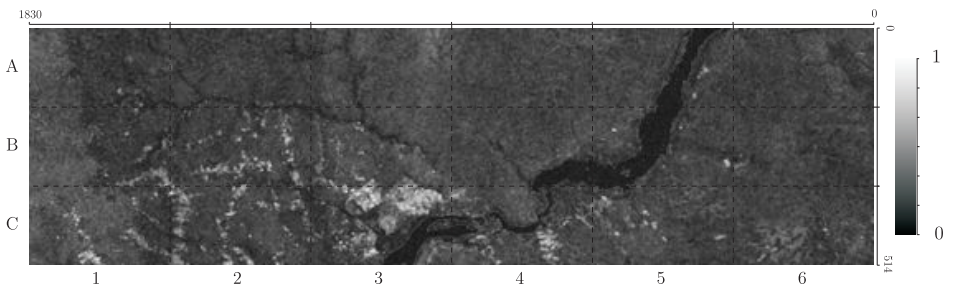
17. As mentioned in Sec. 3.3.1, topography induces a change of the local incidence angle and consequently of the spectral shift between the two acquisitions.



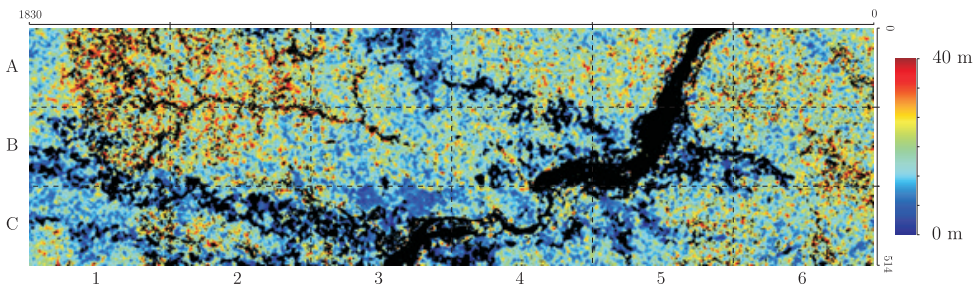
(a) High-phase optimized interferogram



(b) Low-phase optimized interferogram



(c) Maximum optimized coherence level



(d) Uncompensated forest height depending on vertical structure

Figure 3.28: Polarimetric ALOS/PALSAR acquisitions over Amazon forest (Brazil).

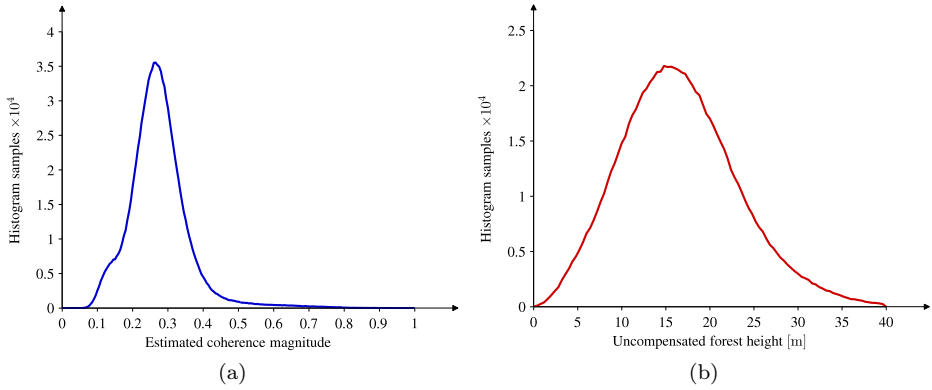


Figure 3.29: Histograms of the optimized coherence shown in Fig. 3.28c and of the uncompensated forest height shown in Fig. 3.28d

separation. The best compromise between computational and accuracy performances is provided by the phase diversity algorithm. The PD algorithm has been executed pixelwise and two coherence maps have been obtained, $\hat{\gamma}_{w_v}$ and $\hat{\gamma}_{w_g}$, corresponding to the scattering top-phase and bottom-phase centers respectively. The flattened optimized interferograms $\arg(\hat{\gamma}_{w_v})$ and $\arg(\hat{\gamma}_{w_g})$ are shown in Fig. 3.28a and Fig. 3.28b. The map of the maximum coherence level of the coherence region is shown in Fig. 3.28c and its histogram in Fig. 3.29a. At this point, the first observation is that both interferograms have the same fringe pattern (cf. tile A4 on the data, for instance), but a systematic phase shift can be observed in the whole scene. This means that fringes correspond to the underlying topography (Fig. 3.28b) and to the vegetation height and structure (Fig. 3.28a). This is certainly a demonstration that SAR interferometry from space benefits from polarimetric diversity for the estimation of the vegetation structure. In order to detect correctly the underlying topography, the line model parameters a and b must be evaluated, as described in Sec. 3.2.3. However, even if the optimized coherence values are taken to calculate the line, the phase separation is expected to be very small (i.e. the visible line length is small) and the noise would corrupt most likely every pixel during the retrieval. This is worsened by the low value of coherence level, which is visibly affected by temporal decorrelation. For this reason, we renounce to retrieve directly the underlying topography in order to have a better estimation of the height using the hybrid phase/magnitude approach discussed in Sec. 3.2.4. To this end, we substitute the factor of the ground topography removal $e^{-j\varphi_g}$ in (3.60) with the bottom-phase coherence $\hat{\gamma}_{w_g}$. Doing so, the problem of the phase topography estimation is overcome,

at the price of a reduced accuracy in the vegetation bias removal. Indeed, $\arg(\hat{\gamma}_{w_g})$ always lifts off the ground and is not located on the ground surface. Therefore, the height estimation strategy in the case of ALOS/PALSAR would be

$$\hat{h}_v = \underbrace{\frac{\arg(\hat{\gamma}_{w_v} \hat{\gamma}_{w_g}^*)}{k_z}}_{\text{uncompensated } h_v} + \underbrace{\nu \frac{2[\pi - 2 \sin^{-1}(|\hat{\gamma}_{w_v}|^{0.8})]}{k_z}}_{\text{not usable due to TD}} \quad (3.71)$$

wherein we have highlighted a second important observation of using ALOS/PALSAR data for height inversion. The first term is a sort of uncompensated forest height that needs to be corrected by the second term proportional to vertical structure. The problem with PALSAR acquisitions is that the second term is completely based on the coherence magnitude, which is strongly affected by temporal correlation. If this temporal correlation is not compensated, then the algorithm would overestimate the height. As temporal decorrelation is unknown and difficult to predict with PALSAR, we must content ourselves with only the uncompensated forest height. Does it contain reliable and reasonable information for the area under study?

To correctly retrieve a measure of the uncompensated height, the areas with low coherence must be masked out from the analysis. In order to derive a threshold for the coherence level, we note that we are interested in retrieving at least a phase difference corresponding to $h_v = 10$ m. In this condition, the phase difference will result $\arg(\hat{\gamma}_{w_v} \hat{\gamma}_{w_g}^*) = k_z h_v \simeq 0.25$ rad. To avoid errors in the retrieval, this phase difference must be greater than the Cramer-Rao bound on the coherence standard deviation

$$\frac{1}{\sqrt{2N_l}} \frac{\sqrt{1-|\gamma|^2}}{|\gamma|} < 0.25 \text{ rad} \quad (3.72)$$

wherein $N_l \simeq 500$ is the number of independent looks. By inverting (3.72) with respect to the coherence magnitude, we found that $|\gamma| > 0.2$ is an acceptable threshold for the validity of the results. The uncompensated forest height map is shown in Fig. 3.28d and its histogram in Fig. 3.29b. We believe that results like those shown in the figures are generally achievable by ALOS/PALSAR over vegetated areas. Two further observations confirm the reliability of the retrieved uncompensated height. First, the phase difference scaled by the vertical wavenumber gives reasonable values between 0 m and 30 m, with 15 m as average value. Despite no ground truth is available in the area, these values are reasonable. Obviously, we have to keep in mind that the effects of the volume penetration and the range slope move the scattering phase centers with respect to the true value; also, using the optimized bottom-phase in (3.71) overlocates the ground reference and further underestimates the height. Temporal decorrelation also

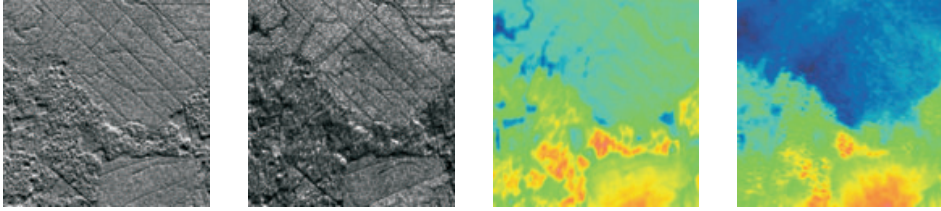
contributes to this phase shift as discussed in Sec. 3.1.3. Secondly, there is a correlation between the scattering phase center height of Fig. 3.28d and the maximum coherence level of Fig. 3.28c. The comparison of the two figures reveals qualitatively that the areas with lower phase height have higher coherence (cf. C3, A3 or B1 for instance). This is in agreement with the height inversion strategy that exploits the phase difference compensated by a magnitude term.

In conclusion, we can confirm that temporal decorrelation is a major limitation for POLINSAR-RVOG inversion over ALOS/PALSAR data. We have clearly shown where this limitation prevents the inversion. It follows that, if somehow we have further information about the structure of vegetation, the forest height retrieval can be still achieved by ALOS/PALSAR, still using POLINSAR, but renouncing at the RVOG inversion strategy as it is today.

3.5 P-band modeling

In previous sections, we have discussed the advantages of using multi-polarization and multi-pass SAR data for vegetation remote sensing. In this section, we broaden the discussion to the *frequency diversity*, i.e. the capability of a radar to operate at different carrier frequencies. If the SAR operates at N_f different frequencies, then the number of observations for a full polarimetric and interferometric system becomes $N_m = 4 N_f (N_b + 1)$, where N_b is the number of the interferometric baselines. The added value of using multi-frequency measurements is that scattering of electromagnetic waves from vegetation is strongly dependent on frequency, and hence the observation space is extended conveniently to support the retrieval of geophysical quantities (Evans, 1995). This is achieved, however, at expense of a major system complexity and higher costs. The objective of this section is to present a model that takes advantage of X- and P-band acquisitions to provide a reliable estimate of forest height. In particular, we propose a method to correct the height bias of the P-band scattering phase center with respect to the ground topography. Somehow, our approach trades dual-frequency with full-polarimetry, as we use only partial polarimetric acquisitions. Although no spaceborne SAR mission is currently planned with such partial-polarization and dual-frequency capabilities, there are some airborne sensors, such as GEOSAR¹⁸, with those characteristics. Therefore, this study is motivated by the opportunities that may arise from the use of these airborne data (cf. note 18).

18. The GeoSAR dual-frequency, interferometric SAR was developed for wide-area, airborne mapping applications by the NASA Jet Propulsion Laboratory (Wheeler and Hensley, 2000) and is now operated commercially on a Gulfstream II jet aircraft. GeoSAR collects X-band (VV, 9.7 GHz) and P-band (HH, 0.35 GHz) interferometric data in single-passes, from which digital elevation models are derived.



(a) X-band backscatter (b) P-band backscatter (c) X-band DSM (d) P-band DTM

Figure 3.30: Examples of X- and P-band GEOSAR acquisitions of an area containing tropical forest and cultivation. Color scales differ between bands.

3.5.1 Introduction

Scattering of electromagnetic waves from vegetation is strongly dependent on frequency (Ulaby et al., 1986b). At X-band, scattering is predominantly *first-surface* and, in general, the X-band VV interferometric phase center is anticipated to be close to the top of vegetation canopies. At lower frequencies, such as P-band, HH returns are, in general, more strongly influenced by ground-volume interactions, and the P-band HH phase center is expected to lie closer to the ground. Thus the difference between the X-band VV digital surface map (DSM) height z_{vv_X} and the P-band HH digital terrain map (DTM) height z_{hh_P} is related to vegetation height

$$h'_v = z_v - z'_g = z_{vv_X} - z'_{hh_P} = \frac{\varphi_{vv_X}}{k_{z_X}} - \frac{\varphi'_{hh_P}}{k_{z_P}} \quad (3.73)$$

wherein φ'_{vv_X} and φ'_{hh_P} are the interferometric X-band VV and P-band HH phase centers, respectively. The *surrogate* vegetation height h'_v in (3.73) has been used in the retrieval of biomass for areas of tropical forest (Neeff et al., 2003). However, both evidence and theory suggest that volume scattering effects will lift the P-band HH phase center above the ground, even though the ground-volume scattering is strong. An example of a raised P-band HH phase center under forest is given in Fig. 3.30b, along with the X-band VV in Fig. 3.30a. The figures show a forested area next to a cultivated area distinguished most clearly in the P-band magnitude data. The edge of the cultivated area is evident in both the X-band DSM (Fig. 3.30c) and the P-band DTM (Fig. 3.30d). Although no ground data were available for this area, the evidence appears to suggest a slight rise in P-band DTM height below the neighboring forest canopy of a few meters. The forest canopy is between 20 m and 25 m tall, which can be deduced from the height difference between X-band and P-band. In order to better exploit the surrogate vegetation height measurement available from such observations

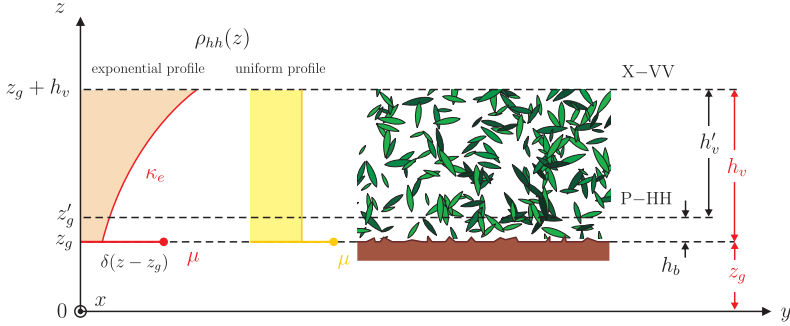


Figure 3.31: Scenario of the P-band scattering model.

we have developed a simple expression based on the coherence modeling exposed in Sec. 3.1.2. The following sections present our development.

3.5.2 P-band dual-polarimetric interferometric model

The key idea to retrieve the forest height is based on (3.73) but uses a *corrected* P-band interferometric scattering phase center to retrieve a better ground topography estimate $z_g = z_{hh_P}$ (Lavalle et al., 2009)

$$h_v = z_{vv_X} - z_{hh_P} = h'_v + h_b \quad (3.74)$$

wherein h_b is the height bias corresponding to the P-HH phase center height (Fig. 3.31). How to estimate h_b at P-band and correct the height in (3.73) is the objective of our theoretical modeling. The core of this modeling lies on the use of the P-band HV backscattering coefficient combined with a calibration parameter estimated from the data to retrieve the ground-to-volume scattering ratio as it is shown hereafter. Since the following equations apply exclusively to P-band measurements and no other frequencies are involved, the band-specific notation will be omitted.

We begin by considering the basic model formulation (3.8) that predicts the P-band HH coherence from the P-band vertical structure function per unit length $\rho_{hh}(z)$ (Fig. 3.31)

$$\gamma_{hh} = \frac{\int_{z_g}^{z_g+h_v} \rho_{hh}(z) e^{jk_z z} dz}{\int_{z_g}^{z_g+h_v} \rho_{hh}(z) dz}. \quad (3.75)$$

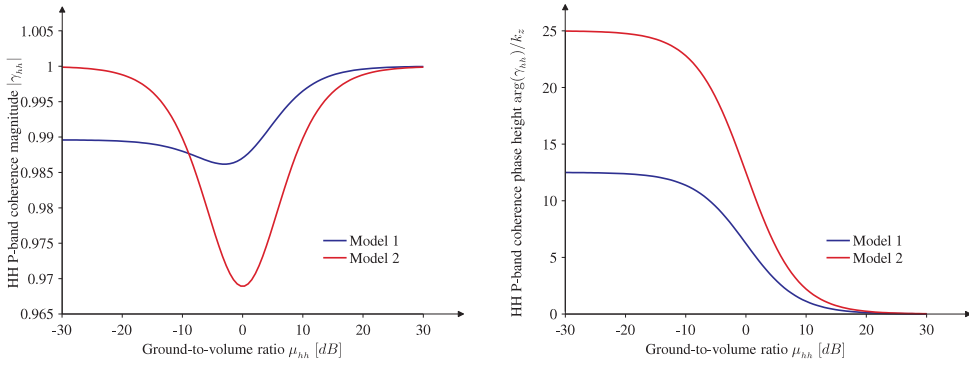


Figure 3.32: Coherence magnitude and phase of the two models (3.77). Model 1 is the uniform profile, Model 2 is the exponential profile.

Conversely to the model at L-band seen in Sec. 3.1.2, $\rho_{hh}(z)$ at P-band is expected to be more dense at ground or, in other words, to have a lower extinction coefficient if an exponential attenuation profile is assumed. This total $\rho_{hh}(z)$ function can be broken into two main components as shown in (3.16), corresponding to the direct-volume and to the ground interactions respectively. At P-band we may make two alternative assumptions about the variation of the scattering along the canopy. These lead to two different expressions of the vertical profile, valid for $z_g < z < z_g + h_v$,

$$\text{exponential profile : } \rho_{hh}(z) = \left(\rho_{hh}^{(dg)} + \rho_{hh}^{(gv)} \right) e^{-\frac{2\kappa_e}{\cos\theta} h_v} \delta(z - z_g) + \rho_{hh}^{(dv)} e^{\frac{2\kappa_e}{\cos\theta} (z - z_g - h_v)} \quad (3.76a)$$

$$\text{uniform profile : } \rho_{hh}(z) = \left(\rho_{hh}^{(dg)} + \rho_{hh}^{(gv)} \right) \delta(z - z_g) + \rho_{hh}^{(dv)} \quad (3.76b)$$

Expression (3.76a) is the same used for modeling the profile at L-band. Expression (3.76b) states that the attenuated direct-volume backscatter at top-canopy is similar to the one at bottom-canopy. This is physically reasonable if we assume that the scatterers at the top-canopy, although they are illuminated by greater wave energy, are less dense than the scatterers at the bottom of the canopy that experience a weaker wave energy. The product of the terms in (3.9) can be therefore considered constant. Inserting (3.76a) or (3.76b) into (3.75), the predicted degree of coherence of the P-band HH observations

becomes

$$\text{exponential profile : } \gamma_{hh} \simeq e^{jk_z z_g} \frac{\mu_{hh} + e^{jk_z h_v}}{\mu_{hh} + 1} \quad (3.77a)$$

$$\text{uniform profile : } \gamma_{hh} = e^{jk_z z_g} \frac{\mu_{hh} + e^{jk_z \frac{h_v}{2}} \text{Sinc}\left(k_z \frac{h_v}{2}\right)}{\mu_{hh} + 1} \quad (3.77b)$$

where μ_{hh} is the HH ground-to-volume scattering ratio defined in (3.18). For the exponential profile, we have used two approximations valid at lower frequencies, $k_z h_v \ll 1$ and $\kappa_e h_v \ll 1$, that allows simplifying the coherence expression

$$\frac{e^{2k_z h_v} - 1}{2k_z} \simeq h_v, \quad \frac{e^{(2k_z + j\kappa_e)h_v} - 1}{2k_z + j\kappa_e} \simeq h_v e^{j\kappa_e h_v}. \quad (3.78)$$

While (3.73) exploits the dual-frequency capabilities, the partial polarimetric acquisitions have not been used so far. In order to support the estimation of the ground-to-volume ratio, we make use of the proportion between the HH and HV direct-volume P-band backscatter, reported by Ulaby et al. (1986a)

$$\sigma_{hh}^{(dv)} \propto \sigma_{hv}^{(dv)}. \quad (3.79)$$

In the case of a cloud of uniform randomly oriented scatterers the proportional factor has been calculated theoretically being equal to 3; in practice, it is species-dependent. In our observations with numerical simulations of a realistic pine forest, the proportional factor has been found dependent linearly on tree height. This means that as pines become taller, the HH direct-volume contribution grows faster than the HV direct-volume contribution. We found this fact reasonable given the pine structure, since the cross-polarization backscatter arises mainly by the bending at the end of the branches, while the HH backscatter is mainly sensitive to the horizontal branches. These latter grow much faster with tree height than their bending and this explains the linear dependence of the proportional factor. Following these considerations, the proportion (3.79) becomes

$$\sigma_{hh}^{(dv)} = \alpha_c h_v \sigma_{hv}^{(dv)} \simeq \alpha_c h_v \sigma_{hv} \quad (3.80)$$

wherein α_c is the proportional factor or *calibration parameter*, and $\sigma_{hv}^{(dv)} \simeq \sigma_{hv}$ has been further assumed since it is generally valid at P-band. The value of α_c needs to be estimated for each species, hence (3.80) should be valid for species other than pine. From (3.80), the ground-to-volume ratio can be estimated using the ratio between the

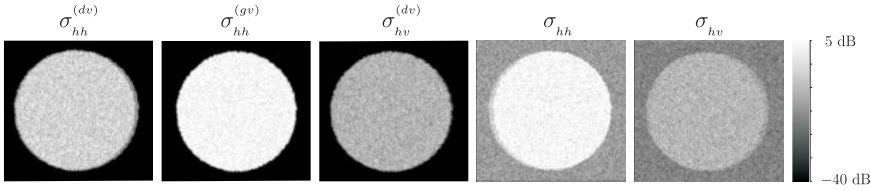


Figure 3.33: Examples of PPSIM outputs at P-band. Vegetation height is 20 m.

co- and cross-polarized backscatter coefficients

$$\mu_{hh} = \frac{\sigma_{hh}^{(gv)}}{\sigma_{hh}^{(dv)}} \simeq \frac{\sigma_{hh} - \sigma_{hh}^{(dv)}}{\sigma_{hh}^{(dv)}} \simeq \frac{1}{\alpha_c h_v} \frac{\sigma_{hh}}{\sigma_{hv}} - 1 \quad (3.81)$$

where we used (3.80) and the approximation $\sigma_{hh} \simeq \sigma_{hh}^{(gv)} + \sigma_{hh}^{(dv)}$, i.e. the direct-ground contribution is negligible. If the ground-to-volume ratio can be estimated from the data, then the height bias of the HH P-band phase center with respect to the ground can be calculated from $\arg(\gamma_{hh})/k_z$ inverting (3.77)

$$\text{exponential profile : } h_b = \frac{1}{k_z} \tan^{-1} \left[\frac{\sin(\varphi_{h/2})}{\mu_{hh} + \cos(\varphi_{h/2})} \right] \quad (3.82a)$$

$$\text{uniform profile : } h_b = \frac{1}{k_z} \tan^{-1} \left[\frac{\text{Sinc}(\varphi_{h/2}) \sin(\varphi_{h/2})}{\mu_{hh} + \text{Sinc}(\varphi_{h/2}) \cos(\varphi_{h/2})} \right] \quad (3.82b)$$

where $\varphi_{h/2} = k_z \frac{h_v}{2}$ is the interferometric phase at half height. The two expressions above predict a height bias between 2 m and 5 m for a 25 m tall canopy and $\mu_{hh} = 16$ dB. A set of PPSIM simulations has been generated at P-band to test the approximations in (3.80), to assess the value of α_c , and to validate expressions (3.82). The set of simulations has been obtained by increasing the forest height from 5 m up to 30 m. A typical GEOSAR acquisition geometry has been assumed with a sensor altitude of 10000 m, a 45 deg incident angle and a 20 m horizontal baseline, which leads to the vertical wavenumber $k_z \simeq 0.02 \text{ m}^{-1}$ and to the ambiguity height $h_a \simeq 31.4$ m. We are interested in simulating the total return, the direct-vegetation and ground-vegetation return of both HH and HV channels. Fig. 3.33 shows the individual scattering mechanisms used for the analysis, i.e. the direct-volume P-HV, direct-volume P-HH, total P-HV, total P-HH and ground-volume P-HH. The factor α_c is estimated from the

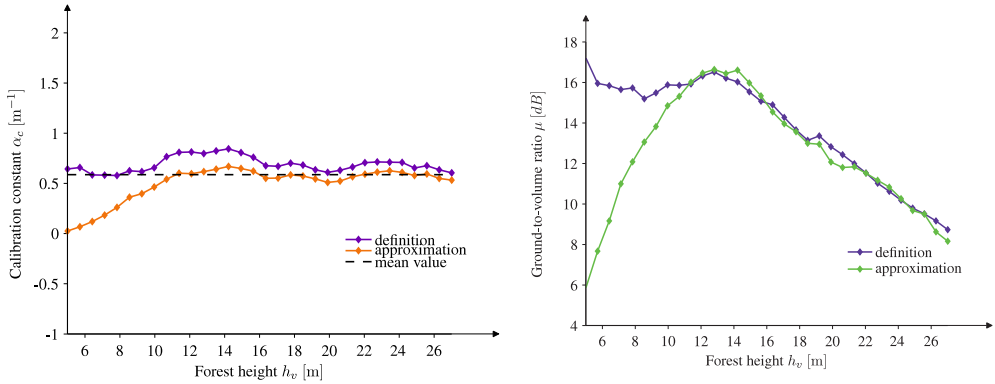


Figure 3.34: Test of the approximations using PSPSIM simulations.

central part of the images, using both the definition and the approximated expression

$$\alpha_c = \frac{\sigma_{hh}^{(dv)}}{h_v \sigma_{hv}^{(dv)}} \simeq \frac{\sigma_{hh}^{(dv)}}{h'_v \sigma_{hv}} \quad (3.83)$$

where h_v is the outset simulated height and h'_v is the difference between h_v and the P–HH phase center height. This difference corresponds to the surrogate height (3.73), i.e. represents the difference between the VV X–band and the HH P–band phase center height¹⁹. Fig. 3.34 shows the comparison between the two α_c estimates and confirms that the two curves are very close, especially for trees taller than 10 m. The average value of α_c valid for pine trees is about 0.45. The second parameter that we have tested is the ground-to-volume scattering ratio (3.81). Again, this ratio can be estimated from the individual simulated scattering mechanisms through its definition, or using α_c through its approximation. In Fig. 3.34 we report the trend of μ_{hh} for the two alternative estimates. The curves prove that our approximated expression holds for forested areas ($h_v > 8$ m).

This analysis ensures that the models (3.82) can be applied to correct the P–HH interferometric phase center height and to obtain a better estimate of forest height. For this purpose, the following procedure is proposed.

1. Estimate the uncorrected canopy depth h'_v using the difference between the X–VV

¹⁹. Despite the surrogate height h'_v is not used to estimate the vegetation canopy height, it *might* be used to estimate the calibration parameters α_c over selected test sites for which the true tree height is known. In this particular case, (3.81) must be used with h'_v in place of h_v . This justifies the test of the approximation (3.83).

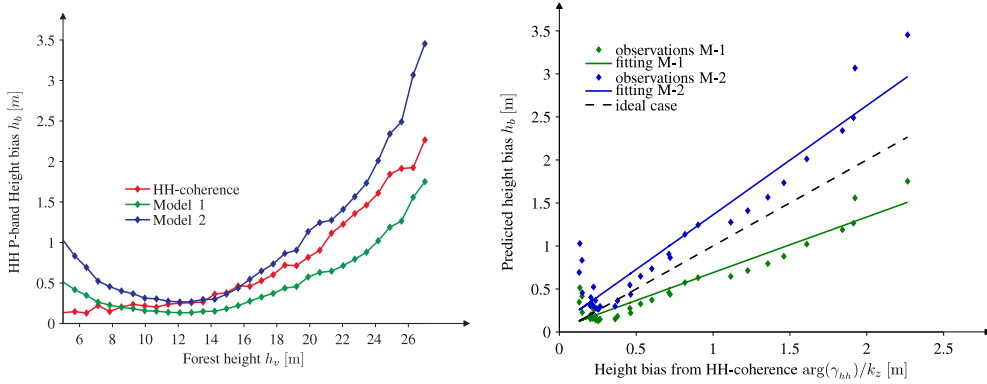


Figure 3.35: Test of the inversion procedure using PSPSIM simulations. Model 1 is the uniform profile, Model 2 is the exponential profile.

and the P–HH scattering phase center as in (3.73).

2. Estimate the calibration parameter α_c from numerical simulations as done in this section (if the tree species is available) or, alternatively, from real calibration test sites (cf. note 19).
3. Estimate the ground-to-volume ratio μ_{hh} from P–HH and P–HV measurements using α_c and the uncorrected canopy height h'_v , as in (3.81).
4. Estimate the unwrapped ground phase and the associated height bias h_b using μ_{hh} and h'_v from the model equations (3.82a) or (3.82b).
5. Correct the height estimate h'_v with the height bias h_b as in (3.74) and iterate the procedure if necessary.

This procedure has been tested using PSPSIM simulated data. Fig. 3.35 shows that both models perform well in the estimation of the height bias h_b . In the case of uniform vertical profile, the height bias is underestimated. On the contrary, using the exponential model, the bias is slightly overestimated. This suggests that, for pine trees, the extinction at P–band along the vertical dimension is between the uniform profile and the exponential profile.

One advantage of introducing α_c is that it does not depend on the terrain slope. This is intuitively true for the P–HV return, which already depends weakly on the range slope, as seen also at L–band. A further investigation on the effect of the slope has led to the conclusion that $\sigma_{hh}^{(dv)}$ and σ_{hv} have a very similar trend. This entails that the value of α_c is very stable against variation of terrain slope and μ can be estimated using the same expression valid for zero-slope. However, it must be noted that this is not the case

of the interferometric phase center P-HH. Therefore, if α_c is estimated by the surrogate height on sloped terrain (cf. note 19), then its value will be affected by slope-induced variations of the scattering phase center that we have discussed in Sec. 3.3.

3.6 Conclusions

In this chapter, we have discussed some aspects of the polarimetric and interferometric technique for forest remote sensing. In particular, we have tried to progress with respect to the current status of the technique. To this end, five novel elements can be recognized, each of them corresponding to a separate section in the chapter.

The first element is the temporal decorrelation modeled by a vertical function. We have shown that it may affect the location of the scattering phase center by several meters and depends, in general, on the polarization through the ground-to-volume scattering ratio μ . It follows that modeling correctly this phase shift would bring benefits to the height estimation procedure. The temporal correlation function is identified by at least one real parameter (the time constant τ_v in the volume) that can be estimated through a similar approach used today to estimate the constant temporal decorrelation. The standard deviation of the scatterers in the canopy has been modeled with a linear trend along the vertical structure. This constraint can be relaxed by expanding the temporal correlation function in a series of functions, using the same idea underlying the PCT. In order to demonstrate the effectiveness of our temporal correlation model, multi-temporal airborne data can be conveniently used. As soon as the data of the ESA/DLR campaign BIOSAR-2 is available, the height inversion procedure that includes the temporal correlation function can be tested and compared with the previous strategy.

The second element concerns the spatial correlation model and its inversion procedure. We have pointed out the importance to include the effects of the range terrain slope distortions. The distortions originate mainly from asymmetries in the crown of trees and in the ground-trunk geometry, hence from the modification of the ground-tree structure. We have found, using PPSIM numerical simulations, that a range slope greater than $\pm 2\%$ can severely affect the performance of the height retrieval for a 15 m tall forest. In order to retrieve information only related to the vegetation, the slope contribution must be properly taken into account in the modelisation and removed during the inversion procedure. To this end, a possible solution is to design a structure function of the form $\rho(z, \alpha_r)$, wherein α_r is the slope in range. This approach goes to the direction of improving the RVOG model by including the slope effects. Note that both the considerations on the spatial and temporal correlation are applicable to tomographic techniques, such as PCT, that uses the basic two-layer model of coherence also adopted in this thesis.

The third point presented in this chapter is the relationship, valid at P-band, that allows to estimate the HH ground-to-volume ratio from the data and hence to simplify the expression of the HH coherence. This relationship is based on the ratio between the co- and cross-polarized channels, and on a calibration parameter α_c that needs to be estimated a priori. One benefit of this approach is that the relationship is independent on the terrain slope and allows correcting reliably the HH phase center height that lifts above the ground. When combined with the reference of the top-canopy, e.g. X-band acquisitions, the height can be retrieved more accurately.

Fourth, as a valuable tool for the POLINSAR community, we have demonstrated the utility of PSPSIM for parametric analysis, and in particular as a tool to study the sensitivity of forest parameters and to design optimal system configurations. As an outcome, we have found that the azimuth terrain slope does not introduce critical distortions conversely to the range slope. Further, the look angle of an interferometer affects the visible scattering mechanisms only on some polarizations, and does not change significantly the μ spectrum. We believe that future POLINSAR SAR missions, such as TERRASAR-L, will benefit from these results.

Finally, we have discussed the potentialities and the limitations of ALOS/PALSAR for POLINSAR forestry applications. We have illustrated through a case study that it is possible to separate ground and top-canopy scattering mechanisms and to obtain an uncompensated value of forest height that depends on the forest structure. This value cannot be compensated using only PALSAR acquisitions as a consequence of the severe temporal decorrelation. Therefore, external information should be used to fully exploit the limited POLINSAR capabilities of PALSAR.

Compact Polarimetric SAR Interferometry

Things should be made as simple as possible, but not any simpler.

Albert Einstein (1879-1955)

In recent years, there have been emerging new SAR modes based on the transmission of polarization states other than the canonical H and V polarizations. There is currently much discussion about the utility of such alternative modes, and also about the trade-off between dual and full polarimetry. The discussion is active at both levels of applications and system design.

This chapter contributes to that discussion by addressing the interferometric potential of the so-called *compact polarimetric* modes. The objective is to present an algorithm for comparing the partial POLINSAR information carried by compact polarimetry with the full polarimetric and interferometric information addressed in Chapter 3.

In the following, we first review the basics of the emerging compact polarimeters (Sec. 4.1); then we introduce the compact interferometric formulation (Sec. 4.2) and finally we discuss some system aspects related to the correct simulation of compact polarimetric data (Sec. 4.3).

4.1 Compact polarimetry

Since SAR sensors have been used for geoscience applications, the polarizations adopted for transmitting and receiving have been horizontal (H) and vertical (V), yielding a scattering matrix in the canonical H,V basis. The selective transmission/reception of H,V polarizations has led to four polarimetric modes: single polarimetric modes (HH or VV), dual (HH/HV or VV/VH), alternating (HH/VV), and quad or full modes

	RX	H	V	H,V	linear 45 deg	circular	circular L,R
TX							
H		single	—	dual	—	—	—
V		—	single	dual	—	—	—
H,V		alternating		full or quad	—	—	—
linear 45 deg		—	—	compact	—	—	—
circular		—	—	compact-hybrid	—	—	dual-circular
circular L,R		—	—	quad-hybrid	—	—	quad-circular

classical modes
compact-pol
hybrid-pol
circular-pol

Figure 4.1: Classification of emerging compact SAR modes in contrast with the classical SAR modes.

(HH/HV/VH/VV)¹. These polarimetric configurations are indicated as *classical* modes in Fig. 4.1, since all present and past SAR sensors for Earth Observation have been operating one or more of these modes. Among them, the advantages of full polarimetry with respect to dual or single polarimetry are well-recognized worldwide (Ulaby and Elachi, 1990; Lee and Pottier, 2009).

Recently, a more general concept of polarimeter has emerged, based on the transmission and/or reception of a polarization state different from the usual H or V states (Souyris and Mingot, 2002). This would be possible for both dual and full polarimetric architectures. Among the infinite combinations of transmit and receive polarizations, three special classes have been considered and are highlighted in Fig. 4.1. The first is named *compact polarimetry*, and denotes a variant of current dual polarimetric modes having a combination of polarization H and V in transmission and the coherent H,V in reception. The transmitted combination is a linear polarization oriented at 45 deg or a circular one (left or right). The second class is named *hybrid polarimetry* (Raney, 2007), wherein the transmission is circular and the reception is linear. Hybrid modes include the circular compact polarimetry and the case of interleaved left and right trans-

1. In monostatic SAR polarimetry, quad-pol and full-pol modes are often used as synonyms. In the nomenclature defined by Raney and Freeman (2009), illustrated in Fig. 4.1, the terms are distinguished based on scattering reciprocity, i.e. $HV=VH$ (quad-pol) and $HV\neq VH$ (full-pol).

mission, which leads to the quad-hybrid mode. The third class of SAR architectures is the *circular polarimetric* mode, whose peculiarity is the transmission and reception at circularly polarized states. One objective of the research in SAR polarimetry is the assessment of the relative performance of such modes: identifying which mode is better is intertwined with system aspects, costs and of course with potential and benefits for geoscience applications.

In this chapter we restrict the analysis to compact polarimetry, i.e. the transmission of linearly polarized wave oriented at 45 deg or left circular polarized wave. These two configurations are often indicated in literature as $\pi/4$ mode and $\pi/2$ mode respectively. Two main motivations stimulated the emerging of compact polarimetry. The first is related to the constraints imposed by full polarimetry, in particular the reduced swath width and the larger amount of data. From this point of view, a compact polarimetric system behaves well as a single polarimetric system. The second motivation is related to the utility of polarimetry for geoscience applications. While full polarimetry is required for point target characterization, there is a large class of applications based on the analysis of distributed targets, like forests, which present some structural symmetries. These symmetries yield redundant information in the polarimetric covariance descriptors: compact polarimetry may avoid this redundancy by carrying the minimal needed information.

Although polarizations different than H and V were used in meteorological and astronomic measurements, the first work on compact polarimetry for Earth Observation appeared in 2002 (Souyris and Mingot, 2002), successively extended by Souyris et al. (2005). That work concerned mainly with the $\pi/4$ mode and stated that, using media symmetries of natural media, the useful covariance elements can be extracted from compact polarimetric data and exploited successfully for classification purposes. Later, some works have been conducted for comparing the compact-pol modes (Dubois-Fernandez et al., 2007; Nord et al., 2009) with the conclusion that the two compact polarimetric configurations lead generally to different results. In particular, the advantages of the $\pi/2$ mode with respect to the $\pi/4$ mode have been emphasized by Raney (2007), concerning the target rotational invariance and system optimization aspects. Further, Dubois-Fernandez et al. (2008); Freeman et al. (2008) discussed the advantages of circular transmission at lower frequency mainly with concern to the Faraday rotation and proposed a calibration approach for the $\pi/2$ mode. Additional investigations on the feasibility of compact polarimetry based on system aspect have been carried out by Touzi (2009).

All contributions proposed so far to assess the effectiveness of compact polarimetry for geoscience applications can be classified in two basic approaches. The first aims at *reconstructing* the full polarimetric information and at applying the same algorithms developed for full polarimetric data. This approach was first proposed by Souyris and

Mingot (2002); Souyris et al. (2005) and further improved by Nord et al. (2009); however, Cloude (2009) showed that some combinations of volume and ground components cannot be sufficiently described using the current pseudo-reconstruction algorithms. The second approach consists in exploiting directly the compact polarimetric information, i.e. developing new and specific algorithms rather than re-use the full polarimetric ones. Two examples of this approach can be found in Raney (2007) and Ainsworth et al. (2008).

Because of these investigations, today it is widely accepted that compact polarimetry can substitute full-polarimetry only for certain classes of observed targets and scattering mechanisms. This does not exclude that some applications may benefit from compact polarimetric acquisitions. Indeed, during the last ESA/POLINSAR2009 conference held in Frascati (Italy), it was recommended a better identification of these applications with respect to classical dual polarimetry. In addition, during that conference it was recognized that compact POLINSAR still requires a deeper investigation. Sec. 4.2 of this dissertation in part fulfills this gap.

Finally, in spite of the open debate, we note that some space agencies are proposing SAR missions that might carry on-board compact polarimetric systems: the American DESDYNI and SMAP missions, and the Argentinean SAOCOM and the Japanese ALOS-2 are some examples.

4.1.1 Theoretical formulation

The formulation of compact polarimetry starts by considering the scattering matrix \mathbf{S} of a generic distributed target. The development in this section includes all possible compact polarimetric modes that receive coherently at H and V polarizations, hence the considered \mathbf{S} matrix is expressed in the H,V basis. According to a general definition, compact polarimetry concept is based on the repeated transmission of a coherent combination of H and V polarizations yielding a generic polarization u . As an extension of dual polarimetry, the radar output of a compact polarimeter is a scattering *vector* $\mathbf{k}_u = (s_{hu} \ s_{vu})^T$, where the lower scripts of the complex amplitudes remark that the transmitted polarization is u . The form of the received compact scattering amplitudes follows straightforwardly by considering the elements of the matrix \mathbf{S} . A convenient way to represent the compact polarimeter is the following

$$\mathbf{k}_u = \begin{pmatrix} s_{hu} \\ s_{vu} \end{pmatrix} = \begin{pmatrix} s_{hh} & s_{hv} \\ s_{vh} & s_{vv} \end{pmatrix} \begin{pmatrix} u_h \\ u_v \end{pmatrix}, \quad u_h u_h^* + u_v u_v^* = 1 \quad (4.1)$$

wherein the complex numbers u_h and u_v select a combination of polarizations H and V and define the compact polarimetric mode. As mentioned previously, two choices of u_h, u_v have been considered so far and are relevant in this chapter. The first corresponds

to the $\pi/4$ mode, i.e. the linear transmission oriented at 45 deg obtained by setting $u_h = u_v = 1/\sqrt{2}$,

$$\mathbf{k}_{(\pi/4)} = \frac{1}{\sqrt{2}}(s_{hh} + s_{hv} \quad s_{vh} + s_{vv})^T \quad (4.2)$$

and the second configuration is the transmission of a left (or right) circular polarized wave, identified by $u_h = 1/\sqrt{2}$ and $u_v = j/\sqrt{2}$,

$$\mathbf{k}_{(\pi/2)} = \frac{1}{\sqrt{2}}(s_{hh} + js_{hv} \quad s_{vh} + js_{vv})^T. \quad (4.3)$$

The factor $\sqrt{2}$ in (4.2) and (4.3) accounts for a 3 dB loss in the radar output with respect to classical dual or full polarimetric modes. This is a direct consequence of the mismatch between transmitting and receiving polarimetric basis. Leaving apart the system issues, the fundamental question here is whether vectors $\mathbf{k}_{(\pi/2)}$ and $\mathbf{k}_{(\pi/4)}$ carry significant information for SAR applications.

A basic approach to answer this question is to consider the polarimetric signature associated with the compact scattering vectors (Ainsworth et al., 2009; van Zyl et al., 1987). The synthesis of any polarization basis in reception allows indeed representing the complete compact polarimetric features of the observed target (or image pixel) within a 3-dimensional plot. However, the utility of compact polarimetric data is more for distributed targets than coherent targets, due to the symmetries that natural media possess. The polarimetric descriptor for such media is the 2×2 compact covariance matrix \mathbf{J}

$$\mathbf{J}_{(\pi/4)} = \langle \mathbf{k}_{(\pi/4)} \mathbf{k}_{(\pi/4)}^\dagger \rangle = \begin{pmatrix} \langle s_{h(\pi/4)} s_{h(\pi/4)}^* \rangle & \langle s_{h(\pi/4)} s_{v(\pi/4)}^* \rangle \\ \langle s_{v(\pi/4)} s_{h(\pi/4)}^* \rangle & \langle s_{v(\pi/4)} s_{v(\pi/4)}^* \rangle \end{pmatrix} = \begin{pmatrix} J_{11} & J_{12} \\ J_{21} & J_{22} \end{pmatrix} \quad (4.4)$$

specified for a $\pi/4$ polarimeter. A similar expression holds for the $\pi/2$ mode. Matrix (4.4) can be formally estimated for any dual polarimetric data and corresponds to the covariance matrix \mathbf{C} used in full polarimetric techniques². The question becomes now how to exploit the information content of \mathbf{J} . As mentioned in the introduction of the chapter, two approaches may be adopted. One considers directly the information embedded in the elements of \mathbf{J} and is based on the development of new algorithms suitable for extracting this information (e.g. the types of scattering mechanisms). As an example, Ainsworth et al. (2008) extended the $H/A/\alpha$ decomposition (Cloude and Pottier, 1997) to the case of dual polarimetric imagery. In this formulation, the compact-pol entropy has a similar expression to the quad-pol entropy and, indeed, the same phys-

2. An alternative descriptor for dual polarimeters is the set of Stokes parameters as proposed by Raney (2007). These parameters are used in Sec. 4.3 to study the effects of the SAR processor on the synthesis of compact polarimetric data.

ical interpretation. In order to derive a parameter similar to the α angle, a simpler parameterization of the eigenvector of the matrix \mathbf{J} has been adopted by Ainsworth et al. (2008). This leads to define a new angle which contains information about the scattering mechanisms seen by a compact polarimeter, but that does not correspond readily to α . Nevertheless, a segmentation of dual-pol data has been proposed based on this new angle and entropy. The second example of decomposition has been proposed by Raney (2007) starting from the Stokes parameters. He considered the polarization ratio (which is somehow related to the entropy) and the phase difference between the two compact-pol channels. He proposed a decomposition based on these two descriptors with emphasis on the advantages of the circular transmission with respect to any other compact polarimetric configuration.

The advantage of these two approaches is that they access directly to the information of the compact covariance matrix, without preprocessing the compact polarimetric return. However, the definition of new algorithms and descriptors does not allow a straightforward comparison between compact polarimetry and full polarimetry. From this point of view, the approach of the pseudo-reconstruction is somehow attractive. It aims at reconstructing the full polarimetric covariance matrix when natural media presents a simplified structure and hence the comparison is straightforward. Our contribution to compact POLINSAR exposed in Sec. 4.2 belongs to this class of methods. Before dealing with compact interferometry, the compact polarimetric pseudo-reconstruction is first treated more in detail in the next section.

4.1.2 Pseudo-reconstruction of the coherency matrix

As discussed above, the utility of compact polarimetry lies on the fact that natural media possess certain properties of symmetry, which yield redundancy of information in the 4×4 full-pol covariance matrix. Once symmetric targets are detected in the scene, the redundancy is usually exploited for calibration purposes, in particular the correction for system cross-talk and channel imbalance (cf. Chapter 5). In this section, we show how this information can be exploited for linking the compact and full covariance matrix elements.

The first assumption on these elements is the backscatter reciprocity as mentioned in Chapter 2. Reciprocity constrains the cross-polarized channels to be equal, i.e. $s_{hv} = s_{vh}$, and hence the rank of the covariance matrix reduces from 4 to 3. In addition to reciprocity, three classes of symmetry are defined and observed for natural media (Nghiem et al., 1992). They are listed hereafter.

Reflection symmetry. A medium is said to have reflection symmetry if it is symmetric about a plane containing the direction of propagation and one of the polarization directions, e.g., the H direction. Reflection symmetry leads to the following

general form of the covariance matrix

$$\mathbf{C}^{\text{ref}} = \begin{pmatrix} \langle |s_{hh}|^2 \rangle & 0 & \langle s_{hh}s_{vv}^* \rangle \\ 0 & 2\langle |s_{hv}|^2 \rangle & 0 \\ \langle s_{vv}s_{hh}^* \rangle & 0 & \langle |s_{vv}|^2 \rangle \end{pmatrix}. \quad (4.5)$$

In this case, the diagonal terms are purely real, and $\langle s_{hh}s_{vv}^* \rangle$ and $\langle s_{vv}s_{hh}^* \rangle$ are complex conjugates. Hence the number of unknowns is 5. As an example, a rough surface can be regarded as a reflection symmetric target.

Rotation symmetry. Rotation symmetry occurs when a medium is invariant under any rotation about an axis parallel to the direction of propagation. By imposing rotation symmetry properties, the form of the covariance matrix is the following

$$\mathbf{C}^{\text{rot}} = \begin{pmatrix} \langle |s_{hh}|^2 \rangle & \sqrt{2}\langle s_{hh}s_{hv}^* \rangle & \langle |s_{hh}|^2 \rangle - 2\langle |s_{hv}|^2 \rangle \\ -\sqrt{2}\langle s_{hh}s_{hv}^* \rangle & 2\langle |s_{hv}|^2 \rangle & \sqrt{2}\langle s_{hh}s_{hv}^* \rangle \\ \langle |s_{hh}|^2 \rangle - 2\langle |s_{hv}|^2 \rangle & -\sqrt{2}\langle s_{hh}s_{hv}^* \rangle & \langle |s_{hh}|^2 \rangle \end{pmatrix}. \quad (4.6)$$

In this case, the diagonal terms are purely real and the term $\langle s_{hh}s_{hv}^* \rangle$ is purely imaginary. Hence, the number of unknowns is 3. A rotation-invariant random distribution of scatterers is a rotationally symmetric target.

Azimuthal symmetry. Finally, azimuthal symmetry can be regarded as a combination of reflection and rotation symmetries. The form of the covariance matrix is the following

$$\mathbf{C}^{\text{az}} = \begin{pmatrix} \langle |s_{hh}|^2 \rangle & 0 & \langle |s_{hh}|^2 \rangle - 2\langle |s_{hv}|^2 \rangle \\ 0 & 2\langle |s_{hv}|^2 \rangle & 0 \\ \langle |s_{hh}|^2 \rangle - 2\langle |s_{hv}|^2 \rangle & 0 & \langle |s_{hh}|^2 \rangle \end{pmatrix}. \quad (4.7)$$

In this case, all terms are purely real and the number of unknowns is 2. A uniform and random distribution of scatterers is an example of azimuthally symmetric target.

When a medium has structural symmetries about the radar line of sight, its covariance matrix is well approximated by one of the symmetric forms above. Those forms follow from specific relationships among the elements of the covariance matrix, derived by imposing symmetry constraints. Fig. 4.2 illustrates how these relationships are associated with the symmetric forms. The figure shows that some relationships are common to the reflection and rotation symmetry. It also suggests that certain *lighter* forms of rotation (or reflection) symmetry can be envisioned if we consider only few sparse ex-

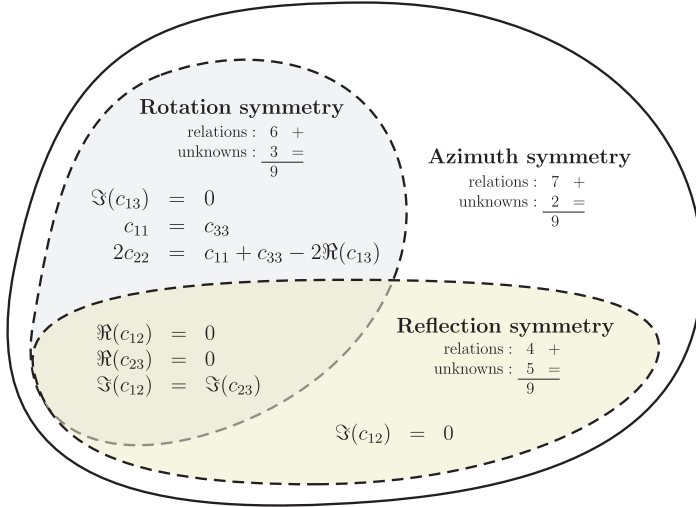


Figure 4.2: Diagram of the relationships among the elements of the covariance matrix under different symmetry assumptions.

pressions. For instance, we could assume reflection symmetry and, in addition, we may only consider the rotation invariance of the cross-polarized term $\langle |s_{hv}| \rangle$, and obtain the following equation (cf. Fig. 4.2)

$$4\langle |s_{hv}|^2 \rangle = \langle |s_{hh}|^2 \rangle + \langle |s_{vv}|^2 \rangle - 2\Re(\langle s_{hh}s_{vv}^* \rangle). \quad (4.8)$$

The relationship (4.8) will be extended to the case of compact POLINSAR and will be used for the pseudo-reconstruction of the full POLINSAR covariance matrix.

Turning back on compact polarimetry, the objective of the pseudo-reconstruction of the polarimetric covariance matrix is to recover some of the second-order elements from the 4 complex elements of the compact covariance matrix \mathbf{J} in (4.4). The expression of the compact scattering vector (4.2) in terms of scattering elements allows expanding the

compact covariance elements as follow

$$\begin{aligned}
 J_{11} &= \frac{1}{2} \left(\langle |s_{hh}|^2 \rangle + \langle s_{hh}s_{hv}^* \rangle + \langle s_{hv}s_{hh}^* \rangle + \langle |s_{hv}|^2 \rangle \right) \\
 J_{12} &= \frac{1}{2} \left(\langle s_{hh}s_{vv}^* \rangle + \langle s_{hh}s_{hv}^* \rangle + \langle s_{hv}s_{vv}^* \rangle + \langle |s_{hv}|^2 \rangle \right) \\
 J_{21} &= \frac{1}{2} \left(\langle s_{vv}s_{hh}^* \rangle + \langle s_{vv}s_{hv}^* \rangle + \langle s_{hv}s_{hh}^* \rangle + \langle |s_{hv}|^2 \rangle \right) \\
 J_{22} &= \frac{1}{2} \left(\langle |s_{vv}|^2 \rangle + \langle s_{vv}s_{hv}^* \rangle + \langle s_{hv}s_{vv}^* \rangle + \langle |s_{hv}|^2 \rangle \right).
 \end{aligned} \tag{4.9}$$

For the purpose of the reconstruction, the compact covariance elements J_{ij} , $i, j = 1, 2$ are the known parameters, whereas the terms in the right hand of (4.9) are the unknown elements. Equations (4.9) contains 9 real unknowns and 4 real compact-pol covariance observations: to invert the linear system additional relationships are required. As anticipated, they are taken reasonably from symmetry properties of natural media. Reflection symmetry, for instance, introduces 4 new equations (cf. Fig. 4.2) imposing lack of correlation between co- and cross-polarized components as in (4.5). Unfortunately, an additional equation is still needed. Such equation may be taken from rotation symmetry, as for instance (4.8). However, if we aim at reconstructing a large variety of targets, such as rough surfaces and forests, (4.8) may be not appropriate: while it may be valid for dense volumetric media, it is violated for flat surfaces wherein $\langle |s_{hv}|^2 \rangle \simeq 0$. To include a larger class of scattering targets in the reconstruction, Souyris et al. (2005) defined a non-linear relationship, lately refined by Nord et al. (2009). This relationship has been found by constraining its validity in the two extreme cases of Bragg surface scattering and completely depolarized wave, and then by assuming a linear trend between these two cases. To derive that expression, we like to start from (4.8), which can be rewritten as

$$\frac{4\langle |s_{hv}|^2 \rangle}{\langle |s_{hh}|^2 \rangle + \langle |s_{vv}|^2 \rangle} = 1 - \frac{2\Re(\langle s_{hh}s_{vv}^* \rangle)}{\langle |s_{hh}|^2 \rangle + \langle |s_{vv}|^2 \rangle}. \tag{4.10}$$

Now, if we impose the two remaining relationships of rotation symmetry (cf. Fig. 4.2), i.e. $\Im(\langle s_{hh}s_{vv}^* \rangle) = 0$ and $\langle |s_{hh}|^2 \rangle = \langle |s_{vv}|^2 \rangle$, we fall into the azimuth symmetry case, and we can rearrange the terms in the following way

$$\frac{4\langle |s_{hv}|^2 \rangle}{\langle |s_{hh}|^2 \rangle + \langle |s_{vv}|^2 \rangle} = 1 - \frac{2|\langle s_{hh}s_{vv}^* \rangle|}{\langle |s_{hh}|^2 \rangle + \langle |s_{vv}|^2 \rangle} = 1 - \frac{|\langle s_{hh}s_{vv}^* \rangle|}{\langle |s_{hh}|^2 \rangle} = 1 - \frac{|\langle s_{hh}s_{vv}^* \rangle|}{\sqrt{\langle |s_{hh}|^2 \rangle \langle |s_{vv}|^2 \rangle}}. \tag{4.11}$$

The extreme left and right terms represent the non-linear equality used for the pseudo-reconstruction of the covariance matrix on a generic distributed target. It has been formally derived under the assumption of azimuth symmetry, but then the discrimination between $\langle |s_{hh}|^2 \rangle$ and $\langle |s_{vv}|^2 \rangle$ has been imposed, claiming that this generalizes its validity on a larger class of targets. Indeed, it is relatively easy to test that it is valid on both cloud of random scatterers and Bragg surface. The former is characterized by a diagonal covariance matrix with two degenerating eigenvalues. The latter has a rank-1 covariance matrix with very small correlation between cross-polarized terms. However, first Nord et al. (2009), and more recently Cloude (2009), showed that many distributed targets may not satisfy (4.11). In particular, Nord et al. (2009) showed experimentally using DLR E-SAR airborne data that the coefficient in (4.11) can be optimized (increased) to include more scattering mechanisms in the reconstruction. Both the original and the refined expressions are non-linear, hence an iterative algorithm has to be used to calculate the covariance elements. The two scenarios for which (4.11) is valid correspond to the extreme cases of the μ spectrum of RVOG model (when Bragg scattering is assumed at surface), as pointed out by Cloude (2009). He showed, using an analytical approach based on RVOG model, that any combination of ground and volume components leads to a violation of (4.11). This happens because the azimuth symmetry is broken by the sum of ground and volume components.

In conclusion, the pseudo-reconstruction can be a useful tool for comparing compact and full polarimetry but depends on the underlying symmetry properties of the target. The non-linear relationship discussed in this section is suitable only for azimuth symmetric target and few particular combinations of volume and surface scattering. This means that if the covariance elements are calculated from compact-pol observations using (4.11), better performances are expected when flat areas or dense forests dominate the scene. It follows also that the reconstruction performances depend in general on the particular compact polarimetric configuration. To support these two arguments we show an example of full polarimetric dataset acquired by ALOS/PALSAR over Flevoland (The Netherlands) on 7 March 2007 with ascending pass. A compact polarimetric acquisition has been first simulated using (4.8) and (4.3), and subsequently the pseudo full-pol covariance matrix has been reconstructed by iteration according to (4.11). The comparison is shown through a Pauli decomposition of the polarimetric information. Although the area is predominately flat, we observe some mismatch between original and reconstructed full polarimetric information. The circular transmission case is generally better, at least by visual inspection, than the $\pi/4$ mode. This example confirms that the reconstruction should be taken with caution if combinations of volume and ground components occur in the scene.

The areas wherein the pseudo-reconstruction is expected to perform well may be de-

tected through statistical tests over full polarimetric data³. Two approaches are available in the open literature for this purpose. One considers the ratio between the determinant of the estimated full-pol covariance matrix and its *forced* symmetric form (Ferro-Famil and Neumann, 2008); the second is based on the difference between the estimated polarimetric α angle and its expected value with azimuth symmetric targets (Cloude, 2009). Both these methods can be used to assess the goodness of the covariance reconstruction over full polarimetric mode.

Our contribution is on the analysis of compact polarimetry *and interferometry*. In light of the recent advances on compact polarimetry, it may appear that POLINSAR inherits all consequences of the pseudo-reconstruction and hence the discussion above is still valid: this is partially true. The most developed (and required) application of POLINSAR is the retrieval of biomass from forests with large carbon stocks (cf. Chapter 1). Hence, in our investigation on the compact POLINSAR capabilities, we renounce at reconstructing over bare surface, aiming at a better exploitation of compact polarimetric data over volumetric media⁴. This is addressed in the next section.

4.2 Compact polarimetric SAR interferometry

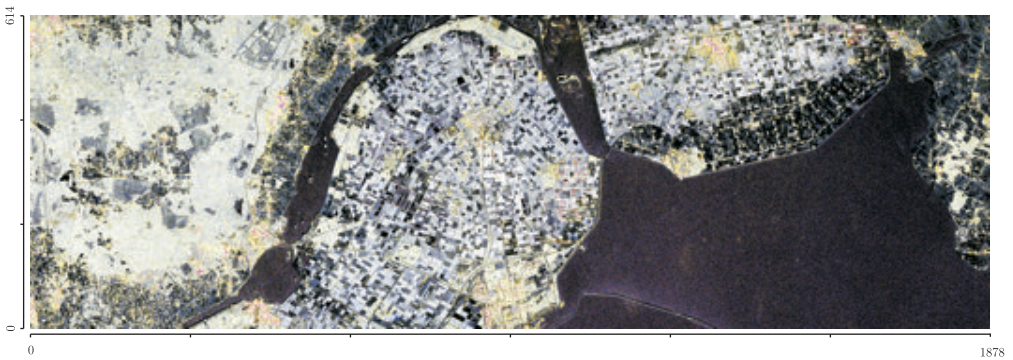
In this section we address the compact POLINSAR (C-POLINSAR) formulation and present a pseudo-reconstruction algorithm of the full POLINSAR (F-POLINSAR) covariance matrix (Lavalle et al., 2008a, 2010; Lavalle, 2008). The reconstruction of the F-POLINSAR covariance matrix is based here on polarimetric *and interferometric* symmetry properties of natural media. As discussed previously, only a limited class of targets can benefit from such pseudo-reconstruction. For this reason, hereafter we discuss also two POLINSAR indicators for detecting the areas wherein symmetries hold. Given two compact polarimetric acquisitions, there are two obvious approaches for studying C-POLINSAR for height retrieval. The first approach looks at all possible polarization combinations in reception and does not involve any reconstruction: the interferometric coherence is estimated for each combination (i.e. the coherence region is evaluated) and the most phase-separated scattering mechanisms are selected. Intuitively, compact polarimetry limits the number of scattering mechanisms seen by polarization diversity: the μ spectrum is contracted and the visible line in the complex

3. If only compact polarimetric data are available, it would be better to identify symmetric areas before performing the pseudo-reconstruction, to avoid a blind application of the algorithm with different performances.

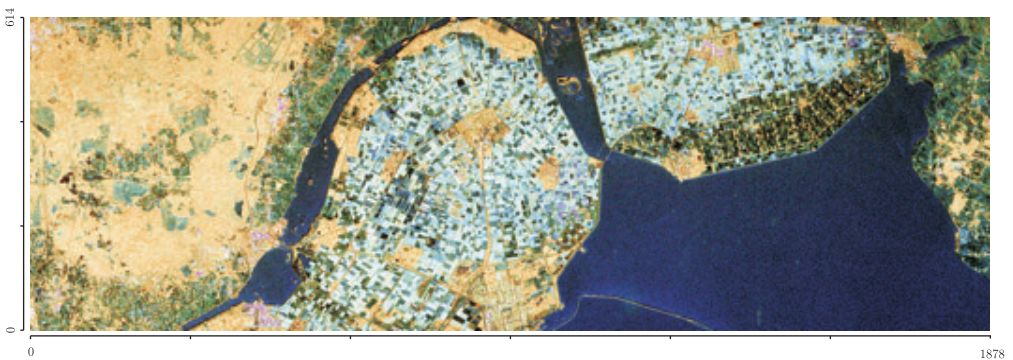
4. This statement is true only if we assume a small ground-to-volume ratio or, in other words, volume-dominated polarimetric channels. As discussed in Chapter 3, POLINSAR techniques over forests are based on the identification of the extreme values of the μ spectrum, hence the highest value of μ might still contain a significant ground component.



(a) Full polarimetry



(b) Compact polarimetry (linear 45 deg)



(c) Compact polarimetry (left-circular)

Figure 4.3: Original full polarimetric Pauli decomposition (a) over Flevoland (The Netherlands) and associated pseudo-reconstruction from compact polarimetry using the $\pi/4$ mode (b) and the $\pi/2$ mode (c). Note the presence of all color components in the reconstructed images. The matching between full-pol and compact-pol, however, depends on the symmetry assumptions.

plane becomes shorter. This does not prevent the inversion but might affect the retrieved height accuracy (Dubois-Fernandez et al., 2007). The second obvious approach is the pseudo-reconstruction of each compact polarimetric dataset as described in the previous section. Some investigations using this approach for height retrieval revealed that good performances are expected if the imaged forest satisfies azimuth symmetry. This approach, however, does not exploit the information contained in the compact cross-covariance matrix, obtained combining the two compact SAR acquisitions.

Our approach differs from the previous ones in two aspects. First, we propose a pseudo-reconstruction of the full POLINSAR matrix \mathbf{C}_6 by considering the *complete* compact POLINSAR information. Secondly, we do not use the non-linear relationship (4.11) but a linear relationship based on partial rotational invariance of the covariance terms. This relationship is, a priori, less stringent than azimuth symmetry and allows avoiding iterations in the reconstruction algorithm.

The performance of C-POLINSAR are investigated using two interferometric acquisitions over the Traunstein forest (Germany) acquired by the DLR L-band E-SAR sensor in 2005. As a remark, the objective of the pseudo-reconstruction is to *extract* the information carried by the degree of coherence in the conventional polarization basis (HH, HV, VV) from a compact polarimetric dataset. The advantage of this approach is an easy and straightforward comparison between C-POLINSAR and F-POLINSAR and the use of C-POLINSAR dataset with current POLSAR and POLINSAR algorithms. In the following, we first review the form of the POLINSAR covariance matrix under specific symmetry properties of the target; then we discuss the C-POLINSAR formulation and the associated reconstruction algorithms for both CP linear transmission and CP circular transmission; finally, we compare the two approaches and illustrate the results using both real data and RVOG predictions.

4.2.1 Theoretical formulation

We start by considering the scattering vectors of a reciprocal polarimetric acquisition in the conventional linear basis

$$\begin{aligned}\mathbf{k}_{L_1} &= (s_{hh_1} \quad \sqrt{2}s_{hv_1} \quad s_{vv_1})^T \\ \mathbf{k}_{L_2} &= (s_{hh_2} \quad \sqrt{2}s_{hv_2} \quad s_{vv_2})^T.\end{aligned}\tag{4.12}$$

Following the same development adopted in Chapter 3 to derive the matrix \mathbf{T}_6 , scattering vectors (4.12) are useful to define the *interferometric* scattering vector $\mathbf{k}_L = (\mathbf{k}_{L_1} \quad \mathbf{k}_{L_2})^T$. In this way, the complete POLINSAR information are embedded in the

6×6 covariance matrix \mathbf{C}_6

$$\mathbf{C}_6 = \langle \mathbf{k}_L \mathbf{k}_L^\dagger \rangle = \begin{pmatrix} \mathbf{C}_{11} & \mathbf{C}_{12} \\ \mathbf{C}_{12}^\dagger & \mathbf{C}_{22} \end{pmatrix}. \quad (4.13)$$

Matrices \mathbf{C}_{11} and \mathbf{C}_{22} are the conventional Hermitian covariance matrices that describe the polarimetric properties of each image separately; \mathbf{C}_{12} is the 3×3 cross-covariance matrix that combines the polarimetric and interferometric information. Also the cross-covariance matrix shows a particular structure in the case of symmetric targets (Nghiem et al., 1992; Moghaddam, 1999). Hereafter we review the canonical symmetric forms of the POLINSAR matrix \mathbf{C}_{12} which are also valid for the polarimetric matrices \mathbf{C}_{11} and \mathbf{C}_{22} .

Reflection symmetry Reflection symmetry leads to the following general form of the covariance and cross-covariance matrices (Moghaddam, 1999)

$$\mathbf{C}_{ij}^{\text{ref}} = \begin{pmatrix} \langle s_{hh_i} s_{hh_j}^* \rangle & 0 & \langle s_{hh_i} s_{vv_j}^* \rangle \\ 0 & 2\langle s_{hv_i} s_{hv_j}^* \rangle & 0 \\ \langle s_{vv_i} s_{hh_j}^* \rangle & 0 & \langle s_{vv_i} s_{vv_j}^* \rangle \end{pmatrix} \quad (4.14)$$

where $i, j = 1, 2$ indicate the two ends of the baseline. When $i = j$, matrix (4.14) reduces to the covariance matrices $\mathbf{C}_{11}^{\text{ref}}$ and $\mathbf{C}_{22}^{\text{ref}}$. In this case, the diagonal terms are purely real and $\langle s_{hh_i} s_{vv_j}^* \rangle$ and $\langle s_{vv_i} s_{hh_j}^* \rangle$ are complex conjugates. Hence the number of unknowns is 5. If $i \neq j$, the cross-covariance matrix $\mathbf{C}_{12}^{\text{ref}}$ contains 5 complex non-zero elements, hence the number of unknowns in the POLINSAR case is 10.

Rotation symmetry By imposing rotation symmetry properties, the form of the covariance and cross-covariance matrices is the following

$$\mathbf{C}_{ij}^{\text{rot}} = \begin{pmatrix} \langle s_{hh_i} s_{hh_j}^* \rangle & \sqrt{2}\langle s_{hh_i} s_{hv_j}^* \rangle & \langle s_{hh_i} s_{hh_j}^* \rangle - 2\langle s_{hv_i} s_{hv_j}^* \rangle \\ -\sqrt{2}\langle s_{hh_i} s_{hv_j}^* \rangle & 2\langle s_{hv_i} s_{hv_j}^* \rangle & \sqrt{2}\langle s_{hh_i} s_{hv_j}^* \rangle \\ \langle s_{hh_i} s_{hh_j}^* \rangle - 2\langle s_{hv_i} s_{hv_j}^* \rangle & -\sqrt{2}\langle s_{hh_i} s_{hv_j}^* \rangle & \langle s_{hh_i} s_{hh_j}^* \rangle \end{pmatrix} \quad (4.15)$$

When $i = j$, matrix (4.15) reduces to the covariance matrices $\mathbf{C}_{11}^{\text{rot}}$ and $\mathbf{C}_{22}^{\text{rot}}$. In this case, the diagonal terms are purely real and the term $\langle s_{hh_i} s_{hv_j}^* \rangle$ is purely imaginary. Hence, the number of unknowns is 3. In the POLINSAR case ($i \neq j$), the cross-covariance matrix $\mathbf{C}_{12}^{\text{rot}}$ contains in general all complex elements and the number of unknowns is 6.

Azimuthal symmetry Finally, azimuthal symmetry can be regarded as a combination of reflection and rotation symmetries. The form of the covariance and cross-covariance matrices is the following

$$\mathbf{C}_{ij}^{\text{az}} = \begin{pmatrix} \langle s_{hh_i} s_{hh_j}^* \rangle & 0 & \langle s_{hh_i} s_{hh_j}^* \rangle - 2\langle s_{hv_i} s_{hv_j}^* \rangle \\ 0 & 2\langle s_{hv_i} s_{hv_j}^* \rangle & 0 \\ \langle s_{hh_i} s_{hh_j}^* \rangle - 2\langle s_{hv_i} s_{hv_j}^* \rangle & 0 & \langle s_{hh_i} s_{hh_j}^* \rangle \end{pmatrix} \quad (4.16)$$

When $i = j$, matrix (4.16) reduces to the covariance matrices $\mathbf{C}_{11}^{\text{rot}}$ and $\mathbf{C}_{22}^{\text{rot}}$. In this case, all terms are purely real and the number of unknowns is 2. In the POLINSAR case ($i \neq j$), the cross-covariance matrix $\mathbf{C}_{12}^{\text{rot}}$ contains in general all complex elements and the number of unknowns is 4.

Here we use the symmetry properties of the geophysical media to reconstruct the full polarimetric and interferometric information from two compact polarimetric datasets and to cope with the intrinsically reduced polarimetric information of a compact interferometer. The theoretical formulation is first presented for the linear transmission and subsequently for the left circular transmission.

Linear $\pi/4$ -transmission

If the SAR transmits and receives in a compact polarimetry and interferometric configuration using the $\pi/4$ mode, the scattering vectors can be written as

$$\begin{aligned} \mathbf{k}_{(\pi/4)_1} &= \frac{1}{\sqrt{2}} (s_{hh_1} + s_{hv_1} \quad s_{vv_1} + s_{hv_1})^T \\ \mathbf{k}_{(\pi/4)_2} &= \frac{1}{\sqrt{2}} (s_{hh_2} + s_{hv_2} \quad s_{vv_2} + s_{hv_2})^T. \end{aligned} \quad (4.17)$$

We define the interferometric compact scattering vector as $\mathbf{k}_{\pi/4} = (\mathbf{k}_{(\pi/4)_1} \quad \mathbf{k}_{(\pi/4)_2})^T$. The complete polarimetric and interferometric information of two CP acquisitions are therefore represented by a 4×4 matrix

$$\mathbf{J}_4 = \langle \mathbf{k}_{\pi/4} \mathbf{k}_{\pi/4}^\dagger \rangle = \begin{pmatrix} \mathbf{J}_{11} & \mathbf{J}_{12} \\ \mathbf{J}_{12}^\dagger & \mathbf{J}_{22} \end{pmatrix} \quad (4.18)$$

where matrices \mathbf{J}_{11} and \mathbf{J}_{22} are the compact covariance matrices and \mathbf{J}_{12} is the compact cross-covariance matrix representative of compact POLINSAR configuration. Matrix \mathbf{J}_4 has the same meaning as the covariance matrix \mathbf{C}_6 in the F-POLINSAR case. Depending on the particular CP mode, the second-order elements of matrix \mathbf{C}_6 are *embedded* in

the elements of \mathbf{J}_4 . Our first objective is to extract these elements and to reconstruct the matrix \mathbf{C}_6 from the observed matrix \mathbf{J}_4 . In view of reconstructing the cross-covariance matrix \mathbf{C}_{12} , we concentrate on the cross-covariance matrix \mathbf{J}_{12}

$$\mathbf{J}_{12} = \begin{pmatrix} J_{11} & J_{12} \\ J_{21} & J_{22} \end{pmatrix} \quad (4.19)$$

which can be linked to the full POLINSAR second-order elements by combining (4.17)-(4.18)

$$\begin{aligned} J_{11} &= \frac{1}{2} (\langle s_{hh_1} s_{hh_2}^* \rangle + \langle s_{hh_1} s_{hv_2}^* \rangle + \langle s_{hv_1} s_{hh_2}^* \rangle + \langle s_{hv_1} s_{hv_2}^* \rangle) \\ J_{12} &= \frac{1}{2} (\langle s_{hh_1} s_{vv_2}^* \rangle + \langle s_{hh_1} s_{hv_2}^* \rangle + \langle s_{hv_1} s_{vv_2}^* \rangle + \langle s_{hv_1} s_{hv_2}^* \rangle) \\ J_{21} &= \frac{1}{2} (\langle s_{vv_1} s_{hh_2}^* \rangle + \langle s_{vv_1} s_{hv_2}^* \rangle + \langle s_{hv_1} s_{hh_2}^* \rangle + \langle s_{hv_1} s_{hv_2}^* \rangle) \\ J_{22} &= \frac{1}{2} (\langle s_{vv_1} s_{vv_2}^* \rangle + \langle s_{vv_1} s_{hv_2}^* \rangle + \langle s_{hv_1} s_{vv_2}^* \rangle + \langle s_{hv_1} s_{hv_2}^* \rangle). \end{aligned} \quad (4.20)$$

The linear system (4.20) contains four complex observables (J_{11} , J_{12} , J_{21} and J_{22}) and nine complex unknowns. To solve the system, we need to reduce the number of unknowns. Imposing rotation symmetry (4.15) allows the three unknowns $\langle s_{hh_1} s_{hh_2}^* \rangle$, $\langle s_{hh_1} s_{hv_2}^* \rangle$, $\langle s_{hv_1} s_{hv_2}^* \rangle$ to be computed and the cross-covariance matrix (4.21) being reconstructed

$$\mathbf{C}_{12} = \frac{1}{2} \begin{pmatrix} J_{11} + J_{22} + J_{12} + J_{21} & \sqrt{2}(J_{12} - J_{21}) & -J_{11} - J_{22} + 3J_{12} + 3J_{21} \\ -\sqrt{2}(J_{12} - J_{21}) & 2(J_{11} + J_{22} - J_{12} - J_{21}) & \sqrt{2}(J_{12} - J_{21}) \\ -J_{11} - J_{22} + 3J_{12} + 3J_{21} & -\sqrt{2}(J_{12} - J_{21}) & J_{11} + J_{22} + J_{12} + J_{21} \end{pmatrix}. \quad (4.21)$$

Note that (4.21) can also be used to compute the reconstructed covariance matrices \mathbf{C}_{11} and \mathbf{C}_{22} if we replace the elements of matrix \mathbf{J}_{12} with the elements of matrices \mathbf{J}_{11} and \mathbf{J}_{22} , respectively.

If the conditions of reflection symmetry (4.5) are imposed as an alternative to rotation symmetry, the number of unknowns is still larger than the number of observables. Rotation invariance of cross-polarization terms provides the following relationship

$$4\langle s_{hv_1} s_{hv_2}^* \rangle = \langle s_{hh_1} s_{hh_2}^* \rangle + \langle s_{vv_1} s_{vv_2}^* \rangle - \langle s_{hh_1} s_{vv_2}^* \rangle - \langle s_{vv_1} s_{hh_2}^* \rangle \quad (4.22)$$

which, coupled with the reflection symmetry conditions, allows the four unknowns $\langle s_{hh_1} s_{hh_2}^* \rangle$, $\langle s_{hh_1} s_{vv_2}^* \rangle$, $\langle s_{vv_1} s_{hh_2}^* \rangle$ and $\langle s_{vv_1} s_{vv_2}^* \rangle$ to be derived and the system (4.20) to be solved. The reconstructed cross-covariance matrix \mathbf{C}_{12} is

$$\mathbf{C}_{12} = \frac{1}{2} \begin{pmatrix} 3J_{11} + J_{12} + J_{21} - J_{22} & 0 & -J_{11} + 5J_{12} + J_{21} - J_{22} \\ 0 & 2(J_{11} - J_{12} - J_{21} + J_{22}) & 0 \\ -J_{11} + J_{12} + 5J_{21} - J_{22} & 0 & -J_{11} + J_{12} + J_{21} + 3J_{22} \end{pmatrix} \quad (4.23)$$

where the assumption of reflection symmetry entails the decorrelation between the cross- and like-polarized terms. Expression (4.23) can be used in general also to reconstruct matrices \mathbf{C}_{11} and \mathbf{C}_{22} .

Left-circular transmission

If the SAR transmits and receives in a $\pi/2$ configuration, the scattering vectors are given by

$$\begin{aligned} k_{(\pi/2)_1} &= \frac{1}{\sqrt{2}} (s_{hh_1} + js_{hv_1} \quad js_{vv_1} + s_{hv_1})^T \\ k_{(\pi/2)_2} &= \frac{1}{\sqrt{2}} (s_{hh_2} + js_{hv_2} \quad js_{vv_2} + s_{hv_2})^T. \end{aligned} \quad (4.24)$$

Following the same approach as for linear transmission, we note that circular polarization provides less information on a rotationally symmetric target than linear polarization. The reason is intrinsic to the rotational invariance of the circular polarization itself. It follows that assuming rotational symmetry does not allow the reconstruction of the FP covariance matrix, since there are more unknowns than observables.

On the contrary, reflection symmetry coupled with the additional constraint of rotation invariance of the cross-polarized terms yields the following expression of the covariance matrix

$$\mathbf{C}_{12} = \frac{1}{4} \begin{pmatrix} 7J_{11} + jJ_{12} - jJ_{21} - J_{22} & 0 & J_{11} + 7jJ_{12} + jJ_{21} + J_{22} \\ 0 & 2(J_{11} - jJ_{12} + jJ_{21} + J_{22}) & 0 \\ J_{11} - jJ_{12} - 7jJ_{21} + J_{22} & 0 & -J_{11} + jJ_{12} - jJ_{21} + 7J_{22} \end{pmatrix} \quad (4.25)$$

This reconstructed form of the POLINSAR covariance matrix can be used to compare the information contents of full polarimetry and compact polarimetry, as discussed in the next section.

The same considerations made for compact polarimetry in Sec. 4.1.2 apply in this section for compact POLINSAR. The assumptions under which expressions (4.21),

(4.23) and (4.25) have been obtained limit their validity to a subset of natural targets. Forests are the most significant example of target generally showing reflection and rotation invariance of the cross-polarization terms in volume-dominated polarimetric channels. When the target properties deviate from the underlying hypotheses, the performances of the reconstruction are expected to worsen. This is the case of forests with an important underlying ground component, as shown analytically in Sec. 4.2.3. In the limit, on a bare surface the assumption of reflection symmetry holds, but the rotation invariance may not be satisfied. Finally, man-made targets, such as buildings, usually do not fall into either of the two symmetry categories (Ferro-Famil and Lavalley, 2009), hence our algorithm is not applicable. A statistical test on the POLINSAR covariance matrix (Ferro-Famil et al., 2008) can identify the areas with suitable symmetry characteristics as shown in the next section.

4.2.2 Experimental results

We now use the reconstructed covariance matrix previously outlined to compute the POLINSAR degree of coherence of a compact polarimetric dataset. Its general expression, valid for full polarimetry, can be written as

$$\gamma = \frac{\mathbf{w}^\dagger \mathbf{C}_{12} \mathbf{w}}{\sqrt{(\mathbf{w}^\dagger \mathbf{C}_{11} \mathbf{w}) (\mathbf{w}^\dagger \mathbf{C}_{22} \mathbf{w})}} \quad (4.26)$$

where the vector \mathbf{w} selects the scattering mechanism. The test dataset for comparing full-pol, linear compact-pol and circular compact-pol is a fully polarimetric and interferometric acquisition taken by the DLR L-band E-SAR sensor in 2005 over the Traunstein forest (Germany). Fig. 4.4 shows the logic steps of the performance evaluation of C-POLINSAR. The FP dataset is processed to simulate a CP dataset according to the polarization synthesis (4.17) and (4.24) for the $\pi/4$ mode and $\pi/2$ mode, respectively. For each CP mode, the C-POLINSAR dataset consists of 4 complex images, which are used to derive the second order elements of the compact covariance matrix (4.18) and subsequently to reconstruct the second-order F-POLINSAR information contained in the \mathbf{C}_6 matrix using expressions (4.23) and (4.25). The visual comparison between the color-composite $|HH|$, $|HV|$, $|VV|$ image from a fully polarimetric acquisition and its reconstruction from compact polarimetric datasets (Fig. 4.5) indicates a general good agreement. Indeed, the normalized RMS error (NRMSE) is respectively 0.9%, 0.56%, 0.71% for the three polarizations for the $\pi/4$ mode, and 0.63%, 0.5%, 0.47% for the $\pi/2$ mode. This case study points out that the three components are reconstructed with comparable accuracies and that the left-circular transmission yields slightly better results compared with the linear-45 one. The impact of this error on the applications

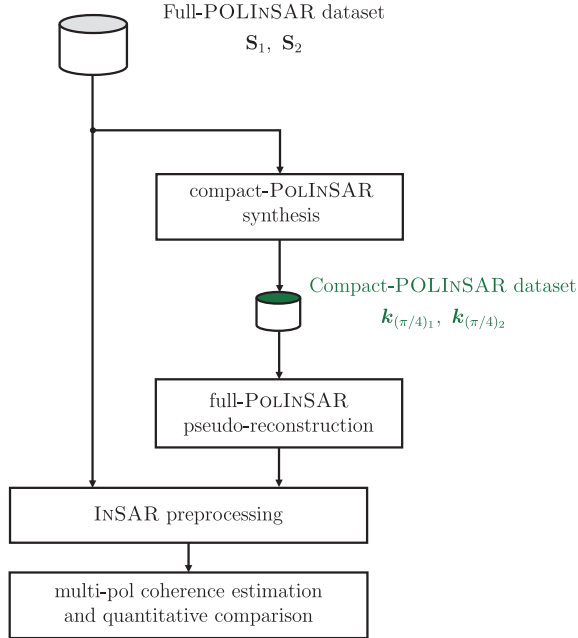


Figure 4.4: Logical steps for the assessment of the performances of compact POLINSAR.

depends on the particular algorithm that exploits the \mathbf{C}_{11} matrix. For the homogeneous areas in Fig. 4.5, the RMS error is lower than the standard deviation of the samples, thus suggesting that the reconstructed images can be used effectively. Some areas containing targets that violate the underlying symmetry assumptions, as mentioned in the previous section, show a considerable mismatch. CP reconstructions are expected to fail for this kind of surfaces.

The POLINSAR degree of coherence is then computed removing the phase contribution of the flat ellipsoid. The coherence maps and the flattened interferograms for the reconstructed HH polarization are shown in Fig. 4.6. The NRMSEs are respectively 0.12% and 0.52% for the magnitude and phase of the $\pi/4$ mode coherence, and 0.73% and 0.35% for the $\pi/2$ mode. The errors in the reconstructed interferograms are consistent with the results of the previous covariance matrix analysis. To better evaluate the difference between C-POLINSAR and F-POLINSAR, the row profiles corresponding to the interferometric coherence at the three polarizations HH, HV, VV are shown in Fig. 4.7. The coherence in the HH polarization is best reconstructed, while the com-

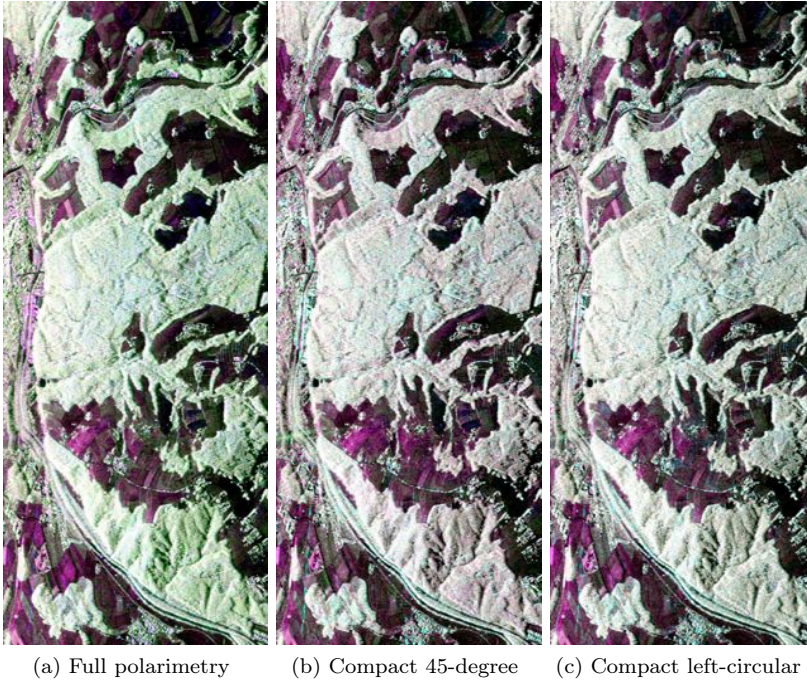


Figure 4.5: Full polarimetric image of the Traunstein forest acquired by the DLR E-SAR sensor (a) and reconstructed polarimetric image from a compact polarimetric dataset (b)-(c). Color coding: red ($|VV|$), blue ($|HH|$), green ($|HV|$). Notice the presence of all color components in the reconstructed images.

compact circular transmission reveals a slightly better agreement with FP than the compact linear transmission. However, all diagrams present a similar trend, although the occasional violation of the underlying symmetry hypothesis leads to small variation. These hypotheses correspond to uncorrelated co- and cross-polarized elements of matrix \mathbf{C}_6 (i.e. reflection symmetry), and to the relationship (4.22) between the autocorrelation of cross-polarized terms and the autocorrelation of co-polarized terms (i.e. rotation symmetry of cross-polarized terms). These symmetry properties affect several elements of the matrix \mathbf{C}_6 . Two maximum-likelihood optimum indicators can be defined in order to quickly assess *how much* the matrix \mathbf{C}_6 deviates from its symmetric form (Ferro-Famil and Lavallo, 2009)

$$\alpha_{\text{ref}} = \frac{|\mathbf{C}_6^{\text{ref}}|}{|\mathbf{C}_6|}, \quad \alpha_{\text{xrot}} = \frac{|\mathbf{C}_6^{\text{xrot}}|}{|\mathbf{C}_6|} \quad (4.27)$$

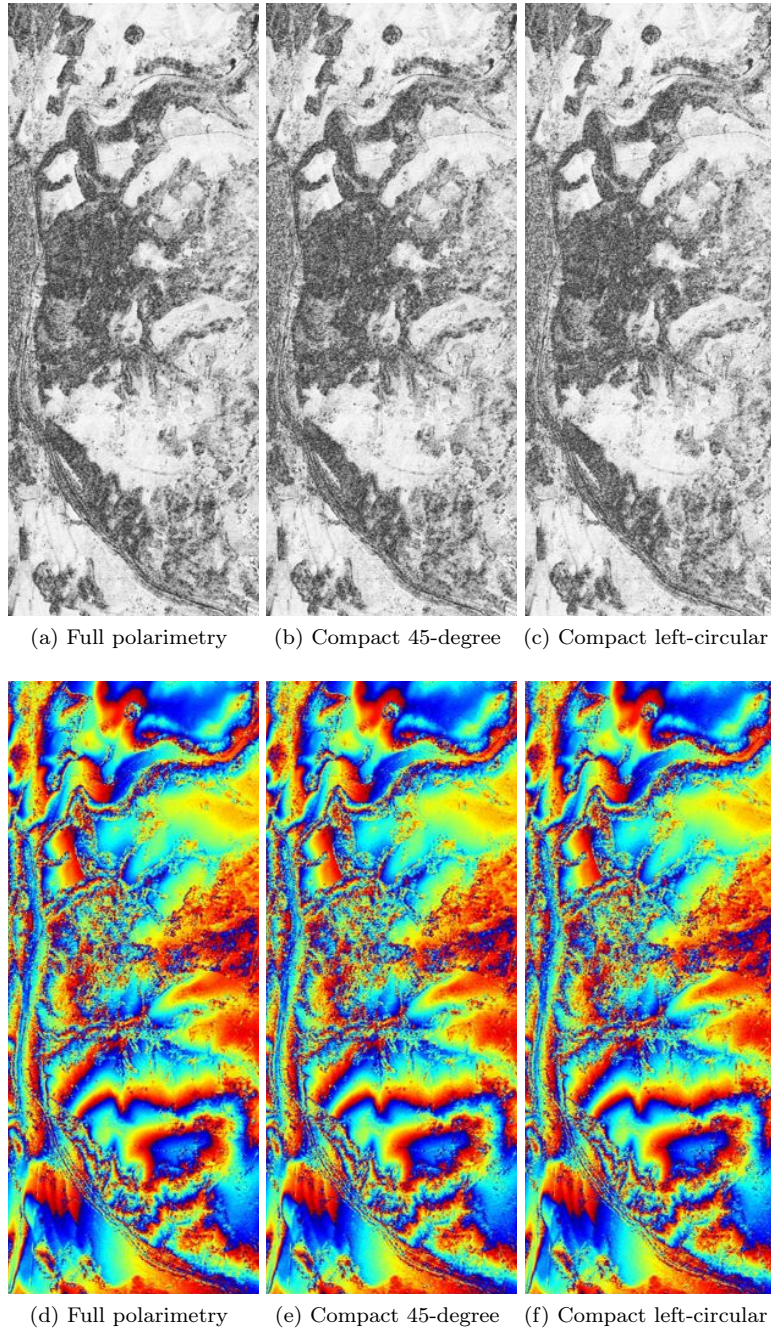
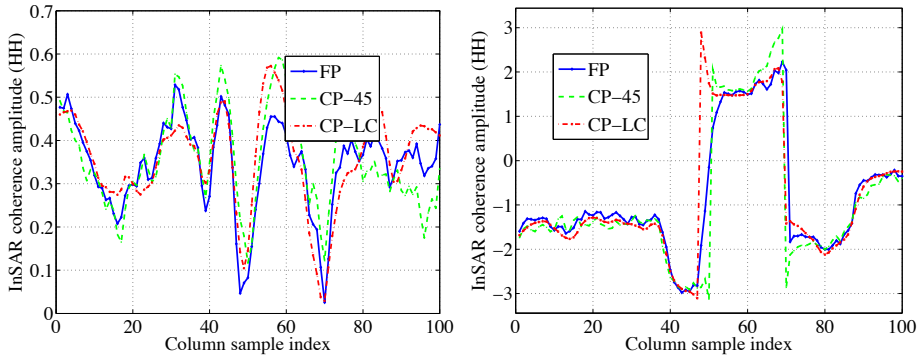
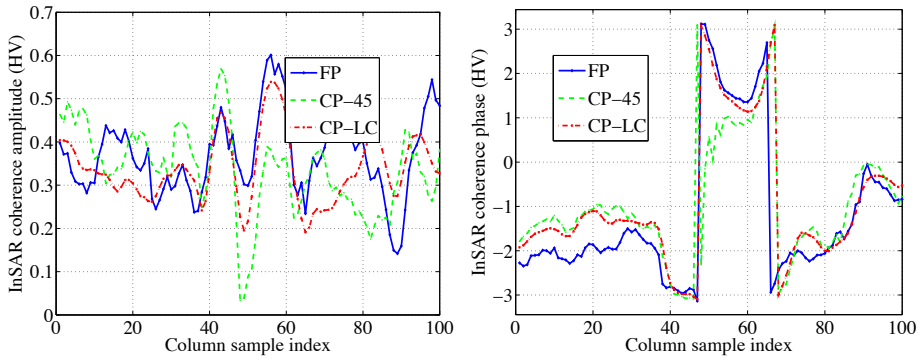


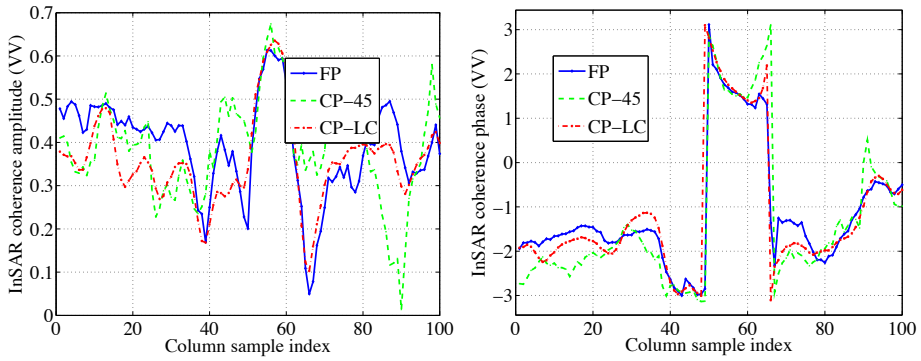
Figure 4.6: Coherence maps (top) and interferograms (bottom) of the HH polarization in the three considered architectures: full polarimetry, compact polarimetry with linear transmission and compact polarimetry with circular transmission. Color coding: black ($|\gamma| = 0$), white ($|\gamma| = 1$), red ($\angle\gamma = -\pi$), blue ($\angle\gamma = \pi$).



(a) HH



(b) HV



(c) VV

Figure 4.7: Row profiles of the magnitude (left plots) and phase (right plots) of the interferometric coherence for the polarizations HH (top), HV (middle), VV (bottom). The transect is across the vegetated area of Fig. 4.5.

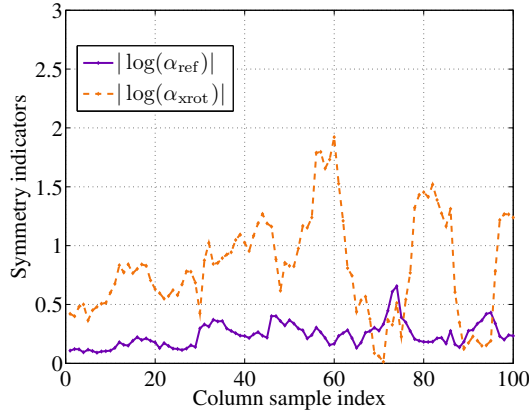


Figure 4.8: Row profiles of the indicators of reflection symmetry and rotation invariance of cross-polarization terms. The transect is across the vegetated area of Fig. 4.5.

wherein $|\cdot|$ indicates the determinant of the matrix, $\mathbf{C}_6^{\text{ref}}$ is the matrix \mathbf{C}_6 with forced reflection symmetry according to (4.5), and $\mathbf{C}_6^{\text{xrot}}$ is the matrix \mathbf{C}_6 with forced rotation symmetry according to (4.22). Values of these parameters close to zero indicate the presence of symmetric features in the imaged scene. Fig. 4.8 shows a plot of the symmetry indicators on the same transect as Fig. 4.7. As the curves deviate from zero, the reconstructed coherence becomes less reliable. These indicators allow identifying the areas wherein our algorithm is expected to yield accurate results. A threshold over these indicators may be identified by comparing the error of our reconstruction with the error accepted for a given application. Although the impact of the error on the final POLINSAR products depends on the subsequent algorithms exploiting matrix \mathbf{C}_6 , we note that generally the mean coherence phase in the two CP modes presents similar trend with the mean phase of FP. This is promising for single polarization interferometric applications that aim at reconstructing topography from CP data and for forestry applications that use the POLINSAR degree of coherence to retrieve biophysical parameters.

4.2.3 Simplified model analysis

In the previous section, the pseudo-reconstruction of the F-POLINSAR covariance matrix has been applied to real SAR data. Its performances have been found dependent on the underlying POLINSAR symmetry assumptions. In this section, we would like to support this result using the *interferometric* RVOG model. We follow the approach suggested by Cloude (2009), who showed that, for compact polarimetry, the non-linear

relationship (4.11) is not valid for all combinations of ground and volume components. We extend his development to the interferometric scenario and analyze the behavior of our assumption (4.22) designed for C-POLINSAR applications. More in general, we focus on the robustness of the POLINSAR symmetry assumptions when model parameters vary, in particular the scattering mechanism and the relative importance of ground and canopy components. For consistence with the formulation of Sec. 4.2, we describe the model using the covariance matrix \mathbf{C} instead of the more commonly used coherency matrix \mathbf{T} .

Let us start from the matrix formulation of the RVOG model (Cloude and Papathanassiou, 2003). The POLINSAR coherence, under the assumptions defined in Sec. 3.2.2, can be written as

$$\gamma = \frac{\mathbf{w}^\dagger \mathbf{C}_{12} \mathbf{w}}{\mathbf{w}^\dagger \mathbf{C} \mathbf{w}} \quad \text{with} \quad \mathbf{C} \doteq \frac{\mathbf{C}_{11} + \mathbf{C}_{22}}{2}, \quad \mathbf{w}_1^\dagger \mathbf{w}_2 = 1. \quad (4.28)$$

The RVOG model defines the form of the matrices \mathbf{C} and \mathbf{C}_{12} . As discussed in Chapter 3, they are based on the (incoherent) sum of a volume component \mathbf{C}^v and a direct/dihedral return \mathbf{C}^s from the underlying surface

$$\mathbf{C} = \mathbf{C}^s + \mathbf{C}^v, \quad \mathbf{C}_{12} = \mathbf{C}_{12}^s + \mathbf{C}_{12}^v. \quad (4.29)$$

The volume component comes from an azimuthally symmetric medium and has a diagonal matrix representation. The ground component is in general modeled by a reflection symmetric target. In this study, we adopt the following form of the covariance matrices (Cloude, 2009)

$$\mathbf{C}^s = \frac{\sigma^{(dg)} + \sigma^{(gv)}}{2} \begin{pmatrix} 1 + \sin 2\alpha \cos \delta & 0 & \cos 2\alpha - j \sin 2\alpha \sin \delta \\ 0 & 0 & 0 \\ \cos 2\alpha + j \sin 2\alpha \sin \delta & 0 & 1 - \sin 2\alpha \cos \delta \end{pmatrix} \quad (4.30)$$

$$\mathbf{C}^v = \frac{\sigma^{(dv)}}{2} \begin{pmatrix} 3/4 & 0 & 1/4 \\ 0 & 1/2 & 0 \\ 1/4 & 0 & 3/4 \end{pmatrix} \quad (4.31)$$

wherein the real parameters α and δ characterize the scattering mechanism, $\sigma^{(dg)}$ and $\sigma^{(gv)}$ stand for the direct-ground and ground-volume attenuated backscatter located on the ground, and $\sigma^{(dv)}$ is the total direct-volume backscatter (cf. Sec. 3.1.2)

$$\sigma^{(dv)} = \rho^{(dv)} \frac{e^{p_1 h_v} - 1}{p_1}, \quad \text{with} \quad p_1 = \frac{2\kappa_e}{\cos \theta}. \quad (4.32)$$

Similarly, the interferometric component of the model is represented by the following matrices, wherein we have set to zero the ground reference z_g without loss of generality,

$$\mathbf{C}_{12}^s = \frac{\sigma^{(dg)} + \sigma^{(gv)}}{2} \begin{pmatrix} 1 + \sin 2\alpha \cos \delta & 0 & \cos 2\alpha - j \sin 2\alpha \sin \delta \\ 0 & 0 & 0 \\ \cos 2\alpha + j \sin 2\alpha \sin \delta & 0 & 1 - \sin 2\alpha \cos \delta \end{pmatrix} \quad (4.33)$$

$$\mathbf{C}_{12}^v = \frac{\sigma_{int}^{(dv)}}{2} \begin{pmatrix} 3/4 & 0 & 1/4 \\ 0 & 1/2 & 0 \\ 1/4 & 0 & 3/4 \end{pmatrix} \quad (4.34)$$

In (4.34), $\sigma_{int}^{(dv)}$ is the cross-correlation between the complex scattering amplitudes and can be interpreted as an interferometric backscatter coefficient (cf. Sec. 3.1.2) given by

$$\sigma_{int}^{(dv)} = \rho^{(dv)} \frac{e^{p_2 h_v} - 1}{p_2}, \quad \text{with } p_2 = \frac{2\kappa_e}{\cos \theta} + jk_z. \quad (4.35)$$

Equations (4.33)-(4.35) define the structure of the cross-covariance matrix according to the RVOG model. It is on this structure that we have argued, in the previous section, the validity of (4.22). To verify this relationship versus the model parameters, we rewrite it more conveniently as

$$\frac{4\langle s_{hv_1} s_{hv_2}^* \rangle}{\langle s_{hh_1} s_{hh_2}^* \rangle + \langle s_{vv_1} s_{vv_2}^* \rangle} = 1 - \frac{2\Re(\langle s_{hh_1} s_{vv_2}^* \rangle)}{\langle s_{hh_1} s_{hh_2}^* \rangle + \langle s_{vv_1} s_{vv_2}^* \rangle}. \quad (4.36)$$

Inspired by the development made by Cloude (2009), all terms in (4.36) can be expanded according to (4.33)-(4.35), yielding a new expression in terms of the interferometric RVOG parameters

$$\frac{\gamma_v}{2\mu + \frac{3}{2}\gamma_v} = 1 - \frac{2\mu \cos 2\alpha + \frac{1}{2}\gamma_v}{2\mu + \frac{3}{2}\gamma_v} \quad (4.37)$$

wherein the ground-to-volume scattering ratio is $\mu = (\sigma^{(dg)} + \sigma^{(gv)}) / \sigma^{(dv)}$ and the coherence of a canopy layer (without ground) comes out from the ratio $\gamma_v = \sigma_{int}^{(dv)} / \sigma^{(dv)}$. All these parameters have been extensively discussed in Chapter 3. Before plotting (4.37), we note that the non-linear expression (4.11) proposed by Souyris et al. (2005) finds easily a counterpart in the interferometric formulation, given the same physical

arguments that have led to (4.22),

$$\frac{4\langle s_{hv_1}s_{hv_2}^* \rangle}{\langle s_{hh_1}s_{hh_2}^* \rangle + \langle s_{vv_1}s_{vv_2}^* \rangle} = 1 - \frac{\langle s_{hh_1}s_{vv_2}^* \rangle}{\sqrt{\langle s_{hh_1}s_{hh_2}^* \rangle \langle s_{vv_1}s_{vv_2}^* \rangle}} \quad (4.38)$$

wherein the only difference with (4.11) is the absence of the absolute value. The absolute value does not hold because here we have a systematic interferometric phase in the covariance elements (according to the RVOG model). Also this last relationship can be expressed in terms of the interferometric RVOG model using the cross-covariance matrix \mathbf{C}_{12} , and further assuming $\delta = 0$ for simplicity,

$$\frac{\gamma_v}{2\mu + \frac{3}{2}\gamma_v} = 1 - \frac{\mu \cos 2\alpha + \frac{1}{4}\gamma_v}{\sqrt{\mu^2(1 - \sin^2 2\alpha) + \frac{3}{2}\mu\gamma_v + \frac{9}{16}\gamma_v^2}}. \quad (4.39)$$

By varying μ and γ_v in (4.37) and (4.39), the equality should always hold for a correct reconstruction. This is tested with μ values ranging from -5 dB to 5 dB, and compared against the extreme cases of volume-only ($\mu = 0$) and surface-only ($\mu \rightarrow \infty$) scenarios. The parameter α ranges from 0 deg, to 90 deg with 15 deg step. The interferometric coherence of the volume-only component should be also set. We observe that in both equations the coherence phase does not influence the test since it is the same between the two hands of the equation. Hence, we replace the coherence by its absolute value and show two sets of plots, respectively for $|\gamma_v| = 0.8$ and $|\gamma_v| = 0.2$. In the trivial case $|\gamma_v| = 1$, there is no interferometry and the analysis falls in the simpler polarimetric case investigated by Cloude (2009). In Fig. 4.9, the results of our analysis are shown; we have labeled the left and right terms in (4.37) by F_1^{xrot} and F_2^{xrot} respectively, and the left and right term in (4.39) by F_1^{az} and F_2^{az} respectively. Some conclusions may be drawn by comparing the plots. First, looking at Fig. 4.9a, the strict validity of the linear expression (4.37) holds for $\alpha = 0$ at any μ , and for any α at $\mu = 0$. This is due to the rotation invariance of the cross-polarized terms, which is satisfied by the ground surface only for $\alpha = 0$. In practice, very small values of α and μ are allowed for the pseudo-reconstruction. The peculiarity of our development lies on the interferometric analysis. Comparing Fig. 4.9a with Fig. 4.9b we note that the effect of the interferometric coherence is to scale the values of μ along the dotted trajectories. In other words, as the coherence lowers, the same performance of the pseudo-reconstruction are obtained with decreasing values of μ . Physically, this means that the coherence of the volume layer and its backscattering properties both affect the POLINSAR symmetries of the cross-covariance matrix that we have required. If we test the alternative non-linear relationship (4.39), the considerations about the coherence apply similarly. In this case,

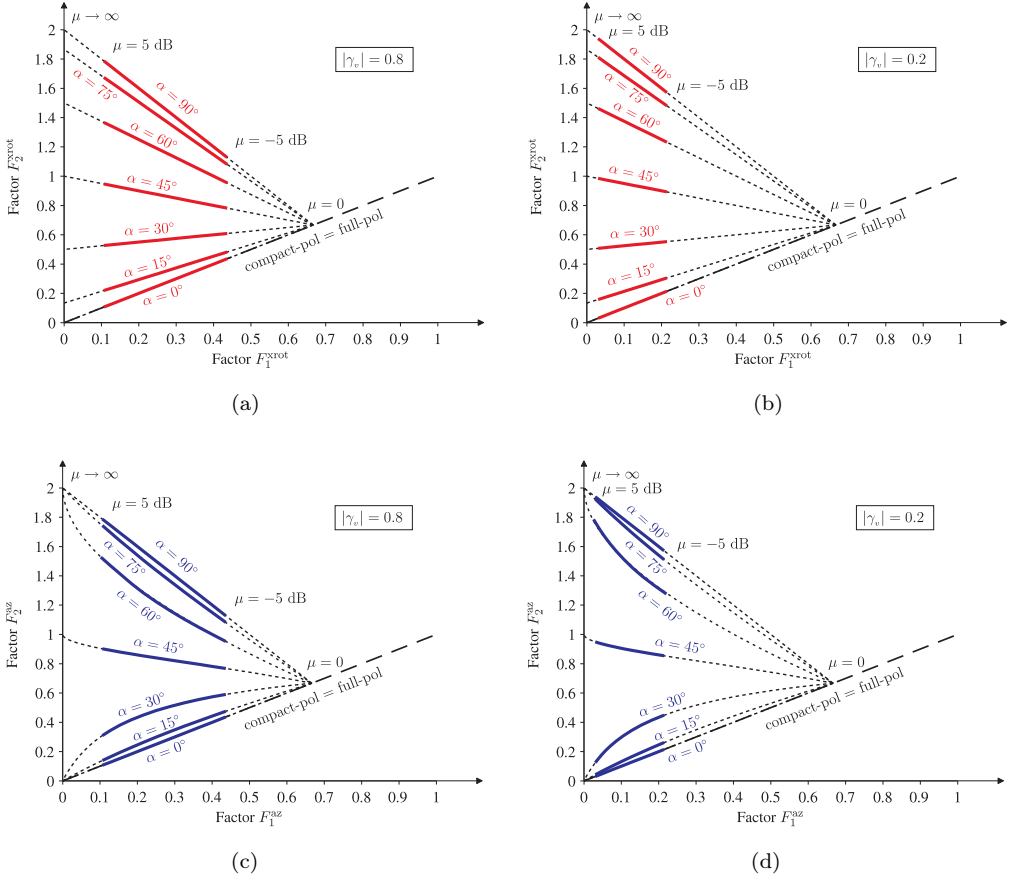


Figure 4.9: Comparison between left (F_1) and right (F_2) hands of equations (4.37) and (4.39), indicated respectively by F_i^{xrot} and F_i^{az} , $i = 1, 2$.

however, the POLINSAR reconstruction works equally well also for high values μ and $\alpha < 45$ deg (Fig. 4.9c-4.9d). It is also interesting to note that (4.37) is asymptotically close to the non-linear relation (4.39) when $\mu \rightarrow 0$, i.e. the target tends to be volume-dominated.

The analytical investigations discussed in this section confirm that a pseudo-reconstruction algorithm can exploit the complete C-POLINSAR information. The expressions already defined for compact polarimetry, can be readily extended with minor modifications to the compact POLINSAR case. Besides the violation of the symmetry assumptions, the interferometric coherence contributes to worsen the performances of the reconstruction

when its value is low. Finally, we have shown that our linear approach based on the rotational invariance of the cross-polarized terms gives similar results compared with the non-linear approach when the ratio μ/γ_v is sufficiently low.

4.3 Effects of the SAR processor and receiver

As shown in Sec. 4.1, one advantage of the polarimetric basis change is the possibility to *simulate* any combinations of polarizations on receive and transmit. All attempts made so far for assessing the performance of compact polarimetry relied on this basic principle: starting from a full polarimetric single look complex (SLC) image, a compact polarimetric dataset has been simulated applying (4.17) or (4.24). However, in a *real* scenario, it is the coherent combination of the electromagnetic energy outside the SAR system that is recorded into compact polarimetric data.

The objective of this section is to investigate the simulation of compact polarimetric data as much as possible close to the real conditions of acquisition and processing. With this goal, we consider two main aspects: (1) the synthesis of compact polarimetric data before the SAR processor and (2) the effects of the SAR receiver chain.

The first point aims at investigating whether the SAR processor affects the synthesis of compact polarimetric data. To this end, we have compared the following two approaches that simulate CP data

$$\begin{array}{ccccccc} \text{raw FP data} & \xrightarrow{\text{focusing}} & \text{slc FP data} & \xrightarrow{\text{CP synthesis}} & \text{slc CP data} \\ \text{raw FP data} & \xrightarrow{\text{CP synthesis}} & \text{raw CP data} & \xrightarrow{\text{focusing}} & \text{slc CP data} \end{array}$$

where the first line corresponds to the way followed so far in all published papers. The difference between the synthesis of compact polarimetric data *before* the focusing and the synthesis *after* the focusing depends on the processing steps performed by the SAR processor and how they are implemented. If the SAR processor executes algorithms that are linear, there must be no difference between the two approaches.

We use ALOS/PALSAR data and the ESA PALSAR Prototype Processor (Pasquali et al., 2007) to illustrate the results of this comparison. The considered processor executes a preliminary orthogonalisation of the raw data signals; then it performs the interference removal, range focusing, Doppler centroid and frequency modulation rate estimation, and finally azimuth focusing using the ω/K algorithm (Rocca, 1987; Cumming and Wong, 2005) including the data coregistration. The processor might perform non linear operations and use of high-order polynomials during data interpolation. Note that raw polarimetric channels are normally not coregistered, and to combine the polarimetric channels we should perform a preprocessing that aligns the raw samples.

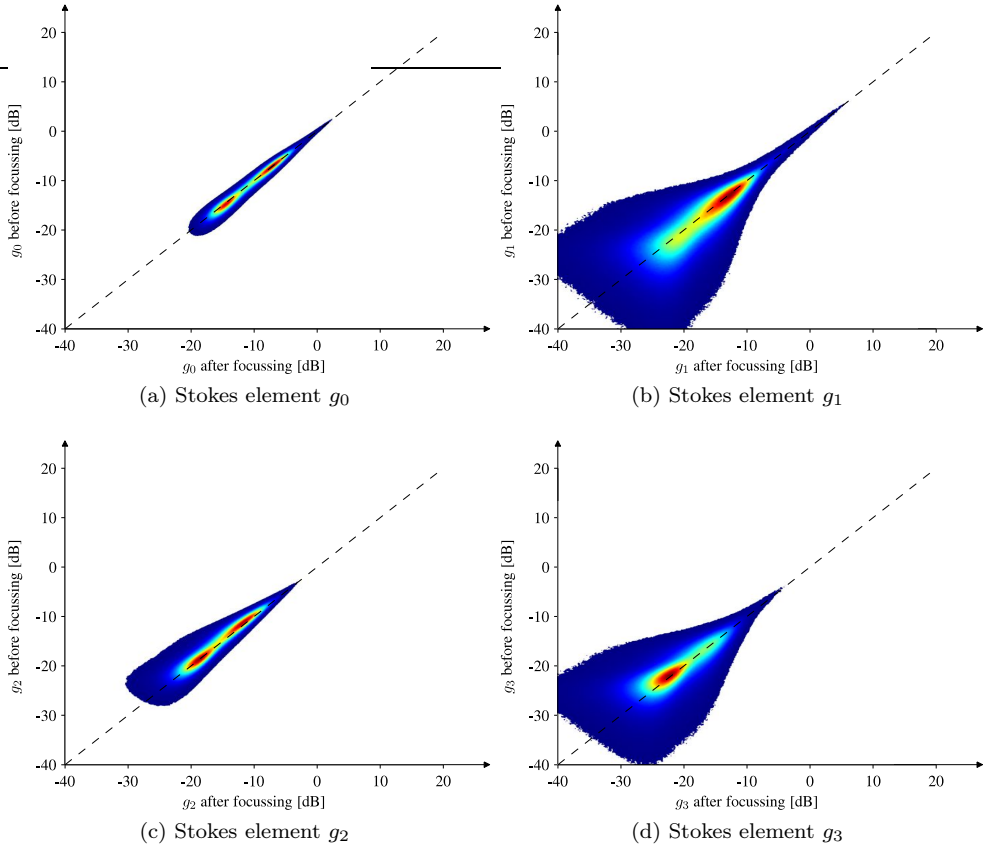


Figure 4.10: Comparison of the four Stokes parameters in the synthesis of the $\pi/4$ mode before and after the SAR focusing.

However, in the case of ALOS/PALSAR at L-band this can be disregarded at first approximation as explained in Chapter 5. In order to show the differences, we consider here the Stokes parameters mentioned in Sec. 4.1. The Stokes vector has four real elements g_i , $i = 1, 2, 3, 4$, and suffices for describing all polarimetric information of a

compact polarimetric dataset

$$g_0 = \langle |s_h(\pi/4)|^2 + |s_v(\pi/4)|^2 \rangle \quad (4.40)$$

$$g_1 = \langle |s_h(\pi/4)|^2 - |s_v(\pi/4)|^2 \rangle \quad (4.41)$$

$$g_2 = 2 \Re \langle s_h(\pi/4) s_v^*(\pi/4) \rangle \quad (4.42)$$

$$g_3 = 2 \Im \langle s_h(\pi/4) s_v^*(\pi/4) \rangle \quad (4.43)$$

where $s_h(\pi/4)$ and $s_v(\pi/4)$ are the received signal at H and V polarization respectively. Fig. 4.10 shows the comparison between pairs of Stokes elements estimated over the PALSAR scene used in Sec. 4.1, Fig. 4.3, in the two cases of CP synthesis before and after focusing. The plots show that the total power of the received wave (element g_0) and the power on the polarization components oriented at 45 deg and 135 deg (element g_2) are well preserved. The miscoregistration among polarimetric channels may be the reason for the observed deviations. The elements g_1 and g_3 that correspond respectively to the power on the H and V polarization components and on the left- and right-circular components, have lower values due to the characteristics of the scene and therefore are more subject to deviations between the two approaches. In all four cases, however, the linear fitting confirms that the synthesis of compact polarimetry before focusing yields similar results compared with the synthesis after focusing.

The second point mentioned at the beginning of the section aims at investigating the effects of the SAR receiver on the synthesis of compact polarimetric data. We limit the discussion to the case of linear 45 deg transmission, which means adding the HH and HV channels. To this end, a simplified SAR architecture similar to the receiver chain of ALOS/PALSAR is considered (Fig. 4.11). Following the antenna subsystem, the chain includes a low noise amplifier (LNA), some filters interleaved by amplifiers and a mixer for the down-conversion of the carrier frequency. The attenuators and the analogic/digital converter deserve attention in our investigation. If we consider a typical full polarimetric acquisition, the dynamic range of the cross-polarized return is usually

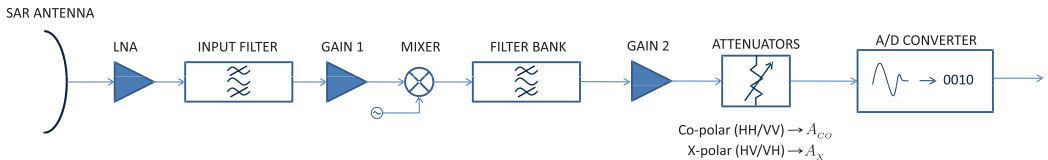


Figure 4.11: Simplified architecture of a SAR receiver chain similar to that of ALOS/PALSAR (courtesy of Dr. M. Shimada).

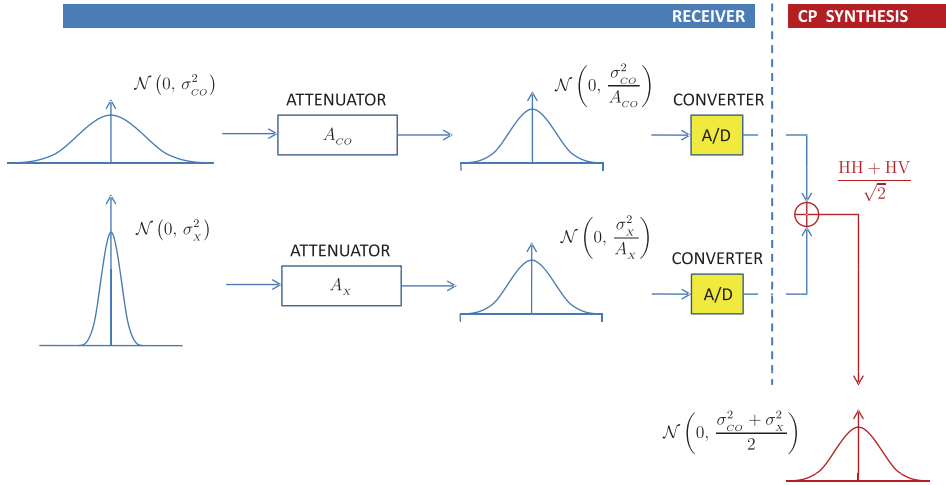


Figure 4.12: Simulation of compact polarimetric data with synthesis after coherent reception.

lower than the one of the co-polarized return. The selective attenuators for the co-polar (A_{co}) and cross-polar (A_x) signals ensure that the dynamic range is adapted for the subsequent blocks, e.g. the analogic/digital converter. In the case of ALOS/PALSAR, the attenuators differs of about 9 dB. As a consequence of the dynamic adaptation, for instance, the quantization noise is minimized.

Now, we consider the combination of polarimetric channels at the entrance of the SAR receiver and focus on the following two cases

$$\begin{array}{l}
 \text{FP echoes} \xrightarrow{\text{receiver}} \text{FP signals} \xrightarrow{\text{CP synthesis}} \text{CP signals} \\
 \text{FP echoes} \xrightarrow{\text{CP synthesis}} \text{CP echoes} \xrightarrow{\text{receiver}} \text{CP signals}
 \end{array}$$

where the second line corresponds to a real compact polarimetric scenario. As an example, we may assume that the typical distribution of the cross-polarized return has half the dynamic range of the co-polarized return, as shown in Fig. 4.12 and Fig. 4.13. In Fig. 4.12, the synthesis of compact polarimetric data is performed after the reception of full polarimetric signals. Therefore, when the HH and HV signals are added, their dynamic ranges have been already optimized for minimizing the quantization noise, and then again restored to the original range (this latter step is not shown in figure).

In a real realization of compact polarimetry operating the $\pi/4$ mode, the two signals HH and HV are mixed in a single return before being detected by the antenna. What

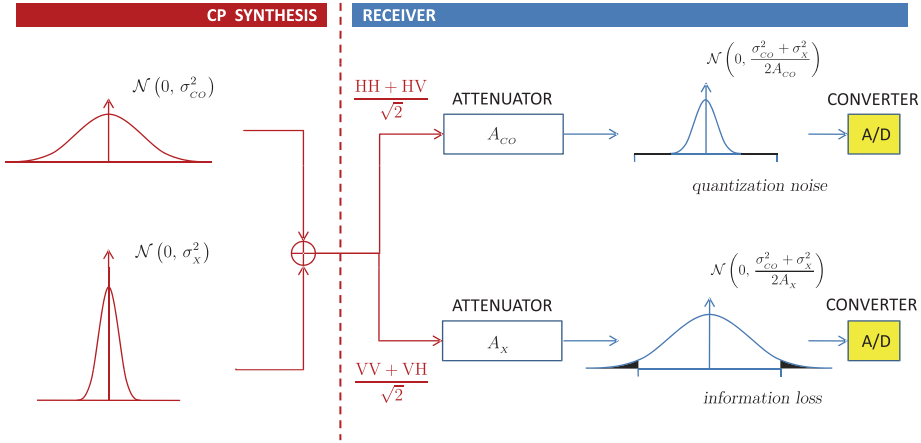


Figure 4.13: Simulation of compact polarimetric data with synthesis before coherent reception.

happens if this return passes through the receiver chain of a SAR receiver? A CP signal has a dynamic range smaller than the HH signal and bigger than the HV signal. This follows directly from the definition in (4.17). Intuitively, the attenuators must be adapted to the maximum dynamic range and hence the HV signal is somehow *hidden* in the HH signal during the analogic/digital conversion. This may increase the signal-to-quantization-noise ratio between HH and HV if no countermeasures are taken. The first observation is that the attenuators of a CP mode must be tuned differently from a classical dual polarimetric mode. If they are left unchanged, the A/D conversion will result with different performance between the two compact polarimetric channels. This is illustrated in Fig. 4.13 wherein it is evident that using $A_{CP_1} = A_{CO}$ leads to a non-optimized conversion (i.e. lower $SQNR$), and using $A_{CP_2} = A_X$ entails a loss of useful information during the conversion. A possible solution may be to choose the same attenuation value given by the average between A_{CO} and A_X . This would mitigate the effects but still does not optimize the conversion between HH and HV. As an example, if HH is digitalized by n_q bits, and HV results digitalized with half the number of bits, then according to a basic expression of the signal-to-quantization-noise ratio

$$SQNR = 3 + 6n_q \quad \text{dB} \quad (4.44)$$

the difference between HH and HV in terms of $SQNR$ would be 6 dB. Most likely, system engineers might envision more sophisticated solutions to reduce or eliminate

the effect. However, in both cases this should be taken into account when a compact polarimetric mode is designed and its advantages are presented and their performances are assessed.

4.4 Conclusions

In this chapter, we have discussed some aspects of compact polarimetry and compact polarimetric SAR interferometry. The chapter can be effectively broken into three parts. The first part dealt with compact polarimetry in general. We have provided a state of the art of compact polarimetry and presented the reconstruction algorithm that aims at recovering the full polarimetric information from a compact polarimetric dataset. The only original contribution in this section was some qualitative observations of the reconstruction for the linear-45 and the circular transmission using ALOS/PALSAR. The observations confirmed what others have already found experimentally and analytically: the compact polarimetric reconstruction can be successfully applied only to certain classes of targets. Azimuth symmetric targets are the most representative media for which best performances are expected.

In the second part, we have described our original contribution to compact polarimetry, namely its interferometric extension. We have introduced a basic formulation for compact POLINSAR and proposed two methods for reconstructing the full POLINSAR information starting from two compact polarimetric acquisitions. Both methods are based on symmetry properties and exploit the complete information of the matrix \mathbf{T}_6 or \mathbf{C}_6 . We have tested on airborne data and through the RVOG model the validity of the relationships used for the reconstruction. As an outcome, three conclusions may be drawn. First, we have now an algorithm for reconstructing the complete POLINSAR information and its formulation is a generalization of the simpler polarimetric case. This can be particularly useful for comparing full POLINSAR and compact POLINSAR. Secondly, a linear reconstruction based on the rotation invariance of the cross-polarized terms can be adopted (without loss of performance) in place of the non-linear and iterative procedure if the ratio μ/γ_v is close to zero. Third, the performances of the reconstruction from compact polarimetry and compact POLINSAR depend on the symmetry assumptions, which cannot be detected from compact polarimetric data. This is perhaps the main limitation of the reconstruction approach, since we cannot generate a sort of mask of validity.

The third part of the chapter was concerned with the correct simulation of compact polarimetric data. We have pointed out that the receiver and the SAR processor could introduce errors when polarimetric channels are added. Indeed, this issue involves all techniques in radar polarimetry that are based on the coherent combination of different polarizations. The presence of non-linearities during the SAR focusing and the increas-

ing of the quantization noise are aspects that should be investigated carefully for a complete assessment of compact polarimetry.

Chapter 5

Polarimetric calibration and Faraday rotation estimation

What we observe is not nature itself, but nature exposed to our method of questioning.

Werner Heisenberg (1901-1976)

In previous chapters, we treated some advances of the technique that combines SAR polarimetry and SAR interferometry. The true scattering matrix of the imaged target has been assumed equal to the radar output. However, as a measurement process, this output is inevitably affected by errors. Therefore, SAR instrument and SAR data must be properly *calibrated*, i.e. the radar output (i.e. the value of the image sample) must correspond really to the physical backscattered field. While the calibration of the *instrument* is normally ensured by space agencies and related industries, the calibration of the *data* is usually addressed by the community responsible for its scientific exploitation. For this reason, calibration of SAR data is an essential preprocessing step for any quantitative retrieval algorithm.

In this chapter, we discuss some aspects of the *polarimetric calibration*, i.e. the procedure that ensures correct relative values among polarimetric SAR returns. The non-ideality of the radar instrument and the anisotropy of the ionosphere are major causes for polarimetric distortions in space-borne SAR data. They affect both dual and full polarimetric data. In the following, we describe in more detail the polarimetric data calibration problem (Sec. 5.1) and propose a new approach for compensating for the effects of the ionosphere (Sec. 5.2). Finally, in Sec. 5.3, two strategies for calibrating dual polarimetric data are presented and assessed for the future ESA mission SENTINEL-1.

5.1 Background

Earlier SAR data, such as those acquired by SEASAT, were exploited mainly with a qualitative approach. Hence, data calibration was not a priority for space agencies and

scientists. With the second generation of SAR satellites in 1980s and 1990s, data calibration became an important step (Freeman, 1992a) needed by the rapid development of SAR applications. Nowadays, calibration and validation of SAR data is the initial task performed after launch (and before the distribution of the data) and is timely performed over the whole mission life. We recognize three main reasons that justify the use of well-calibrated SAR data. First, relating the pixel intensity to the backscattered power is clearly essential for the quantitative analysis of the Earth's surface. Second, the use of multi-channels data requires the complex amplitude (including the relative phase) to be correctly assessed. Third, the emerging data fusion techniques that combine SAR data from different missions require a common quantity being measured and stored in the image pixel.

Among several types of multi-channel data, we focus here on single-acquisition polarimetric data, therefore on the polarimetric data quality. An interferometric calibration would also make sense, as well as a POLINSAR calibration. Indeed our discussion brings direct benefits to the POLINSAR technique, although its calibration is not addressed in all aspects¹. As mentioned before, the SAR system and the ionosphere are at the origin of the space-borne polarimetric distortions. In Fig. 5.1, it is sketched the acquisition process along with the sources of miscalibration. The case of H-transmission is shown; the V-transmission has an identical diagram. Following the generation of the waveform to be transmitted, the five blocks shown in figure affect the polarimetric characteristics of the waveform and the value at the output of the receiver. Each block is characterized by a complex matrix that distorts the transmitted signal. Obviously, in our case, the target (i.e. the scattering matrix) is a source of information rather than an unwanted distortion. On the contrary, matrices \mathbf{T} , \mathbf{R} (transmitter/receiver) and \mathbf{F} (ionosphere) need to be *removed* as much as possible from the radar output to extract the true scattering matrix. The procedures to remove the effects of these matrices are named respectively *radiometric polarimetric calibration* (or, simply, polarimetric data calibration) and *Faraday rotation correction*. They are introduced in the following two sections.

5.1.1 Polarimetric data calibration

Given a full polarimetric acquisition, some system distortion parameters² can be identified for their inclusion in a calibration model. These parameters account for the

1. For instance, in repeat-pass interferometry the stability over the time of the calibration parameters should be also included in the calibration. Similarly, in a single-pass scenario the interference caused by the second transmitter/receiver should be taken into account for a correct calibration.

2. In the following, we indicate indifferently distortion parameters as calibration parameters and vice versa. The distinction is only conceptual, based on their use into distortion models or calibration procedures.

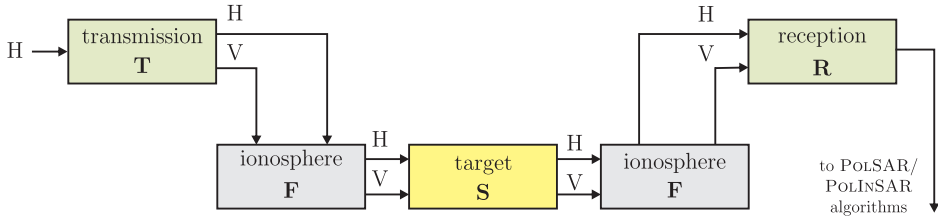


Figure 5.1: Logical scheme of the SAR acquisition process showing the sources of polarimetric distortions (system transmission/reception and ionosphere) and the associated matrices (\mathbf{T} , \mathbf{R} and \mathbf{F}).

instrument *cross-talk* and *channel imbalance*. The former denotes the lack of perfect isolation between the polarimetric chains, hence a signal component is transferred between the polarimetric channels. The latter indicates the mismatch in amplitude and phase between the transmitted (or received) H and V components. Several calibration procedures have been proposed in literature to cope with these polarimetric distortions (van Zyl, 1990; Freeman, 1992b; Quegan, 1994; Ainsworth et al., 2006). We do not expose here in detail these procedures: they are all based on the identification of symmetric targets (as described in Chapter 4) and in exploiting the relationships among the covariance elements to estimate the calibration parameters.

Instead, there is an interesting aspect of the polarimetric calibration that deserves investigation. Most of the polarimetric SAR missions launched so far operated the full polarimetric mode and, in addition, dual and single polarimetric modes. Much effort has been dedicated to calibrate full-pol data with only minor attention to the polarimetric calibration of dual-pol data. Indeed, the calibration of dual-pol data for those sensors that operate *also* in quad-pol mode is straightforward. Assuming that the system characteristics do not change from dual-pol to quad-pol acquisition, the calibration of the HH/HV mode (or VV/VH mode) is performed using the same receiving distortion matrix estimated from quad-pol data. However, when the SAR sensor operates only a single- or a dual-pol mode (like the future mission SENTINEL-1), the calibration procedure must be adapted and the calibration parameters estimated using dual-pol data.

To this end, we have studied the response of particular passive point targets according to a dual-pol calibration model that we derived from the full-pol distortion model developed by Freeman (1992b). The feasibility of calibrating dual-pol data, HH/HV (or VV/VH), is discussed in Sec. 5.3. The final aim of the study is to propose a polarimetric calibration procedure for dual-pol SAR data such as those of the C-band SENTINEL-1.

5.1.2 Faraday rotation correction

A second important effect that superimposes to the previous one is related to the medium in which the electromagnetic field travels, i.e. the atmosphere, rather to system issues. A radio wave propagating through the ionosphere undergoes *Faraday rotation* (FR), i.e. the rotation of its polarization plane. Faraday rotation is caused by the anisotropy of the ionospheric tenuous plasma in presence of a persistent magnetic field and can significantly affect the quality of polarimetric SAR data. Propagation in an anisotropic medium is not reciprocal, hence the HV return deviates from VH return, causes errors in the estimation of polarimetric calibration parameters and therefore impacts current POLSAR/POLINSAR applications. SAR sensors, such as ALOS/PALSAR, that operate at L-band, are more affected by Faraday rotation than higher frequency SAR systems, as evident from (5.2). Once detected and estimated, FR must be compensated over the SAR scene. Apart from the use of reference point targets, such as *triangular corner reflectors*, Faraday rotation angle can be

estimated from full-pol data by considering the difference between the cross-polarized acquisitions HV and VH (Freeman, 2004);

estimated from full-pol data by simulating the circularly polarized wave in transmission and reception (Bickel and Bates, 1965);

predicted from model simulations using real measurements of total electron content (TEC) in the ionosphere.

In previous works, the first two approaches above have been applied to each sample of *focused SLC data*. Hence, they have high spatial accuracy, but rely on the phase and cross-talk calibration of the SLC data (Quegan, 1994). The third approach makes use of external information (TEC maps) that usually has lower spatial resolution. In our work, we argue that the estimation of the Faraday rotation from SAR data is more appropriate using *unfocussed raw data* than SLC data. Since the FR is estimated from a single received echo, this approach has a better physical justification and some practical advantages (and disadvantages).

In the next section, we describe the procedure for estimating FR from raw data and show the results of an extensive analysis over more than 30 scenes acquired by ALOS/PALSAR. In addition, our analysis indicates low values of Faraday rotation angle (lower than 8 deg) for ALOS/PALSAR acquisitions, acceptable for current polarimetric applications (Wright et al., 2003b). This value, however, might increase in the next years because of the cyclic solar activity that increases the average TEC in the ionosphere (CODE, 2009).

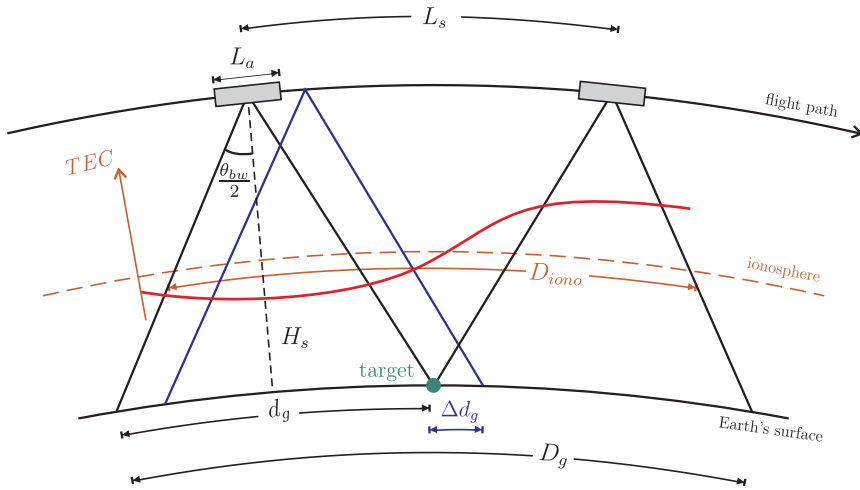


Figure 5.2: Synthetic aperture and ionospheric effect. In the case of ALOS/PALSAR $D_{iono} = 27$ km, $d_g = 16$ km and $\Delta d_g = 1.8$ m.

5.2 Faraday rotation from unfocussed SAR data

As discussed previously, two methods have been published for detecting and estimating Faraday rotation from SAR data (Bickel and Bates, 1965; Freeman, 2004). Several studies have also been conducted for assessing the effects of ionosphere, and in particular of Faraday rotation, on ALOS/PALSAR data (Meyer and Nicoll, 2007; Wright et al., 2008). All these works are based on the estimation of Faraday rotation from focused SLC data. Our key idea is to estimate Faraday rotation from unfocussed raw data rather than focused SLC data. This approach is motivated by a fundamental observation: Faraday rotation originates and occurs in the ionosphere, and does not depend on the imaged target. It suggests that necessary information for detecting and estimating Faraday rotation is embedded in the raw data. Moreover, focusing algorithms might corrupt this information leading to wrong results. The details of our method as well as its advantages are discussed in the next section. We illustrate the results using ALOS/PALSAR data and the ESA ALOS/PALSAR Prototype Processor Pasquali et al. (2007).

5.2.1 Unfocussed Faraday rotation model

As mentioned in Sec. 5.1, Faraday rotation and system-induced distortions combine with similar effects in polarimetric SAR imagery. To a certain extent, the system can be realized so that cross-talk and channel imbalance are significantly lower than ionospheric effects. Hence, in presence of high Faraday rotation, system distortions are often negligible. If this is not the case, system distortions can be estimated first on several acquisitions with expected low Faraday rotation. Then, as the system is assumed more stable than ionospheric effects, the calibration matrices can be applied before the estimation of Faraday rotation. This latter approach is commonly used by the ALOS/PALSAR Quality Working Group at ESA (Wright et al., 2008). In the following, we assume that the system distortions have been compensated. The relationship between the measured scattering matrix \mathbf{M} of the target and true scattering matrix \mathbf{S} subject to Faraday rotation can be expressed by (disregarding the additive noise)

$$\mathbf{M} = \mathbf{F} \mathbf{S} \mathbf{F} = \begin{pmatrix} \cos \Omega & \sin \Omega \\ -\sin \Omega & \cos \Omega \end{pmatrix} \begin{pmatrix} s_{hh} & s_{hv} \\ s_{vh} & s_{vv} \end{pmatrix} \begin{pmatrix} \cos \Omega & \sin \Omega \\ -\sin \Omega & \cos \Omega \end{pmatrix}. \quad (5.1)$$

Matrix \mathbf{F} carries the information of rotation of the scattering matrix and contains the Faraday rotation angle Ω . The knowledge of Ω entails the full knowledge of Faraday rotation and the possibility to compensate for it. For a better physical understanding of the phenomenon, we report hereafter the expression of Ω in terms of ionospheric characteristics and the SAR observation geometry (Wright et al., 2003b)

$$\Omega = \frac{K}{f^2} B \cos \psi \sec \theta \text{TEC} \quad (5.2)$$

wherein the frequency f appears at denominator, K is a constant of value 2.365×10^4 in S.I. units, B is the magnitude of the Earth magnetic field, angles ψ and θ express the relative orientation of the magnetic field with the wave propagation direction, and TEC is the total electron content of the ionosphere. Eq. (5.2) is used to predict Faraday rotation without using SAR data. The magnetic field is usually known from specific models and the spatial distribution of the TEC is measured by GNSS network (CODE, 2009). The same expression may be adopted for generating TEC maps from SAR data, once Ω is known. We note also that Ω depends directly on the TEC in the ionosphere, therefore a spatial or temporal variation of electron content during the acquisition may deform the polarimetric characteristics within the scene. This condition is depicted in Fig. 5.2 with the simplified acquisition scenario of ALOS/PALSAR. Fundamental parameters of this scenario are the *real aperture length* of the antenna $L_a \simeq 9$ m, the central wavelength $\lambda \simeq 0.23$ m, the satellite velocity $V_s \simeq 7.6$ km/s and the satellite alti-

tude $H_s \simeq 700$ km. The look angle is $\theta \simeq 23$ deg and the squint angle is assumed equal to zero. From these parameters it follows that the azimuth beamwidth of PALSAR is $\theta_{bw} = 0.886\lambda/L_a \simeq 1.3$ deg, and the azimuth footprint is $d_g = 2H_s \tan(\theta_{bw}/2) \simeq 16$ km. In the figure, it is shown how a target on the Earth's surface is illuminated by the moving SAR antenna during the *exposure time*³ T_a . The distance covered by the spacecraft during this time, i.e. the *synthetic aperture length*, is $L_s \simeq 18$ km. In terms of ground surface, the total distance illuminated by the SAR is $D_g = 2d_g \simeq 32$ km, which corresponds to $D_{iono} \simeq 27$ km in the ionosphere⁴. This means that, when the raw echoes are integrated by the SAR focuser, the effects of 27 km of ionosphere collapse into a single SLC image pixel. It appears evident that, if there is a spatial variation of TEC, then the focused sample might be affected. In addition, the estimated Faraday rotation map results with low resolution due the long synthetic aperture. Hence, it would be preferable to detect, estimate and correct Faraday rotation from unfocused raw data. Finally, note that the impact of ionosphere on the SAR focusing is known mainly concerning the range delay, which induces a spatial shift of the targets among sub-looks (Meyer and Nicoll, 2007). The effect that we point out here concerns the polarimetric signature of the targets, which are threatened by the variation of Faraday rotation. This effect stimulated the following development (Lavalle et al., 2009).

Let us consider a polarimetric raw SAR image, i.e. a succession of samples arranged in terms of slow- and fast-time coordinates, instead of the more familiar range and azimuth coordinates. Each sample corresponds to the energy backscattered by the real antenna footprint and coherently recorded by the SAR receiver. In this sense, according to the definitions of Chapter 2, each raw data sample contains a scattering matrix. Indeed, from an electromagnetic point of view, the pure scattering matrix that relates the transmitted wave to the received wave is embedded in the raw data more than SLC data. The SLC scattering matrix is rather an artificial (i.e. synthesized through signal processing) representation of the backscattering process.

However, as consequence of the interleaved pulse transmission, the H-transmission is slightly delayed from the V-transmission by $PRF/2$, where PRF is the *pulse repetition frequency*. This suggests that, before manipulating polarimetric raw samples as scattering matrices, we should co-register the polarimetric channels. From Fig. 5.2, each raw sample corresponds to the ground distance defined by the PALSAR azimuth footprint, i.e. $D_g \simeq 18$ km. While the sensor moves along its path flight, H- and V-transmissions

3. The target exposure time defines how long the target stays in the 3-dB beam limits of the SAR antenna. In the case of ALOS/PALSAR, the exposure time is $T_a \simeq 2.4$ s.

4. This value is derived by simple geometrical considerations on Fig. 5.2, assuming the altitude of ionosphere H_{iono} corresponding to the maximum TEC (Meyer and Nicoll, 2007). Also, the effect of the *range migration* is not considered and contributes to stretch the total distance traveled by the SAR return in the ionosphere.

are interleaved every $T_i = 1/(2PRF) \simeq 261 \mu s$. It follows that the ground portions imaged by H and V differ by only $\Delta D_g = T_i V_s k_g \simeq 1.8$ m, where k_g is a coefficient accounting for the decreased velocity of the ground footprint compared to the satellite velocity⁵. This difference is considerably smaller than the azimuth footprint, hence the imaged target can be considered unchanged with good approximation and the raw polarimetric channels co-registered⁶. The visual inspection of PALSAR raw data confirms this statement.

The model of Faraday rotation (5.1) applies straightforward to raw data, and it is even more appropriate since we consider each received echo and not the focused scattering matrix. The relationship between the raw scattering return \mathbf{W} and the true scattering return \mathbf{R} is

$$\mathbf{W} = \mathbf{F} \mathbf{R} \mathbf{F} \quad (5.3)$$

or, in expanded form,

$$\begin{pmatrix} w_{hh} & w_{hv} \\ w_{vh} & w_{vv} \end{pmatrix} = \begin{pmatrix} \cos \Omega & \sin \Omega \\ -\sin \Omega & \cos \Omega \end{pmatrix} \begin{pmatrix} r_{hh} & r_{hv} \\ r_{vh} & r_{vv} \end{pmatrix} \begin{pmatrix} \cos \Omega & \sin \Omega \\ -\sin \Omega & \cos \Omega \end{pmatrix} \quad (5.4)$$

wherein w_{pq} and r_{pq} , $p, q = h, v$ are the measured and true raw scattering returns respectively. Since the model is formally the same compared to the SLC approach, we estimate the Ω angle in the same way as proposed by Bickel and Bates (1965)

$$\Omega = \frac{1}{4} \arg(w_{lr} w_{rl}^*) \quad (5.5)$$

where w_{lr} and w_{rl} are respectively the left-right and right-left polarized scattering elements of the \mathbf{W} matrix

$$\begin{pmatrix} w_{ll} & w_{lr} \\ w_{rl} & w_{rr} \end{pmatrix} = \begin{pmatrix} 1 & j \\ j & 1 \end{pmatrix} \begin{pmatrix} w_{hh} & w_{hv} \\ w_{vh} & w_{vv} \end{pmatrix} \begin{pmatrix} 1 & j \\ j & 1 \end{pmatrix} \quad (5.6)$$

that can optionally be averaged on several samples to reduce the effects of the noise. In the next section, expressions (5.5)-(5.6) are tested over a sample scene acquired by ALOS/PALSAR and the results are discussed by outlining the advantages.

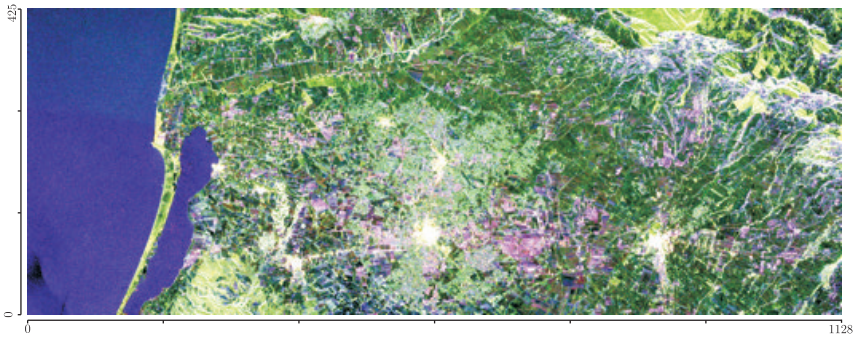
5. The sweep velocity of the PALSAR footprint on the ground is about 10% lower than the actual satellite velocity in ALOS. The coefficient can be calculated from geometrical considerations, yielding $k_g = R_e/(H_s + R_e)$, wherein R_e is the mean Earth's radius.

6. An alternative strategy that would lead to co-registered polarimetric raw channels, is the backward focusing. In practice, the user can perform a simple and linear forward focusing, co-register the SLC pairs, and perform a backward focusing.

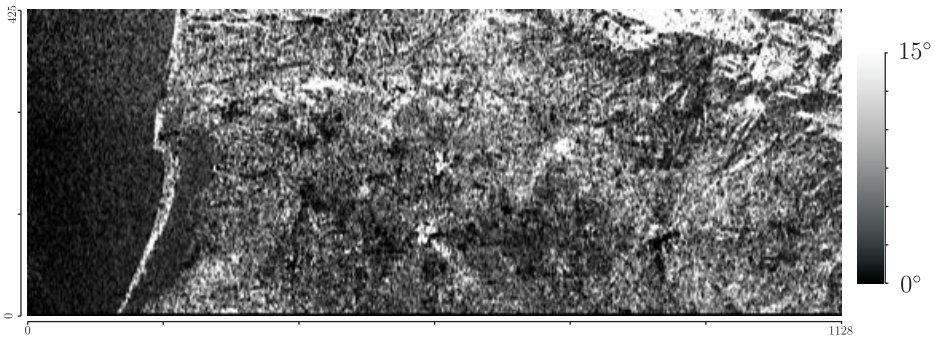
5.2.2 PALSAR data observations

In order to show the effectiveness of the method described in the previous section, we have conducted two separate tests using PALSAR data. The first is a case study, i.e. a detailed analysis over a single scene with relatively high Faraday rotation. The second is an extensive analysis over about 30 products, based on the mean value of Faraday rotation estimated in the scene.

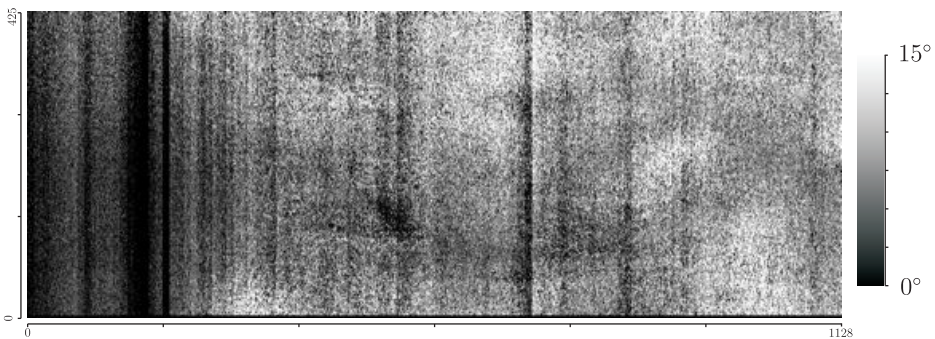
The objective of the first test is to investigate whether the estimation of Faraday rotation from raw data gives different results within the scene compared to the usual approach. With this aim, we have found a polarimetric dataset with relatively high Faraday rotation acquired over South Italy in April 2008 at 10:15 local time. Both raw and SLC data are considered, in order to apply pixelwise (5.5) and to compare the results along range and azimuth directions. Fig. 5.3 shows the Pauli image associated with the SLC dataset. The scene is dominated by hilly vegetated areas. Sea surface and urban areas are also present and this may affect the estimation at L-band. Indeed, the presence of areas with low SNR may lead to wrong estimation of Faraday rotation and the presence of interference with ground radars can severely corrupt the data. In the same figure, the two maps of Faraday rotation estimated from SLC data and raw data are shown. They are obtained directly by averaging (5.1) over 7×7 pixels and 15×15 pixels, on raw and SLC data respectively. A preprocessing of raw data has been performed for gain/offset compensation and interference removal. The first operation is a linear shift and scaling of the pixel values for co-polar and cross-polar data. The second processing aimed at removing the in-band and out-band interferences that occur at L-band. Comparing the two maps, the method for estimating the Faraday rotation angle seems to depend on the focused target on the Earth's surface (in this particular example). Nevertheless, the estimated mean value of FR angle from SLC data is about 8.3 deg and from raw data is about 8.4 deg (cf. Fig. 5.4a). A qualitative inspection of the histograms in Fig. 5.4a also suggests that a Gaussian distribution is more appropriate for modeling Ω estimated from raw data. The standard deviation of the estimates is 0.93 deg from SLC and 0.85 deg from raw data. The accordance of the two values in this case study confirms that the PALSAR SAR processor does not corrupt the *mean* estimation of Faraday rotation. However, the local variations of FR angle estimation are also of interest. Fig. 5.4b and Fig. 5.4c show the averaged range and azimuth profiles respectively. Range profiles are almost preserved in the focusing process and FR estimation. Azimuth profiles have also a mean value around 8 deg, but show local deviations. They may be due to pixels corrupted by interferences that have not been interpolated (as done in the focuser). One example of such variation is centered on the row 200 in Fig. 5.4c. Another reason may be the rapid spatial variation of TEC in the ionosphere, but we disregard this possibility since in Fig. 5.3c the transitions appear net and clear along the range direction.



(a) Pauli decomposition



(b) Faraday rotation angle estimated from SLC data



(c) Faraday rotation angle estimated from raw data

Figure 5.3: Full polarimetric image acquired by ALOS/PALSAR over South Italy. Note the features in the Faraday rotation angle estimated from SLC data.

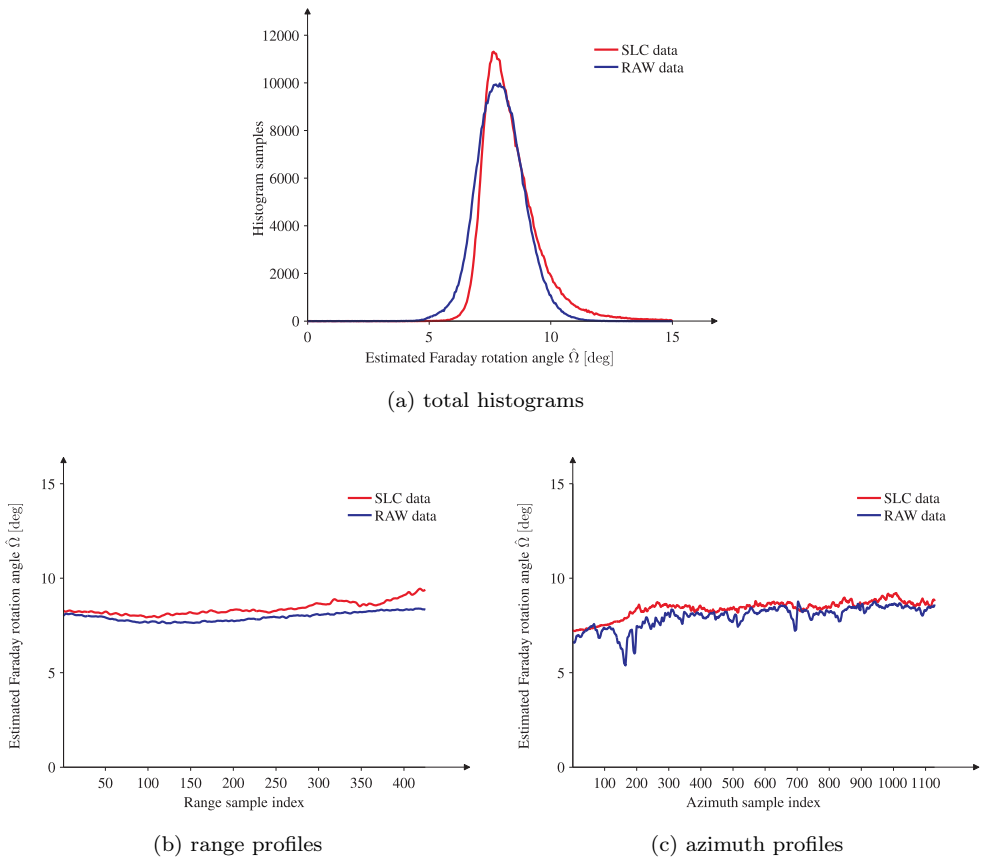
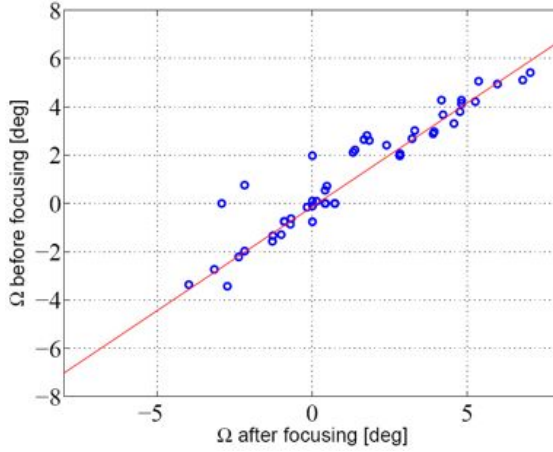
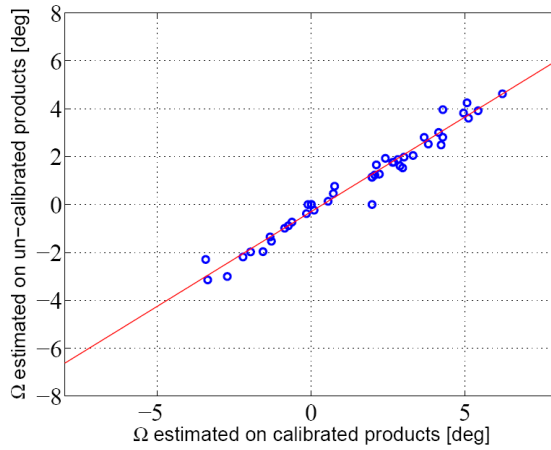


Figure 5.4: Comparison of Faraday rotation angle estimated from SLC data and raw data using the PALSAR product of Fig. 5.3. Histograms and profiles averaged along range and azimuth directions are shown.

The same procedure described above have been applied to an extensive analysis over more than 30 PALSAR products. Fig. 5.5a illustrates the comparison between the FR angle estimated from SLC and raw data. The linear trend confirms that the mean estimate of FR from raw data is in good agreement with the mean value of the FR angle estimated from SLC data. In the analysis above, the system has been considered calibrated, i.e. the polarimetric distortion matrices on receive and transmit has been neglected. Fig. 5.5b shows the Faraday rotation estimates from calibrated and un-calibrated SLC data and confirms the good calibration conditions of the PALSAR system.



(a) impact of the SAR processor



(b) impact of the calibration matrices

Figure 5.5: Extensive analysis over several PALSAR products for the assessment of the effects of the SAR processor (a) and the effects of the polarimetric calibration matrices (b).

As an outcome, we identify some advantages in estimating FR from unfocussed raw data instead of SLC data.

1. Received echoes travel through different portions of the ionosphere, they are potentially affected by different FR angles and their integration in the SAR processor might lead to wrong estimation of FR when performed from SLC data.
2. As consequence of the long synthetic aperture at lower frequency, several pulses contribute to the focused target. If rapid spatial variations of TEC in the ionosphere are present, the polarimetric characteristics of the targets may be corrupted.
3. Some operations in the SAR processor can be nonlinear with respect to the polarimetric channels and this might corrupt the estimation of FR angles from SLC data.
4. The spatial distribution of TEC in the ionosphere corresponds more closely to the raw data than SLC data and hence the generation of TEC map is more realistic.
5. Faraday rotation can be estimated and corrected before any operations in the ground segment, without need to generate necessarily SLC data. This, for instance, would save time when detected products are requested.
6. The simplicity of the method makes it fast to implement. Programming code already designed for SLC can be easily reused for raw data.

Despite the encouraging results, we recognize some weak points of the proposed method.

1. For a faster implementation, we have disregarded the delay between H- and V-transmission. In order to co-register raw data, specific algorithm should be designed for the purpose.
2. The effects of the calibration matrix may not be negligible. Polarimetric system distortions are usually calculated on SLC data. Even if they can be removed easily from raw data, it is not ensured that the calculated values agree.
3. Selecting appropriate targets in the scene, such as those respecting reflection symmetry or high SNR, may be difficult on raw data, which indeed is an average of all these targets.

Further investigations over test sites with known Faraday rotation are in progress in the radar geoscience community. In particular, some acquisitions over Alaska have been used for crosschecking the results and would serve to test our approach. Finally, we remark that future and proposed missions such as TERRASAR-L, BIOMASS, DESDynI and SAOCOM that operate at lower frequencies may benefit from the estimation and correction of Faraday rotation from raw data.

5.3 Dual Polarimetric calibration model

In this section, we discuss the radiometric calibration of dual polarimetric SAR data (Lavalle et al., 2008, 2009). We have reduced the full-pol distortion model to the dual-pol case. This dual-pol formulation includes four calibration complex parameters: the cross-talk on transmit, the receiving channel imbalance and two receiving cross-talks. While these parameters can be estimated in a full-pol system using distributed targets with reflection symmetry, we show hereafter that the absolute and polarimetric calibration of a dual-pol mode requires a *trihedral-like* and an *oriented dihedral-like* response inside the SAR scene, plus a distributed target having azimuthal symmetry. An alternative approach might use two *gridded trihedrals* in place of the distributed target and the dihedral. For both approaches, we derive the expression of the distortion parameters and assess the performance using the system characteristics of SENTINEL-1. The reciprocity assumption between transmit and receive is not needed. It will be shown that gridded trihedrals are more appropriate for the dual-pol calibration since they have low polarimetric noise compared with the calibration requirements.

5.3.1 Calibration distortion model

The distortion model of a dual-pol acquisition mode can be directly derived from a quad-pol distortion model under some assumptions. The direct output of a full polarimetric SAR is the uncalibrated 2-by-2 complex matrix \mathbf{M} . Ignoring the system noise, \mathbf{M} is related to the true scattering matrix \mathbf{S} by the following model (Freeman, 1992a)

$$\mathbf{M} = Ae^{j\varphi} \mathbf{R} \mathbf{F} \mathbf{S} \mathbf{F} \mathbf{T} \quad (5.7)$$

which can be expanded as

$$\mathbf{M} = Ae^{j\varphi} \begin{pmatrix} 1 & \delta_2 \\ \delta_1 & f_1 \end{pmatrix} \begin{pmatrix} \cos \Omega & \sin \Omega \\ -\sin \Omega & \cos \Omega \end{pmatrix} \begin{pmatrix} s_{hh} & s_{hv} \\ s_{vh} & s_{vv} \end{pmatrix} \begin{pmatrix} \cos \Omega & \sin \Omega \\ -\sin \Omega & \cos \Omega \end{pmatrix} \begin{pmatrix} 1 & \delta_3 \\ \delta_4 & f_2 \end{pmatrix} \quad (5.8)$$

wherein \mathbf{R} and \mathbf{T} are the receive and transmit distortion matrices that include the complex cross-talks $\delta_1, \delta_2, \delta_3, \delta_4$ and channel imbalances f_1 and f_2 , matrix \mathbf{F} contains the Faraday rotation angle Ω , A is the absolute calibration factor and φ an irrelevant phase.

We can follow the same approach that led to (5.8) to derive the distortion model of a dual-pol mode. Let us consider the case of H-transmission by multiplying (5.8) by the vector $(1 \ 0)^T$. The following considerations apply similarly to the V-transmission case with minor modifications. If we focus on C-band and ignore the Faraday rotation

for the moment, the distortion model becomes

$$\begin{pmatrix} M_{hh} \\ M_{vh} \end{pmatrix} = Ae^{j\varphi} \begin{pmatrix} 1 & \delta_2 \\ \delta_1 & f \end{pmatrix} \begin{pmatrix} s_{hh} & s_{hv} \\ s_{vh} & s_{vv} \end{pmatrix} \begin{pmatrix} 1 \\ \delta_3 \end{pmatrix} \quad (5.9)$$

Equation (5.9) represents the dual-pol calibration model when the SAR transmits an H-polarized wave and receives on both H and V channels. To invert the model and calibrate a single dual-pol mode, four complex unknowns must be estimated: $\delta_1, \delta_2, \delta_3$ and f . In the case of V-transmission, the only parameter that might change is δ_3 since it is a measure of the transmit cross-talk.

5.3.2 Targets

To estimate the parameters in (5.9), we examine some particular targets within the SAR scene. We consider distributed targets with reflection symmetry or azimuthal symmetry (Nghiem et al., 1992), such as flat surfaces or forests, and man-made point targets, such as trihedrals, dihedrals and gridded trihedral corner reflectors.

Distributed targets

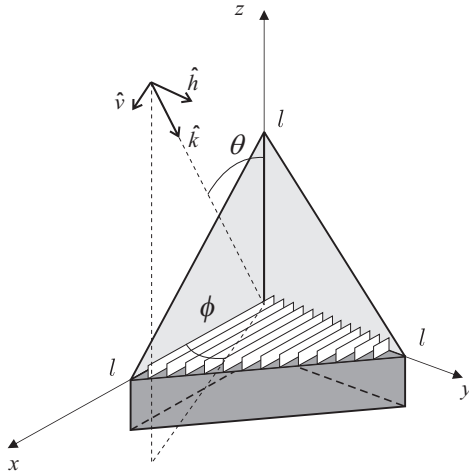
The estimation of the distortion parameters from distributed targets is based on the second order statistics of the measured scattering matrix. In the dual-pol case, only three observables are available $O_{11} = \langle |M_{hh}|^2 \rangle$, $O_{12} = \langle M_{hh} M_{vh}^* \rangle$ and $O_{22} = \langle |M_{vh}|^2 \rangle$, where M_{hh} and M_{vh} are from (5.9)

$$\begin{aligned} M_{hh} &= Ae^{j\varphi} (s_{hh} + \delta_3 s_{hv} + \delta_2 s_{vh} + \delta_2 \delta_3 s_{vv}) \\ M_{vh} &= Ae^{j\varphi} (\delta_1 s_{hh} + \delta_1 \delta_3 s_{hv} + f s_{vh} + f \delta_3 s_{vv}) \end{aligned} \quad (5.10)$$

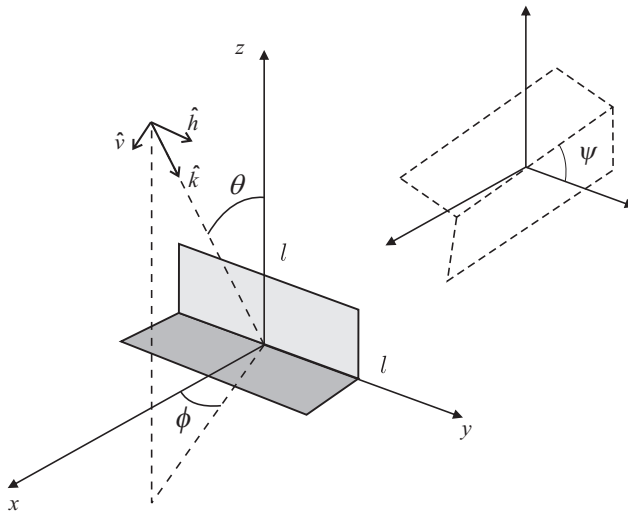
The previous expressions, apart from the absolute constant factor, contain 9 complex unknowns. To reduce the number of unknowns, we consider a target having reflection symmetry. This assumption entails the reciprocity condition ($s_{hv} = s_{vh}$) and that the correlation between like- and cross-polarized waves is small compared with the other elements of the covariance matrix. By expanding the unknowns at first order, from (5.10) we obtain

$$\begin{aligned} O_{11} &\simeq \langle |s_{hh}|^2 \rangle \\ O_{12} &\simeq \delta_1^* \langle |s_{hh}|^2 \rangle + \delta_3^* f^* \langle s_{hh} s_{vv}^* \rangle + (\delta_3 + \delta_2) f^* \langle |s_{vh}|^2 \rangle \\ O_{22} &\simeq |f|^2 \langle |s_{vh}|^2 \rangle \end{aligned} \quad (5.11)$$

where we have omitted the absolute calibration factor since it does not influence the polarimetric calibration. Using a reflection symmetric target, the number of unknown elements containing the elements of the scattering matrix \mathbf{S} is equal to the number of



(a) Gridded trihedral



(b) Dihedral

Figure 5.6: Targets proposed for the polarimetric calibration of a dual-pol SAR data. The gridded trihedral is depicted with the modification proposed by Ainsworth (2008).

observables. This means that it is not possible to estimate any distortion parameters using a distributed target possessing reflection symmetry.

By considering azimuthal symmetry, instead, we can add the relationship $\langle s_{hh}s_{vv}^* \rangle = \langle |s_{hh}|^2 \rangle - 2\langle |s_{vh}|^2 \rangle$, so that (5.11) becomes

$$\begin{aligned} O_{11} &\simeq \langle |s_{hh}|^2 \rangle \\ O_{12} &\simeq (\delta_1^* + \delta_3^* f^*) \langle |s_{hh}|^2 \rangle + (\delta_3 f^* + \delta_2 f^* - 2f^* \delta_3^*) \langle |s_{vh}|^2 \rangle \\ O_{22} &\simeq |f|^2 \langle |s_{vh}|^2 \rangle \end{aligned} \quad (5.12)$$

System (5.12) contains four real observables (three real and one imaginary) and two real terms related to the scattering matrix, i.e. $\langle |s_{hh}|^2 \rangle$ and $\langle |s_{vh}|^2 \rangle$. It follows that a distributed target having azimuthal symmetry can be used to estimate one complex distortion parameter. For instance, cross-talks can be measured pre-launch and (5.12) can be solved for the channel imbalance f . However, without any assumptions, system (5.12) reduces to the equation

$$|f|^2 \delta_3^* O_{11} + f(\delta_1^* O_{11} - O_{12}) + (\delta_2 + \delta_3 - 2\delta_3^*) O_{22} = 0 \quad (5.13)$$

Eq. (5.13) has four unknowns, hence we need three additional equations to calculate the distortion parameters. We also note that if (5.13) is solved for f , two solutions exist. One way to solve the ambiguity is to consider the average, which is equivalent to set up the condition $(\delta_3^* + \delta_2 - 2\delta_3^*) \langle |s_{vh}|^2 \rangle \simeq 0$, usually true in practice at C-band.

Point targets

If a point target with an ideal pure co-polar return is available, an additional equation using its cross-polar response can be used for the dual-pol calibration. A common example is the trihedral corner reflector with the ideal response shown in Tab. (5.1). Inserting the trihedral ideal response into (5.9), we obtain two equations

$$M_{hh}^t = A_{cf} A_t e^{j\phi_t} (1 + \delta_1 \delta_3) \simeq A_{cf} A_t e^{j\phi_t} \quad (5.14)$$

$$M_{vh}^t = A_{cf} A_t e^{j\phi_t} (\delta_1 + f \delta_3) \quad (5.15)$$

where M_{hh}^t and M_{vh}^t are the complex scattering returns on the co-polar and cross-polar channels respectively and $A_t e^{j\phi_t}$ is the ideal response of the trihedral that depends on its geometry. The co-polar response is affected by cross-talk, but the cross-talk term $\delta_1 \delta_3$ can be neglected in a second-order approximation. Hence the co-polar response can be used to derive the absolute calibration factor $A_{cf} = \frac{M_{hh}^t}{A_t e^{j\phi_t}}$. The cross-polar response can be used as second relation to estimate the distortion parameters.

Beside the trihedral response, another useful reference signal is a pure cross-polar return. This polarimetric signature can be obtained by an oriented dihedral corner reflector forming an angle of 45 deg with the incident wave direction. In this case, we have two additional equations

$$M_{hh}^d = A_d e^{j\phi_d} (\delta_3 + \delta_2) \quad (5.16)$$

$$M_{vh}^d = A_d e^{j\phi_d} (\delta_1 \delta_3 + f) \simeq A_d e^{j\phi_d} f \quad (5.17)$$

where M_{hh}^d and M_{vh}^d are the dihedral-like returns according to Tab. (5.1) and $A_d e^{j\phi_d}$ is the ideal response of the dihedron that depends on its geometric characteristics. Combining (5.13) with (5.15)-(5.17) yields a system of four equations and four unknowns that provides the distortion parameters of the model (5.9). The solution of such a system of equations is discussed in Sec. 5.3.3. The only drawback of this approach is that the dihedron has a narrow beamwidth and pointing might be difficult.

For this reason, we consider a second approach that uses an alternative point target, i.e. the gridded trihedral (GT) (Ainsworth, 2008). The GT is a trihedral corner reflector with one of the conducting faces replaced by a grid array of closely spaced (relative to the wavelength) parallel conductors over a microwave absorbing layer (cf. Fig. 5.6). The grid array of wires changes the polarization of the incident wave and results in a target with a significant cross-polarized reflection (Sheen et al., 1992). The ideal response of the gridded trihedral can be expressed in terms of the incident angle θ_i and the angle θ_p that the parallel grid forms with the vertically polarized component of the incident wave

$$\mathbf{S}^{gt} = \frac{A_{gt} e^{j\phi_{gt}}}{\cos^2 \theta_i + \sin^2 \theta_i \sin^2 \theta_p} \begin{pmatrix} \sin^2 \theta_p & -\sin \theta_p \cos \theta_p \cos \theta_i \\ -\sin \theta_p \cos \theta_p \cos \theta_i & \cos^2 \theta_i \cos^2 \theta_p \end{pmatrix} \quad (5.18)$$

Two configurations of GT are interesting for the calibration: wires parallel or perpendicular to the H-polarized direction. The ideal response of the trihedral for $\theta_p = 0$ and $\theta_p = \pi/2$ is shown in Tab. (5.1). After substituting the ideal response for $\theta_p = 0$ into (5.9), the measured scattering elements are

$$M_{hh_0}^{gt} = A_{gt} e^{j\phi_{gt}} \delta_2 \delta_3 \quad (5.19)$$

$$M_{vh_0}^{gt} = A_{gt} e^{j\phi_{gt}} f \delta_3 \quad (5.20)$$

and, for $\theta_p = \pi/2$,

$$M_{vh_{\pi/2}}^{gt} = A_{gt} e^{j\phi_{gt}} \delta_1. \quad (5.21)$$

The response $M_{hh\pi/2}^{gt}$ is not useful for the polarimetric calibration since it does not contain any distortion parameters. Eqs. (5.20)-(5.21) can be coupled with (5.15) to form a second system of four equations that represents an alternative approach to the estimation of the distortion parameters.

Target Type	Ideal Response	Measured Response
Azimuthal	$\mathbf{C} = \begin{pmatrix} s_{hh} ^2 & 0 \\ 0 & s_{vh} ^2 \end{pmatrix}$	$\mathbf{O} = \begin{pmatrix} O_{11} & O_{12} \\ O_{12}^* & O_{22} \end{pmatrix}$
Trihedral	$\mathbf{S}^t = A_t e^{j\phi_t} \begin{pmatrix} 1 & 0 \\ 0 & 1 \end{pmatrix}$	$M^t = \begin{pmatrix} M_{hh}^t \\ M_{vh}^t \end{pmatrix}$
45-Dihedral	$\mathbf{S}^d = A_d e^{j\phi_d} \begin{pmatrix} 0 & 1 \\ 1 & 0 \end{pmatrix}$	$M^d = \begin{pmatrix} M_{hh}^d \\ M_{vh}^d \end{pmatrix}$
GT ($\theta_p = 0$)	$\mathbf{S}_0^{gt} = A_{gt} e^{j\phi_{gt}} \begin{pmatrix} 0 & 0 \\ 0 & 1 \end{pmatrix}$	$M_0^{gt} = \begin{pmatrix} M_{hh_0}^{gt} \\ M_{vh_0}^{gt} \end{pmatrix}$
GT ($\theta_p = \pi/2$)	$\mathbf{S}_{\pi/2}^{gt} = A_{gt} e^{j\phi_{gt}} \begin{pmatrix} 1 & 0 \\ 0 & 0 \end{pmatrix}$	$M_{\pi/2}^{gt} = \begin{pmatrix} M_{hh\pi/2}^{gt} \\ M_{vh\pi/2}^{gt} \end{pmatrix}$

Table 5.1: Targets and their ideal/measured response used for the dual-pol calibration.

5.3.3 Calibration Procedure

In the previous section, we have derived the response of some targets according to the dual-pol distortion model. We identified two alternative approaches to estimate the system distortion parameters. The first uses a trihedral-like and an oriented dihedral-like response in the SAR scene, plus a distributed target with azimuthal symmetry (e.g. a forest). The second uses a trihedral-like response and two gridded trihedrals with different orientation of the grid wire array. In both cases we obtain a balanced system of four equations and four unknowns for the absolute and polarimetric data calibration.

First approach: distributed target, one trihedral and one oriented dihedral

The values of the absolute calibration factor and the value of M_{vh}^t are derived from the trihedral response; the values of the channel imbalance and the value of M_{hh}^d are derived from the dihedral response; the values of O_{11} , O_{12} and O_{22} are estimated from the distributed target. The analytical solution of (5.13)-(5.17) leads to the estimation

of the distortion parameters

$$\begin{aligned}
f &= \tilde{M}_{vh}^d \\
\delta_1 &= \tilde{M}_{vh}^t - \tilde{M}_{vh}^d \frac{\tilde{M}_{vh}^{d*} \tilde{M}_{vh}^t O_{11}^* + \tilde{M}_{hh}^{d*} O_{22}^* - O_{12}^*}{2O_{22}^*} \\
\delta_2 &= \tilde{M}_{hh}^d - \frac{\tilde{M}_{vh}^{d*} \tilde{M}_{vh}^t O_{11}^* + \tilde{M}_{hh}^{d*} O_{22}^* - O_{12}^*}{2O_{22}^*} \\
\delta_3 &= \frac{\tilde{M}_{vh}^{d*} \tilde{M}_{vh}^t O_{11}^* + \tilde{M}_{hh}^{d*} O_{22}^* - O_{12}^*}{2O_{22}^*}
\end{aligned} \tag{5.22}$$

where the tilded elements are normalized with respect to the theoretical response of the calibration object (e.g. $\tilde{M}_{vh}^d = M_{vh}^d / A_d e^{j\phi_d}$)

Second approach: one trihedral and two gridded trihedrals

The values of the absolute calibration factor and the value of M_{vh}^t are derived from the trihedral response; the value of the cross-talk δ_1 is derived directly from the gridded trihedral oriented with an angle $\theta_p = \pi/2$; the second gridded trihedral is used to derive the other parameters. The analytical solution of (5.15) and (5.20)-(5.21) yields the estimation of the distortion parameters

$$\begin{aligned}
f &= \sqrt{\frac{\tilde{M}_{vh_0}^{gt}}{\tilde{M}_{hh_0}^{gt}}} \left(\tilde{M}_{vh}^t - \tilde{M}_{vh_{\pi/2}}^{gt} \right) \\
\delta_1 &= \tilde{M}_{vh_{\pi/2}}^{gt} \\
\delta_2 &= \sqrt{\frac{\tilde{M}_{hh_0}^{gt}}{\tilde{M}_{vh_0}^{gt}}} \left(\tilde{M}_{vh}^t - \tilde{M}_{vh_{\pi/2}}^{gt} \right) \\
\delta_3 &= \frac{\tilde{M}_{vh_0}^{gt}}{\sqrt{\frac{\tilde{M}_{vh_0}^{gt}}{\tilde{M}_{hh_0}^{gt}}} \left(\tilde{M}_{vh}^t - \tilde{M}_{vh_{\pi/2}}^{gt} \right)}
\end{aligned} \tag{5.23}$$

To calibrate a dual-pol dataset we use only the receiving distortion parameters by inverting (5.9)

$$\begin{pmatrix} M_{hh}^{cal} \\ M_{vh}^{cal} \end{pmatrix} = \frac{1}{\delta_1 \delta_2 - f} \begin{pmatrix} f & -\delta_2 \\ -\delta_1 & 1 \end{pmatrix} \begin{pmatrix} M_{hh} \\ M_{vh} \end{pmatrix} \tag{5.24}$$

The transmit cross-talk δ_3 does not appear in (5.24) because it is not possible to recover the true scattering elements using a dual-pol mode, hence it is not possible to compen-

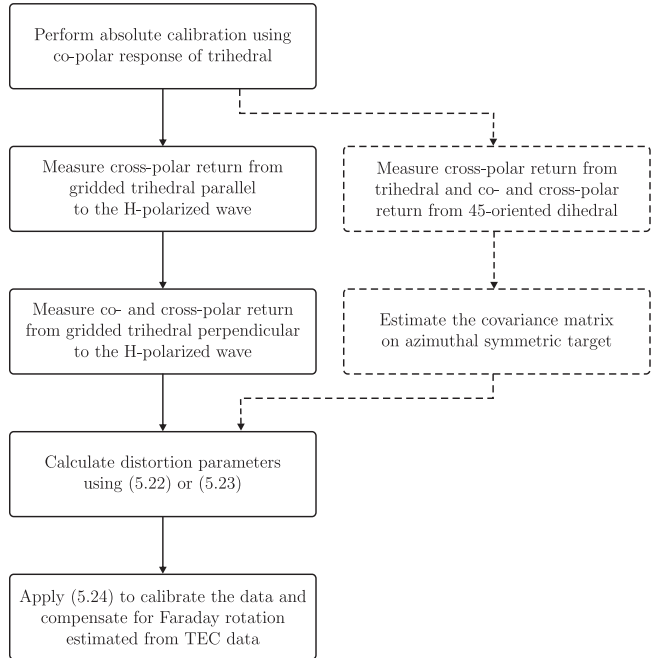


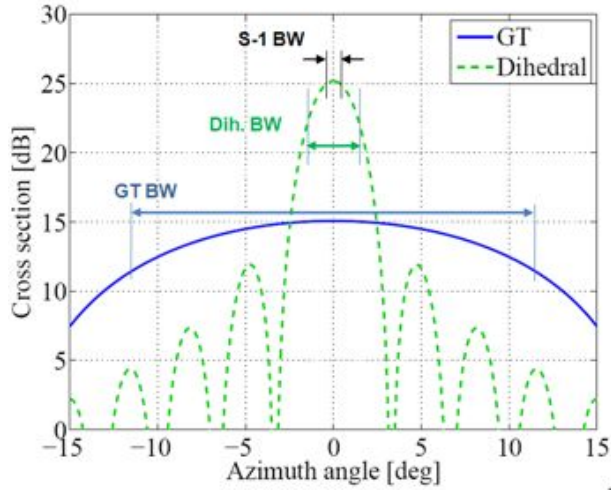
Figure 5.7: Basic steps for the polarimetric calibration of dual-pol SAR data.

sate for the transmitting distortions. The importance of δ_3 remains, however, because it is an estimate of the transmit cross-talk and indicates how much we can trust the dual-pol measurements, i.e. $M_{hh}^{\text{cal}} = s_{hh} + \delta_3 s_{hv} \simeq s_{hh}$ and $M_{vh}^{\text{cal}} = s_{vh} + \delta_3 s_{vv} \simeq s_{vh}$. Finally, the Faraday rotation can be estimated from the total electron content (TEC) data and its compensation can be performed according to the general model (5.1). Fig. (5.7) shows the basic steps of the calibration procedure for the two approaches.

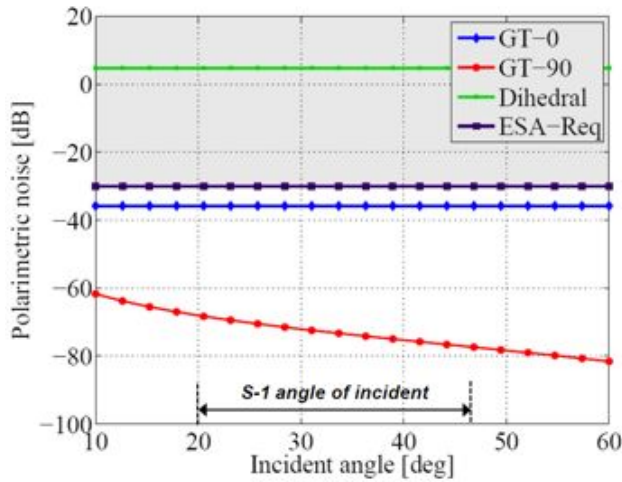
In the case of SENTINEL-1, this procedure could be used without particular remarks. It remains to be investigated the impact of the antenna beam steering due to the TOP-SAR burst-mode (De Zan and Monti Guarnieri, 2006) with respect to the beamwidth of the calibration targets. The next section concerns with the general performance of the procedure.

5.3.4 Sentinel-1 performance analysis

In this section, we assess the performance of the polarimetric procedure using the characteristics of SENTINEL-1. The performance analysis of the calibration procedure



(a) Targets beamwidth



(b) Polarimetric noise

Figure 5.8: Plots of targets beamwidth and polarimetric noise for the gridded trihedral and dihedral using the system parameters of the future ESA mission SENTINEL-1.

and calibration targets is based on two criteria:

1. the beamwidth of the considered calibration target shall be large with respect to the azimuth antenna beamwidth of SENTINEL-1;
2. the scattering matrix of the calibration targets shall have enough polarimetric stationarity during the along-track acquisition.

The first criterium can be expressed by the following relationship

$$BW_{S-1} = \phi_a + \Delta\phi_y < BW_{tg} \quad (5.25)$$

where BW_{S-1} is the beamwidth of SENTINEL-1 given by the sum of the antenna azimuth beamwidth ϕ_a and the yaw antenna stability $\Delta\phi_y$; BW_{tg} is the beamwidth of the calibration targets, i.e. $tg = GT, DIH$ for the gridded trihedral or the dihedral respectively. From the SENTINEL-1 system specifications, the beamwidth BW_{S-1} is about 0.25 deg. The beamwidth of the gridded trihedral can be assumed equal to the beamwidth of the flat trihedral, derived in turn from its radar cross section (Ruck et al., 1970)

$$RCS_{GT}(\theta, \phi) \approx \frac{4\pi}{\lambda^2} l^4 \left(v - \frac{2}{v} \right)^2, \quad v = \cos \theta + \sin \theta (\sin \theta + \cos \phi) \quad (5.26)$$

wherein l is the short side of the trihedral as indicated in Fig. 5.6. The beamwidth of the oriented dihedral is derived from an approximate expression of the radar cross section valid for small angles with respect to boresight direction (Hayashi et al., 2006; Ruck et al., 1970)

$$RCS_{DIH}(\theta, \phi) \approx \frac{16\pi}{\lambda^2} l^4 \sin^2 \left(\frac{\pi}{4} - \theta \right) \frac{\sin^2 u}{u^2}, \quad u = \frac{4\pi}{\lambda} l \cos \theta \sin \phi. \quad (5.27)$$

Fig. 5.8a shows the comparison between the three beamwidths and confirms that the gridded trihedral has a large beamwidth compared with the azimuth beamwidth of SENTINEL-1 and that the dihedral proves difficult to point since its beamwidth is close to the SENTINEL-1 beamwidth.

The second criterium is based on the coherent averaging of the target scattering matrix along different directions. The *polarimetric noise* δ_{tg} resulting from this averaging must be smaller than the system cross-talk imposed by the requirements of SENTINEL-1

$$\delta_{tg} < \delta_{req} \quad (5.28)$$

with $tg = GT, DIH$ and $\delta_{req} = -30$ dB. In the case of the gridded trihedral, the polarimetric noise is calculated using the average of the target vector $\mathbf{k}(\theta, \phi)$ on the

azimuth and elevation plane, taking as averaging intervals for θ and ϕ the azimuth beamwidth and pitch stability respectively

$$\delta_{GT} = 1 - \mathbf{k}(\theta_{ref}, 0) \cdot \left(\frac{1}{N_\theta N_\phi} \sum_i \sum_j \mathbf{k}(\theta_i, \phi_j) \right)^* \quad (5.29)$$

where $\mathbf{k}(\theta_{ref}, 0)$ is the reference scattering return at boresight direction, on which the average vector is projected, and $\theta_{ref} = 30$ deg the incident angle. In the case of the dihedral, the polarimetric noise is calculated by averaging the scattering vectors around the roll stability of the satellite

$$\delta_{DIH} = 1 - \mathbf{k}(0) \cdot \left(\frac{1}{N_\psi} \sum_i \mathbf{k}(\psi_i) \right)^* \quad (5.30)$$

where $\mathbf{k}(0)$ is the reference scattering return at boresight direction. Fig. 5.8b shows the polarimetric noise (5.29) and (5.30) versus the incident angle for the dihedral and the two gridded trihedrals. The curves reveal that the dihedral is not suitable for the calibration since the polarimetric noise would be higher than the required cross-talk. On the contrary, the two gridded trihedrals present a polarimetric noise lower than -30 dB and hence they can be used for the dual-pol calibration. We remark that this result refers to best conditions since a perfect realization of the grid and absence of pointing errors have been assumed.

5.4 Conclusions

In this chapter, we have discussed two main aspects of the polarimetric data quality: the Faraday rotation and the calibration of dual-pol data. For each aspect, we have proposed some improvements with respect to the current calibration techniques.

We have proposed the estimation and the correction for Faraday rotation from raw data, i.e. before the focusing process. This approach is particularly important when rapid spatial and temporal variations occur in the ionosphere within the synthetic aperture length. Each raw data sample will have an estimate of Faraday rotation that is not influenced by the algorithms adopted in the focuser. Tests conducted using the ESA PALSAR processor revealed that the mean Faraday rotation angle estimated from raw data is in agreement with the one estimated from SLC data. Some deviations have been observed on the range and azimuth profiles, which may be due to non-linearities of the processor, miscoregistration of the raw data and uncompensated interference. The main conclusion, however, is that it is possible to retrieve and correct Faraday rotation from

raw data and consequently improve the quality of focusing and the product annotations of raw data.

Concerning the dual-pol calibration, we have studied the response of some distributed and passive point targets according to a distortion model that we have derived from the full polarimetric calibration model. It has been shown that using a flat trihedral and two gridded trihedrals the four distortion parameters can be estimated and dual polarimetric data calibrated. A relatively new target, the gridded trihedral, has been studied with attention to its beamwidth and its polarimetric stationarity. We have compared these characteristics with the system parameters of SENTINEL-1 and we found that the calibration performance of the gridded trihedral is in accordance with the polarimetric quality required for SENTINEL-1 data.

Conclusions and future perspectives

*The important thing is not to stop
questioning; curiosity has its own reason
for existing.*

Albert Einstein (1879-1955)

In this work, we have presented some advances of polarimetric and interferometric radar techniques for the remote sensing of random media, in particular forests. In recent years, the role played by polarimetry for monitoring status and evolution of forests has increased due to two main reasons, related to a technological and a scientific aspect respectively. From one side, we have witnessed the planning and the launch of new polarimetric missions, especially at lower frequency, that allowed demonstrating operationally and experimentally radar polarimetry for different applications. Secondly, the progress of multidimensional radar techniques, such as polarimetric SAR interferometry, has provided a solid and scientific basis for retrieving structural characteristics of forests and, from those, the biomass.

When this thesis initiated in the late 2006, the L-band polarimetric sensor ALOS/PALSAR had just been launched and first polarimetric data started to be distributed. At the same time, the so-called RVOG model had just been validated using airborne data, and the radar community was aiming to further understand and improve the tools of the POLINSAR technique.

In this context, the initial objective of the thesis was the demonstration of the RVOG inversion using ALOS/PALSAR data, hence a novel and challenging task for the theoretical modeling aspects and the practical processing aspects. Our approach was a systematic approach, i.e. the detailed processing of PALSAR data starting from raw data and by performing the complete basic SAR, interferometric and polarimetric algorithms for the subsequent ingestion in model-based inversion procedures. This was necessary since at that time no one was aware about the data quality of PALSAR data and its potential for interferometric applications. Concerning the understanding of the theoretical modeling and POLINSAR technique, we also found helpful the detailed investigation of every single step, in order to find out possible sources of error in both

the forward and inverse modeling. This was also necessary since POLINSAR was at an early stage and there was much discussion about its effectiveness.

Today it is widely accepted that ALOS/PALSAR provides high quality SAR data and performs excellent acquisitions as a polarimeter. However, as an interferometer, at least over forested areas, its potentialities are limited by the long temporal baseline. On the other side, the POLINSAR technique and the RVOG model reached a good level of maturity, especially thanks to airborne campaigns, and it is really on the way to contribute to the worldwide biomass retrieval. We proved these two points in Chapter 3, wherein ALOS/PALSAR POLINSAR observations are shown: the polarimetric-optimized interferograms show that polarimetry adds a value to spaceborne interferometry. This value, however, is difficult to convert into a quantitative measure of forest height due to the effects of temporal decorrelation.

As mentioned, the characteristics of the thesis and the initial objectives naturally led to a large variety of topics to be considered: the polarimetric calibration of the data, the propagation through the ionosphere, the effects of the focuser, the temporal decorrelation, the fidelity of the forward modeling, the parameterization of the model and the optimization of the interferometric coherence are only a few examples. While this could appear confusing, I had extremely pleasure in discovering that many results and methods apply similarly at different stages of the SAR processing and data exploitation. For instance, the properties of symmetry of natural media can be effectively used for calibration purposes, or for testing compact polarimetric applications or for increasing the robustness of POLINSAR coherence optimization. Therefore, I felt that broadening the view on different aspects of the SAR processing and modeling provided a deeper understating of the phenomena, besides a better understanding of the relationships among the various elements of the SAR data exploitation chain.

The present dissertation reflected this peculiarity: several ideas from different topics have been gathered in a single volume. Most of them have been proposed, tested and validated over simulated or real data (e.g. the P-band modeling or the raw Faraday rotation estimation). Others have been provided with a theoretical formulation and look into the future for a deeper validation on real data (e.g. the height-dependent temporal decorrelation). We grouped these ideas into three topics, which originated three separate chapters: the full POLINSAR technique, the compact POLINSAR technique and data quality issues.

Chapter 3 presented our developments and advances concerning full POLINSAR techniques. The reference model adopted to describe the spatial correlation of vertical distribution of scatterers is the RVOG model. We have presented it starting from SAR interferometry and converging into SAR polarimetry, rather than the more common (opposite) approach that involves the definition of the covariance matrices first. An introduction to this matrix formulation is presented in Chapter 4 with regard to com-

pact POLINSAR. The core of our POLINSAR development is the investigation and the improvement of the forward modeling, both concerning the spatial correlation and the temporal correlation terms.

Temporal decorrelation has been modeled as a height-dependent function that shapes the vertical structural profile of the vegetation. This allows for instance to model the effects of the wind which are normally stronger at the top-canopy than on the ground. Some interesting consequences follow from this improvement. The first is that the temporal correlation factor has a non-zero imaginary part, hence the effective location of the scattering phase center depends on the amount of decorrelation. In the complex plane, the visible coherence locus is still a straight segment, but it shrinks and its center moves towards the ground reference while the temporal baseline increases. This is common to any (monotonic) expression of the temporal correlation function. In our development, the temporal decorrelation is now dependent on the scattering center location and hence on the selected polarization. In its simplest linear approach, the characterization of the temporal decorrelation does not require additional parameters: one real parameter would suffice to define the slope of the function once the temporal correlation of the ground is assumed unitary. The height retrieval procedure, on the contrary, does require a more accurate strategy to cope with the complex nature of the temporal correlation. We have proposed a variant of previously published strategies based on the correction of the height shift introduced by temporal decorrelation. Once the temporal correlation function is estimated, this shift depends on the actual forest height and, for this reason, we propose to iterate and correct at each step the height estimates. The theoretical results were shown choosing a linear trend for the standard deviation motion of the scatters along the vertical dimension; this leads to an exponential temporal correlation function into the canopy. We envision two directions to further advance in the modelisation of temporal decorrelation. One involves the recent ESA campaign BIOSAR-2, which acquired polarimetric and interferometric data supported by LIDAR measurements. The availability of a priori forest height (through ground or LIDAR measurements) would allow to retrieve our temporal correlation function and to validate the inversion procedure. The second direction concerns an improved and extended modeling. In the same way as RVOG model has evolved into the PCT technique, the temporal correlation function may be relaxed into a generic function expansion. This would have immediate benefits to any tomographic technique that aims at retrieving the vertical structure of vegetation.

Concerning the spatial correlation modeling, Chapter 3 also contains some novel elements. The most relevant are the study on the effect of terrain slope and the simplified form of the RVOG model for the P-band HH scattering. In both developments, we used numerical simulations provided by PSPSIM. In particular, it is demonstrated how PSPSIM can serve not only as an image simulator for testing algorithms, but also as

tool for investigating the properties and the sensitivity of POLINSAR descriptors. For instance, we have examined the dependence of the POLINSAR coherence phase and magnitude, as well as of the ground-to-volume scattering ratio, versus forest height and azimuth/range terrain slope. Scots pines have been used in the numerical simulations and the inversion strategy commonly adopted for retrieving forest height was tested. The results confirmed that the RVOG forward model reliably predicts the interferometric coherence when forest height and azimuth slope vary. The inversion procedure in these cases retrieves the forest height within the requested accuracy (10% of the total forest height). Unfortunately, we have found that for range-sloped terrain this is not the case. The variation of the ground-to-volume ratio induces a variation of the predicted coherence according to the RVOG model; this dependence is violated, at least for pines, if terrain slope is greater than $\pm 2\%$. The effect is a lower accuracy on the retrieved height. For this reason, the evolution of the RVOG modelisation might consider the inclusion of the range terrain slope as an input parameter to the model. This parameter would reasonably appear in the structure function and influence the complex value of the predicted coherence. Note also that this improvement would bring benefits to any approach based on the RVOG model, such as PCT. The increasing dimensionality of the problem, finally, could be resolved by using classic interferometric unwrapping algorithms on HH interferograms (or optimized low phase interferograms) to derive an estimate of terrain slope.

The third novel element discussed in Chapter 3, besides the temporal decorrelation function and the effects of terrain slope, is the RVOG modelisation at P-band. Several airborne and spaceborne missions have been designed to operate at P-band: the Earth Explorer BIOMASS and the commercial GEOSAR are two examples. We have shown that, at P-band, some simplifications are possible in the model expression. In particular, an additional relationship between the ground-to-volume ratio and the HH/HV scattering ratio allows estimating the HH ground-to-volume ratio from the data. This turns useful for estimating and correcting the ground phase bias in the HH coherence. The only drawback is that the relationship contains a sort of calibration parameter, whose value needs to be estimated a priori from proper test sites or numerical simulations. We have assessed these calibration parameters through simulated Scots pines and we found that it is stable versus changes in forest height and range terrain slope. Hence, the proposed approach is promising for a robust estimation of the ground phase even when full polarimetric acquisitions are available.

The second topic treated in this dissertation concerns compact polarimetric techniques and, specifically, compact POLINSAR. Chapter 4 contains the theory and related results of this very recent topic. The key question in compact polarimetry is whether transmitting a single polarization state (different than the simple H or V) and receiving coherently at H and V gives similar performance compared to full polarimetric modes.

In other words, the debate is whether full polarimetry is really necessary for all applications and if we can relax the system constraints in order to have a sort of advanced dual polarimetric mode. Although the debate is still open, today it is widely accepted that compact polarimetry does not represent a substitute for full polarimetry, at least not for all applications. Nevertheless, a set of selected applications might benefit from compact polarimetry, especially in terms of the larger swath coverage and shorter revisit time.

POLINSAR forestry techniques are in principle possible using compact polarimetric data. The only difference would be the reduced spectrum of observed ground-to-volume ratio, which is a direct consequence of the reduced detectable scattering mechanisms. The narrowed spectrum of the ground-to-volume ratio reduces the length of the visible segment in the complex plane, hence may affect the inversion procedure and worsen the accuracy of the retrieved forest height. In our contribution, we have generalized the approach of pseudo-reconstruction of compact polarimetry to compact POLINSAR. Since we are interested in forests, we have proposed originally an algorithm based on the rotation invariance of cross-polarized terms in the cross-covariance matrix. Coupled with reflection symmetry assumptions, this approach allows to obtain in a closed form the symmetric full POLINSAR coherence matrix. We have shown that the reconstruction of the HH, VV and HV polarimetric channels is almost well preserved if the symmetry assumptions are satisfied. In order to detect the areas wherein our assumptions are valid, two statistic indicators have been defined based on the determinant of the covariance matrix. Unfortunately, these indicators rely on the use of full polarimetric data. Currently, if only compact polarimetric data are received, the pseudo-reconstruction should be applied blindly and the performances remain unknown. For this reason, we have matured the feeling that such reconstruction algorithms are especially useful for comparing compact polarimetry modes among them and with full polarimetry. They do not add further information to the data, but rather visualize the information in a more familiar way. Therefore, it is not excluded that these methods may bring benefits to the compact polarimetric data exploitation. For instance, if a symmetry assumption is satisfied, it is expected that the POLINSAR reconstruction enlarges the coherence region in the complex plane so that the robustness of the height retrieval is increased. This has not been investigated yet and might represent a future direction of research. Contextually, we have tested the effects of our POLINSAR reconstruction algorithm using the interferometric form of the RVOG model. This idea was already developed for compact polarimetry and our contribution extended the development to the interferometric scenario. In this case, as the symmetry relationships involve the single covariance elements, a simplified matrix formulation of the RVOG model has been adopted. According to this form, the symmetry relationships have been rewritten and their validity tested versus model parameters. The outcome of our analysis is that the

relationships valid for compact polarimetry can be extended straightforwardly to the compact POLINSAR case. The linear relationship based on the rotation invariance of the cross-polarized terms converges for low values of ground-to-volume ratio to the non-linear relationship based on azimuth symmetry. Moreover, if the interferometric coherence of the volume layer is high, this convergence is faster. This analysis gave a further understanding of the reconstruction. The validity of the symmetry assumptions depends on the relative presence of volume and ground component. This latter component breaks the symmetry assumptions and therefore leads to poor reconstruction. In POLINSAR applications, the objective is to find interferograms with maximum and minimum ground-to-volume ratios. Depending on the characteristics of the forest, these values may correspond to combinations of ground and volume components, which do not satisfy symmetry assumptions. The condition of complete azimuth symmetry is the only case for which the reconstruction gives results independently on the ground-to-volume ratio. For this reason, the model analysis on compact POLINSAR remarked the importance of testing the symmetry assumptions before the reconstruction.

The third novel aspect pointed out within the compact polarimetric domain is the simulation of the data. All investigations made so far are based on the simulation of compact polarimetry starting from full polarimetric data. The real realization of a compact polarimeter, however, may lead to slightly different results due to the increasing signal-to-quantization noise into the receiver and the non-linear effects of the SAR processor. These effects are apparently negligible but merit attention when compact polarimetry is assessed for a real operational scenario.

The third topic addressed is the calibration and in general the quality of SAR images, and has been presented in Chapter 5. The discussion revolved around two main arguments: the Faraday rotation correction and the dual polarimetric data calibration. Concerning the Faraday rotation estimation, the key idea was the estimation and correction of Faraday rotated scattering matrices in raw data rather than SLC data. We have developed a simple model that copes with this task and validated using several ALOS/PALSAR acquisitions. There are some important outcomes of our method. First, the mean Faraday angle is the same if estimated on raw data and SLC data. This means that the miscoregistration of the polarimetric raw channels can be disregarded and the FR can be always estimated reliably on raw data without need to generate SLC data. Secondly, the possibility to detect and correct Faraday rotation before the focusing potentially improves the SLC quality. Third, the local variations of TEC in the ionosphere are more reasonably observed in raw data, since the effect of focused targets are not present. An interesting investigation can be performed by correcting Faraday rotation from raw data, focus the data and then testing the improvement in terms of focusing quality and new Faraday rotation estimates. Given its simplicity and usability, this method is recommended for future and proposed low frequency SAR missions such

as TERRASAR-L, DESDYNI and SAOCOM.

In the second part of the chapter, we discussed the polarimetric calibration of dual polarimetric data. This topic becomes especially important when the sensor does not operate the full polarimetric mode but only as a dual polarimeter, such as GEOSAR or the future ESA mission SENTINEL-1. In this case, our contribution was the derivation of a dual polarimetric distortion model and the design of a calibration procedure based on the use of gridded trihedrals, which are passive point targets relatively easy to construct and deploy. We have also considered a second approach based on dihedrals, but for such targets the narrow beamwidth is a severe limiting issue. The performances of gridded trihedrals as calibrators have been assessed using the acquisition geometry of SENTINEL-1. We have found that the polarimetric stationarity of the calibrator and its beamwidth give a polarimetric noise below the requirements of data calibration imposed for SENTINEL-1. As additional investigation, we are executing scattering numerical simulations that are further confirming the effectiveness of our calibration approach.

Bibliography

- Abramowitz, M. and I. A. Stegun (Eds.) (1965). *Handbook of Mathematical Functions; with Formulas, Graphs, and Mathematical Tables* (9th ed.). Dover Publications, New York.
- Ainsworth, T. (2008). Personal communication.
- Ainsworth, T., L. Ferro-Famil, and J.-S. Lee (2006). Orientation angle preserving a posteriori polarimetric sar calibration. *Geoscience and Remote Sensing, IEEE Transactions on* 44(4), 994–1003.
- Ainsworth, T., J. Kelly, and J.-S. Lee (2008). Polarimetric Analysis of dual Polarimetric SAR Imagery. *EUSAR 2008, Proceedings of, Friedrichshafen, Germany*.
- Ainsworth, T., J.-S. Lee, and L. Chang (2009). Classification Comparisons Between Dual-Pol and Quad-Pol SAR Imagery. *PolInSAR Workshop, Proceedings of, Frascati, Italy*.
- Askne, J. I. H., P. B. G. Dammert, L. M. H. Ulander, and G. Smith (1997). C-Band Repeat-Pass Interferometric SAR Observations of the Forest. *IEEE Transactions on Geoscience and Remote Sensing* 35(1), 25–35.
- Attema, E. P. W. and F. T. Ulaby (1978). Vegetation modeled as a water cloud. *Radio Science* 13, 357–364.
- Ballester-Berman, J., J. Lopez-Sanchez, and J. Fortuny-Guasch (2005). Retrieval of biophysical parameters of agricultural crops using polarimetric sar interferometry. *Geoscience and Remote Sensing, IEEE Transactions on* 43(4), 683–694.
- Ballester-Berman, J. D. and J. M. Lopez-Sanchez (2009). Applying the freeman-durden decomposition concept to polarimetric sar interferometry. *Geoscience and Remote Sensing, IEEE Transactions on* PP(99), 1–1.
- Bamler, R. (1992). A comparison of range-Doppler and wave-number domain SAR focusing algorithms. *IEEE Transactions on Geoscience and Remote Sensing* 30(4), 706–713.
- Bamler, R. and P. Hartl (1998). Synthetic Aperture Radar Interferometry. *Inverse Problems* 14, R1–R54.
- Beaudoin, A., T. Le Toan, S. Goze, E. Nezry, A. Lopes, E. Mougin, C. Hsu, H. Han, J. Kong, and R. Shin (1994). Retrieval of forest biomass from sar data. *Int. J. of Remote Sensing* 15(14), 2777 – 2796.

- Bickel, S. and R. Bates (1965). Effects of Magneto-Ionic Propagation on the Polarization Scattering Matrix. *Proc. IRE* 53, 1089–1091.
- Boerner, W.-M., M. El-Arini, C.-Y. Chan, and P. Mastoris (1981). Polarization dependence in electromagnetic inverse problems. *Antennas and Propagation, IEEE Transactions on* 29(2), 262–271.
- Cafforio, C., C. Prati, and F. Rocca (1991). SAR data focusing using seismic migration techniques. *IEEE Transactions on Aerospace and Electronic Systems* 27(2), 199–207.
- Cloude, S. (2008). POL-InSAR Training Course. *Tutorial of the ESA Polarimetric SAR Processing (PolSARPro) Toolbox*.
- Cloude, S. (2009). Dual versus Quadpol: a new test statistic for radar polarimetry. *PolInSAR Workshop, Proceedings of, Frascati, Italy*.
- Cloude, S. and K. Papathanassiou (1997). Polarimetric optimisation in radar interferometry. *Electronics Letters* 33(13), 1176–1178.
- Cloude, S. and K. Papathanassiou (1998). Polarimetric SAR Interferometry. *Geoscience and Remote Sensing, IEEE Transactions on* 36(5), 1551–1565.
- Cloude, S. and K. Papathanassiou (2002). A 3-stage inversion process for polarimetric sar interferometry. In *European Conference on Synthetic Aperture Radar (EUSAR), Proceedings of, Cologne, Germany*, pp. 279–282.
- Cloude, S. and K. Papathanassiou (2003). Three-stage Inversion Process for Polarimetric SAR Interferometry. *Radar, Sonar and Navigation, IEE Proceedings - 150(3)*, 125–134.
- Cloude, S. and E. Pottier (1996). A review of target decomposition theorems in radar polarimetry. *Geoscience and Remote Sensing, IEEE Transactions on* 34(2), 498–518.
- Cloude, S. and E. Pottier (1997). An entropy based classification scheme for land applications of polarimetric sar. *Geoscience and Remote Sensing, IEEE Transactions on* 35(1), 68–78.
- Cloude, S., I. Woodhouse, J. Hope, J. Suarez Minguez, P. Osborne, and G. Wright (2001). The glen affric radar project: Forest mapping using dual baseline polarimetric radar interferometry. In *ESA Symposium on Retrieval of Bio and Geophysical Parameters from SAR for Land Applications*, University of Sheffield, England, pp. 333–338.
- Cloude, S. R. (2006). Polarization coherence tomography. *Radio Sci.* 41.
- CODE (2009). Global Ionosphere Maps Produced by CODE. *Internet resource available at, <http://www.aiub.unibe.ch>*.
- Colin, E., C. Titin-Schnaider, and W. Tabbara (2006). An interferometric coherence optimization method in radar polarimetry for high resolution imagery. *IEEE Transactions Geoscience and Remote Sensing* 44(1), 167–175.

- Cumming, I. and F. Wong (2005). *Digital Processing Of Synthetic Aperture Radar Data: Algorithms And Implementation*. New York: Artech House Publishers. ISBN 1580530583.
- Curlander, J. C. and R. N. McDonough (1991). *Synthetic aperture radar: systems and signal processing*. New York: John Wiley & Sons, Inc.
- Davidson, G. W. (1997). Signal properties of spaceborne squint-mode SAR. *IEEE Transactions on Geoscience and Remote Sensing* 35(3), 611–617.
- Davidson, M. (2008). *SP1313/2 - Candidate Earth Explorer Core Missions, Report for Assessment: Biomass*. European Space Agency.
- de Roo, R., Y. Du, F. Ulaby, and M. Dobson (2001). A semi-empirical backscattering model at l-band and c-band for a soybean canopy with soil moisture inversion. *Geoscience and Remote Sensing, IEEE Transactions on* 39(4), 864–872.
- De Zan, F. and A. Monti Guarnieri (2006). Topsar: Terrain observation by progressive scans. *Geoscience and Remote Sensing, IEEE Transactions on* 44(9), 2352–2360.
- Della Vecchia, A. (2006). *Advances in modeling microwave interactions with vegetation for active and passive remote sensing*. Ph. D. thesis, University of Rome Tor Vergata, Geoinformation PhD School.
- Della Vecchia, A., P. Ferrazzoli, and L. Guerriero (2004). Modelling microwave scattering from long curved leaves. *Waves in Random and Complex Media* 14(2), 333–343.
- Dobson, M., F. Ulaby, M. Hallikainen, and M. El-Rayes (1985). Microwave dielectric behavior of wet soil-part ii: Dielectric mixing models. *Geoscience and Remote Sensing, IEEE Transactions on GE-23*(1), 35–46.
- Dubois-Fernandez, P., S. Angelliaume, J.-C. Souyris, F. Garestier, and I. Champion (2007). The specificity of P-band PolInSAR data over vegetation. *PolInSAR Workshop, Proceedings of, Frascati, Italy*.
- Dubois-Fernandez, P., S. Angelliaume, M.-L. Truong-Loi, and J.-C. Souyris (2008). Compact polarimetry mode for a low frequency sar in space. In *Geoscience and Remote Sensing Symposium, 2008. IGARSS 2008. IEEE International*, Volume 5, pp. V –279–V –282.
- Dubois-Fernandez, P., S.-C. Souyris, S. Angelliaume, and F. Garestier (2007). The compact polarimetry alternative for spaceborne sar at low frequency. In *ESA Symposium on Retrieval of Bio and Geophysical Parameters from SAR for Land Applications*, Bari, Italy.
- El-Rayes, M. and F. Ulaby (1987). Microwave dielectric spectrum of vegetation-part i: Experimental observations. *Geoscience and Remote Sensing, IEEE Transactions on GE-25*(5), 541–549.
- Elachi, C. (1988). *Spaceborne radar remote sensing: applications and techniques*. New York: Institute of Electrical and Electronics Engineers.

- Enquist, B. J., J. H. Brown, and G. B. West (1998). Allometric scaling of plant energetics and population density. *Nature* 395, 163–165.
- Eom, H. and A. Fung (1984). A scatter model for vegetation up to ku-band. *Remote Sensing of Environment* 15(3), 185 – 200.
- ESA (2007). *InSAR Principles: Guidelines for SAR Interferometry, Processing and Interpretation*. European Space Agency publications.
- Evans, D. (1995). *Spaceborne Synthetic Aperture Radar: Current Status and Future Directions*. Nasa Technical Memorandum 4679, NASA Scientific and Technical Office.
- Ferrazzoli, P. and L. Guerriero (1995). Radar sensitivity to tree geometry and woody volume: a model analysis. *Geoscience and Remote Sensing, IEEE Transactions on* 33(2), 360–371.
- Ferretti, A., A. Monti-Guarnieri, C. Prati, F. Rocca, and D. Massonnet (2007). *InSAR Principles: Guidelines for SAR Interferometry Processing and Interpretation*. European Space Agency (ESA) Publications.
- Ferro-Famil, L. and M. Lavalley (2009). Detection and analysis of urban areas using polarimetric data. In *Geoscience and Remote Sensing Symposium, 2009. IGARSS 2009. IEEE International*.
- Ferro-Famil, L. and M. Neumann (2008). Recent advances in the derivation of polarimetric statistics: study and applications. In *European Conference on Synthetic Aperture Radar (EUSAR), Proceedings of, Friedrichshafen, Germany*.
- Ferro-Famil, L., M. Neumann, and Y. Huang (2009). Multi-baseline polarimetric statistical techniques for the characterization of distributed media. *Geoscience and Remote Sensing Symposium, 2009. IGARSS '09. 2009 IEEE International*.
- Ferro-Famil, L., M. Neumann, and C. Lopez-Martinez (2008). Analysis of natural scenes using polarimetric and interferometric SAR data statistics in particular configurations. In *Geoscience and Remote Sensing Symposium, 2008. IGARSS 2008. IEEE International*, Volume 4, pp. IV –33–IV –36.
- Flynn, T., M. Tabb, and R. Carande (2002). Coherence region shape estimation for vegetation parameter estimation in POLINSAR. *Proceedings of IGARSS, Toronto, Canada*, 2596–2598.
- Fornaro, G., F. Serafino, and F. Soldovieri (2003). Three-dimensional focusing with multipass SAR data. *Geoscience and Remote Sensing, IEEE Transactions on* 41(3), 507–517.
- Freeman, A. (1992a). SAR calibration: An overview. *IEEE Transactions on Geoscience and Remote Sensing* 30(6), 1107–1121.
- Freeman, A. (1992b). SAR calibration: an overview. *Geoscience and Remote Sensing, IEEE Transactions on* 30(6), 1107–1121.

- Freeman, A. (2004). Calibration of Linearly Polarized Polarimetric SAR Data Subject to Faraday Rotation. *Geoscience and Remote Sensing, IEEE Transactions on* 42(8), 1617–1624.
- Freeman, A., P. Dubois-Fernandez, and M. Truong-Loi (2008). Compact Polarimetry at longer wavelengths SAR calibration. *EUSAR 2008, Proceedings of, Friedrichshafen, Germany 1*.
- Fung, A. (1979). Scattering from a vegetation layer. *Geoscience Electronics, IEEE Transactions on* 17(1), 1–6.
- Fung, A. (1994). *Microwave scattering and emission models and their applications*. Artech House.
- Fung, A. and F. Ulaby (1978). A scatter model for leafy vegetation. *Geoscience Electronics, IEEE Transactions on* 16(4), 281–286.
- Gabriel, A. K. and R. M. Goldstein (1988). Crossed orbit interferometry: theory and experimental results from SIR-B. *Int.J. Remote Sensing* 9(5), 857–872.
- Garestier, F., P. Dubois-Fernandez, X. Dupuis, P. Paillou, and I. Hajnsek (2006). Polinsar analysis of x-band data over vegetated and urban areas. *Geoscience and Remote Sensing, IEEE Transactions on* 44(2), 356–364.
- Garestier, F., P. Dubois-Fernandez, and K. Papathanassiou (2008). Pine forest height inversion using single-pass x-band polinsar data. *Geoscience and Remote Sensing, IEEE Transactions on* 46(1), 59–68.
- Gatelli, F., A. Monti Guarnieri, F. Parizzi, P. Pasquali, C. Prati, and F. Rocca (1994). The wavenumber shift in SAR interferometry. *IEEE Transactions on Geoscience and Remote Sensing* 32(4), 855–865.
- Goodman, J. W. (1976). Some fundamental properties of speckle. *J. Opt. Soc. Am.* 66(11), 1145–1150.
- Graham, L. C. (1974). Synthetic interferometer radar for topographic mapping. *Proceedings of the IEEE* 62(6), 763–768.
- Gustafson, K. and D. Rao (1997). *Numerical Range*. Springer-Verlag.
- Hagberg, J. O., L. M. H. Ulander, and J. Askne (1995). Repeat-Pass SAR Interferometry over Forested Terrain. *IEEE Transactions on Geoscience and Remote Sensing* 33(2), 331–340.
- Hajnsek, I., T. Jagdhuber, H. Schon, and K. Papathanassiou (2009). Potential of estimating soil moisture under vegetation cover by means of polsar. *Geoscience and Remote Sensing, IEEE Transactions on* 47(2), 442–454.

- Hallikainen, M., F. Ulaby, M. Dobson, M. El-Rayes, and L.-K. Wu (1985). Microwave dielectric behavior of wet soil-part 1: Empirical models and experimental observations. *Geoscience and Remote Sensing, IEEE Transactions on GE-23*(1), 25–34.
- Hanssen, R. F. (2001). *Radar Interferometry: Data Interpretation and Error Analysis*. Dordrecht: Kluwer Academic Publishers.
- Hayashi, K., R. Sato, Y. Yamaguchi, and H. Yamada (2006). Polarimetric Scattering Analysis for a Finite Dihedral Corner Reflector. *IEICE Trans Commun E89-B*(1), 191–195.
- Henderson, F. M. and A. J. Lewis (Eds.) (1998). *Principles and applications of Imaging Radar* (3 ed.), Volume 2 of *Manual of Remote Sensing*. New York: John Wiley & Sons, Inc.
- Horn, R. and C. Johnson (1985). *Matrix Analysis*. Cambridge, UK, Cambridge University Press.
- Horn, R. and C. Johnson (1991). *Topics in Matrix Analysis*. Cambridge, UK, Cambridge University Press.
- Huynen, J. (1970). *Phenomenological Theory of Radar Targets*. Ph. D. thesis, University of Technology, Delft, The Netherlands.
- Imhoff, M. (1995). Radar backscatter and biomass saturation: ramifications for global biomass inventory. *Geoscience and Remote Sensing, IEEE Transactions on* 33(2), 511–518.
- IPCC (2007). *Climate Change 2007 - The Physical Science Basis: Working Group I Contribution to the Fourth Assessment Report of the IPCC (Climate Change 2007)*. Cambridge University Press.
- Ishimaru, A. (1978). *Wave Propagation and Scattering in Random Media*, Volume 2. New York: Academic Press.
- Isola, M. and S. Cloude (2001). Forest height mapping using space-borne polarimetric sar interferometry. In *Geoscience and Remote Sensing Symposium, 2001. IGARSS '01. IEEE 2001 International*, Volume 3, pp. 1095–1097 vol.3.
- Joughin, I. R., R. Kwok, and M. A. Fahnestock (1998). Interferometric estimation of three-dimensional ice-flow using ascending and descending passes. *IEEE Transactions on Geoscience and Remote Sensing* 36(1), 25–37.
- Just, D. and R. Bamler (1994). Phase statistics of interferograms with applications to synthetic aperture radar. *Applied Optics* 33(20), 4361–4368.
- Karam, M., A. Fung, and Y. Antar (1988). Electromagnetic wave scattering from some vegetation samples. *Geoscience and Remote Sensing, IEEE Transactions on* 26(6), 799–808.
- Karam, M., A. Fung, R. Lang, and N. Chauhan (1992). A microwave scattering model for layered vegetation. *Geoscience and Remote Sensing, IEEE Transactions on* 30(4), 767–784.

- Kennaugh, E. (1951). Effects of the type of polarization on echo characteristics. *Report 389-9, Antenna Laboratory, Ohio State University.*
- Kugler, F., F. Koudogbo, K. Papathanassiou, and K. Gutjari (2006). Frequency effects in polinsar forest height estimation. *EUSAR 2006, Proceedings of, Dresden, Germany.*
- Kwok, R. and M. A. Fahnestock (1996). Ice sheet motion and topography from radar interferometry. *IEEE Transactions on Geoscience and Remote Sensing 34*(1), 189–200.
- Lanari, R., P. Lundgren, and E. Sansosti (1998). Dynamic deformation of Etna volcano observed by satellite radar interferometry. *Geophysical Research Letters 25*, 1541–1544.
- Lanari, R., G. Zeni, M. Manunta, S. Guardino, P. Berardino, and E. Sansosti (2004). An integrated SAR/GIS approach for investigating urban deformation phenomena: a case study of the city of Naples, Italy. *International Journal of Remote Sensing 25*(14), 2855–2862.
- Lavalle, M. (2008). Compact polarimetric SAR interferometry: theory and PALSAR observations. In *Proceedings of IEEE GOLD Conference 2008*, Frascati, Italy.
- Lavalle, M., B. Rosich, N. Miranda, E. Pottier, and D. Solimini (2008). Dual-polarimetric SAR data calibration: A possible approach for Sentinel-1. In *Proceedings of CEOS Workshop 2008*, Oberpfaffenhofen-Wessling, Germany.
- Lavalle, M., M. Simard, and S. Hensley (2012). A temporal decorrelation model for polarimetric radar interferometers. *IEEE Transactions on Geoscience and Remote Sensing 50*(7), 2880–2888.
- Lavalle, M., D. Solimini, E. Pottier, and Y.-L. Desnos (2007). Comparison of models of PolInSAR coherence for forest height retrieval using PolInSAR simulated data. In *Proceedings of Fringe Workshop 2007, European Space Agency*, Frascati, Italy.
- Lavalle, M., D. Solimini, E. Pottier, and Y.-L. Desnos (2008a). Investigation of Compact Polarimetry in SAR Interferometry. In *Proceedings of European SAR Conference (EUSAR) 2008*, Friedrichshafen, Germany, pp. 45–48.
- Lavalle, M., D. Solimini, E. Pottier, and Y.-L. Desnos (2008b). PolInSAR for forest biomass retrieval: PALSAR observations and model analysis. In *Geoscience and Remote Sensing Symposium, 2008. IGARSS 2008. IEEE International*, Volume 3, pp. III –302 –III –305.
- Lavalle, M., D. Solimini, E. Pottier, and Y.-L. Desnos (2009). The dependence of the PolInSAR degree of coherence on forest parameters. In *Proceedings of PolInSAR workshop 2009*, Frascati, Italy.
- Lavalle, M., D. Solimini, E. Pottier, and Y.-L. Desnos (2010). Compact polarimetric SAR interferometry. *Radar, Sonar Navigation, IET 4*(3), 449–456.

- Lavalle, M., D. Solimini, E. Pottier, Y.-L. Desnos, B. Rosich, N. Miranda, and M. Santuari (2009). A new approach for PolInSAR forest parameters inversion: results using the ESA ALOS-PALSAR prototype processor. In *Proceedings of PolInSAR workshop 2009*, Frascati, Italy.
- Lavalle, M., D. Solimini, E. Pottier, and N. Miranda (2009). Faraday rotation estimation from unfocussed raw data: Analysis using ALOS-PALSAR data. In *Proceedings of PolInSAR workshop 2009*, Frascati, Italy.
- Lavalle, M., D. Solimini, B. Rosich, and E. Pottier (2009). Calibration of dual polarimetric C-band SAR data: A possible approach for Sentinel-1. In *Proceedings of PolInSAR workshop 2009*, Frascati, Italy.
- Lavalle, M., M. Williams, S. Hensley, E. Pottier, and D. Solimini (2009). Dependence of P-band interferometric height on forest parameters from simulation and observation. In *Geoscience and Remote Sensing Symposium, 2009 IEEE International, IGARSS 2009*, Volume 4, pp. IV-5 –IV-8.
- Le Toan, T., A. Beaudoin, J. Riom, and D. Guyon (1992). Relating forest biomass to sar data. *Geoscience and Remote Sensing, IEEE Transactions on* 30(2), 403–411.
- Lee, J. and E. Pottier (2009). *Polarimetric Radar Imaging: From Basics to Applications*. CRC Press.
- Lee, J.-S., S. Cloude, K. Papathanassiou, M. Grunes, and I. Woodhouse (2003). Speckle filtering and coherence estimation of polarimetric sar interferometry data for forest applications. *Geoscience and Remote Sensing, IEEE Transactions on* 41(10), 2254–2263.
- Lee, J.-S., M. Grunes, T. Ainsworth, L.-J. Du, D. Schuler, and S. Cloude (1999). Unsupervised classification using polarimetric decomposition and the complex wishart classifier. *Geoscience and Remote Sensing, IEEE Transactions on* 37(5), 2249–2258.
- Lee, J. S., K. W. Hoppel, S. A. Mango, and A. R. Miller (1994). Intensity and phase statistics of multilook polarimetric and interferometric sar imagery. *IEEE Transactions on Geoscience and Remote Sensing* 30, 1017.
- Lee, S., F. Kugler, I. Hajnsek, and K. Papathanassiou (2009). The impact of temporal decorrelation over forest terrain in polarimetric sar interferometry. In *PolInSAR workshop 2009*, Frascati, Italy.
- Lombardini, F. and M. Pardini (2008). 3-D SAR Tomography: The Multibaseline Sector Interpolation Approach. *IEEE Geoscience and Remote Sensing Letters* 5(4), 630–634.
- Lucas, R., A. Lee, and M. Williams (2006). Enhanced simulation of radar backscatter from forests using lidar and optical data. *Geoscience and Remote Sensing, IEEE Transactions on* 44(10), 2736–2754.

- Massonnet, D., P. Briole, and A. Arnaud (1995). Deflation of Mount Etna monitored by spaceborne radar interferometry. *Nature* 375, 567–570.
- Massonnet, D., M. Rossi, C. Carmona, F. Adagna, G. Peltzer, K. Feigl, and T. Rabaute (1993). The displacement field of the Landers earthquake mapped by radar interferometry. *Nature* 364(8), 138–142.
- Matzler, C. (1994). Microwave (1-100 ghz) dielectric model of leaves. *Geoscience and Remote Sensing, IEEE Transactions on* 32(4), 947–949.
- Mette, T., K. Papathanassiou, and I. Hajnsek (2004). Biomass estimation from polarimetric sar interferometry over heterogeneous forest terrain. In *Geoscience and Remote Sensing Symposium, 2004. IGARSS '04. Proceedings. 2004 IEEE International*, Volume 1, pp. 511–514.
- Meyer, F. and J. Nicoll (2007). Ionospheric effects on SAR, InSAR, and SAR Polarimetry - Theory and experiences with ALOS/PALSAR. *Fringe 2007 Workshop, Proceedings of, Frascati, Italy*.
- Moghaddam, M. (1999). Effect of medium symmetries in limiting the number of parameters estimated with polarimetric interferometry. *Geoscience and Remote Sensing Symposium, 1999. IGARSS '99 Proceedings. IEEE 1999 International 4*, 2221–2223 vol.4.
- Neeff, T., L. Dutra, J. dos Santos, C. da Costa Freitas, and L. Araujo (2003). Tropical forest biomass measurement by backscatter and dem information as derived from airborne sar. In *Geoscience and Remote Sensing Symposium, 2003. IGARSS '03. Proceedings. 2003 IEEE International*, Volume 4, pp. 2571–2573 vol.4.
- Neumann, M. (2009). *Remote sensing of vegetation using multi-baseline polarimetric SAR interferometry: theoretical modeling and physical parameter retrieval*. Ph. D. thesis, University of Rennes 1.
- Neumann, M., L. Ferro-Famil, and A. Reigber (2008). Multibaseline polarimetric sar interferometry coherence optimization. *Geoscience and Remote Sensing Letters, IEEE* 5(1), 93–97.
- Nghiem, S. V., S. H. Yueh, R. Kwok, and F. K. Li (1992). Symmetry properties in polarimetric remote sensing. *Radio Science* 27, 693–711.
- Nord, M., T. Ainsworth, J.-S. Lee, and N. Stacy (2009). Comparison of compact polarimetric synthetic aperture radar modes. *Geoscience and Remote Sensing, IEEE Transactions on* 47(1), 174–188.
- Novak, L. and M. Burl (1990). Optimal speckle reduction in polarimetric sar imagery. *Aerospace and Electronic Systems, IEEE Transactions on* 26(2), 293–305.
- Ogilvy, J. (1991). *Theory of Wave Scattering From Random Rough Surfaces*. Taylor & Francis.

- Oh, Y., Y.-M. Jang, and K. Sarabandi (2002). Full-wave analysis of microwave scattering from short vegetation: an investigation on the effect of multiple scattering. *Geoscience and Remote Sensing, IEEE Transactions on* 40(11), 2522–2526.
- Papathanassiou, K. (1999). *Polarimetric SAR Interferometry*. Ph. D. thesis, Technische Universität Graz.
- Papathanassiou, K. and S. Cloude (2001). Single-Baseline Polarimetric SAR Interferometry. *Geoscience and Remote Sensing, IEEE Transactions on* 39(11), 2352–2363.
- Papathanassiou, K. and S. Cloude (2003). The Effect of Temporal Decorrelation on the Inversion of Forest Parameters from PolInSAR Data. *Geoscience and Remote Sensing Symposium 2003 (IGARSS '03), IEEE International Proceedings of* 2.
- Papathanassiou, K., I. Hajnsek, T. Nagler, , and H. Rott (2005). Polarimetric sar interferometry for snow cover parameter estimation. *ESA PolInSAR 2005 Workshop, Proceedings of, Frascati, Italy*.
- Papathanassiou, K., L. Marotti, and I. Hajnsek (2008). Alos/palsar pol-insar results. In *International ALOS PI Symposium 2008*, Rhodes, Greece.
- Papathanassiou, K. P., S. Cloude, A. Liseno, T. Mette, and H. Pretzsch (2005). Forest Height Estimation by means of Polarimetric SAR Interferometry: Actual Status and Perspectives. *ESA PolInSAR 2005 Workshop, Proceedings of, Frascati, Italy*.
- Papoulis, A. (1991). *Probability, Random variables, and stochastic processes*. McGraw-Hill series in Electrical Engineering. New York: McGraw-Hill.
- Pasquali, P., A. Monti-Guarnieri, D. D'aria, L. Costa, D. Small, M. Jehle, and B. Rosich (2007). Alos palsar verification processor. In *Proceedings of Envisat Symposium 2007*, Montreaux, Switzerland.
- Pham, D. (1996). Blind separation of instantaneous mixture of sources via an independent component analysis. *Signal Processing, IEEE Transactions on* 44(11), 2768–2779.
- Pottier, E., L. Ferro-Famil, S. Allain, S. Cloude, I. Hajnsek, K. Papathanassiou, A. Moreira, M. Williams, A. Minchella, M. Lavallo, and Y.-L. Desnos (2009). Overview of the PolSARpro v4.0 software. In *PolInSAR workshop 2009*, Frascati, Italy.
- Prati, C., F. Rocca, and A. Monti Guarnieri (1989). Effects of speckle and additive noise on the altimetric resolution of interferometric SAR (ISAR) surveys. In *Proc. IGARSS'89, Vancouver*, pp. 2469–2472.
- Prevot, L., M. Dechambre, O. Taconet, D. Vidal-Madjar, M. Normand, and S. Gallej (1993). Estimating the characteristics of vegetation canopies with airborne radar measurements. *International Journal of Remote Sensing* 14(15), 2803–2818.

- Quegan, S. (1994). A unified algorithm for phase and cross-talk calibration of polarimetric data-theory and observations. *Geoscience and Remote Sensing, IEEE Transactions on* 32(1), 89–99.
- Raney, R. (2007). Hybrid-polarity sar architecture. *Geoscience and Remote Sensing, IEEE Transactions on* 45(11), 3397–3404.
- Raney, R. and A. Freeman (2009). Hybrid-Polarity SAR Architecture. *PolInSAR Workshop, Proceedings of, Frascati, Italy*.
- Raney, R. K., H. Runge, R. Bamler, I. G. Cumming, and F. H. Wong (1994). Precision SAR processing using chirp scaling. *IEEE Transactions on Geoscience and Remote Sensing* 32(4), 786–799.
- Reigber, A. and A. Moreira (2000). First demonstration of airborne sar tomography using multibaseline l-band data. *Geoscience and Remote Sensing, IEEE Transactions on* 38(5), 2142–2152.
- Rignot, E. and R. Chellappa (1992). Segmentation of polarimetric synthetic aperture radar data. *Image Processing, IEEE Transactions on* 1(3), 281–300.
- Rocca, F. (1987). Synthetic aperture radar: A new application for wave equation techniques. *Stanford Exploration Project Report SEP-56*, 167–189.
- Rocca, F. (2007). Modeling Interferogram Stacks. *Geoscience and Remote Sensing, IEEE Transactions on* 45(10), 3289–3299.
- Rodriguez, E. and J. M. Martin (1992). Theory and Design of Interferometric Synthetic Aperture Radars. *IEE Proceedings-F* 139(2), 147–159.
- Rosenqvist, A., M. Shimada, N. Ito, and M. Watanabe (2007). ALOS PALSAR: A pathfinder mission for global-scale monitoring of the environment. *Geoscience and Remote Sensing, IEEE Transactions on* 45(11), 3307–3316.
- Ruck, G. T., D. E. Barrick, W. D. Stuart, and C. K. Krichbaum (1970). *Radar Cross Section Handbook. Volumes 1 & 2*. Plenum.
- Sagues, L., J. Lopez-Sanchez, J. Fortuny, X. Fabregas, A. Broquetas, and A. Sieber (2000). Indoor experiments on polarimetric sar interferometry. *Geoscience and Remote Sensing, IEEE Transactions on* 38(2), 671–684.
- Schneider, R., K. Papathanassiou, I. Hajnsek, and A. Moreira (2005). Polarimetric interferometry over urban areas: information extraction using coherent scatterers. In *Geoscience and Remote Sensing Symposium, 2005. IGARSS '05. Proceedings. 2005 IEEE International*, Volume 2, pp. 1089–1092.

- Sheen, D., E. Johansen, L. Elenbogen, and E. Kasischke (1992). The gridded trihedral: a new polarimetric sar calibration reflector. *Geoscience and Remote Sensing, IEEE Transactions on* 30(6), 1149–1153.
- Shiffer, R. and K. Thielheim (1979). Light scattering by dielectric needles and disks. *J. Applied Physics* 50(4), 2476–2483.
- Shimada, M., O. Isoguchi, T. Tadono, R. Higuchi, and K. Isono (2007). Palsar calval summary and update 2007. In *Geoscience and Remote Sensing Symposium, 2007. IGARSS 2007. IEEE International*, pp. 3593–3596.
- Sinclair, G. (1950). The transmission and reception of elliptically polarized waves. *Proceedings of the IRE* 38(2), 148–151.
- Souyris, J.-C., P. Imbo, R. Fjortoft, S. Mingot, and J.-S. Lee (2005). Compact polarimetry based on symmetry properties of geophysical media: the $\pi/4$ mode. *Geoscience and Remote Sensing, IEEE Transactions on* 43(3), 634–646.
- Souyris, J.-C. and S. Mingot (2002). Polarimetry based on one transmitting and two receiving polarizations: the $\pi/4$ mode. In *Geoscience and Remote Sensing Symposium, 2002. IGARSS '02. 2002 IEEE International*, Volume 1, pp. 629–631 vol.1.
- Stiles, J. and K. Sarabandi (2000). Electromagnetic scattering from grassland. i. a fully phase-coherent scattering model. *Geoscience and Remote Sensing, IEEE Transactions on* 38(1), 339–348.
- Tabb, M., J. Orrey, T. Flynn, and R. Carande (2002). Phase diversity: A decomposition for vegetation parameter estimation using polarimetric sar interferimetry. *EUSAR 2002, Proceedings of*, 721–724.
- Tarantola, A. (2005). *Inverse Problem Theory and Model Parameter Estimation*. SIAM.
- Tatarskii, V. (1964). Propagation of electromagnetic wave in a medium with strong dielectric constant fluctuations. *Soviet Phys. JEPT* 19, 946–953.
- Touzi, R. (2009). Compact-hybrid mode versus linear-dual and fully polarimetric SAR. *PolIn-SAR Workshop, Proceedings of, Frascati, Italy*.
- Touzi, R., A. Lopes, J. Bruniquel, and P. W. Vachon (1999). Coherence estimation for SAR imagery. *IEEE Transactions on Geoscience and Remote Sensing* 1(37), 135–149.
- Treuhaft, R. and P. Siqueira (2000). Vertical structure of vegetated land surfaces from interferometric and polarimetric radar. *Radio Science* 35(1), 141–178.
- Tsang, L., K.-H. Ding, G. Zhang, C. Hsu, and J. A. Kong (1995). Backscattering enhancement and clustering effects of randomly distributed dielectric cylinders overlying a dielectric half space based on monte-carlo simulations. *Antennas and Propagation, IEEE Transactions on* 43(5), 488–499.

- Tsang, L., J. Kong, and K. Ding (2000). *Scattering of Electromagnetic Waves: Theories and Applications*, Volume 1. John Wiley & Sons.
- Tsang, L., J. Kong, and R. Shin (1985). *Theory of Microwave Remote Sensing*. Wiley Series in Remote Sensing.
- Tsang, L. and J. A. Kong (1981). Application of strong fluctuation random medium theory to scattering from vegetation-like half space. *Geoscience and Remote Sensing, IEEE Transactions on GE-19*(1), 62–69.
- Twomey, S., H. Jacobowitz, and H. Howell (1966). Matrix methods for multiple-scattering problems. *Journal of the Atmospheric Sciences* 23(3), 289–298.
- Ulaby, F. and M. El-Rayes (1987). Microwave dielectric spectrum of vegetation - part ii: Dual-dispersion model. *Geoscience and Remote Sensing, IEEE Transactions on GE-25*(5), 550–557.
- Ulaby, F. T. and C. Elachi (1990). *Radar Polarimetry for Geoscience Applications*. Artech House.
- Ulaby, F. T., R. K. Moore, and A. K. Fung (1986a). *Microwave Remote Sensing: Active and Passive*, Volume 2. Artech House.
- Ulaby, F. T., R. K. Moore, and A. K. Fung (1986b). *Microwave Remote Sensing: Active and Passive*, Volume 3. Artech House.
- Ulaby, F. T., K. Sarabandi, K. Y. L. E. McDonald, M. Whitt, and M. C. Dobson (1990). Michigan microwave canopy scattering model. *International Journal of Remote Sensing* 11(7), 1223–1253.
- van Zyl, J. (1989). Unsupervised classification of scattering behavior using radar polarimetry data. *Geoscience and Remote Sensing, IEEE Transactions on* 27(1), 36–45.
- van Zyl, J. (1990). Calibration of polarimetric radar images using only image parameters and trihedral corner reflector responses. *Geoscience and Remote Sensing, IEEE Transactions on* 28(3), 337–348.
- van Zyl, J., H. Zebker, and C. Elachi (1987). Imaging radar polarization signatures: Theory and observations. *Radio Science* 22, 529–543.
- Wheeler, K. and S. Hensley (2000). The geosar airborne mapping system. In *Radar Conference, 2000. The Record of the IEEE 2000 International*, pp. 831–835.
- Williams, M. (2006a). PolSARproSim: A Coherent, Polarimetric SAR Simulation of Forests for PolSARpro. *Design Document and Algorithm Specification (u1.0)* <http://earth.esa.int/polsarpro/>.

- Williams, M. (2006b). The Theory of a forward SAR Model: Implementations, Applications and Challenges. *EUSAR 2006, Proceedings of, Dresden, Germany*.
- Williams, M., E. Pottier, L. Ferro-Famil, S. Allain, S. Cloude, I. Hajnsek, K. Papathanassiou, A. Moreira, A. Minchella, and Y.-L. Desnos (2007). Forest Coherent SAR Simulator within PolSARPro: an Educational Toolbox for PolSAR and PolInSAR Data Processing. *Asian Conference on Remote Sensing, Kuala Lumpur, Malaysia*.
- Wright, P., P. Meadows, G. Mack, N. Miranda, and M. Lavalley (2008). Aden ALOS-PALSAR product verification. In *Proceedings of International ALOS PI Symposium 2008*, Rhodes, Greece.
- Wright, P., S. Quegan, N. Wheadon, and C. Hall (2003a). Faraday rotation effects on l-band spaceborne sar data. *Geoscience and Remote Sensing, IEEE Transactions on* 41(12), 2735–2744.
- Wright, P., S. Quegan, N. Wheadon, and C. Hall (2003b). Faraday rotation effects on l-band spaceborne sar data. *Geoscience and Remote Sensing, IEEE Transactions on* 41(12), 2735–2744.
- Zebker, H. and J. Villasenor (1992a). Decorrelation in interferometric radar echoes. *Geoscience and Remote Sensing, IEEE Transactions on* 30(5), 950–959.
- Zebker, H. A. and R. M. Goldstein (1986). Topographic mapping from interferometric synthetic aperture radar observations. *Journal of Geophysical Research* 91(B5), 4993–4999.
- Zebker, H. A., P. A. Rosen, R. M. Goldstein, A. Gabriel, and C. L. Werner (1994). On the derivation of coseismic displacement fields using differential radar interferometry: The Landers earthquake. *Journal of Geophysical Research* 99(B10), 19617–19634.
- Zebker, H. A. and J. J. van Zyl (1991). Imaging radar polarimetry: A review. *Proceedings of the IEEE* 79(11), 1583–1606.
- Zebker, H. A. and J. Villasenor (1992b). Decorrelation in Interferometric Radar Echoes. *IEEE Transactions on Geoscience and Remote Sensing* 30(5), 950–959.